

**PHOTOVOLTAICS AND SPECTRO-
ELECTROCHEMISTRY OF NiCuZn ORGANIC-
INORGANIC HYBRID PEROVSKITE
NANOMATERIALS**



By

MOLEKO SAMUEL MKEHLANE

A thesis submitted in fulfilment of the requirements for the degree

of

PHILOSOPHAE SCIENTIAE

In the

**Department of Chemistry, Faculty of Science
University of the Western Cape, South Africa**

Supervisor: Prof Emmanuel I. Iwuoha

Co-supervisors: Dr Milua Masikini and Dr Suru V. John-Denk

October 2021

ABSTRACT

Despite the remarkable progress made by hybrid perovskite thin film materials $\text{CH}_3\text{NH}_3\text{PbI}_3$ in the arena of thin film photovoltaics, their shift to penetrating the commercial market is still an on-going research due to poor intrinsic stability and the issue of eco-toxicity posed by metal Pb. The chief aim of this study was to prepare air-stable hybrid perovskite thin film materials incorporating earth abundant and non-toxic transition metals which include Ni, Cu & Zn (doped at 1, 5 and 10%); $\text{CH}_3\text{NH}_3\text{PbI}_3\cdot\text{Ni}$, $\text{CH}_3\text{NH}_3\text{PbI}_3\cdot\text{Cu}$ & $\text{CH}_3\text{NH}_3\text{PbI}_3\cdot\text{Zn}$, employing a two-step solution deposition technique. The terephthalic acid (TPA) additive was utilized to stabilize thin film materials from deterioration upon exposure to air.

The successful incorporation of transition metals; Ni, Cu, and Zn into the perovskite crystal structure was confirmed by core level X-ray Photoelectron Spectroscopy (XPS) measurements. X-ray diffraction (XRD) measurements revealed that all hybrid perovskite thin film materials assumed a pure perovskite phase in the tetragonal crystal system without a significant impact on the lattice parameters and space group. XRD analyses also revealed that the two-step solution deposition technique employed in this study resulted in strained hybrid perovskite thin films with structural defects/dislocation density. The $\text{CH}_3\text{NH}_3\text{PbI}_3\cdot\text{Zn}$ thin films (followed by $\text{CH}_3\text{NH}_3\text{PbI}_3\cdot\text{Ni}$) were the least strained and highly crystalline among all NiCuZn hybrid perovskite thin films. High degree of dislocation density and poor crystallinity were observed for $\text{CH}_3\text{NH}_3\text{PbI}_3\cdot\text{Cu}$ thin films. The differences in degree of crystallinity and dislocation densities (defects) were attributed to different mechanical properties of Ni, Cu and Zn dopants.

High Resolution Scanning Electron Microscopy (HR-SEM) revealed a layer of small sheet-shaped perovskite grains at the vicinity of pristine $\text{CH}_3\text{NH}_3\text{PbI}_3$. HR-SEM also revealed that Ni and Zn dopants (at 10% concentration) suppressed the growth of these sheet-shaped

perovskite grains at the vicinity of $\text{CH}_3\text{NH}_3\text{PbI}_3\cdot\text{Ni}$ and $\text{CH}_3\text{NH}_3\text{PbI}_3\cdot\text{Zn}$ thin films, respectively. However, $\text{CH}_3\text{NH}_3\text{PbI}_3\cdot\text{Cu}$ exhibited a coarse morphology as the Cu content was increased from 1 to 10% suggesting high degree of structural defects imposed by Cu dopant. Atomic Force Microscopy (AFM) results correlated with the HR-SEM and XRD results. Reduced surface roughness was observed for thin films devoid of a layer of small sheet-shaped perovskite grains at the vicinity of hybrid perovskite grain boundaries; i.e. $\text{CH}_3\text{NH}_3\text{PbI}_3\cdot 10\%\text{Ni}$ and $\text{CH}_3\text{NH}_3\text{PbI}_3\cdot 10\%\text{Zn}$, respectively. AFM results also revealed that the Cu dopant resulted in $\text{CH}_3\text{NH}_3\text{PbI}_3\cdot\text{Cu}$ hybrid perovskite thin films with drastically heightened surface roughness attributed to the high degree of surface defects.

Optical studies by Ultra Violet visible (UV-vis) and Photoluminescence (PL) spectroscopy showed that NiCuZn hybrid perovskite thin film materials ($E_g \approx 1.56$ eV) explored in this study largely absorb from the visible (≈ 500 nm) to the near infra-red (≈ 800 nm) and emit towards the near infra-red region (770 nm to 795nm) of the solar spectrum. PL studies revealed quenching effect (non-radiative recombination emission effect) for $\text{CH}_3\text{NH}_3\text{PbI}_3\cdot\text{Ni}$ and $\text{CH}_3\text{NH}_3\text{PbI}_3\cdot\text{Cu}$ thin films induced by Ni and Cu dopants. However, for Zn doped thin film materials $\text{CH}_3\text{NH}_3\text{PbI}_3\cdot\text{Zn}$, a reverse effect was observed, Zn dopant advanced the radiative recombination emissions exhibited in higher PL emission intensity as the Zn content was increased from 1 to 10%. These results were attributed to high crystallinity, compact surface morphology and topography, relaxed micro-strain and lower degree of dislocation density induced by Zn in $\text{CH}_3\text{NH}_3\text{PbI}_3\cdot\text{Zn}$ thin films, positioning Zn as the best candidate amongst Ni and Cu for Pb-substitution in the traditional $\text{CH}_3\text{NH}_3\text{PbI}_3$. This study contributes substantially to the ongoing research in pursuit for non-toxic and air-stable hybrid perovskite thin film materials for photovoltaic (PV) applications.

$\text{Cu}_2\text{ZnSn}(\text{S},\text{Se})_4$ (CZTSSe) kesterite absorber materials have emerged as potential candidates for earth abundant and non-toxic PVs with great prospects for long-term sustainability in the arena of solar cell technology. However, the low open circuit voltage (V_{OC}) in kesterite absorber materials is the common constraint limiting the photovoltaic performance in all kesterite-based solar cells chiefly when compared to the highest possible V_{OC} value ruled by the Shockley-Queisser radiative limit ($V_{\text{OC,SQ}}$). This study seeks to address the issue of low V_{OC} and it was inspired by the beneficial impacts demonstrated by nanometric layers of Ge (as well partial substitution of Sn atoms by Ge atoms) on the photovoltaic performance (especially the V_{OC}) and the advance material quality of CZTSe-based solar cells reported in literature.

The development of pure germanium kesterite $\text{Cu}_{1.8}\text{Zn}_{1.2}\text{GeSe}_4$ (CZGSe) solar cells with architecture: Mo/p-CZGSe/n-CdS/i-ZnO:ITO, produced employing a two-step sequential co-sputtering technique was explored. The optimal CZGSe absorber ($E_g = 1.42$ eV) produced in this study from the corresponding optimal stack order: Mo/Cu(4nm, for 20s)/Zn/Cu/Ge subjected to the thermal treatment with annealing profile; $T = 535$ °C, dwelling time $t = 15$ min, $P = 1$ bar and 20 °C/min heating rate, yielded a corresponding solar cell device which attained record power conversion efficiency $\text{PCE} = 5.0\%$, open circuit voltage $V_{\text{OC}} = 564.53$ mV, V_{OC} (deficit) = 563.64 mV, short-circuit current density $J_{\text{SC}} = 17.60$ mA/cm² and a fill factor (FF) of 50.53% . A remarkable improvement in the $V_{\text{OC}} = 592.66$ mV with the corresponding $\text{PCE} = 4.46\%$, $J_{\text{SC}} = 14.19$ mA/cm² and $\text{FF} = 53.12\%$ attained through CdS buffer layer optimization was a milestone in comparison to the previously reported value of 558 mV for CZGSe in literature.

Raman spectroscopy revealed the presence of ZnSe ($E_g = 2.7$ eV) secondary phases (defects) on the surface of CZGSe ($E_g = 1.42$ eV) absorbers. High-Resolution Scanning Electron

Microscopy (HR-SEM) cross sectional area images also revealed the presence of defects at the Mo/CZGSe interface; i.e. a layer of voids and blisters attributed to the formation of GeSe₂(g) volatile species during thermal treatment. External Quantum Efficiency (EQE) measurements demonstrated that these defects; i.e. ZnSe ($E_g = 2.7$ eV) secondary phases and a layer of voids and blisters at the Mo/CZGSe interface, had detrimental impact on charge carrier collections and as a result limited the overall photovoltaic performance of solar cell devices ($PCE \leq 5\%$). This study contributes substantially to the development of CZGSe based kesterite solar cells as it provides a baseline standard and inspires future studies with the goal of improving the absorber quality and the PCE beyond 5%.



KEYWORDS

Dislocation density

Eco-toxicity

Grain boundaries

Germanium

Hybrid perovskite thin films

Kesterite

Micro-strain

Open-circuit voltage

Optical bandgap

One-step annealing profile

Photoluminescence

Photovoltaics

Power conversion efficiency

Secondary phases

Stability

Transition metals NiCuZn

Two-step solution deposition

Two-step co-sputtering

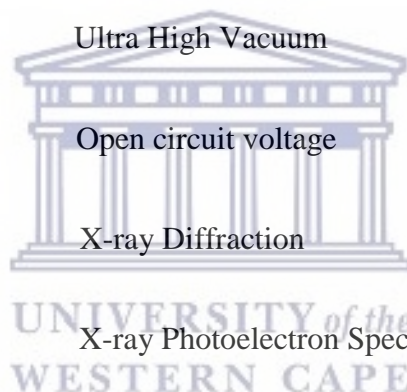


ABBREVIATIONS

AFM	Atomic Force Microscopy
Cu	Copper
CZGSe	Copper Zinc Germanium Selenide
CdS	Cadmium sulphide
CBE	Chemical Bath Etching
CBD	Chemical Bath Deposition
DMF	Dimethylformamide
DC	Direct Current
EQE	External Quantum Efficiency
FF	Fill Factor
FWHM	Full Width at Half Maximum
Ge	Germanium
He-Cd	Helium-Cadmium
HR-SEM	High-Resolution Scanning Electron Microscopy
ITO	Indium Tin Oxide
J_{sc}	Short circuit current density
Mo	Molybdenum
Ni	Nickel



PL	Photoluminescence
PMT	Photomultiplier
PCE	Power Conversion Efficiency
SLG	Soda Lime Glass
TPA	Terephthalic Acid
UV-vis	Ultra-violet visible
UHV	Ultra High Vacuum
V_{oc}	Open circuit voltage
XRD	X-ray Diffraction
XPS	X-ray Photoelectron Spectroscopy
XRF	X-ray Fluorescence
Zn	Zinc
ZnSe	Zinc selenide



DECLARATION

I declare that **Photovoltaics and spectro-electrochemistry of NiCuZn organic-inorganic hybrid perovskite nanomaterials** is my own work, that it has not been submitted before for any degree or examination in any other university, and that all the sources I have used or quoted have been indicated and acknowledged as complete references.

Signature:



Moleko Samuel Mkehlane

11 October 2021



DEDICATION

This thesis is dedicated to the loving memory of my late father; TLHORISO JOEL MKEHLANE, for raising me up to be a resilient and patient man I am today, for all the lessons of life he has taught me, for all the sacrifices he has made for me to have a better future and for all the bruises he took for me to survive in this jungle called life! I would like to thank you Papa, for never forsaking us when you were alive on earth. I will forever be indebted to you for your love and all you have done and provided for us when you walked the earth plane. Losing you was the hardest thing I ever dealt with in my entire life. Your death ripped my heart apart ...but it is well with my soul. I'm going to live the rest of my life to honour you and make you proud.

May your soul continue to rest in peace NDLANGISA!



ACKNOWLEDGEMENTS

First and foremost I would like to thank the Almighty God of Mount-Zion for giving me the strength and wisdom to complete this project and achieve this milestone. Lord I thank you; I could not have made it on my own.

I would like to express my gratitude to my supervisor *Prof Emmanuel Iwuoha* for the opportunity he has granted me to pursue my life goals. I would like to thank him for nominating me for the National Research Foundation (NRF) scholarship to finance my PhD studies.

I would like to thank my research colleague, a friend and a brother *Kevin Tambwe* for the assistance, significant inputs, support and useful discussions during difficult times. Thank you for the valuable and constructive interactions. This project wouldn't be a success without your significant inputs. May the Almighty God of Mount-Zion bless you and your family.

I would like to extend my sincere gratitude to my family, my late father (*Tlhoriso Joel Mkehlane*), my late nephew (*Orebabaletse Sihle Ishmael Mkehlane*), my mother (*Mamokgothunyana Merriam Kopamotse*), my younger sister (*Nthabiseng Evelyn Mkehlane*), my older brother (*Moratehi Petrus Mkehlane*), my two nieces (*Realeboga Mkehlane and Reamogetse Mkehlane*), for their support, understanding, patience, prayers, encouragements, and care when I needed them most. Thank you very much and may the Almighty God of Mount Zion continue to bless you abundantly in every area of your lives and keep you safe at all times.

LIST OF PUBLICATIONS

- Milua Masikini, **Moleko Samuel Mkehlane**, and Emmanuel Iwuoha, Synthesis and Characterizations of Mixed Tellurium and Iodine Anions based Chalcogen-Halogen Lead Perovskite, *Electroanalysis*, **2020**, 32, 2870 – 2881. (**Published**).
- **Moleko Samuel Mkehlane**, Milua Masikini, and Emmanuel Iwuoha, Electrochemical and Optical Studies of Organo-chalcogenic Perovskite nanomaterials with Potential Application in Single-Junction Solar Cells, *Electroanalysis*. (**To be submitted**).
- **Moleko Samuel Mkehlane** and Emmanuel Iwuoha, Structural, optical and microscopic analysis of NiCuZn doped hybrid perovskite thin films in quest for Pb-free hybrid perovskite materials, *Vacuum*. (**To be submitted**).
- **Moleko Samuel Mkehlane** and Emmanuel Iwuoha, Development of pure germanium kesterite CZGSe solar cells: Optimization studies, *Thin Solid Films*. (**To be submitted**).
- **Moleko Samuel Mkehlane** and Emmanuel Iwuoha, Review of the latest developments in Pb-free and air-stable hybrid perovskite photovoltaics, *Nano-Micro Letters*. (**To be submitted**).
- **Moleko Samuel Mkehlane** and Emmanuel Iwuoha, Review of the latest developments in germanium kesterite photovoltaics, *Nano-Micro Letters*. (**To be submitted**).

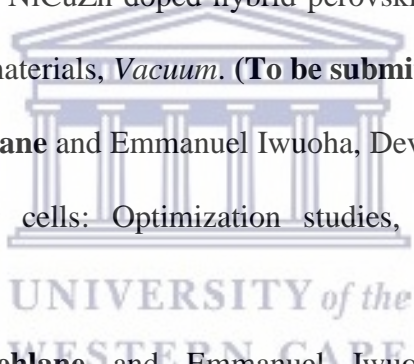
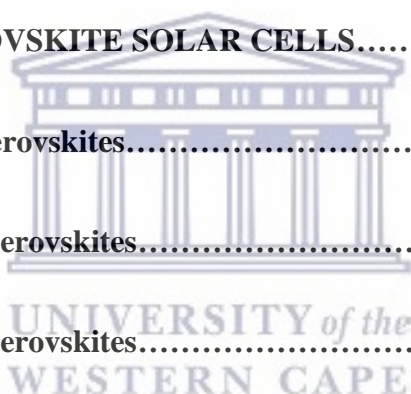



TABLE OF CONTENTS

TITLE PAGE.....	i
ABSTRACT.....	ii
KEYWORDS.....	vi
ABBREVIATIONS.....	vii
DECLARATION.....	ix
DEDICATION.....	x
ACKNOWLEDGEMENTS.....	xi
LIST OF PUBLICATIONS.....	xii
TABLE OF CONTENTS.....	xiii
LIST OF FIGURES.....	xix
LIST OF TABLES.....	xxv
CHAPTER 1: INTRODUCTION	
1.1 BACKGROUND ON PEROVSKITE AND KESTERITE MATERIALS.....	1
1.2 PROBLEM STATEMENT.....	4
1.3 MOTIVATION/RATIONAL.....	5
1.4 AIM AND OBJECTIVES.....	7
1.5 THESIS LAYOUT.....	9
Bibliography.....	11

CHAPTER 2: LITERATURE REVIEW

2.1 HYBRID PEROVSKITE SOLAR CELL MATERIALS.....	22
2.1.1 INTRODUCTION.....	22
2.1.2 STRUCTURAL CONFIGURATION OF PEROVSKITES.....	25
2.1.3 METAL HALIDE PEROVSKITES.....	28
2.1.4 DOPING MECHANISMS IN PEROVSKITES.....	32
2.1.5 LEAD AND OTHER TOXICITY.....	36
2.1.6 LEAD-FREE PEROVSKITE SOLAR CELLS.....	37
i. Sn-based halide perovskites.....	38
ii. Ge-based halide perovskites.....	39
iii. Bi-based halide perovskites.....	40
iv. Sb-based halide perovskites.....	41
2.1.7 FABRICATION TECHNIQUES OF PEROVSKITE THIN FILMS.....	42
2.1.8 STABILITY OF HYBRID PEROVSKITE MATERIALS.....	50
2.2 KESTERITE SOLAR CELL MATERIALS.....	52
2.2.1 INTRODUCTION.....	52
2.2.2 DOPING MECHANISMS IN KESTERITE MATERIALS.....	57
i. Intrinsic Doping.....	58
ii. Extrinsic Doping.....	62



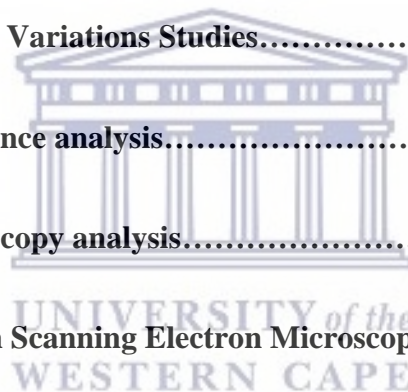
2.2.3 OPTIMIZING THE ENERGY BANDGAP OF KESTERITE ABSORBER AND ENGINEERING ITS ENERGY BANDGAP.....	68
i. Engineering Absorber Bandgap and Conduction Band Off-set at Junction Interface.....	69
2.2.4 Ge-ALLOYING IN KESTERITE MATERIALS.....	73
2.2.5 PHYSICAL ROUTES FOR THE SYNTHESIS OF KESTERITES.....	76
Bibliography.....	79
	
CHAPTER 3: EXPERIMENTAL DETAILS	
3.1 INTRODUCTION.....	145
3.2 REAGENTS.....	148
3.3 PROCEDURE FOR HYBRID PEROVSKITE THIN FILMS.....	148
3.3.1 Preparation of CH₃NH₃PbI₃ thin films.....	148
3.3.2 Preparation of Ni doped CH₃NH₃PbI₃•Ni thin films.....	149
3.3.3 Preparation of Cu doped CH₃NH₃PbI₃•Cu thin films.....	150
3.3.4 Preparation of Zn doped CH₃NH₃PbI₃•Zn thin films.....	151
3.3.5 Hybrid perovskite thin films characterization/analyses.....	152
3.4 PROCEDURE FOR DEVELOPMENT OF GZGSe SOLAR CELLS.....	153
3.4.1 Stack Order and Reactive Annealing Pressure Variations.....	153

3.4.2 Annealing Temperature Variations Studies.....	154
3.4.3 Chemical Bath Etching (CBE) studies with different solutions.....	155
3.4.4 CdS buffer layer optimization.....	155
3.4.5 General sample fabrication procedure.....	156
3.4.6 CZGSe sample characterization/analyses.....	158
Bibliography.....	160

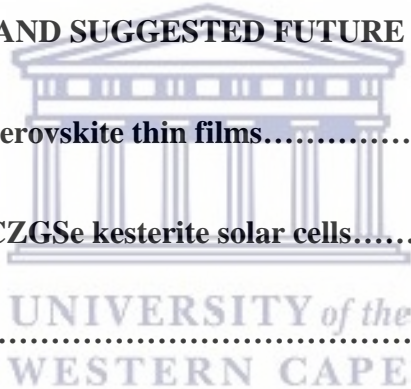
CHAPTER 4: EXPERIMENTAL RESULTS AND DISCUSSION

4.1 INTRODUCTION.....	167
4.2 NiCuZn HYBRID PEROVSKITE THIN FILMS.....	169
4.2.1 Structural Analysis by X-ray Diffraction (XRD).....	169
i. Purity and Degree of Crystallinity (peak-to-noise ratio).....	169
ii. Crystallite (grain) size.....	182
iii. Micro-strain.....	184
iv. Dislocation density.....	187
4.2.2 Surface analysis by X-ray Photoelectron Spectroscopy (XPS).....	190
4.2.3 Photo-physics studies by Ultra-violet visible (UV-vis) spectroscopy and Photoluminescence (PL).....	198
4.2.4 Microscopic analysis by High-Resolution Scanning Electron Microscopy	

HR-SEM).....	211
4.2.5 Microscopic analysis by Atomic Force Microscopy (AFM).....	221
4.3 DEVELOPMENT OF CZGSe-KESTERITE SOLAR CELLS.....	228
4.3.1 Stack Order and Reactive Annealing Pressure Variations.....	228
4.3.1.1 Raman spectroscopy analysis.....	228
4.3.1.2 High Resolution Electron Microscopy (HR-SEM) Analysis.....	229
4.3.1.3 Photovoltaic performance of solar cell devices.....	231
4.3.2 Annealing Temperature Variations Studies.....	235
4.3.2.1 X-ray Fluorescence analysis.....	235
4.3.2.2 Raman spectroscopy analysis.....	238
4.3.2.3 High Resolution Scanning Electron Microscopy (HR-SEM) analysis.....	239
4.3.2.4 Impact of the annealing temperature on the photovoltaic parameters...	243
4.3.3 Chemical Bath Etching (CBE) studies with different solutions.....	245
4.3.3.1 X-ray Fluorescence analysis.....	246
4.3.3.2 Raman spectroscopy analysis.....	247
4.3.3.3 High Resolution Scanning Electron Microscopy (HR-SEM) analysis and photovoltaic performance.....	249
4.3.4 CdS buffer layer optimization.....	255
4.3.4.1 XRF measurements.....	256



4.3.4.2 Photovoltaic performance measurements.....	258
Bibliography.....	261
CHAPTER 5: CONCLUSIVE SUMMARY AND RECOMMENDATIONS	
5.1 GENERAL CONCLUSION.....	291
5.1.1 NiCuZn hybrid perovskite thin films.....	291
5.1.2 Development of CZGSe kesterite solar cells.....	296
5.2 RECOMMENDATIONS AND SUGGESTED FUTURE WORK	
5.2.1 NiCuZn hybrid perovskite thin films.....	299
5.2.2 Development of CZGSe kesterite solar cells.....	300
Bibliography.....	303



LIST OF FIGURES

- Figure 2.1:** Different phase transitions of perovskite structures. Reproduced with permission from Ref. [82]. Copyright 2017, Elsevier.....27
- Figure 2.2:** Change in properties of metal halide perovskites after doping. Reproduced with permission from Ref. [110]. Copyright 2018, American Chemical Society.....33
- Figure 2.3:** Optical performance characteristics due to ion exchange mechanism. (a) Schematic of the ion exchange between CsPbBr_3 and $\text{CsPb}_{0.88}\text{Mn}_{0.12}\text{Cl}_3$ NCs. (b) UV (dashed line) and PL (solid line) spectrum of $\text{Cs}(\text{Pb}_x\text{Mn}_{1-x})(\text{Cl}_y\text{Br}_{1-y})_3$ with different Mn doping concentrations. (c) Ultraviolet photoelectron spectroscopy (UPS) of (i) of CsPbBr_3 , (ii) CsPbCl_3 , (iii) $\text{CsPb}_{0.88}\text{Mn}_{0.12}\text{Cl}_3$ and (iv), $\text{CsPb}_{0.93}\text{Mn}_{0.07}(\text{Cl}_{0.5}\text{Br}_{0.5})_3$ NCs. Reproduced with permission from Ref. [130]. Copyright 2017, Royal Society of Chemistry.....35
- Figure 2.4:** One-step and two-step spin-coating procedures for $\text{CH}_3\text{NH}_3\text{PbI}_3$ formation [179] used in accordance with the Creative Commons Attribution (CC BY) license.....43
- Figure 2.5:** (a) Schematic illustration of perovskite film formation through VASP, (b) cross-sectional SEM image, (c) current density-voltage (J - V) characteristics of the solar cell based on the as-prepared perovskite films under AM 1.5G illumination, and cross-section; SEM image of the device (inset). Reproduced with permission from Ref. [187]. Copyright, 2013, American Chemical Society.....45
- Figure 2.6:** (a) Hot-casting technique and (b) optical micrographs of grain formation as a function of substrate temperature with casting solution maintained at 70°C . (c) Large area grain formation using casting solvents with high boiling points. (d) Comparison of grain size as a function of processing temperature obtained for the hot-casting and conventional post-

annealing. Reproduced with permission from Ref. [191]. Copyright reserved 2015 by American Association for the Advancement of Science.....48

Figure 2.7: Schematic road map of substitution strategies considered, from $\text{Cu}_2\text{ZnSnS}_4$ (CZTS) to $\text{Cu}_2\text{CdGeS}_3\text{Se}$ (CCdGSSe), where C is Cu^{1+} , Z is Zn^{2+} , M is Mg^{2+} , T is Sn^{4+} , G is Ge^{4+} , $\downarrow\text{CZTGS}$ is $\text{Cu}_2\text{ZnSn}_{0.875}\text{Ge}_{0.125}\text{S}_4$, and $\uparrow\text{CZTGS}$ is $\text{Cu}_2\text{ZnSn}_{0.5}\text{Ge}_{0.5}\text{S}_4$. The horizontal and vertical axes correspond, respectively, to the concentration of Shockley-Read-Hall recombination centers (x_{SRH}) [250,251] and the energy bandgap (E_g), where E_g^{SQ} is the energy bandgap that maximizes the Shockley-Queisser (SQ) limit [254,255]. Red and green contours indicate regions of lower and higher solar cell efficiency, respectively. Reproduced with permission from Ref. [256]. Copyright 2021, The Royal Society of Chemistry.....54

Figure 2.8: Schematic representation of some sections of the Periodic Table, highlighting the most interesting candidates for doping and alloying in kesterite. Reproduced with permission from Ref. [289].....58

Figure 2.9: (a) First off-stoichiometric types kesterite (A-, B-, and C-type) proposed by Lafond *et al.* Reproduced with permission from Ref. [295]. Copyright 2012, Wiley-VCH. (b) Complete classification of off-stoichiometric kesterite presented by Gurieva *et al.* Reproduced with permission from Ref. [296]. Copyright 2018, Wiley-VCH.....59

Figure 2.10: (a) Combinatorial experiment showing the relationship of conversion efficiency with composition. (b) Secondary phases composition (at the surface) as a function of the kesterite composition. (a,b) Reproduced with permission from Ref. [302]. Copyright 2016, Elsevier.....61

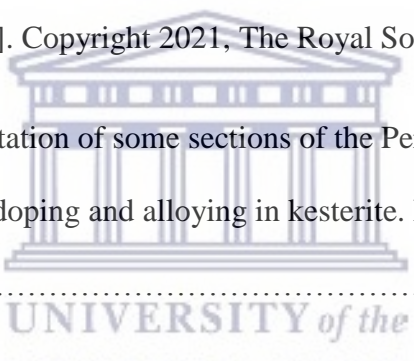


Figure 2.11: (a) Efficiency improvements of CZTSe solar cells with very small quantities of Ge. Reproduced with permission from Ref. [312]. Copyright 2015, Wiley-VCH. (b) Effect of Ge doping on the different optoelectronic properties. Reproduced with permission from Ref [315]. Copyright 2016, John Wiley and Sons.....65

Figure 2.12: Evolution of the maximum efficiency $\eta_{max}[\%]$ for (a) CZTS-based and (b) CZT(S,Se)-based cells over the period of 2016 – 2019. In figure legend WR stand for world record and EA stands for effective area. Reproduced with permission from Ref. [403].....78

Figure 4.1: Simulated crystal structure of tetragonal $\text{CH}_3\text{NH}_3\text{PbI}_3$ by VESTA (a). XRD patterns of pure traditional $\text{CH}_3\text{NH}_3\text{PbI}_3$ perovskite.....170

Figure 4.2: Simulated crystal structure of tetragonal Ni doped $\text{CH}_3\text{NH}_3\text{PbI}_3 \cdot \text{Ni}$ by VESTA (a). XRD patterns of pure and Zn doped $\text{CH}_3\text{NH}_3\text{PbI}_3$ (1, 5 and 10% Ni) perovskite thin films (b).....172

Figure 4.3: Simulated crystal structure of tetragonal Cu doped $\text{CH}_3\text{NH}_3\text{PbI}_3 \cdot \text{Cu}$ by VESTA (a). XRD patterns of pure and Cu doped $\text{CH}_3\text{NH}_3\text{PbI}_3$ (1, 5 and 10% Cu) perovskite thin films (b).....175

Figure 4.4: Simulated crystal structure of tetragonal Zn doped $\text{CH}_3\text{NH}_3\text{PbI}_3 \cdot \text{Zn}$ by VESTA (a). XRD patterns of pure and Zn doped $\text{CH}_3\text{NH}_3\text{PbI}_3$ (1, 5 and 10% Zn) perovskite thin films (b).....178

Figure 4.5: Crystallite size of transition metal perovskites; $\text{CH}_3\text{NH}_3\text{PbI}_3 \cdot \text{Ni}$ (a), $\text{CH}_3\text{NH}_3\text{PbI}_3 \cdot \text{Cu}$ (b), and $\text{CH}_3\text{NH}_3\text{PbI}_3 \cdot \text{Zn}$ (c).....183

Figure 4.6: Impact of transition metals content on macrostrain for $\text{CH}_3\text{NH}_3\text{PbI}_3 \cdot \text{Ni}$ (a), $\text{CH}_3\text{NH}_3\text{PbI}_3 \cdot \text{Cu}$ (b) and $\text{CH}_3\text{NH}_3\text{PbI}_3 \cdot \text{Zn}$ (c).....185

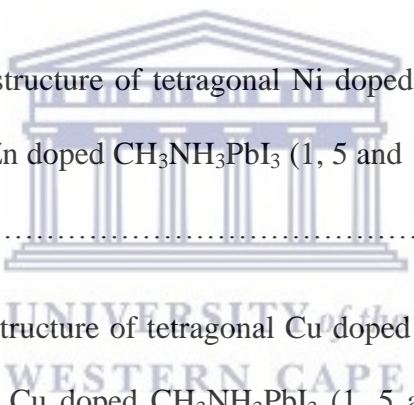


Figure 4.7: The relationship between micro-strain and crystallite size for $\text{CH}_3\text{NH}_3\text{PbI}_3\cdot\text{Ni}$ (a), $\text{CH}_3\text{NH}_3\text{PbI}_3\cdot\text{Cu}$ (b) and $\text{CH}_3\text{NH}_3\text{PbI}_3\cdot\text{Zn}$ (c).....	187
Figure 4.8: Impact of transition metals content on dislocation density for $\text{CH}_3\text{NH}_3\text{PbI}_3\cdot\text{Ni}$ (a), $\text{CH}_3\text{NH}_3\text{PbI}_3\cdot\text{Cu}$ (b) and $\text{CH}_3\text{NH}_3\text{PbI}_3\cdot\text{Zn}$ (c).....	188
Figure 4.9: The relationship between dislocation density and crystallite size for $\text{CH}_3\text{NH}_3\text{PbI}_3\cdot\text{Ni}$ (a), $\text{CH}_3\text{NH}_3\text{PbI}_3\cdot\text{Cu}$ (b) and $\text{CH}_3\text{NH}_3\text{PbI}_3\cdot\text{Zn}$ (c).....	190
Figure 4.10: XPS survey spectrum of a pure $\text{CH}_3\text{NH}_3\text{PbI}_3$ thin film. Most represents unique electronic atomic orbitals allowing for elemental identification.....	191
Figure 4.11: XPS high resolution scan for Pb4f (a), I3d (b), C1s (d), N1s (c).....	192
Figure 4.12: XPS high resolution scan for Ni2P _{1/2} and Ni2P _{3/2} for Ni doped $\text{CH}_3\text{NH}_3\text{PbI}_3\cdot\text{Ni}$ perovskite thin films (a, b and c).....	194
Figure 4.13: XPS high resolution scan for Cu2P _{1/2} and Cu2P _{3/2} for Cu doped $\text{CH}_3\text{NH}_3\text{PbI}_3\cdot\text{Cu}$ perovskite thin films.....	196
Figure 4.14: XPS high resolution scan for Zn2P _{1/2} for Zn doped $\text{CH}_3\text{NH}_3\text{PbI}_3\cdot\text{Zn}$ perovskite thin films.....	197
Figure 4.15: Absorption spectrum (a), $(ah\nu)^2$ vs. $h\nu$ (b) and photoluminescence spectrum of $\text{CH}_3\text{NH}_3\text{PbI}_3$ (c).....	199
Figure 4.16: Absorption spectrum (a), $(ah\nu)^2$ vs. $h\nu$ (b) and photoluminescence spectra (c, d, e) and photoluminescence quenching of $\text{CH}_3\text{NH}_3\text{PbI}_3\cdot\text{Ni}$ thin films (f).....	201
Figure 4.17: Absorption spectrum (a), $(ah\nu)^2$ vs. $h\nu$ (b) and photoluminescence spectra (c, d, e) and photoluminescence quenching (f) of $\text{CH}_3\text{NH}_3\text{PbI}_3\cdot\text{Cu}$ thin films.....	204

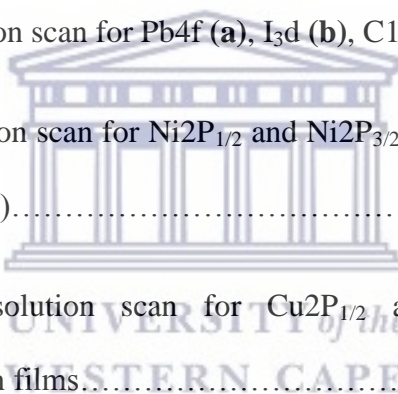
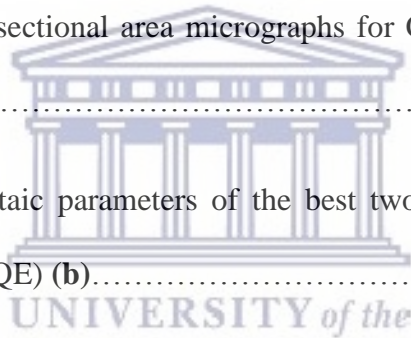


Figure 4.18: Absorption spectrum (a), $(ah\nu)^2$ vs. $h\nu$ (b) and photoluminescence spectra (c, d, e) and photoluminescence quenching (f) of $\text{CH}_3\text{NH}_3\text{PbI}_3\cdot\text{Zn}$ thin films.....	206
Figure 4.19: Top view HR-SEM images of pure tetragonal $\text{CH}_3\text{NH}_3\text{PbI}_3$ perovskite thin-films (a) morphology and (a') surface coverage.....	212
Figure 4.20: Top view HR-SEM images of Ni doped $\text{CH}_3\text{NH}_3\text{PbI}_3\cdot\text{Ni}$ perovskite thin films; $\text{CH}_3\text{NH}_3\text{PbI}_3\cdot 1\%\text{Ni}$ (a), $\text{CH}_3\text{NH}_3\text{PbI}_3\cdot 5\%\text{Ni}$ (b) and $\text{CH}_3\text{NH}_3\text{PbI}_3\cdot 10\%\text{Ni}$ (c).....	214
Figure 4.21: Top view HR-SEM images of Cu doped $\text{CH}_3\text{NH}_3\text{PbI}_3\cdot\text{Cu}$ perovskite thin films; $\text{CH}_3\text{NH}_3\text{PbI}_3\cdot 1\%\text{Cu}$ (a), $\text{CH}_3\text{NH}_3\text{PbI}_3\cdot 5\%\text{Cu}$ (b) and $\text{CH}_3\text{NH}_3\text{PbI}_3\cdot 10\%\text{Cu}$ (c).....	216
Figure 4.22: Top view HR-SEM images of Zn doped $\text{CH}_3\text{NH}_3\text{PbI}_3\cdot\text{Zn}$ perovskite thin films; $\text{CH}_3\text{NH}_3\text{PbI}_3\cdot 1\%\text{Zn}$ (a), $\text{CH}_3\text{NH}_3\text{PbI}_3\cdot 5\%\text{Zn}$ (b) and $\text{CH}_3\text{NH}_3\text{PbI}_3\cdot 10\%\text{Zn}$ (c).....	218
Figure: 4.23: Top view AFM images of pure tetragonal $\text{CH}_3\text{NH}_3\text{PbI}_3$ perovskite thin-film, 1D (a) and 3D (a') representation.....	221
Figure: 4.24: Top view AFM images of Ni doped $\text{CH}_3\text{NH}_3\text{PbI}_3\cdot\text{Ni}$ perovskite thin films; $\text{CH}_3\text{NH}_3\text{PbI}_3\cdot 1\%\text{Ni}$ (a), $\text{CH}_3\text{NH}_3\text{PbI}_3\cdot 5\%\text{Ni}$ (b) and $\text{CH}_3\text{NH}_3\text{PbI}_3\cdot 10\%\text{Ni}$ (c).....	222
Figure: 4.25: Top view AFM images of Cu doped $\text{CH}_3\text{NH}_3\text{PbI}_3\cdot\text{Cu}$ perovskite thin films; $\text{CH}_3\text{NH}_3\text{PbI}_3\cdot 1\%\text{Cu}$ (a), $\text{CH}_3\text{NH}_3\text{PbI}_3\cdot 5\%\text{Cu}$ (b) and $\text{CH}_3\text{NH}_3\text{PbI}_3\cdot 10\%\text{Cu}$ (c).....	224
Figure: 4.26: Top view AFM images of Zn doped $\text{CH}_3\text{NH}_3\text{PbI}_3\cdot\text{Zn}$ perovskite thin films; $\text{CH}_3\text{NH}_3\text{PbI}_3\cdot 1\%\text{Zn}$ (a), $\text{CH}_3\text{NH}_3\text{PbI}_3\cdot 5\%\text{Zn}$ (b) and $\text{CH}_3\text{NH}_3\text{PbI}_3\cdot 10\%\text{Zn}$ (c).....	226
Figure 4.27: Raman spectra at an excitation wavelength of 532 nm for CZGSe thin films prepared at different annealing pressures; 700 mbar and 1bar.....	228
Figure 4.28: HR-SEM images (cross sectional area) for CZGSe devices prepared at 700 mbar and 1 bar.....	230

Figure 4.29: Record photovoltaic parameters of the best performing device (a) and external quantum efficiency (EQE) (b) for CZGSe (A).....	233
Figure 4.30: Ge content as a function of temperature (a). Se content as a function of temperature (b).....	237
Figure 4.31: Raman spectra near the absorber CZGSe surface samples prepared at different temperatures (500, 525, 535 and 550 °C) at 442 nm excitation wavelength.....	238
Figure 4.32: HR-SEM cross sectional area micrographs for CZGSe absorber annealed at 500 °C.....	240
Figure 4.33: HR-SEM cross sectional area micrographs for CZGSe absorbers annealed at 500, 525, 535 and 5500 °C.....	241
Figure 4.34: Record photovoltaic parameters of the best two performing devices (a) and external quantum efficiency (EQE) (b).....	244
Figure 4.35: Raman spectra of CZGSe absorbers post CBE stage at an excitation wavelength of 442 nm.....	248
Figure 4.36: HR-SEM top view micrographs for the CZGSe absorbers etched with different solutions (post CBE).....	250
Figure 4.37: Record photovoltaic parameters of the best performing devices (a) and external quantum efficiency (EQE) (b).....	252
Figure 4.38: Record photovoltaic parameters for the best performing CZGSe devices (a) and external quantum efficiency (EQE) (b).....	258



LIST OF TABLES

Table 2.1. Examples of perovskites doped with different elements at their A-, B- and X-sites.....	34
Table 2.2. Defects considered and their effects on the physics of kesterite solar cells and solar cell parameters. X is Zn, Cd, or Mg; Y is Sn, Ge, or Si; E_g is the bandgap; V_{OC} is the open-circuit voltage; and I_{SC} is the short-circuit current.....	55
Table 2.3. Compilation of some of the most relevant devices reported in the literature which includes extrinsic doping. The V_{OC} deficit and V_{OC} gain are included for comparison of the different strategies. N/A: Not Available.....	67
Table 2.4. Energy bandgap (E_g) of CZTGeS and CZTGeSe absorber layers with different Ge/(Ge+Sn) ratio.....	73
Table 2.5. Compilation of some of the most relevant devices reported in the literature which includes alloying with Ge, Cd, and Ag.....	75
Table 4.1. Lattice parameters for crystal structure simulations by VESTA software.....	171
Table 4.2. Determination of the degree of crystallinity (peak to noise ratio).....	171
Table 4.3. Calculated lattice parameters for $CH_3NH_3PbI_3 \cdot Ni$ thin films.....	173
Table 4.4. Ni content in $CH_3NH_3PbI_3 \cdot Ni$ determined using Vergad's Law.....	174
Table 4.5. Determination of the degree of crystallinity (peak to noise ratio).....	174
Table 4.6. Calculated lattice parameters for $CH_3NH_3PbI_3 \cdot Cu$ thin films.....	176
Table 4.7. Cu content in $CH_3NH_3PbI_3 \cdot Cu$ determined using Vergad's Law.....	177

Table 4.8. Determination of the degree of crystallinity (peak to noise ratio).....	177
Table 4.9. Calculated lattice parameters for CH ₃ NH ₃ PbI ₃ •Zn thin films.....	179
Table 4.10. Zn content in CH ₃ NH ₃ PbI ₃ •Zn determined using Vergad’s Law.....	180
Table 4.11. Determination of the degree of crystallinity (peak to noise ratio).....	180
Table 4.12. Crystallite (grain) sizes of Ni, Cu, and Zn doped perovskites.....	182
Table 4.13. Summary of the elemental binding energies.....	193
Table 4.14. Summary of the Ni binding energies.....	195
Table 4.15. Summary of the Cu binding energies.....	196
Table 4.16. Summary of the Zn binding energy.....	198
Table 4.17. Record efficiencies for best performing devices annealed at 1bar.....	232
Table 4.18. Record efficiencies for best performing devices annealed at 700 mbar.....	233
Table 4.19. XRF measurements of the CZGSe precursor.....	236
Table 4.20. XRF measurements of CZGSe absorber after reactive selenization.....	236
Table 4.21. Record efficiencies of the devices annealed at different temperatures.....	243
Table 4.22. XRF measurements of the CZGSe absorber post reactive selenization.....	246
Table 4.23. XRF measurements of the CZGSe absorber post CBE stage.....	247
Table 4.24. Photovoltaic parameters of CZGSe devices fabricated from absorbers etched with different solutions.....	251

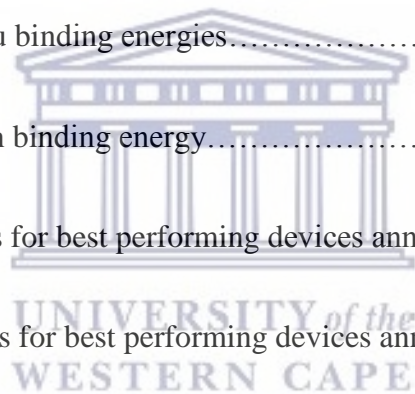


Table 4.25. XRF measurements of the CZGSe absorber prior chemical bath etching (CBE).....256

Table 4.26. XRF measurements of the CZGSe absorbers post chemical bath etching (CBE).....257

Table 4.27. Photovoltaic parameters of CZGSe devices fabricated with the optimized CdS buffer layer.....258

Table 4.28. Summary of photovoltaic parameters for CZGSe solar cell devices etched utilizing $\text{KMnO}_4/\text{H}_2\text{SO}_4$ followed by $(\text{NH}_4)_2\text{S}$ passivation route.....259

Table 4.29. Summary of record photovoltaic parameters for CZGSe solar cell devices etched utilizing $\text{KMnO}_4/\text{H}_2\text{SO}_4$ followed by $(\text{NH}_4)_2\text{S}$ passivation route.....260



CHAPTER 1

Introduction

1.1 BACKGROUND ON PEROVSKITE AND KESTERITE MATERIALS

The constant global population growth and urbanization call for the increasing demand for renewable energy resources and this demand cannot be satisfied with the limited fossil fuel resources [1,2]. The demand in renewable energy resources has been satisfied by natural renewable energy resources which include air, water, and sunlight over the last few decades. Developmental systems have been engineered for the harvest and storage of renewable energy resources. Energy storage devices which include batteries, supercapacitors, and fuel cells are used to store the energy after harvest through windmills and solar cells [2,3]. Nonetheless, devices that harvest and store energy must have the capacity to maintain the cost viability with advanced output performance. There are, however, several challenges faced in developing such devices with desired specifications in terms of adapting their shape, size, cyclic stability and lifespan. Most of these challenges are solved by the selection of suitable types of materials for device fabrication [4–8]. The harvesting and storage materials that are satisfactorily efficient have been applied to address the issue and limitations faced by the contemporary existing technologies. Perovskite materials have been recognized as the potential candidates among various existing materials owing to their valuable physical and chemical properties alongside with their solid-state characteristics through superconducting, insulating, metallic and semiconducting nature [9,10]. These valuable properties of

perovskites have awarded great potential for application in energy harvesting and storage [11–17].

The mineral CaTiO_3 (ABX_3) was discovered in 1839 in Ural Mountains by Geologist Gustav Rose (1778 – 1873) and was further studied and characterized by a Russian mineralogist known as Coun Lev Alekseyevich von Perovski (1792 – 1853) [18]. Perovskites are materials with the general formula of ABX_3 . In the general formula ABX_3 ; A lies in the center of the cube, X ions form the octahedron that surrounds the B ion. The most abundant perovskite compounds found in the earth's crust are MgSiO_3 and FeSO_3 [19]. In 1926, Victor Goldschmidt carried out detailed structural studies which led to the conceptualisation of tolerance factor calculated by taking into account the radii of the cations and anions organized in the crystal structure. The stability of the perovskite material is determined from the tolerance factor and this stability is dependent on the ionic sizes of the cations and anions at the A, B and X sites in the crystal structure [18–20]. Distortions in the perovskite crystal structure occur by replacing/substituting the cations/anions which yields different crystallographic arrangements. Atomic arrangements of different elements in the perovskite crystal structure determine the properties of the perovskite material and thus by changing the arrangement of those atoms will lead into many phase transitions yielding different optical, chemical and electrical properties [21–23]. The chemistry of perovskite materials and their fascinating flexible properties has made them well-known in solid-state physics and they have also generated research interest in different fields which include electronics, optoelectronics, medicine, optics, and sensors [24–26].

Another family of thin film PVs material explored in this study is kesterite material which is normally based on $\text{Cu}_2\text{ZnSn}(\text{S},\text{Se})_4$ (CZTSSe). The fascinating thing about kesterite PVs is that they combine the advantages of thin films technology with the utilization of earth-abundant and environmentally benign elements (or less toxic for Se compounds) in PVs. Ito

and Nakazawa reported for the first time the high absorption coefficient and ideal energy bandgap of Se-free $\text{Cu}_2\text{ZnSnS}_4$ (CZTS) light harvesters for application in solar cells technology [27]. Friedlmeier *et al.* [28], Seol *et al.* [29], and Katagiri *et al.* [30], reported early results for the device performance of CZTS in terms of power conversion efficiency. In 2010, record power conversion efficiency beyond 10% for CZTSSe solar cell devices was reached later on at IBM as well the 12.6% record power conversion efficiency achieved in 2013 [31]. Power conversion efficiency of 12.6% was also achieved for a larger area device in 2018 by researcher from DGIST [32]. The architecture for kesterite solar cells was initially emulated from that of $\text{Cu}(\text{In,Ga})\text{Se}_2$, (CIGSe) thin films solar cells. This architecture is constructed by sequential deposition technique on soda lime glass substrate, Mo back contact, the absorber, a CdS buffer layer, and a ZnO/ZnO:Al bi-layer window. Thin films solar cells based on kesterite are almost similar to the more developed CIGS and CdTe based thin films absorbers. A total device thickness of only few micrometers composed of absorber/emitter pn-heterojunction is used for the construction of these three technologies. The advantage of kesterite solar cells is that they can be made without toxic elements in comparison to CdTe and high efficiency Pb-based hybrid perovskite solar cells. Thin films solar cell devices based on kesterites have been explored on transparent [33] and flexible substrates [34,35]. Moreover, intense electromagnetic radiation hardness for space applications has been explored as well [36]. Long term stability studies have been reported for kesterite mono-grain solar cells attaining beyond 90% of initial power conversion efficiency after 3000 h of un-encapsulated dry heat exposure [37], showing remarkable stability of the material.

1.2 PROBLEM STATEMENT

Hybrid perovskite materials have gained significant attention in the arena of photovoltaic solar cell technology in the past decade owing to their exceptional electron-photon conversion efficiency, simple fabrication routes, and extraordinary tolerance defects. Pb-based hybrid perovskites; $\text{CH}_3\text{NH}_3\text{PbI}_3$, have demonstrated remarkable device performance owing to their strong absorption and emission properties related to direct bandgaps [38]. However, eco-toxicity posed by harmful Pb compounds as well as the issue of photo-stability hinders their practical application and marketability in the photovoltaic industry [39]. Pb-based hybrid perovskite solar cell devices are the most generally explored and more stable, but unfortunately they are not environmentally benign and therefore pose threat to human health. There is an ongoing debate in the scientific community concerning the hazardous effects of elemental Pb to the environment and human health because currently there are no systematic studies available to comprehensively address this issue [40]. It has been suggested by scientist that one of the possible ways to address this issue of eco-toxicity it could be through the reduction of the Pb quantity in the hybrid perovskite material. However, the question about the quantity of Pb is still not yet answered. Another important question is: can this quantity be compared with lead-incorporating devices such as batteries? This question is also not yet answered.

For kesterite thin film solar cells, an advanced solar cell device performance of 12.6 % (certified record efficiency [31]) was achieved in 2008 – 2012 period by employing conventional Sn-based CZTSSe absorbers [41]. Power conversion efficiencies beyond 10% have been demonstrated recently by employing different absorber compositions [42,43]. However, the low open circuit voltage (V_{OC}) is the common constraint restricting the performance in all of these kesterite-based solar cells chiefly when compared to the highest possible V_{OC} value ruled by the Shockley-Queisser radiative limit ($V_{OC,SQ}$) [44]. It was

pointed out by Bourdais *et al.* that all Sn-based kesterites devices fail to attain 60% of $V_{OC,SQ}$ [45,46], and this is not in agreement with the corresponding short circuit current densities (J_{SC}) and fill factors (FF) attaining beyond 80% of their individually determined limits by calculations. The improved/advanced open circuit voltage (V_{OC}) seems to be a requirement to position kesterite-based solar cells on par with their counterparts, namely; CdTe and Pb-based hybrid perovskites.

1.3 MOTIVATION/RATIONALE

Energy from the sun (solar energy) is an enormous and abundant renewable energy source [47]. About 1500 exawatt-hours of global solar energy are consumed [48], although the terrestrial solar energy demand was only 0.03 exawatt-hours in 2018. Photovoltaics (PVs) are arguably the cleanest process of converting solar energy into electricity with no carbon-based by-products [47]. Nonetheless, in 2018, about only 440 terawatt-hours of solar energy was produced, with about 500 gigawatts of PV capacity installed globally by the end of 2018 [47]. It is predicted that 37 – 180 TW of PV capacity would be in demand to realise the goal of over 60 nations achieving net-zero carbon emissions, although PV deployment is estimated to soon reach the terawatt level [49]. The challenges hindering the scaling of PV capacity have been examined through various techno-economic analyses systems, some of which are thoroughly discussed in [47,49,50]. This goal could be realised by reducing the levelized cost of electricity (LCOE) and capital-intensity of manufacturing [50], which can be done by using thin film solar cells, in tandem solar cell devices. In tandem solar cells, two sub-cells absorbing in complementary region of the solar spectrum are combined together, thus transcending the theoretical limit of a single-junction solar cell device. Thin film solar cells technology forms part of the Internet of Things (IoT) since it can be integrated in buildings

(e.g. solar windows) and it also used indoors to provide power for small standalone gadgets [51]. Pb-based hybrid perovskite solar cell materials have recently emerged showing higher device learning-rates transcending any other PV material [51]. As of the end of 2020, Pb-based hybrid perovskite PVs have now achieved a certified power conversion efficiency of 25.5% (laboratory based scale) [52] since their first report in PV industry in 2009 (with power conversion efficiency of 3.8% [53]), transcending multi-crystalline silicon and nearly approaching the certified record efficiency of crystalline silicon solar cells (26.7% [52]). A perovskite-silicon tandem solar cell utilising Pb-based hybrid perovskite top cell and Si-based bottom solar cell have achieved a certified efficiency of 29.15% after only a period of 6 years of development [54,55]. To modulate (tune) the energy bandgap of hybrid perovskite materials, a vast range of compositional modification is done. This led to the realization of perovskite-perovskite tandems with power conversion efficiency of 25% [56]. Lower LCOEs than single-junction silicon solar cells have been estimated to be achieved by both tandem structures [51]. A power conversion efficiency of 35.2% has been achieved by single-junction perovskite devices under indoor lighting conditions [57]. These high power conversion efficiencies are accomplished through low-temperature and simplistic solution-processing and thermal evaporation processing. Therefore Pb-based hybrid perovskite solar cells hold substantial potential for the reduction of LCOE and capital-intensity of PVs. The development of non-toxic Pb-free perovskite solar cells is also another avenue explored for industrial application in the photovoltaic markets, mainly for interior power generation like wearable power households with stringent limitations on the eco-toxic Pb content [58–60].

The European Commission classified some elements as critical raw materials (CRM) [61] posing as a threat to the environmental and human health. This classification by the European Commission has sparked an interest in developing CRM-free thin film PV technologies. Indium, gallium, and tellurium were among the CRM [62–65] classified by the European

Commission and this has called for the partial or total substitution in PV technologies. This has called for an upgrade design and advancement of solutions by developing CRM-free PV technologies with viable processes based on circular economy for the long-term maintenance of these novel technologies. Based on this context, numerous all-inorganic PV technologies employing non-toxic and earth abundant elements have been explored on different levels in the PV research industry [66] achieving success on different levels. The aim of these explorations (research) was to find out if it feasible to attain a cost-efficient all-inorganic PV technological solution which exclusively utilizes earth abundant and non-toxic elements. Kesterites materials have so far attained the highest power conversion efficiency in the range 11 – 13% [31,67,68] among the emerging CRM-free technologies. Kesterite solar cell materials are closely related to the more developed $\text{Cu}(\text{In,Ga})(\text{S,Se})_2$ (CIGSSe) technology which have already penetrated the commercial market [69] with device performance close to that of multi-crystalline silicon.



1.4 AIM AND OBJECTIVES

For NiCuZn hybrid perovskite thin films, the chief aim of this study is to synthesize and characterize air-stable hybrid perovskite thin film materials incorporating earth abundant and non-toxic transition metals which include Ni, Cu & Zn for potential application in planar heterojunction (PHJ) solar cells to address the issue of eco-toxicity posed by metal Pb in $\text{CH}_3\text{NH}_3\text{PbI}_3$ and the issue of poor stability against air (oxygen) and humidity (moisture).

For the development of CZGSe-based kesterite solar cells, this study seeks to address the issue of low open circuit voltage (V_{OC}) which is the common constraint limiting the performance in all kesterite-based solar cells mainly when compared to the highest possible

V_{OC} value ruled by the Shockley-Queisser radiative limit ($V_{OC,SQ}$). This is done by utilizing Ge as a substitute for Sn in CZTSSe-based solar cells.

The aim of this study will be achieved by the following objectives (in sequence);

1. Prepare the reported lead triiodide perovskite thin films $CH_3NH_3PbI_3$ (pristine perovskite) employing two step solution deposition technique for comparison purposes.
2. Prepare new perovskites thin films employing Ni, Cu & Zn transition metals (at a doping level; from 1 to 10%); $CH_3NH_3PbI_3 \cdot Ni$, $CH_3NH_3PbI_3 \cdot Cu$ and $CH_3NH_3PbI_3 \cdot Zn$ employing two step solution deposition technique.
3. Confirm the perovskite structure formation and structural properties of all perovskite thin film materials under investigation by X-ray Diffraction (XRD) measurements.
4. Confirm the chemical (elemental) composition of all the perovskite thin films by X-ray Photoelectron Spectroscopy (XPS).
5. Interrogate the microscopic properties of all the perovskite thin films under investigation by High Resolution Scanning Electron Microscopy (HR-SEM), and Atomic Force Microscopy (AFM).
6. Probe the optical properties of all the hybrid perovskites thin films under investigation by Ultraviolet-visible (UV-vis) Spectroscopy and Photoluminescence (PL) Spectroscopy.
7. Prepare the new CZGSe absorbers from various precursor stack order to determine the best one for a high quality absorber, i.e.;

Stack Order (A): Mo/Cu(4nm)/Zn/Cu/Ge

Stack Order (B): Mo/Zn/Cu/Ge

Stack Order (C): Mo/Cu/Zn/Ge

8. Determine the optimal reactive annealing profile by varying the pressure and temperature.
9. Explore different solutions to determine the best one for the elimination of secondary phases via chemical bath etching (CBE) technique.
10. Optimize the CdS buffer layer by adopting the optimal parameters reported in literature.

1.5 THESIS LAYOUT

This section gives the layout of the five chapters discussed in this thesis.

Chapter 1: Introduction

This chapter gives the background on photovoltaic (solar cell) technologies, research progress of the work done on both hybrid perovskite solar cells and kesterite solar cells, the shortcomings and challenges facing the commercialization of both hybrid perovskites solar cells and kesterites solar cells (problem statement), motivation, aim and objectives of the study.

Chapter 2: Literature review

A detailed literature review discussing progress on perovskite thin films solar cell technology, structural configurations of hybrid perovskites, doping mechanisms in hybrid perovskite materials, Pb-toxicity and Pb-free hybrid perovskite materials, thin films preparation techniques of hybrid perovskite materials and stability studies against relative humidity is outlined.

A detailed literature review discussing progress on kesterite solar cell technology, doping mechanisms in kesterite materials, energy bandgap optimization studies, Ge-alloying in kesterites and physical routes for the preparation of kesterite absorber materials and solar cells is also outlined.

Chapter 3: Experimental Details

This chapter discusses the experimental details of the study which include reagents and glass substrates used for the preparation of both the NiCuZn hybrid perovskites thin films and CZGSe kesterite absorber materials. The deposition techniques that were followed (procedure) to produce both the NiCuZn hybrid perovskite thin film and CZGSe absorber materials are also discussed. Lastly, details regarding the characterization techniques/instruments that were employed to interrogate the structural, optical, microscopic and electrical properties of the materials under investigation are also discussed.

Chapter 4: Experimental Results and Discussion

This chapter discusses in details the experimental results obtained in chapter 3. For NiCuZn hybrid perovskite thin film materials, the impact of transition metal dopants Ni, Cu & Zn on the structural, photo-physical and microscopic properties of $\text{CH}_3\text{NH}_3\text{PbI}_3$ (host) is thoroughly discussed. For the development of CZGSe kesterite solar cells, a thorough discussion on the impact of precursor metallic stack order, annealing profile, secondary phases and CdS parameters on the CZGSe absorber quality and the photovoltaic performance of the resultant solar cell devices is also given.

Chapter 5: Conclusive Summary, Recommendations and Suggested Future Work

Draws a conclusive summary from experimental results obtained in chapter 4. Recommendations are made at the end and future works are also suggested.

Bibliography

- [1] H.D. Pham, T.C.J. Yang, S.M. Jain, G.J. Wilson, P. Sonar, Development of Dopant-Free Organic Hole Transporting Materials for Perovskite Solar Cells, *Advanced Energy Materials*. 10 (2020) 1903326. <https://doi.org/10.1002/aenm.201903326>.
- [2] A.M. Abdalla, S. Hossain, A.T. Azad, P.M.I. Petra, F. Begum, S.G. Eriksson, A.K. Azad, Nanomaterials for solid oxide fuel cells: A review, *Renewable and Sustainable Energy Reviews*. 82 (2018) 353–368. <https://doi.org/10.1016/j.rser.2017.09.046>.
- [3] Hannah Ritchie, *Energy – Our World in Data*, (2014).
<https://ourworldindata.org/energy-mix>
- [4] B. Luo, S. Liu, L. Zhi, Chemical approaches toward graphene-based nanomaterials and their applications in energy-related areas, *Small*. 8 (2012) 630–646.
<https://doi.org/10.1002/smll.201101396>.
- [5] Q. Zhang, J.Q. Huang, W.Z. Qian, Y.Y. Zhang, F. Wei, The road for nanomaterials industry: A review of carbon nanotube production, post-treatment, and bulk applications for composites and energy storage, *Small*. 9 (2013) 1237–1265.
<https://doi.org/10.1002/smll.201203252>.
- [6] M. Pumera, Graphene-based nanomaterials for energy storage, *Energy and Environmental Science*. 4 (2011) 668–674. <https://doi.org/10.1039/c0ee00295j>.
- [7] Q. Wei, F. Xiong, S. Tan, L. Huang, E.H. Lan, B. Dunn, L. Mai, Porous One-Dimensional Nanomaterials: Design, Fabrication and Applications in Electrochemical Energy Storage, *Advanced Materials*. 29 (2017) 1602300.
<https://doi.org/10.1002/adma.201602300>.

- [8] A.H. Khan, S. Ghosh, B. Pradhan, A. Dalui, L.K. Shrestha, S. Acharya, K. Ariga, Two-dimensional (2D) nanomaterials towards electrochemical nanoarchitectonics in energy-related applications, *Bulletin of the Chemical Society of Japan*. 90 (2017) 627–648. <https://doi.org/10.1246/bcsj.20170043>.
- [9] *Structure, Properties and Preparation of Perovskite-Type Compounds*, Elsevier, 1969. <https://doi.org/10.1016/c2013-0-02117-2>.
- [10] K.K. Hansen, E.M. Skou, H. Christensen, T. Turek, Perovskites as catalysts for the selective catalytic reduction of nitric oxide with propene: Relationship between solid state properties and catalytic activity, *Journal of Catalysis*. 199 (2001) 132–140. <https://doi.org/10.1006/jcat.2000.3153>.
- [11] J. Huang, S. Xiang, J. Yu, C.Z. Li, Highly efficient prismatic perovskite solar cells, *Energy and Environmental Science*. 12 (2019) 929–937. <https://doi.org/10.1039/c8ee02575d>.
- [12] Q. Wang, N. Phung, D. Di Girolamo, P. Vivo, A. Abate, Enhancement in lifespan of halide perovskite solar cells, *Energy and Environmental Science*. 12 (2019) 865–886. <https://doi.org/10.1039/c8ee02852d>.
- [13] S.A. Kulkarni, S.G. Mhaisalkar, N. Mathews, P.P. Boix, Perovskite Nanoparticles: Synthesis, Properties, and Novel Applications in Photovoltaics and LEDs, *Small Methods*. 3 (2019) 1800231. <https://doi.org/10.1002/smt.201800231>.
- [14] Y. Wei, Z. Cheng, J. Lin, An overview on enhancing the stability of lead halide perovskite quantum dots and their applications in phosphor-converted LEDs, *Chemical Society Reviews*. 48 (2019) 310–350. <https://doi.org/10.1039/c8cs00740c>.

- [15] P. Maji, A. Ray, P. Sadhukhan, A. Roy, S. Das, Fabrication of symmetric supercapacitor using cesium lead iodide (CsPbI_3) microwire, *Materials Letters*. 227 (2018) 268–271. <https://doi.org/10.1016/j.matlet.2018.05.101>.
- [16] R. Chiba, F. Yoshimura, Y. Sakurai, Investigation of $\text{LaNi}_{1-x}\text{Fe}_x\text{O}_3$ as a cathode material for solid oxide fuel cells, *Solid State Ionics*. 124 (1999) 281–288. [https://doi.org/10.1016/S0167-2738\(99\)00222-2](https://doi.org/10.1016/S0167-2738(99)00222-2).
- [17] T. Zhang, H. Li, P. Yang, J. Wei, F. Wang, H. Shen, D. Li, F. Li, Room-temperature synthesized formamidinium lead halide perovskite quantum dots with bright luminescence and color-tunability for efficient light emitting, *Organic Electronics*. 68 (2019) 76–84. <https://doi.org/10.1016/j.orgel.2019.02.007>.
- [18] A.S. Bhalla, R. Guo, R. Roy, The perovskite structure - A review of its role in ceramic science and technology, *Materials Research Innovations*. 4 (2000) 3–26. <https://doi.org/10.1007/s100190000062>.
- [19] R.M. Wentzcovitch, B.B. Karki, S. Karato, C.R.S. Da Silva, High pressure elastic anisotropy of MgSiO_3 perovskite and geophysical implications, *Earth and Planetary Science Letters*. 164 (1998) 371–378. [https://doi.org/10.1016/S0012-821X\(98\)00230-1](https://doi.org/10.1016/S0012-821X(98)00230-1).
- [20] C.J. Bartel, C. Sutton, B.R. Goldsmith, R. Ouyang, C.B. Musgrave, L.M. Ghiringhelli, M. Scheffler, New tolerance factor to predict the stability of perovskite oxides and halides, *Science Advances*. 5 (2019) eaav0693. <https://doi.org/10.1126/sciadv.aav0693>.

- [21] P.S. Whitfield, N. Herron, W.E. Guise, K. Page, Y.Q. Cheng, I. Milas, M.K. Crawford, Structures, Phase Transitions and Tricritical Behavior of the Hybrid Perovskite Methyl Ammonium Lead Iodide, *Scientific Reports*. 6 (2016) 1–16.
<https://doi.org/10.1038/srep35685>.
- [22] W.J. Wei, C. Li, L.S. Li, Y.Z. Tang, X.X. Jiang, Z.S. Lin, Phase transition, optical and dielectric properties regulated by anion-substitution in a homologous series of 2D hybrid organic-inorganic perovskites, *Journal of Materials Chemistry C*. 7 (2019) 11964–11971. <https://doi.org/10.1039/c9tc04479e>.
- [23] K. Matsuishi, T. Ishihara, S. Onari, Y.H. Chang, C.H. Park, Optical properties and structural phase transitions of lead-halide based inorganic-organic 3D and 2D perovskite semiconductors under high pressure, *Physica Status Solidi (B) Basic Research*. 241 (2004) 3328–3333. <https://doi.org/10.1002/pssb.200405229>.
- [24] A. Kostopoulou, K. Brintakis, N.K. Nasikas, E. Stratakis, Perovskite nanocrystals for energy conversion and storage, *Nanophotonics*. 8 (2019) 1607–1640.
<https://doi.org/10.1515/nanoph-2019-0119>.
- [25] F. Dogan, H. Lin, M. Guilloux-Viry, O. Peña, Focus on properties and applications of perovskites, *Science and Technology of Advanced Materials*. 16 (2015) 020301.
<https://doi.org/10.1088/1468-6996/16/2/020301>.
- [26] M. Grätzel, N.G. Park, Organometal halide perovskite photovoltaics: A diamond in the rough, *Nano*. 9 (2014) 14400025. <https://doi.org/10.1142/S1793292014400025>.
- [27] K. Ito, T. Nakazawa, Electrical and optical properties of stannite-type quaternary semiconductor thin films, *Japanese Journal of Applied Physics*. 27 (1988) 2094–2097.
<https://doi.org/10.1143/JJAP.27.2094>.

- [28] Friedlmeier T M *et al.* 1997 14th European PVSEC.
<https://www.tib.eu/en/search/id/TIBKAT%3A247543462/Fourteenth-European-Photovoltaic-Solar-Energy-Conference/>
- [29] J.S. Seol, S.Y. Lee, J.C. Lee, H.D. Nam, K.H. Kim, Electrical and optical properties of Cu₂ZnSnS₄ thin films prepared by rf magnetron sputtering process, *Solar Energy Materials and Solar Cells*. 75 (2003) 155–162. [https://doi.org/10.1016/S0927-0248\(02\)00127-7](https://doi.org/10.1016/S0927-0248(02)00127-7).
- [30] H. Katagiri, N. Sasaguchi, S. Hando, S. Hoshino, J. Ohashi, T. Yokota, Preparation and evaluation of Cu₂ZnSnS₄ thin films by sulfurization of E-B evaporated precursors, *Solar Energy Materials and Solar Cells*. 49 (1997) 407–414.
[https://doi.org/10.1016/S0927-0248\(97\)00119-0](https://doi.org/10.1016/S0927-0248(97)00119-0).
- [31] W. Wang, M.T. Winkler, O. Gunawan, T. Gokmen, T.K. Todorov, Y. Zhu, D.B. Mitzi, Device characteristics of CZTSSe thin-film solar cells with 12.6% efficiency, *Advanced Energy Materials*. 4 (2014) 1301465.
<https://doi.org/10.1002/aenm.201301465>.
- [32] M.A. Green, Y. Hishikawa, E.D. Dunlop, D.H. Levi, J. Hohl-Ebinger, M. Yoshita, A.W.Y. Ho-Baillie, Solar cell efficiency tables (Version 53), *Progress in Photovoltaics: Research and Applications*. 27 (2019) 3–12.
<https://doi.org/10.1002/pip.3102>.
- [33] M. Espindola-Rodriguez, D. Sylla, Y. Sánchez, F. Oliva, S. Grini, M. Neuschitzer, L. Vines, V. Izquierdo-Roca, E. Saucedo, M. Placidi, Bifacial Kesterite Solar Cells on FTO Substrates, *ACS Sustainable Chemistry and Engineering*. 5 (2017) 11516–11524.
<https://doi.org/10.1021/acssuschemeng.7b02797>.

- [34] I. Becerril-Romero, L. Acebo, F. Oliva, V. Izquierdo-Roca, S. López-Marino, M. Espíndola-Rodríguez, M. Neuschitzer, Y. Sánchez, M. Placidi, A. Pérez-Rodríguez, E. Saucedo, P. Pistor, CZTSe solar cells developed on polymer substrates: Effects of low-temperature processing, *Progress in Photovoltaics: Research and Applications*. 26 (2018) 55–68. <https://doi.org/10.1002/pip.2945>.
- [35] Todorov T *et al.* (2015) IEEE 42nd Photovoltaic Specialist Con. <http://toc.proceedings.com/28560webtoc.pdf>
- [36] S.S. Suvanam, J. Larsen, N. Ross, V. Kosyak, A. Hallén, C.P. Björkman, Extreme radiation hard thin film CZTSSe solar cell, *Solar Energy Materials and Solar Cells*. 185 (2018) 16–20. <https://doi.org/10.1016/j.solmat.2018.05.012>.
- [37] C. Neubauer, A. Samiepour, S. Oueslati, M. Danilson, D. Meissner, Ageing of kesterite solar cells 1: Degradation processes and their influence on solar cell parameters, *Thin Solid Films*. 669 (2019) 595–599. <https://doi.org/10.1016/j.tsf.2018.11.043>.
- [38] D. Kong, D. Cheng, X. Wang, K. Zhang, H. Wang, K. Liu, H. Li, X. Sheng, L. Yin, Solution processed lead-free cesium titanium halide perovskites and their structural, thermal and optical characteristics, *Journal of Materials Chemistry C*. 8 (2020) 1591–1597. <https://doi.org/10.1039/c9tc05711k>.
- [39] A.F. Akbulatov, S.A. Tsarev, M. Elshobaki, S.Y. Luchkin, I.S. Zhidkov, E.Z. Kurmaev, S.M. Aldoshin, K.J. Stevenson, P.A. Troshin, Comparative Intrinsic Thermal and Photochemical Stability of Sn(II) Complex Halides as Next-Generation Materials for Lead-Free Perovskite Solar Cells, *Journal of Physical Chemistry C*. 123 (2019) 26862–26869. <https://doi.org/10.1021/acs.jpcc.9b09200>.

- [40] J. Li, H.L. Cao, W. Bin Jiao, Q. Wang, M. Wei, I. Cantone, J. Lü, A. Abate, Biological impact of lead from halide perovskites reveals the risk of introducing a safe threshold, *Nature Communications*. 11 (2020) 310. <https://doi.org/10.1038/s41467-019-13910-y>.
- [41] S. Giraldo, Z. Jehl, M. Placidi, V. Izquierdo-Roca, A. Pérez-Rodríguez, E. Saucedo, Progress and Perspectives of Thin Film Kesterite Photovoltaic Technology: A Critical Review, *Advanced Materials*. 31 (2019) 1806692 .
<https://doi.org/10.1002/adma.201806692>.
- [42] Y.E. Romanyuk, S.G. Haass, S. Giraldo, M. Placidi, D. Tiwari, D.J. Fermin, X. Hao, H. Xin, T. Schnabel, M. Kauk-Kuusik, P. Pistor, S. Lie, L.H. Wong, Doping and alloying of kesterites, *JPhys Energy*. 1 (2019) 044004. <https://doi.org/10.1088/2515-7655/ab23bc>.
- [43] J. Li, D. Wang, X. Li, Y. Zeng, Y. Zhang, Cation Substitution in Earth-Abundant Kesterite Photovoltaic Materials, *Advanced Science*. 5 (2018) 1700744.
<https://doi.org/10.1002/advs.201700744>.
- [44] W. Shockley, H.J. Queisser, Detailed balance limit of efficiency of p-n junction solar cells, *Journal of Applied Physics*. 32 (1961) 510–519.
<https://doi.org/10.1063/1.1736034>.
- [45] S. Bourdais, C. Choné, B. Delatouche, A. Jacob, G. Larramona, C. Moisan, A. Lafond, F. Donatini, G. Rey, S. Siebentritt, A. Walsh, G. Dennler, Is the Cu/Zn Disorder the Main Culprit for the Voltage Deficit in Kesterite Solar Cells?, *Advanced Energy Materials*. 6 (2016) 1502276. <https://doi.org/10.1002/aenm.201502276>.
- [46] L. Grenet, M.A.A. Suzon, F. Emieux, F. Roux, Analysis of Failure Modes in Kesterite Solar Cells, *ACS Applied Energy Materials*. 1 (2018) 2103–2113.

<https://doi.org/10.1021/acsaem.8b00194>.

- [47] N.M. Haegel, H. Atwater, T. Barnes, C. Breyer, A. Burrell, Y.M. Chiang, S. De Wolf, B. Dimmler, D. Feldman, S. Glunz, J.C. Goldschmidt, D. Hochschild, R. Inzunza, I. Kaizuka, B. Kroposki, S. Kurtz, S. Leu, R. Margolis, K. Matsubara, A. Metz, W.K. Metzger, M. Morjaria, S. Niki, S. Nowak, I.M. Peters, S. Philipps, T. Reindl, A. Richter, D. Rose, K. Sakurai, R. Schlatmann, M. Shikano, W. Sinke, R. Sinton, B.J. Stanbery, M. Topic, W. Tumas, Y. Ueda, J. Van De Lagemaat, P. Verlinden, M. Vetter, E. Warren, M. Werner, M. Yamaguchi, A.W. Bett, Terawatt-scale photovoltaics: Transform global energy Improving costs and scale reflect looming opportunities, *Science*. 364 (2019) 836–838. <https://doi.org/10.1126/science.aaw1845>.
- [48] W.A. Hermann, Quantifying global exergy resources, *Energy*. 31 (2006) 1685–1702. <https://doi.org/10.1016/j.energy.2005.09.006>.
- [49] S.R. Kurtz, A.M. Leilaieoun, R.R. King, I.M. Peters, M.J. Heben, W.K. Metzger, N.M. Haegel, Revisiting the Terawatt Challenge, *MRS Bulletin*. 45 (2020) 159–164. <https://doi.org/10.1557/mrs.2020.73>.
- [50] D.B. Needleman, J.R. Poindexter, R.C. Kurchin, I. Marius Peters, G. Wilson, T. Buonassisi, Economically sustainable scaling of photovoltaics to meet climate targets, *Energy and Environmental Science*. 9 (2016) 2122–2129. <https://doi.org/10.1039/c6ee00484a>.
- [51] A. Polman, M. Knight, E.C. Garnett, B. Ehrler, W.C. Sinke, Photovoltaic materials: Present efficiencies and future challenges, *Science*. 352 (2016) aad4424. <https://doi.org/10.1126/science.aad4424>.

- [52] NREL, Best Research-Cell Efficiency Chart (National Renewable Energy Laboratory, (2021). <https://www.nrel.gov/pv/assets/pdfs/cell-pv-eff-emergingpv-rev210726.pdf>.
- [53] A. Kojima, K. Teshima, Y. Shirai, T. Miyasaka, Organometal halide perovskites as visible-light sensitizers for photovoltaic cells, *Journal of the American Chemical Society*. 131 (2009) 6050–6051. <https://doi.org/10.1021/ja809598r>.
- [54] J.P. Mailoa, C.D. Bailie, E.C. Johlin, E.T. Hoke, A.J. Akey, W.H. Nguyen, M.D. McGehee, T. Buonassisi, A 2-terminal perovskite/silicon multijunction solar cell enabled by a silicon tunnel junction, *Applied Physics Letters*. 106 (2015) 121105. <https://doi.org/10.1063/1.4914179>.
- [55] C.D. Bailie, M.G. Christoforo, J.P. Mailoa, A.R. Bowring, E.L. Unger, W.H. Nguyen, J. Burschka, N. Pellet, J.Z. Lee, M. Grätzel, R. Noufi, T. Buonassisi, A. Salleo, M.D. McGehee, Semi-transparent perovskite solar cells for tandems with silicon and CIGS, *Energy and Environmental Science*. 8 (2015) 956–963. <https://doi.org/10.1039/c4ee03322a>.
- [56] Z. Li, Y. Zhao, X. Wang, Y. Sun, Z. Zhao, Y. Li, H. Zhou, Q. Chen, Cost Analysis of Perovskite Tandem Photovoltaics, *Joule*. 2 (2018) 1559–1572. <https://doi.org/10.1016/j.joule.2018.05.001>.
- [57] J. Dagar, S. Castro-Hermosa, G. Lucarelli, F. Cacialli, T.M. Brown, Highly efficient perovskite solar cells for light harvesting under indoor illumination via solution processed SnO₂/MgO composite electron transport layers, *Nano Energy*. 49 (2018) 290–299. <https://doi.org/10.1016/j.nanoen.2018.04.027>.

- [58] M. Konstantakou, T. Stergiopoulos, A critical review on tin halide perovskite solar cells, *Journal of Materials Chemistry A*. 5 (2017) 11518–11549.
<https://doi.org/10.1039/c7ta00929a>.
- [59] E.W.G. Diau, E. Jokar, M. Rameez, Strategies to improve performance and stability for tin-based perovskite solar cells, *ACS Energy Letters*. 4 (2019) 1930–1937.
<https://doi.org/10.1021/acsenerylett.9b01179>.
- [60] J. Cao, F. Yan, Recent progress in tin-based perovskite solar cells, *Energy and Environmental Science*. 14 (2021) 1286–1325. <https://doi.org/10.1039/d0ee04007j>.
- [61] Innovation Union, Communication From the Commission to the European Parliament, the Council, the European Economic and Social Committee and the Committee of the Regions, (2010). <http://aei.pitt.edu/46014/>
- [62] C. Wadia, A.P. Alivisatos, D.M. Kammen, Materials availability expands the opportunity for large-scale photovoltaics deployment, *Environmental Science and Technology*. 43 (2009) 2072–2077. <https://doi.org/10.1021/es8019534>.
- [63] B.A. Andersson, Materials availability for large-scale thin-film photovoltaics, *Progress in Photovoltaics: Research and Applications*. 8 (2000) 61–76.
[https://doi.org/10.1002/\(SICI\)1099-159X\(200001/02\)8:1<61::AID-PIP301>3.0.CO;2-6](https://doi.org/10.1002/(SICI)1099-159X(200001/02)8:1<61::AID-PIP301>3.0.CO;2-6).
- [64] A. Zuser, H. Rechberger, Considerations of resource availability in technology development strategies: The case study of photovoltaics, *Resources, Conservation and Recycling*. 56 (2011) 56–65. <https://doi.org/10.1016/j.resconrec.2011.09.004>.
- [65] V. Fthenakis, Sustainability of photovoltaics: The case for thin-film solar cells, *Renewable and Sustainable Energy Reviews*. 13 (2009) 2746–2750.

<https://doi.org/10.1016/j.rser.2009.05.001>.

- [66] A. Zakutayev, J.D. Major, X. Hao, A. Walsh, J. Tang, T.K. Todorov, L.H. Wong, E. Saucedo, Emerging inorganic solar cell efficiency tables (version 2), *JPhys Energy*. 3 (2021) 032003. <https://doi.org/10.1088/2515-7655/abebca>.
- [67] S. Giraldo, E. Saucedo, M. Neuschitzer, F. Oliva, M. Placidi, X. Alcobé, V. Izquierdo-Roca, S. Kim, H. Tampo, H. Shibata, A. Pérez-Rodríguez, P. Pistor, How small amounts of Ge modify the formation pathways and crystallization of kesterites, *Energy and Environmental Science*. 11 (2018) 582–593. <https://doi.org/10.1039/c7ee02318a>.
- [68] C. Yan, J. Huang, K. Sun, S. Johnston, Y. Zhang, H. Sun, A. Pu, M. He, F. Liu, K. Eder, L. Yang, J.M. Cairney, N.J. Ekins-Daukes, Z. Hameiri, J.A. Stride, S. Chen, M.A. Green, X. Hao, $\text{Cu}_2\text{ZnSnS}_4$ solar cells with over 10% power conversion efficiency enabled by heterojunction heat treatment, *Nature Energy*. 3 (2018) 764–772. <https://doi.org/10.1038/s41560-018-0206-0>.
- [69] V. Bermudez, A. Perez-Rodriguez, Understanding the cell-to-module efficiency gap in $\text{Cu}(\text{In,Ga})(\text{S,Se})_2$ photovoltaics scale-up, *Nature Energy*. 3 (2018) 466–475. <https://doi.org/10.1038/s41560-018-0177-1>.

CHAPTER 2

Literature review

2.1 HYBRID PEROVSKITE SOLAR CELL MATERIALS

2.1.1 INTRODUCTION

The development of clean and renewable energy is on high demand due to a rapid increase in energy consumption and pressure concerning environmental issues. Since solar energy is clean (environmentally benign) and cannot be exhausted, its utilization will play a significant role in effectively addressing the issue of global energy crisis and global warming in the near future. To date, solar cells based on silicon are still the main commercialized PV technology in the industry and they have reached the same level (equal price) to the conventional electricity generation technology, nevertheless, the preparation of advanced quality silicon wafers undertakes a complex preparation process resulting in expensive costs, which to some degree hinders their popularity [1–3]. Owing to their unique benefits such as low-temperature solution processibility [4–6], tunable energy bandgap [7–10], large absorption coefficient [11–13], long carrier diffusion length and lifetime [14–16], high electron and hole mobility [17–20], low exciton binding energy [21] and low defect density [22–25], Pb-based hybrid perovskites with structure of $APbX_3$ (where $A = MA^+/FA^+/Cs^+$ and $X =$ halogen anion) have gained a significant amount of global attention. The power conversion efficiency of Pb-based hybrid perovskite solar cells has skyrocketed from the first reported value of 3.8 % to the current certified record efficiency value of 25.5% (which satisfy the requirements for

commercialization) over the past few years [26,27]. This was achieved by the optimization of deposition technology and the regulation of structural composition of Pb-based hybrid perovskite thin films [26,27]. However, the eco-toxicity posed by elemental Pb hinders the hybrid perovskite solar cells from penetrating the commercial market. Instability under relentless bombardments such as electromagnetic radiation [28–30], persistent heat [31–33], persistent humidity [34–37], exposure to oxygen molecules [38] and persistent exposure to electrical field [39] (which consequently hinders their commercialisation process), is the first issue faced by advanced Pb-based hybrid perovskite solar cells. There have been significant efforts to address this issue in order to revamp their environmental stability through compositional engineering [21,40,41], dimensional engineering [42,43], and encapsulation technology [44–47]. The significant improvement of the long-term stability of hybrid perovskites solar cells is showed by A site substitution of APbX₃ by Cs⁺ cation to produce fully-inorganic perovskites and their resultant solar cell devices, largely for the thermal stability [48,49]. Moreover, it has been reported recently that the multi-halide perovskite solar cells can sustain 1800 h of Damp Heat test and 75 cycles of Humidity Freeze by an inexpensive polymer/glass stack pressure-tight encapsulation, exceeding the condition of IEC61215:2016 standard, showing the issue of stability facing the hybrid perovskite solar cells will be addressed in the near future [50]. Eco-toxicity posed by elemental Pb has slowly became another issue faced by Pb-based hybrid perovskite solar cells since Pb is harmful to the environment and biological health although Pb-based hybrid perovskite solar cells have achieved remarkable device performance. There is a lack of studies (research) dedicated in addressing this issue [51]. It has been determined by calculations that about 0.75 g m⁻² of Pb is still present in a classic 550 nm-thick Pb-based hybrid perovskite solar cell, making it 100 times more than that of the popular Pb-containing paints (0.007 g m⁻²) which adversely affects our biological health [52,53]. Two main approaches have been utilized to address this

issue and these approaches include the reduction of Pb leakage (outflow) [52,54] and partial or thorough substitution of elemental Pb [55–59]. The total substitution of elemental Pb is more collective and favourable for future commercialisation of stable and lead-free hybrid perovskites in the research fraternity [46]. Although hybrid perovskites solar cell materials have been extensively explored, little research has been dedicated in addressing the issue of eco-toxicity posed by elemental Pb. Metals ions that are less to non-toxic such as equivalent Sn^{2+} or Ge^{2+} , trivalent Bi^{3+} or Sb^{3+} , tetravalent Sn^{4+} or Ge^{4+} can be utilized for partial or total substitution of the eco-toxic Pb^{2+} . The total substitution of Pb^{2+} by Sn^{2+} or Ge^{2+} ions holds great prospects thanks to their similar properties to Pb-based hybrid perovskites. However, the two bivalent ions (i.e. Sn^{2+} or Ge^{2+}) are very sensitive to oxygen and can easily transition to Sn^{4+} and Ge^{4+} , respectively, preventing their future development [51,60,61]. One of the ways that is considered as a good strategy to improve the stability of Pb-based hybrid perovskite is by the replacement of two Pb^{2+} cations with one tetravalent M(IV) cation to produce double perovskite $\text{A}_2\text{M(IV)X}_6$ [$\text{A} = \text{MA}^+/\text{FA}^+/\text{Cs}^+$, $\text{M(IV)} = \text{Sn}^{4+}$, Ge^{4+} , Ti^{4+} or Pd^{4+}] and another way is by the replacement of three Pb^{2+} cations with two trivalent (MIII) cations to produce $\text{A}_3\text{M(III)}_2\text{X}_9$ [$\text{M(III)} = \text{In}^{3+}$, Sb^{3+} or Bi^{3+}][61–64]. Ordered metallic vacancies will be formed in order to maintain charge neutrality and this will result in the reduction of electronic dimensionality (0D or 2D) and poorer carrier mobility [65]. Thus, a vast variety of desirable sunlight absorbers can be produced through quaternary double perovskite compounds with a representative formula of $\text{A}_2\text{M(I)M(III)X}_6$ [$\text{M(I)} = \text{Na}^+$, K^+ , Rb^+ , Cu^+ , Ag^+ , Ag^+ , Au^+ , In^+ or Tl^+] [64,66,67]. A family of lead-free double perovskites named elpasolite, $\text{A}_2\text{M(I)M(III)X}_6$, has generated a lot of interest as emerging novel sunlight absorbers for hybrid perovskite solar cells [68–73]. To date, $\text{Cs}_2\text{AgBiCl}_6$ and $\text{Cs}_2\text{AgBiBr}_6$ lead free double perovskite materials hold great prospects as non-toxic alternatives for Pb-based hybrid perovskites since they had been reported for the first time by Slavney *et al.* [55]. Regardless

of their wide indirect energy bandgap, $\text{Cs}_2\text{AgBiBr}_6$ has showed a long photoluminescence lifetime (ca. 660 ns) and outstanding thermal and intrinsic stability in when compared to the popular MAPbI_3 . Till today, poor power conversion efficiency has been demonstrated by Pb-free solution processed halide perovskite in comparison to Pb-based halide perovskite solar cells. Sn-based perovskite solar cell device has attained the highest power conversion efficiency of 13.24% [74] and only about 3% power conversion efficiency has been achieved by Bi-based perovskite [72], making these Pb-free halide perovskites inferior in comparison to that of the state-of-the-art perovskite solar cells. The poor thin-film quality which consequently produces undesirable defects and intense charge carrier recombination is the main cause of inferior power conversion efficiency. Preparation methods (or techniques) like hydrothermal method, hot injection approach, vapour deposition, pressure assisted solution deposition technique [75–78] have been developed recently as a way to advance the thin film quality of lead-free halide perovskite materials. Thus, more work needs to be dedicated to understand the structure, properties and recombination mechanisms of lead-free double perovskites in broader terms and to ultimately improve the photovoltaic performance of the devices.

2.1.2 STRUCTURAL CONFIGURATION OF PEROVSKITES

Perovskites are a class of materials with generic formula ABX_3 belonging to the family of CaTiO_3 minerals. Perovskite materials form stable structures from the 12- and 6-fold coordination of A and B cations, respectively. Despite the fact that CaTiO_3 has structural distortions at respective corners, an ideal cubic perovskite structure is not common. What make perovskite materials appealing in many industrial applications are their attractive properties and their capacity to accommodate most elements in their structure. The work

concerning the information related to basic structure and configuration of perovskites was pioneered by Goldschmidt and co-workers in the 1920s [79,80]. The most common arrangement of the atoms in perovskites is the simple cubic structure. In the perovskite crystal structure, the body center of the cube is taken by the A-site cation while at the 8 corners of the cube rest the B-site with a share equal to 1. Anions with share equal to 3 on the face centered positions occupy the X-site. The ABX_3 structure is the result of this 3-dimensional atomic configuration. A large cation (either organic or inorganic) usually occupies the A-site, while small divalent metallic cations (e.g., Mn^{2+} , Cu^{2+} , Co^{2+} , Mg^{2+} , Ni^{2+} , Sn^{2+} , Pb^{2+} , and Eu^{2+}) occupies the B-site. Moreover, oxygen or halide ion (Cl, Br, I) occupies the X-site and these ions bind to both A and B cations[81]. Perovskites can be prepared by a wide range of elements with different valences while at the same time maintaining the overall charge neutrality of the compound [79]. The A – X and B – X bond distances are expressed as $\sqrt{2} (a/2)$ and $a/2$, where a = lattice constant, for an ideal cubic structure. Therefore,

$$\sqrt{2} (r_A + r_X) = (r_B + r_X) \quad (2.1)$$

is used to express the relationship between the ionic radii of the cations and anion. Goldschmidt proposed the principle tolerance factor (t), which gives information on the nonconformity from the ideal cubic structure, based on the relationship above (equation 1) [79].

$$t = (r_A + r_X) / [\sqrt{2}(r_B + r_X)] \quad (2.2)$$

Therefore, r_A , r_B , and r_X are the ionic radii of the A-site cations and B-site anions, respectively. In simple words, the tolerance factor (t), gives the relationship between the ionic radii of the A, B, and X species. The magnitude of the tolerance factor (t) indicates the structural orientation of the resulting perovskite material. For instance, the resultant perovskite structure for (i) $0.7 < t < 0.9$: is an orthorhombic, for (ii) $0.9 < t < 1$: a

rhombohedral, for (iii) $t = 1$ a simple cubic structure is obtained, and for (iv) $1 < t < 1.13$: a hexagonal structure is obtained.

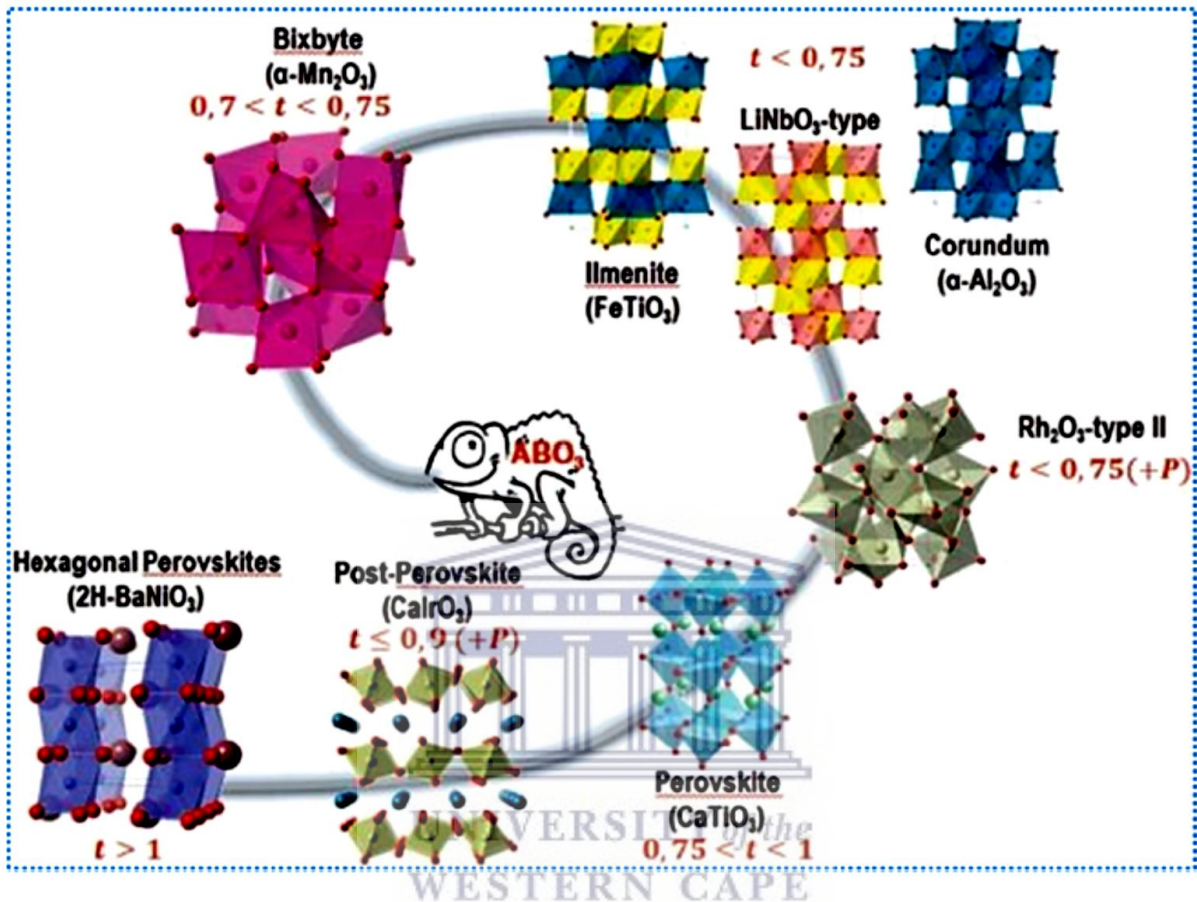


Figure 2.1: Different phase transitions of perovskite structures. Reproduced with permission[82]. Copyright 2017, Elsevier.

The formation of different structures discussed above results from the tilting of octahedral formed by the X anion. It is indicated in **Figure 2.1** how the different perovskites can adopt the different values of the tolerance factor [82]. There are two requirements that must be satisfied for the formation of perovskites. Firstly, perovskite compounds must have an overall net charge of zero (charge neutrality, electroneutrality). This means that the net charge of A-site and B-site site cations must be equivalent to that on the X-site anions. The charge distribution can be determined in the forms of $A^{1+}B^{5+}X_3$, $A^{4+}B^{2+}X_3$, or $A^{3+}B^{3+}X_3$. Secondly, $R_A > 0.090$ nm and $R_B > 0.051$ nm where R_A = ionic radii of the A-site atoms and R_B = ionic

radii of the B-site atoms. Moreover, $0.8 < t < 1.0$ (accepted range for the tolerance factor). Another stability measure for the perovskites is known as the octahedral factor (μ) which is expressed by the following equation:

$$\mu = \frac{r_B}{r_X} \quad (2.3)$$

The coordination numbers of B-site cations and X-anions are determined with the help of the octahedral factor. Additionally, the valence, chemical stability and the operating temperature are few parameters that play a major role in determining the distortion, formation and stability of the perovskite structures.

2.1.3 METAL HALIDE PEROVSKITES

Owing to their attractive properties like high-efficiency optoelectronic characteristics (at inexpensive cost), metal halide perovskites holds great prospects as semiconductors for the next-generations optoelectronic devices. The utilization of metal halide perovskites has inspired the development of perovskite photovoltaic cells (solar cells). The power conversion efficiencies of the cutting-edge perovskite solar cells are competing on the same level with the best silicon crystalline silicon solar cells. $\text{CH}_3\text{NH}_3\text{PbX}_3$ and CsPbX_3 (where X = Cl, Br, or I) are some of the important metal halide perovskites explored in the arena of solar cell devices. Since metal halide perovskites have a tolerance factor close to 1, this submits that they can sustain a stable and symmetrical structure similar to those of perovskite type oxides. Researchers have reported that different phases of metal halide perovskites can be attained at different temperatures (i.e. orthorhombic: $T \leq 165$ K, tetragonal: $165 < T \leq 327$ K, cubic: $T > 327$ K). The co-existence of tetragonal and cubic phases at room temperature has been proposed by some studies of thin films metal halide perovskites [83,84]. Additionally, an

introduction of super lattice can be utilized to enable metal halide perovskites self-adjust the configuration of phases and automatically create a buffer layer at boundaries [85]. Metal halide perovskites have a tunable energy bandgap and they display large absorption coefficients and exciton emissions at room temperature. Thus, metal halide perovskites have been reported as semiconductors materials with a direct energy bandgap [86].

The modifications of organic cation molecules and halide anions have been utilized as a strategy to attain metal halide perovskites which exhibit strong and tunable photoluminescence emissions even at room temperature. The tunability of the energy bandgap of metal halide perovskites makes them suitable for various light-emitting applications such as lasers, light emitting diodes (LEDs), and optical sensors. The basic properties of metal halide perovskites which include type, concentration, and charge carrier mobility, can be largely influenced by the synthesis techniques of metal halide perovskite [83,87,88]. For example, an easy fabrication route is followed to produce polycrystalline thin films of metal halide perovskites and these thin films contain lesser structural defects in comparison to those of traditional semiconductors thin films. Since metal halide perovskites have gained so much significance in optoelectronic applications, the synthesis techniques of metal halide perovskites thin films has been a widely explored research topic [89,90]. The two most commonly employed synthesis techniques for the fabrications of metal halide perovskites include solution processing and vapour evaporation. In solution processing synthesis technique, precursors are evaporated, followed by mixing in the ideal solvents which will subsequently lead to the precipitation of metal halide perovskites attained via heating or spin coating. The commonly used precursors include metal and organic halides (e.g., methylammonium iodide (MAI) and lead iodide PbI_2). N, N-dimethylformamide (DMF), hexane, dimethylsulfoxide (DMSO), toluene, γ -butyrolactone (GBL) are the commonly used solvents. The precursor's concentrations and the reaction temperature play a

critical role in determining the phases of the organometal halide perovskites. However, tunable morphologies are not achieved via these processes (solution processing synthesis technique) and thus induce difficulties in large-scale applications of metal halide perovskites. Vapour evaporation technique is the second fabrication technique for the production of metal halide perovskite thin films. Although lower power conversion efficiency is attained employing this technique, in comparison to the solution processing technique, this technique produces metal halide perovskite thin films with higher crystallinity. Therefore, to produce metal halide perovskites thin films with better homogeneity and high crystallinity, researchers prefer thermal evaporation. For organometal halide perovskites, the A-site is occupied by an organic cation molecule, the B-site is occupied by the metal cation and the X-site is occupied by a halide anion. Organometal halide perovskites therefore benefits from the properties of both the inorganic and the organic molecules. Methylammonium lead triiodide (MAPbI₃) has become a significant member of organometal halide perovskites and it has been extensively explored in photovoltaic applications owing to its high absorption coefficient, high electron-hole mobilities (i.e., ambipolar nature) and long charge carrier diffusion lengths. Organometal halide perovskite nanoparticles are utilized in the manufacturing of LEDs owing to their high photoluminescence quantum efficiency (PLQE) and high colour purity. These attractive properties of organometal halide perovskites have awarded them with great prospects for future application in organic LEDs [91–95]. Organometal halide perovskites have for been utilized for various applications in the photovoltaic industry. Recently, a huge interest for the development of perovskite solar cells has been ignited by the utilization of different halide anions with different compositions. Within a period of 5 years, perovskite solar cells have attained power conversion efficiency beyond 20%. The achievement of this remarkable power conversion efficiency is owed to the excellent properties which include tunable energy bandgap, ambipolar semiconducting behaviour, and high conductivity.

Notably, there are concerns regarding the stability of organometal halide perovskites under ambient conditions and it is for this reason that they are not yet industrially commercialized. However, organometal halide perovskites have been used in many sensing applications e.g., gases [96,97], humidity [98] and explosives, etc. [90,99–101] due to their delicate (sensitive) nature. A reversible chemoresistive ammonia sensor based on $\text{CH}_3\text{NH}_3\text{PbI}_3$ thin film has been reported with a good LOD [102,103]. The sensing of ammonia with high selectivity and fast response (61 s) has been done by taking advantage of the luminescent properties of $\text{CH}_3\text{NH}_3\text{PbBr}_3$ [104]. An organometal halide perovskite material with mixed anions $(\text{CH}_3\text{NH}_3)\text{PbBr}_{3-x}\text{I}_x$ was utilized for ammonia sensing whereby the weak bonding that exist between MA^+ and NH_4^+ permitted a sensitive detection with high selectivity [105]. The all inorganic lead halide perovskites (e.g., lead halide nanocubes CsPbBr_3) have also been studied for gas sensing applications, despite the organolead halide perovskites [106]. These nanocubes demonstrated high surface reactivity toward ozone with high sensitivity and fast response/recovery times [106]. Nanoparticles of metal halide perovskites have been utilized in many various types of applications. The synthesis of organometal halide perovskites nanoparticles was reported by Schmidt et al., among the first research groups who reported their synthesis. During the synthesis process, initial precursor solutions of $\text{CH}_3\text{NH}_3\text{Br}$ and PbBr_3 were mixed in dimethylformamide (DMF) solvent. The following step was the precipitation of the organolead halide perovskite $\text{CH}_3\text{NH}_3\text{PbBr}_3$ with acetone solvent. The product $\text{CH}_3\text{NH}_3\text{PbI}_3$ exhibited a cubic phase perovskite structure with spherical morphology (≈ 6 nm) and a sharp absorption band at a wavelength of 525 nm, and this absorption was blue shifted when compared to the bulk crystal [95]. This discovery inspired many research scientists in the photovoltaics field to work in the development of organolead halide perovskite nanocrystals. All inorganic cubic perovskite nanocrystals of CsPbX_3 ($X = \text{Cl}, \text{Br}, \text{I}$, and mixed Cl/Br and Br/I), with the particle size in the range of 4 – 15 nm, were

synthesized by Protesescu *et al.* [92]. Since the energy bandgap of CsPbX₃ can be tuned by substitution of halide anions at X-site (i.e. X = Cl/Br or Br/I), the product CsPbX₃ can exhibit a wide range of photoluminescence emissions at different wavelengths (i.e. 400 – 800 nm) [107].

2.1.4 DOPING MECHANISMS IN PEROVSKITES

The primary physical and chemical properties of perovskite materials are modified by the incorporation of foreign atoms at different sites (it could be the A-site and/or the B-site) of the perovskite structure. This process is called doping. The modification of structural, microstructural, electrical, and magnetic properties of organometal halide perovskites can be attained via doping with anions and cations of different sizes and charges [108]. During the doping process, variations in the chemical state, mobility of the oxygen vacancies in the lattice, and the formation of crystal defects, or generations of anion vacancies result in such modifications in perovskite properties. The basic characteristics of the perovskite are determined by the bond between the X-anion and the B-site cation. In the event whereby the B-site cation is partially substituted with other metals (e.g., AB_{1-y}M_yX₃), a hybrid perovskite structure with properties of two cations is realized [108]. The usual oxidation state of the B-site is stabilized with the help of A-site cation forming a crystal vacancy. Since different cation molecules have different individual properties, the synthesis of different perovskites with different material properties and performances is possible. By doping both the A-site and the B-site with other species (e.g., different metal ions), the physical/chemical properties such as electronic conductivity and catalytic activity of the resulting modified perovskites can be altered. Thus, the development of perovskite materials with potential applications in several research fields can be attained through doping. The doping of oxygen vacancies at the

A-site in perovskite type oxides (PTOs) influences the morphology and surface area. The synthesis of $\text{La}_x\text{Sr}_{1-x}\text{Co}_{0.1}\text{Mn}_{0.9}\text{O}_{3-\delta}$ ($0.3 \leq x \leq 1$) nanofibers employing the electrospinning technique was first reported by Cao *et al.* [109]. The experimental results demonstrated that the diameters of the nanofibers decreased and the grain size and surface area increased when various concentrations of Sr (from 0 to 0.3) were doped on the La site [109]. This was due to the alteration of Mn-O bond length and the Mn-O-Mn bond angle induced by the Sr dopants.

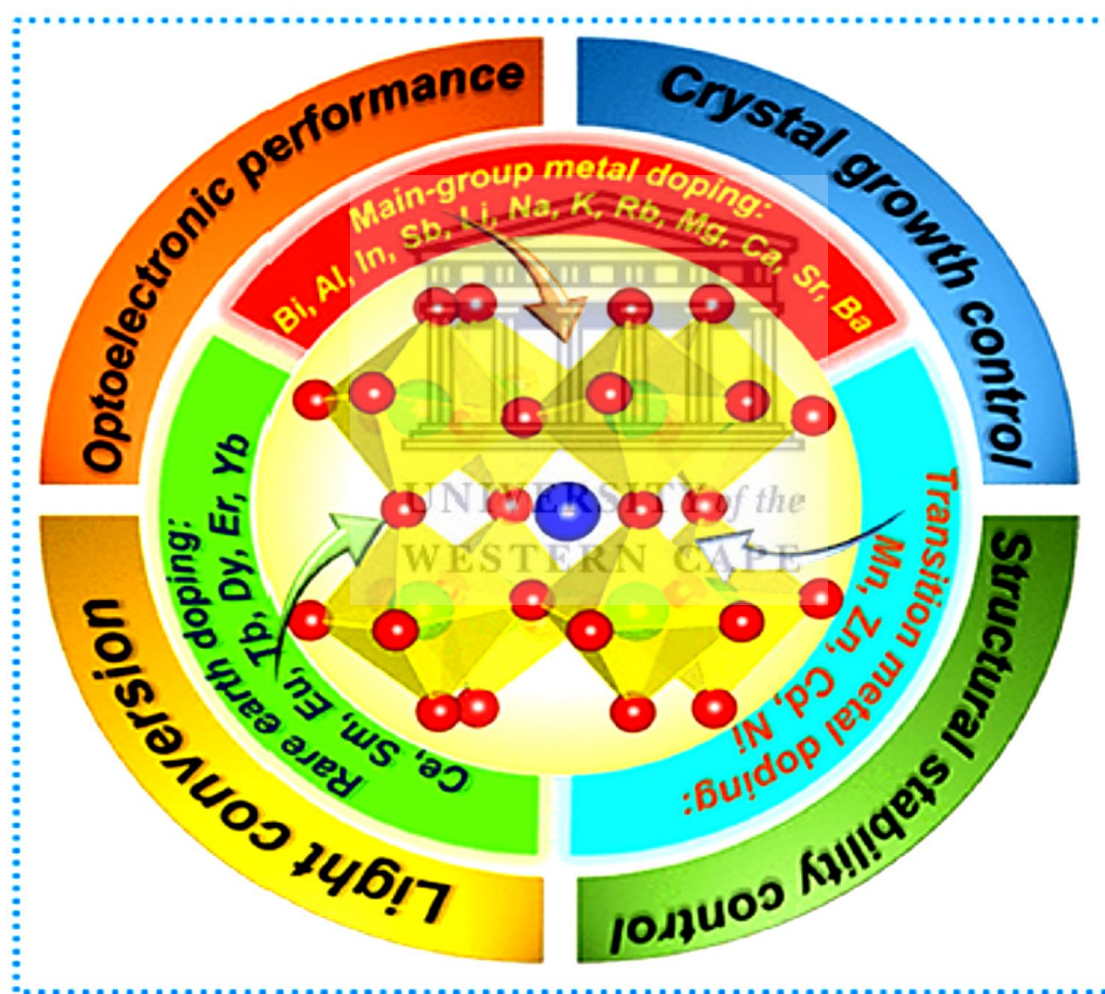


Figure 2.2: Change in properties of metal halide perovskites after doping. Reproduced with permission from Ref. [110]. Copyright 2018, American Chemical Society.

The perovskite material stability and catalytic behaviour have been improved by doping of perovskites with transition metals at the B-site. The inclusion of two different ions at the B-site of the perovskite structure results in the doubling of the unit cell structure $\text{AB}_{0.5}\text{B}'_{0.5}\text{O}_3$

along the x-axis. The oxygen atom is shifted toward more positive ions by doping with ions of different charges. Some examples of A- and B-site doped perovskites are given in **Table 2.1**.

Table 2.1. Examples of perovskites doped with different elements at their A-, B- and X-sites.

A site	B site	X site
$\text{La}_{1-x}\text{Pr}_x\text{GaO}_3$ [111]	$\text{LaNi}_{0.25}\text{Co}_{0.75}\text{O}_3$ [112]	$\text{MAPbI}_{3-x}\text{Cl}_x$ [113]
$\text{La}_{1-x}\text{Nd}_x\text{GaO}_3$ [111,114]	$\text{PrBaCo}_2\text{O}_{5+x}$ [115]	MAPbCl_2Br [113]
$\text{La}_{1-x}\text{Ca}_x\text{MnO}_3$ [116]	$\text{LaTi}_{0.65}\text{Fe}_{0.35}\text{O}_{3-\delta}$ [117]	MAPbClBr_2 [113]
$\text{La}_x\text{Sr}_{1-x}\text{CoO}_{3-\delta}$ [118]	$\text{La}_{0.75}\text{Sr}_{0.25}\text{Co}_{0.5}\text{Mn}_{0.5}\text{O}_{3-\delta}$	MAPbBr_2I [113]
	[119]	
$\text{Sm}_{0.92}\text{Bi}_{0.08}\text{FeO}_3$ [120]	$\text{PrBa}_{0.94}\text{Co}_2\text{O}_{5+\delta}$ [121]	MAPbBrI_2 [113]
$\text{La}_{0.5}\text{Sr}_{0.5}\text{CoO}_{3-x}$ [122]	$\text{MAPb}_{0.75}\text{Sn}_{0.25}\text{Br}_3$ [123]	
$\text{La}_x\text{Ce}_x\text{FeO}_{3-\delta}$ [124]	$\text{MASn}_x\text{Pb}_{(1-x)}\text{I}_3$ [123]	

Advanced optoelectronic properties were particularly demonstrated by metal halide perovskites after doping with a combination of halide ions or different individual halide ions. The eco-toxicity and eco-stability posed by elemental Pb on the B-site are some of the downsides encountered by metal halide perovskites. The substitution/doping of Pb^{2+} ions with other metal cations (e.g. Ln^{2+} and Mn^{2+}) has been recommended in recent studies as a strategy to address these issues [125–129]. The doping of CsPbBr_3 with Mn^{2+} and Cl^- (doping on both B and X-sites), respectively, has resulted in advanced photoluminescence and quantum yield properties [130]. The photoluminescence was tuned from 402 nm to 514 nm by utilizing this doping strategy, as seen in **Figure 2.3** [130]. The effect of substitution of various elements in

A-, B-, and X-sites for the modification of the properties of metal halide perovskites is demonstrated in **Figure 2.2** [110].

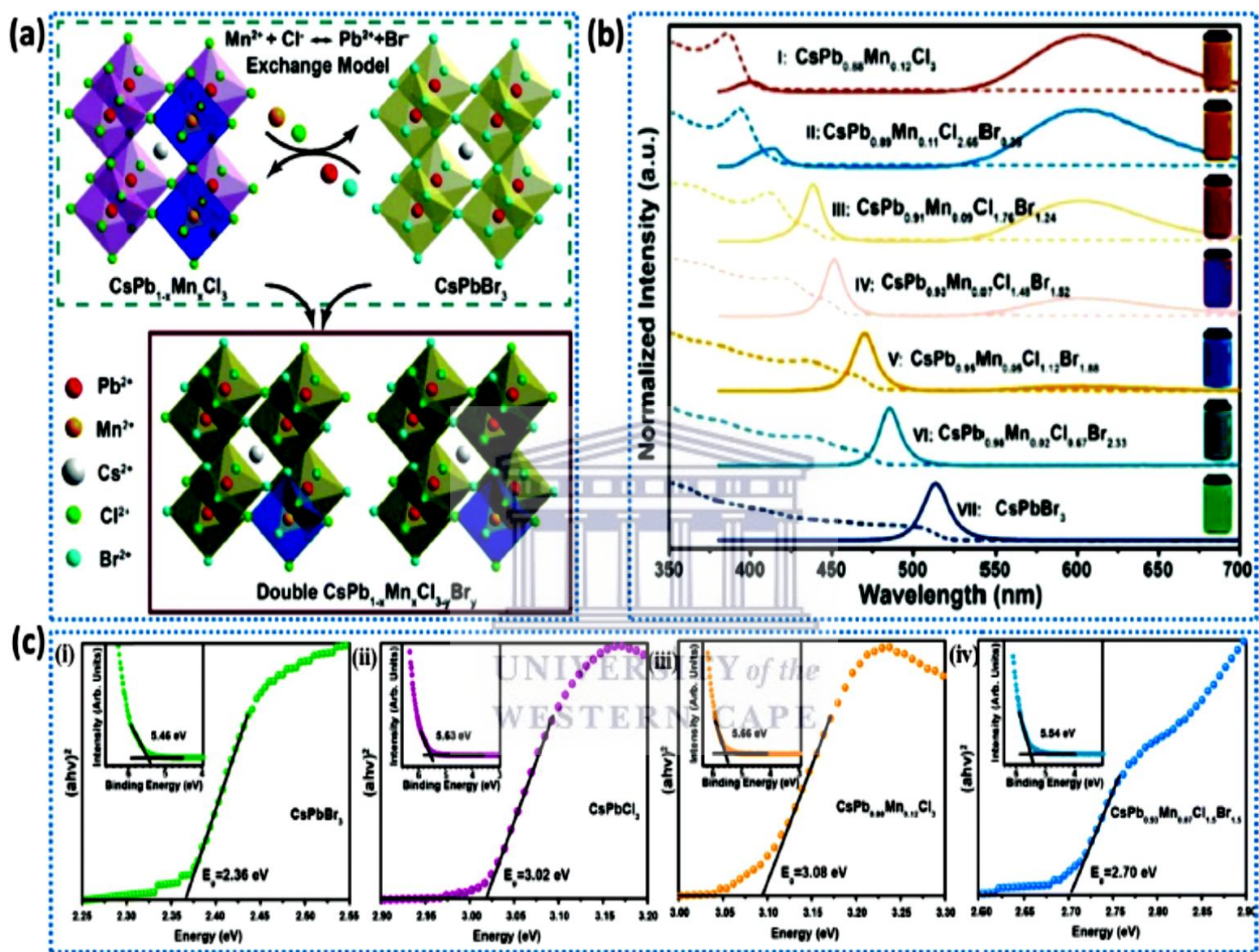


Figure 2.3: Optical performance characteristics due to ion exchange mechanism. (a) Schematic of the ion exchange between CsPbBr₃ and CsPb_{0.88}Mn_{0.12}Cl₃ NCs. (b) UV (dashed line) and PL (solid line) spectrum of Cs(Pb_xMn_{1-x})(Cl_yBr_{1-y})₃ with different Mn doping concentrations. (c) Ultraviolet photoelectron spectroscopy (UPS) of (i) CsPbBr₃, (ii) CsPbCl₃, (iii) CsPb_{0.88}Mn_{0.12}Cl₃ and (iv), CsPb_{0.93}Mn_{0.07}(Cl_{0.5}Br_{0.5})₃ NCs. Reproduced with permission from Ref. [130]. Copyright 2017, Royal Society of Chemistry.

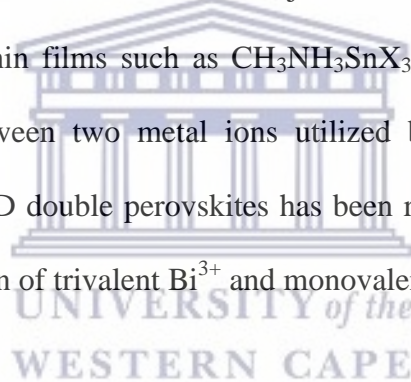
The synthesis of single phase and eco-stable CsPb_xMn_{1-x}Cl_yBr_{3-y} under ambient conditions was proposed by doping CsPbCl₃ with high and sustained content of Mn²⁺ [131]. An orange-red photoluminescence emission at 600 nm was exhibited by the material CsPb_xMn_{1-x}Cl_yBr_{3-y}

owing to the high content of Mn^{2+} dopant [131]. $\text{CsPb}_x\text{Mn}_{1-x}\text{Cl}_y\text{Br}_{3-y}$ (Mn-doped perovskites) materials are recommended for sensing and actuating device applications. Similarly, the nanocrystals of $\text{Mn}:\text{CsPbCl}_3$ have also been recommended for oxygen photoluminescent sensing probes [132]. As oxygen concentrations elevated from 0% to 100%, the phosphorescence intensity of $\text{Mn}:\text{CsPbCl}_3$ reduced to 53% from its original value [132].

2.1.5 LEAD AND OTHER TOXICITY

The composition of elemental lead [133] that leads to eco-toxicity [134] and bioaccumulation in ecosystems [135] impedes the industrial commercialization of perovskite solar cells based on organic-inorganic lead perovskites. $\text{CH}_3\text{NH}_3\text{PbI}_3$ -based perovskite solar cells contains about one third of lead (Pb) weight. The hybrid perovskite material will dissolve completely in water leaving PbI_2 behind when exposed to rainwater [136]. It has been shown by analytical evaluations that only 70 ppm of lead is released by perovskite solar cell panel. When compared to the standards for low levels of contamination, this concentration (i.e. 70 ppm) is moderately low [137]. There is no adequate non-toxic threshold for lead exposure, even though it is detrimental and not cataclysmic. Moreover, a high degree of toxicity is also demonstrated by other elements such as iodine [138,139] and methylamine [140]. The nanoparticles of $\text{CH}_3\text{NH}_3\text{PbI}_3$ are toxic to the health of human anatomy, and they can also reach and affect the neurological and the nervous system [141]. The synthesis of lead-free perovskite solar cells utilising the transition metal Cu has been reported by Daniele *et al* [142]. In the work of Daniele *et al.*, $(\text{CH}_3\text{NH}_3)_2\text{CuCl}_x\text{Br}_{4-x}$ compound was synthesized and the green photoluminescence emission was observed owing to Cu^+ ions formation. The stability of $\text{MA}_2\text{CuCl}_x\text{Br}_{4-x}$ can be attained by mixing halides and chlorine since it is highly deliquescent [142]. The performance was evaluated by electrochemical impedance

spectroscopy. It was found that low absorption and strong anisotropy impedes the photovoltaic performance of these cells. The thin film thickness and the photovoltaic requirements with restricted diffusion length are decided by the exact material combination. Since elemental tin Sn [60,143–146] belongs to group 14 transition metals, with four electrons in its outer shell, it is also considered to be suitable for Pb replacement. Since group 14 transition metals have bigger atomic size, Sn causes the instability of +2 oxidation state [123]. It has been demonstrated by theoretical studies that I-5p orbitals of I₃⁻ groups have an influence on the band-edge reconstruction. The new conduction-band minimum is then realized at the Brillouin zone, which enables the lead-free perovskite formation [147]. Vapour-assisted solution process [143,148] and hot injection technique [145] are employed to prepare lead-free perovskite thin films such as CH₃NH₃SnX₃ (X = I, Br, Cl). This end is attained by the interplay between two metal ions utilized by halide double perovskites [149,150]. The synthesis of 3-D double perovskites has been realized by the replacement of Pb²⁺ sites with an amalgamation of trivalent Bi³⁺ and monovalent Ag⁺ cations [151,152].



2.1.6 LEAD-FREE PEROVSKITE SOLAR CELLS

To achieve high power conversion efficiency for solar cell devices, there are several key parameters that must be satisfied by the light-absorbing semiconductor materials used to fabricate the photovoltaics which include; narrow energy bandgap, low defect density, long carrier diffusion length, excellent carrier transfer kinetics and suitable conduction-band minimum/valence-band maximum. The unparalleled power conversion efficiency of the advance perovskite solar cells is dependent upon the electronic structure of Pb²⁺ due to the 6p orbital of the Pb-atom which plays a crucial role in the band structure of the traditional Pb-based hybrid perovskite materials [153]. There are specific metallic ions, namely; Sn, Ge, Bi, Sb etc., which serve as the ideal alternative ions for Pb²⁺. For instance, the 5p orbital for Sn is

not as much dispersive and shallower, and this feature is advantageous for the narrowing of energy bandgap and improvement of charge carrier mobility, demonstrating great potential for application in lead free perovskites.

i. Sn-based halide perovskites

Likewise to the conventional APbX₃ perovskite crystal structure, perovskites based on Sn²⁺ consist of SnX₆ octahedra network, and the A cation molecule is integrated into the open site to attain a stable structure with a balanced net charge [154]. The energy bandgaps of Sn²⁺ based perovskites are determined to be indirect in the range of 0.75 eV to 1.3 eV, making them great potential candidates for photovoltaic application [155]. In 2012, Chen *et al.* reported for the first time a Sn²⁺-containing photovoltaic cell based on CsSnI₃ perovskite thin film semiconductor synthesized through vacuum deposition technique, whereby charge separation resulting in lower power conversion efficiency of 0.9% (due to slow-moving charge extraction mobility) was realized by manufacturing a Schottky junction [156]. In 2014, Noel *et al.* fabricated for the first time CH₃NH₃SnI₃ thin film onto mesoporous -TiO₂ scaffold employing a spin-coating technique to launch an analogous solar cell device as a strategy to further improve the performance of Sn²⁺-based lead free perovskite solar cells, and this strategy resulted in significantly improved power conversion efficiency up to 6.4% [1]. Simultaneously, the optical energy bandgap of CH₃NH₃SnI_{3-x}Br_x was systematically optimized from 1.3 eV to 2.15 eV with increasing content of Br by Hao *et al.* and this eventually produced an advanced architecture of FTO/TiO₂/CH₃NH₃SnIBr₂/Spiro-MeOTAD/Au which attained a power conversion efficiency of 5.73% [123]. Many strategies were since then explored to revamp the power conversion efficiency of Sn-based lead free perovskite solar cells.

ii. Ge-based halide perovskites

Another potential candidate to replace the eco-toxic Pb is elemental germanium (Ge), for lead-free halide perovskites. It has been predicted by many theoretical studies that perovskites containing elemental Ge hold excellent optoelectronic properties for potential application in solar cell devices [157–160]. Nonetheless, power conversion efficiencies of only about 0.11% and 0.2% for CsGeI₃ and MAgGeI₃, respectively, were demonstrated by the first Ge²⁺-based perovskite solar cells [160]. Likewise to Sn²⁺ ions, the low photovoltaic performance of Ge-containing perovskite solar cells is chiefly attributed to the fast oxidation of Ge²⁺ to Ge⁴⁺ which produces devices with poor stability; additionally, wider energy bandgaps of 1.63 and 2.0 eV for CsGeI₃ and MAgGeI₃, respectively, matching well to that of perovskites based on Sn²⁺ [160]. It has been demonstrated recently by both theoretical and experimental studies that the mixed Ge-Sn is a good choice to optimize the photovoltaic performance of perovskite solar cells based on Ge²⁺ [157–164]. The properties of Ge-Sn mixed halide perovskites (exhibiting tunable energy bandgap from 0.9 eV to 3.15 eV) with perovskite crystal structure formulation of AB'_{0.5}B''_{0.5}X₃ and A'_{0.5}A''_{0.5}B'_{0.5}B''_{0.5}X₃ have been predicted by Zeng *et al.* [161]. RbSn_{0.5}Ge_{0.5}I₃ (with energy bandgap from 0.9 to 1.6 eV) is one of the best solar absorber materials among all of the anticipated solar cell materials, with a potential to produce up to 25% Shockley-Queisser efficiency for single-junction solar cells [161]. A series of mixed halide perovskites based on Ge-Sn, MASn_(1-x)Ge_xI₃ (0 ≤ x ≤ 1) (with energy bandgap of 1.3 – 2.0 eV) was further prepared by Nagane *et al.*, showing that they are the best candidates for solar cell applications from single junction device to tandem solar cells [162]. The power conversion efficiency of FA_{0.75}MA_{0.25}SnI₃ was improved to 4.48% which was attained through doping small amount of Ge²⁺ (at 5%) to form mixed halide perovskites based on Ge-Sn [163]. Remarkably, a power conversion efficiency of 6.9% was attainable after 72 h under inert N₂ atmosphere. The advanced power conversion

efficiency can be ascribed to Ge-induced reduction of the Sn vacancy concentration, showing the synergistic outcome between elemental Ge and Sn [165]. A recent study demonstrated that the trap density can be decreased significantly from 10^{15} to 10^{17} cm^{-3} (devoid of Ge) to 10^8 - 10^{14} cm^{-3} [164]. The carrier diffusion length could be improved to 1 μm through compositional engineering, and the addition of SnF_2 resulted in Ge-Sn mixed halide based perovskite solar cells with a record power conversion efficiency of 7.9% [164]. More experimental work is still needed to thoroughly explore this family of lead-free perovskite materials.

iii. Bi-based halide perovskites

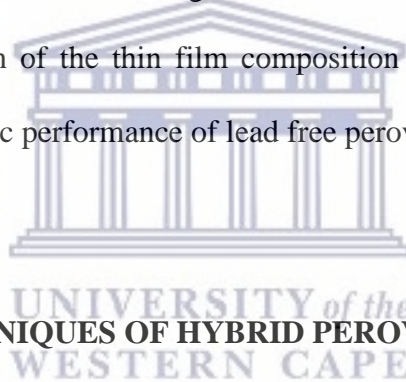
Elemental bismuth (Bi) is one of the eco-friendly metals with the same electronic configuration and ionic radius as elemental Pb and elemental Sn, making it a favourable potential candidate for application in eco-friendly and eco-stable lead-free perovskite solar cells. Since Bi has a +3 valence state, perovskites based on ternary Bi^{3+} mostly assume a structure with a formula $\text{A}_3\text{Bi}_2\text{X}_9$ achieved by the replacement of Pb^{2+} with two Bi^{3+} whereby A is occupied by a monovalent cation like MA^+ , FA^+ , Cs^+ or Ag^+ , and X is occupied with a halogen anion like I or Br^- [166]. The structure and optoelectronic properties of Bi^{3+} based perovskites have been explored to find out their potential application in solar cell devices [167–169]. A new kind of sunlight absorber materials; $\text{MA}_3\text{Bi}_2\text{I}_9$ and $\text{Cs}_3\text{Bi}_2\text{I}_9$, was successfully synthesized by Eckhardt and Park *et al.* in 2015 [168,169]. These Bi^{3+} -based perovskite materials both demonstrated a 0D structure (with face-sharing octahedral) in contrast to corner-sharing octahedral for 3D MAPbI_3 . $\text{Cs}_3\text{Bi}_2\text{I}_9$ perovskite materials attained an optimal power conversion efficiency of 1.09% by constructing a photovoltaic device with glass/FTO/ TiO_2 /($\text{Cs}_3\text{Bi}_2\text{I}_9$)/HTM/Ag architecture [169]. The poor power conversion

efficiency was attributed to wider energy bandgap (over 2.0 eV) and poor thin film quality [170]. Sulphur doping strategy was employed as an attempt to advance the photovoltaic performance and this strategy could regulate the energy bandgap from 2.1 eV to 1.45 eV. The advanced thin film quality (attained through sulfur doping strategy) resulted in carrier mobility of $2.28 \text{ cm}^2\text{V}^{-1}\text{s}^{-1}$ which was 5 times greater than that of the benchmark $\text{Cs}_3\text{Bi}_2\text{I}_9$ [171]. The energy band gap structure of $\text{MA}_3\text{Bi}_2\text{I}_9$ and $\text{Cs}_3\text{Bi}_2\text{I}_2$ perovskite materials can be modulated by altering the stoichiometric ratio in perovskite precursors charting a course to high-efficient photovoltaic platforms [172].

iv. Sb-based halide perovskites

The trivalent antimony (Sb^{3+}), likewise to Bi^{3+} , has also been extensively explored for potential application in eco-friendly lead-free perovskite solar cells. Perovskites based on Sb, assuming the structural formula: $\text{A}_3\text{Sb}_2\text{X}_9$, whereby A is occupied by a monovalent cation: MA^+ , FA^+ or Cs^+ and X is occupied by the halogen anion: I^- , Br^- and Cl^- , have demonstrated potential for application in photovoltaics (solar cells) ascribed to the analogous crystal structure and properties of species based on Bi [46,173]. $\text{MA}_3\text{Sb}_2\text{I}_9$ perovskites with a wide energy bandgap of 2.14 eV and an absorption coefficient of 10^5 cm^{-1} was reported for the first time in the year 2016 by Hebig *et al.* Nonetheless, a poor power conversion efficiency of 0.49% was attained through constructing solar cell device with planar heterojunction architecture [174]. The poor photovoltaic performance was ascribed to wide bandgap, poor thin film quality, non-uniform thin film morphology and low photocurrent densities. Hydroiodic (HI) acid additive was integrated into $\text{A}_3\text{Sb}_2\text{I}_9$ ($\text{A} = \text{MA}^+$, Cs^+) precursor solution to produce perovskite thin films with high quality and less toxic defects as a strategy to address the issue of poor photovoltaic performance [175,176]. Optimal power

conversion efficiencies of 2.04% and 0.84% were attained for perovskite solar cells based on $\text{MA}_3\text{Sb}_2\text{I}_9 + \text{HI}$ and $\text{Cs}_3\text{Sb}_2\text{I}_9 + \text{HI}$, respectively, when constructing solar cells with architecture of glass/ITO/PEDOT:PSS/ $\text{A}_3\text{Sb}_2\text{I}_9$ /PC₇₁BM/C₆₀/BCP/Al [175]. The manufacturing of highly efficient solar cells is generally achieved by employing doping engineering since it is a simple and effective technique. The incorporation of elemental Cl into the crystal lattice prevents the formation of 0D dimer phase and this doping strategy has produced a 2D layered $\text{MA}_3\text{Sb}_2\text{Cl}_x\text{I}_{9-x}$ perovskites with an optimal power conversion efficiency of 2.1% ($J_{\text{SC}} = 5.04 \text{ mAcm}^{-2}$, $V_{\text{OC}} = 0.69 \text{ V}$, $\text{FF} = 63\%$). The 2D layered perovskite phase becomes more stabilized under ambient conditions (due to increased decomposition enthalpies ΔH_{dec}) and this was achieved through increased Cl-doped concentrations [177]. In this approach, the optimization of the thin film composition and quality is crucial for the advancement of the photovoltaic performance of lead free perovskite solar cells.



2.1.7 FABRICATION TECHNIQUES OF HYBRID PEROVSKITE THIN FILMS

The synthesis technique employed for the fabrication of hybrid perovskite thin films materials plays a crucial role in the study and development of perovskite solar cells technology. The crystallization of perovskite thin films is chiefly effected by fabrication factors such as time, doping, solvent mixtures, and humidity[178]. Additional fabrication paths and the carefully chosen solvents lead to intermediate phases and also influence the photovoltaic performance of the devices based on the quality of thin film deposited[178]. There is a difference between the synthesis and analysis protocol for large-scale production and laboratory analysis. In this study, the synthesis and analysis protocol employed will be for laboratory analysis. Hybrid perovskite solar cell devices that attained high power conversion efficiency based on the laboratory scale (small solar cell devices), do not hold

potential for industrial commercialization. Sustained eco-stability, lucrative, and sustained advance power conversion efficiency perovskite solar cells are required for large-scale production and commercialization.

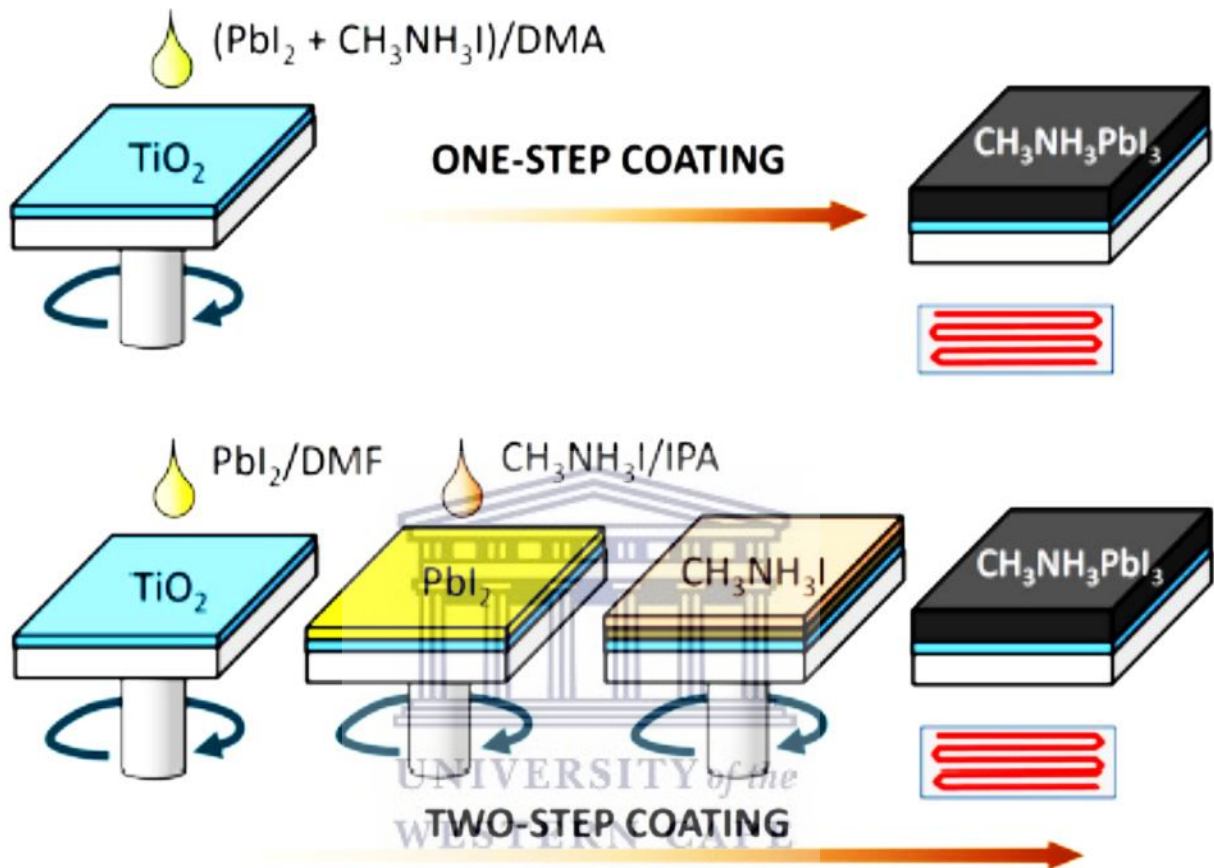


Figure 2.4: One-step and two-step spin-coating procedures for $\text{CH}_3\text{NH}_3\text{PbI}_3$ formation [179] used in accordance with the Creative Commons Attribution (CC BY) license.

A one-step and two-step spin-coating techniques are shown in **Figure 2.4**. In a one-step spin-coating technique, the hybrid perovskite thin film is obtained by thoroughly stirring the perovskite precursor solution, followed by casting it onto the substrate and thereafter accelerated at an optimal speed to evaporate the solvent [180]. The crystalline hybrid perovskites are attained in the second step after thermal annealing at a suitable temperature to remove the residual solvent. Scattered nanodots [181] and very thin layers of hybrid perovskites [11] are obtained when $\text{CH}_3\text{NH}_3\text{PbI}_3$ or $\text{CH}_3\text{NH}_3\text{PbI}_{3-x}\text{Cl}_x$ are synthesized by spin-coating technique. To manage common disadvantages such as poor quality of the thin

film, small grain sizes, and dense pinholes, additive engineering [182,183] is utilized to attain hybrid perovskite thin film materials with ideal grain sizes. An advanced power conversion efficiency of 19.19% was attained through this process. The formation of non-uniform thickness from center to edges of hybrid perovskite thin film is another chief shortcoming of spin coating technique. PbI_2 full coverage with cube-like perovskite structure is delivered by two-step spin-coating technique [179]. In 2013, the two-step spin-coating technique was reported for the first time as an effective method for the fabrication of perovskite solar cells. In a two-step spin-coating technique, a step-by-step spin-coating of PbI_2 solution and methylammonium iodide (MAI) solution is carried out on the glass substrate. To drive the interdiffusion process of precursors, a whole spin-coating system is thermally annealed at a temperature of 100°C . In one-step spin-coating technique, an uncontrolled precipitation of hybrid perovskites is produced and this results in enormous variations in morphology which hinders potential for industrial applications and commercialisations. Therefore, in performance sequential deposition technique [184], PbX_2 solution is spin-coated first on the substrate, followed by dipping (soaking) into MAI solution. The variations of performance are carried out in accordance to soaking time, usually varied from 5 s to 2 h. It was found that the ideal soaking (dipping) time is 15 min, which produced hybrid perovskite solar cell device with advanced current density and open circuit voltage from 10.1 mA/cm^2 and 933 mV (5 s) to 15.1 mA/cm^2 and 1036 mV (15 min) [185], respectively. This technique can perform effectively for nanostructured hybrid perovskite devices constructed following planar heterojunction archetype. The two-step spin-coating deposition technique is an analogue of sequential vapour deposition technique except that the latter utilizes vapour deposition which produces layered multi-stack hybrid perovskite thin films over a large area [186].

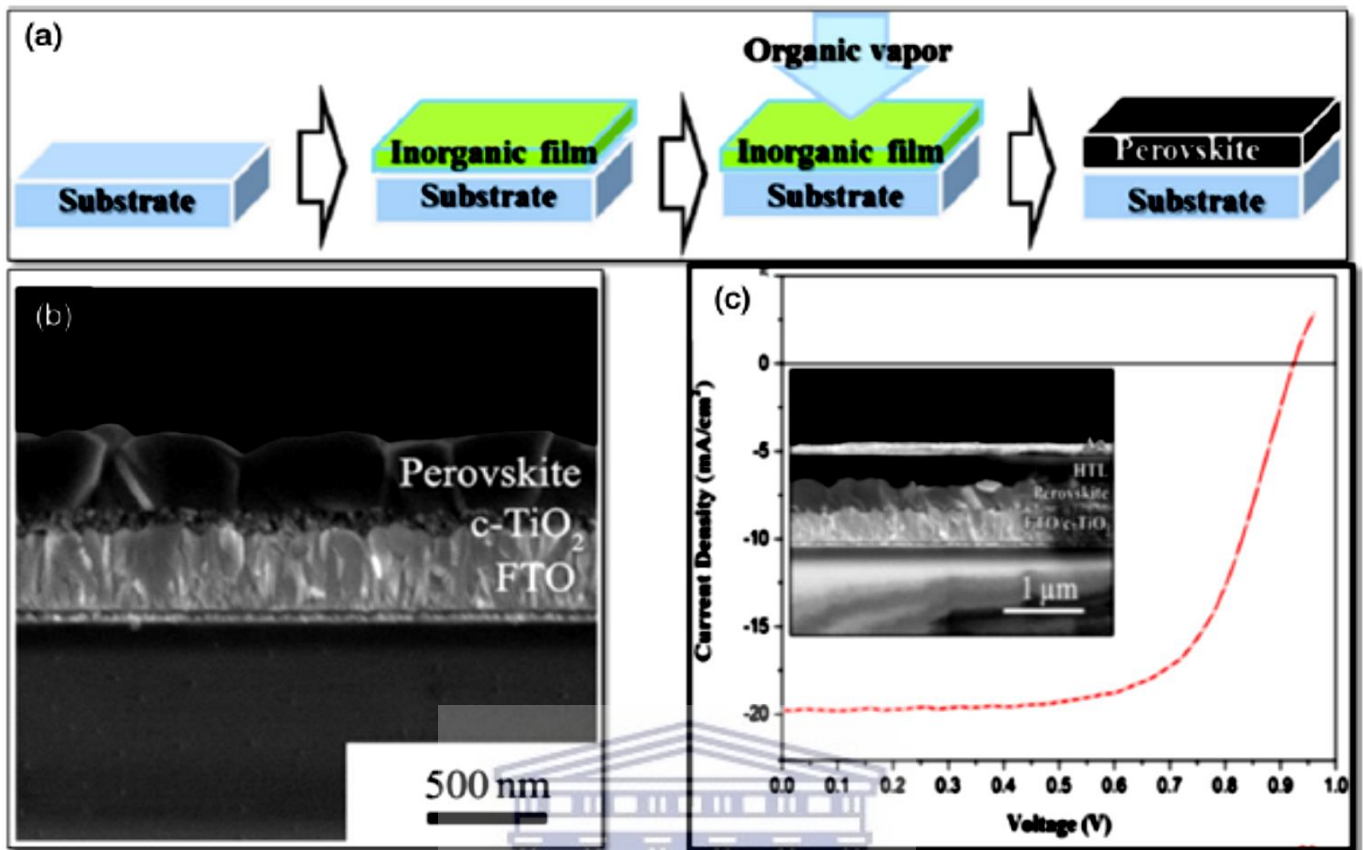


Figure 2.5: (a) Schematic illustration of perovskite film formation through VASP, (b) cross-sectional SEM image, (c) current density-voltage (J - V) characteristics of the solar cell based on the as-prepared perovskite films under AM 1.5G illumination, and cross-section; SEM image of the device (inset). Reproduced with permission from Ref. [187]. Copyright, 2013, American Chemical Society.

Before thermal annealing was done, MAI and PbI₂ were first vapour deposited on top of a substrate as layers. Vapour-assisted solution technique which is also known as blended deposition technique was employed by Yang *et al.* to fabricate MAPbI₃ thin films as demonstrated in **Figure 2.5** [187]. Spin-coating technique was used to deposit a solution of PbI₂ (dissolved in *N,N*-dimethylformamide solvent) on top of the substrate. The substrate coated with PbI₂ was later annealed in MAI vapour at a temperature of 150°C in a glovebox filled with inert nitrogen gas to yield hybrid perovskite thin film over a desired time. Although the production of hybrid perovskite thin films with good thin film quality (good thin film uniformity) is attained employing spin-coating techniques for experiments performed on a laboratory scale, there are however, downsides regarding wastage of precursor solutions (solutions spill out of the substrates) during spin-coating at a specific

speed, and this makes the techniques undesirable for large-area (or large-scale) production due to low material transfer efficiency. Nonetheless, perovskite solar cells are primarily fabricated employing vacuum and solution processing techniques by starting with the organic and inorganic complements of the hybrid composition. Hybrid perovskite thin films with rough surface are undesirably produced by solution process technique. For a technique that involves a vacuum process, high energy is required to create vacuum conditions, and since MAI powder is flaky, this makes the whole synthesis difficult to control. The controllable thin film quality was attained through vapour assisted solution process (VASP). In VASP technique, the hybrid nature of the perovskite materials is exploited, the organic halides have the low sublimation temperature and the reaction taking place between the organic and inorganic groups occurs at a very fast rate. This approach (VASP technique), attained hybrid perovskite thin film with full surface coverage, 100% precursor transformation, uniform grain structure, and print size up to 2 μm . Moreover, this technique (VASP) produces hybrid perovskite thin films free of pinhole defects and produces photovoltaic devices with power conversion efficiency of 15.4% [186]. A dual-source vacuum deposition technique was utilized to fabricate hybrid perovskite solar cells by Snaith *et al.* To achieve advanced thin films uniformity employing the dual-source vacuum deposition technique, MAI and PbCl_2 were respectively preheated to 120°C and 325°C [186]. There are few issues encountered by vapour-based deposition processes which include expensive manufacturing cost and the ability to attain high efficiencies, in comparison to solution-based deposition processes [188,189]. It has been demonstrated through analysis that large crystal would have a visible effect on the power conversion efficiency of hybrid perovskite photovoltaic devices, charting a course to the development of hot-casting deposition technique. Large output and ultrafast production is guaranteed by this technique [190]. In hot-casting technique, the temperature of the MAI precursor is sustained at 70°C and transferred instantly to the spin-coater (at a

specific rotating speed) in a period of less than 5s. The thin film with large grain size is attained by spin-coating for about 30s as it helps in cooling and fast quenching of the thin film. A schematic diagram of the hot-casting technique is demonstrated in **Figure 2.6** and the proportional relation between temperature and large grain synthesis is demonstrated. A comparative chart of grain size and processing temperature for the hot-casting technique and conventional annealing technique are illustrated in **Figure 2.6 (d)** [191]. It was confirmed by this comparison that the formation (synthesis) of large crystals is defined by the evaporation rate. A fully printed planar-heterojunction perovskite solar cell fabricated by slot-die coating was constructed by Vak's group in the year 2015 [192,193]. Various techniques which include screen printing, inkjet printing, knife coating, gravure printing, slot-die coating, spray coating, and flexo-graphic printing have been employed for the large-scale (large-area) hybrid perovskite production for roll-to-roll fabrication [194]. Mass flow determines the thin film thickness in slot-die coating since it is a pre-metered coating process. The formation (synthesis) of thin film stripes of uniform thickness is controlled by the metered solution feed. Additionally, zero loss of solvent can be attained through complete transfer of the solution to the substrate. There are two steps involved in this process. The heating of the glass substrate at a temperature of 70°C which yields dense and glassy PbI_2 takes place at the first step [184,194].

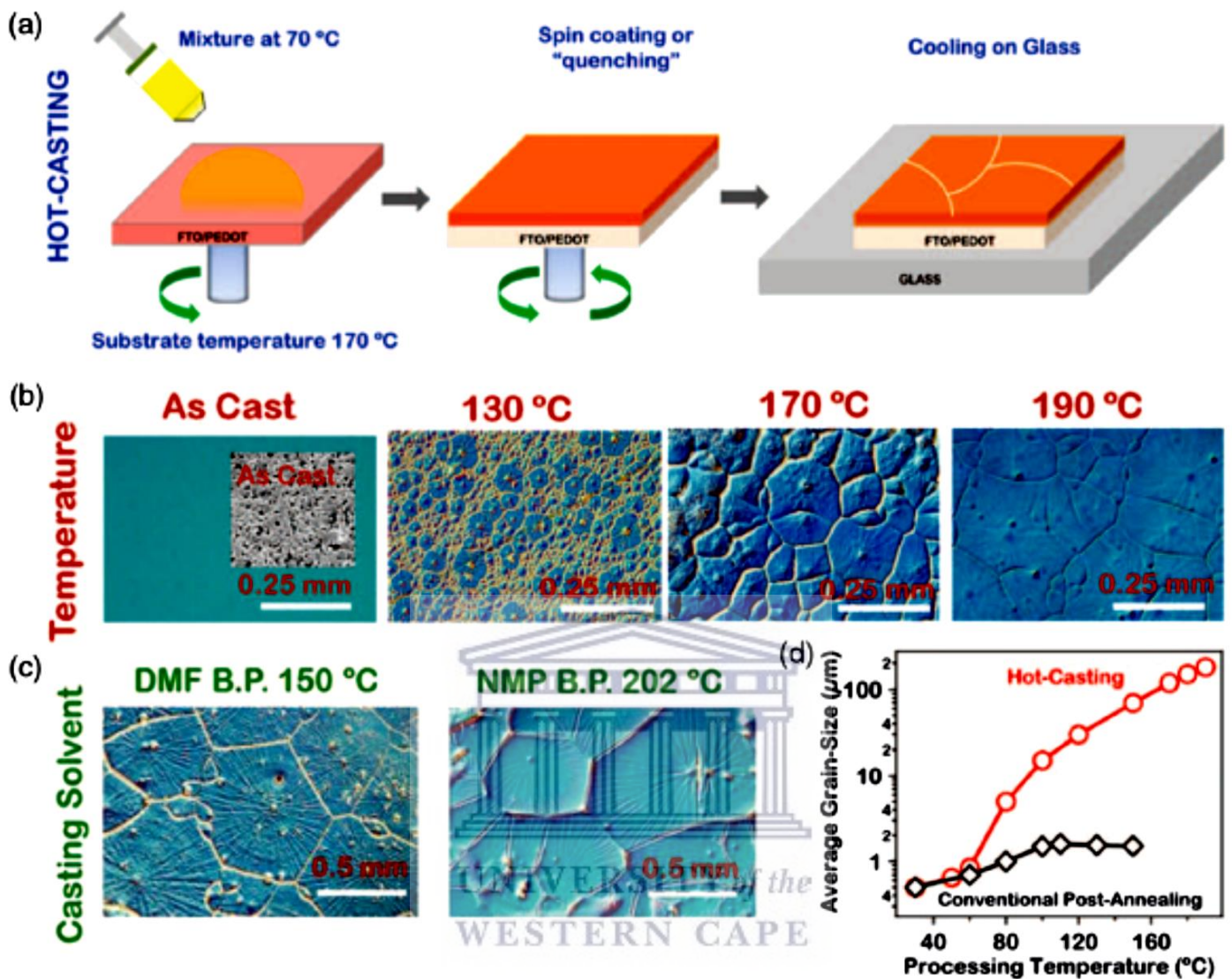


Figure 2.6: (a) Hot-casting technique and (b) optical micrographs of grain formation as a function of substrate temperature with casting solution maintained at 70°C. (c) Large area grain formation using casting solvents with high boiling points. (d) Comparison of grainsize as a function of processing temperature obtained for the hot-casting and conventional post-annealing. Reprinted with permission from Ref. [191]. Copyright reserved 2015 by American Association for the Advancement of Science.

The quenching mechanism is replicated in the second step for the purpose of avoiding large crystals. The process entails nitrogen flow at a high pressure that permits rapid drying of the layers. The integration of spray coating and doctor blading with the roll-to-roll process are few techniques that are beneficial. Spray coating technique originates from the fabrication of polymer solar cells [195]. The large-scale (large area) production of hybrid perovskite solar cells at room temperature is assisted by combining the spray coating with ultrasonic spray.

This technique produced hybrid perovskite solar cells that attained a power conversion efficiency of 13% on top of a glass substrate with 0.0651 cm² active area [196]. It has been reported that the spray coating technique is good for the fabrication of tandem structural devices and halide perovskites with mixed cations that attains improved photovoltaic device performance and eco-stability [197]. This technique (spray coating) utilizes least solid concentration for the fabrication of large scale (large area) hybrid perovskites, however, its downside is too much restrictions on boiling points of solvents used. The inkjet process technique is the production of hybrid perovskite thin films through a programmable process; however, its downside is the limits owed to ink properties [198]. The advantages of doctor blade technique include better crystal quality, higher thin film surface coverage, cost-efficient, slower evaporation time, nil solution waste, and the process can be carried out under ambient conditions [199]. This technique has been reported to be complementary with the roll-to-roll production process for the fabrication of optoelectronic devices [192,200,201]. Large crystalline domains, high quality thin films, and air-resistant CH₃NH₃PbI_{3-x}Cl_x hybrid perovskite thin films can be prepared by applying doctor blade coating technique under ambient conditions. Better crystals and higher thin film surface coverage are attained through slower evaporation time. Slow solvent drying process boosts the large crystalline domains formation on the uniformly wet thin film formed by solution blading for hybrid perovskite materials [202,203].

2.1.8 STABILITY OF HYBRID PEROVSKITE MATERIALS

The existence, readiness, and commercialization of perovskite solar cells are largely affected by issues and parameters such as stability and degradation. Perovskite solar cells have been reported to degrade within a few hundred hours of operation and hence the issue of stability is such a concern. Perovskite solar cells have also been reported to only sustain 80% of original power conversion efficiency after 500 h of operation even after the essential coating (or encapsulation). It has been observed that as the degradation (decomposition) increases over time, the power conversion efficiency of perovskite solar cells decreases (inversely proportional). The perovskite solar cells stability is evaluated by the International Electrotechnical Commission damp heat test (at 85°C, 85% relative humidity) standard. A stable solar cell device can sustain its power conversion efficiency with less than 10% decrease of its initial value after 1000 h of heat and humidity exposure [204,205]. This goal has not yet been realized for hybrid perovskite solar cell devices. There are significant factors that affect the stability of perovskite solar cells which include ultraviolet exposure, sensitivity to moisture (humidity) and thermal stress [206,207]. Additionally, eco-toxicity and safety issues posed by metal Pb have been the prominent impediment for the commercialization of perovskite solar cells [134]. The best fabrication technique for the large-scale production of perovskite solar cells is still under investigation. Cross-linking additives and compositional engineering can be utilized to regulate the hybrid perovskite material stability [208]. The addition of $\text{Pb}(\text{CH}_3\text{CO}_2)_2 \cdot 3\text{H}_2\text{O}$ and PbCl_2 combination in precursors is the best example [209], in addition, utilizing cation cascade which include Rb and Cs cations [7,32]. The instability is also induced by the supplementary layers of the perovskite solar cells. The stability status is described by the drop of different photovoltaic performance parameters which include short circuit current density (J_{SC}), open circuit voltage (V_{OC}), fill factor (FF), and power conversion efficiency (η). The photovoltaic performance parameters are also

influenced by factors such as the fabrication technique employed, charge separation, light absorption, charge carriers transport mechanisms of different layers. In contrast to organic solar cells, there are three steps involved in the deterioration behaviour of V_{OC} in hybrid perovskite solar cells, $CH_3NH_3PbI_3$. The first step involved is the rapid partial deterioration within 10 to 100 μs , the second step is a very slow deterioration between 1 and 100 ms and then a last fast deterioration occurs on the 10-s timescale [210]. For a hybrid perovskite solar cell, the first deterioration occurs until 70%, in contrast to organic solar cell which deteriorates rapidly on a 1s timescale. The time required to reach half of the initial absorbance in set conditions is called half-life. The strength of decomposition is determined by half-life, predominantly due to relative humidity. The half-life of perovskite solar cell based on $CH_3NH_3PbI_3$ films are estimated to be 4, 34, 1000, and 10000 h for relative humidity of 98%, 80%, 50%, and 20%, respectively. It has been found that under ambient conditions (at specific relative humidity), the moisture diffuses into the bottom of the perovskite layer alongside the grain boundaries confirmed by the finding that the half-life is not be dependent on the thin film depth [211]. The technique through which the stability of hybrid perovskite materials is evaluated is also a crucial factor. It has been found by a group of researchers at Aalto University that only a little portion of stability tests performed on solar cells based on hybrid perovskite materials and dye sensitized solar cells (DSSCs) satisfy the proper requirements [212]. About 261 aging tests performed on solar cell devices were analysed by a research team and major limitations were observed in the procedure of reporting test results and testing technique. The significance of the standardization of testing technique was stressed by these defects. Tests are presently carried out on a single cell and only in a dark area [212]. It has been stated by many reports that samples that are stable when exposed to humidity were found to display instability in ultra-violet light [212]. About 15 tests were carried out outdoors and cells were connected to three of them (tests), producing

inaccurate results; indicating that verifications need to be done in real-world conditions by performing tests in groups of several cells to achieve standardization [212]. A new technique has been developed by the same team which saves time, effort, and could evaluate degradation (deterioration) with improved accuracy. The degradation of hybrid perovskite thin films is displayed by a yellow colour which occurs when they get heated, turning from dark brown (black) to lead iodide colour (yellow). This degradation does not occur in its bulk form, owing to the catalytic activity of humidity and decreased surface area in comparison to thin films [212]. PMMA [poly(methylmethacrylate)] can be utilized to protect perovskite solar cells from humidity to a certain degree. PMMA also promotes nucleation and formation of compact hybrid perovskite thin films [213].



2.2 KESTERITE SOLAR CELL MATERIALS

2.2.1 INTRODUCTION

Solar energy is the best candidate to satisfy the global energy demands owing to its sustainability (unlimited supply) while at the same time reducing global warming because of its carbon neutrality. Researchers have devoted a lot of effort searching efficient photovoltaic materials that can harness solar energy (or sunlight) directly into electrical energy [214]. Numerous solar cell technologies have penetrated the commercial market, chiefly those that are Si-based [215–218], CdTe thin-film-based technologies [219–221], Cu(In,Ga)Se₂ [222–224], GaAs [225–227], hybrid organic-organic halide perovskites [32,228,229], conductive organic polymers [230–232], and molecular dye-based [233–235]. Even though environmentally benign printing techniques have been employed to produce cheap, eco-friendly organic/polymer photovoltaic cells [236,237], advance performing solar cells fabricated utilizing inorganic materials with great potential are so far incompetent to replace

fossil fuel power stations because they incorporate costly (Te, In, and Ga) and/or eco-toxic (Cd, Pb, and As) elements or, with regard to hybrid organic-inorganic perovskite solar cells, they demonstrate poor stability against moisture and/or humidity [238–240]. Therefore, to fabricate an advance performing, scalable and eco-friendly solar cell structure; researchers must in tandem take into consideration the power conversion efficiency, expenditure, eco-toxicity, simplicity of production, and eco-stability. The solar absorber material $\text{Cu}_2\text{ZnSnS}_4$ (CZTS) incorporating cheap and eco-friendly elements, possessing optimum energy bandgap of $\approx 1.39 - 1.52$ eV [241] and demonstrating stability against moisture/humidity [242–245] has been attracted significant attention in the arena of photovoltaics over the last decade. Nevertheless, the growth of defects (e.g., antisites, vacancies, and their clusters) can materialize at high annealing temperature of 600K [246,247], yielding solar cell inefficiencies [248,249]. The energy bandgap and the content of Shockley-Read-Hall (SHR) recombination centers [250,251] (x_{SRH}) are the two critical factors for the optimization of kesterite solar cells as shown in **Figure 2.7**. The energy bandgap of the kesterite absorber material which is determined by the polymorph ($E_g^{\text{Stannite}} < E_g^{\text{Kesterite}}$, typically [252,253]), is directly proportional to the open circuit voltage (V_{OC}) of the photovoltaic device while x_{SRH} determines the short-circuit current (I_{SC}), with concentration inversely proportional to current. Granted that the power conversion efficiency is in direct proportion to the product of V_{OC} and I_{SC} , it is clear that the solar cell power conversion efficiency is increased by increasing I_{SC} (i.e., decreasing x_{SRH}) (from high to low x_{SRH} , contours become greener in **Figure 2.7**). However, the V_{OC} cannot be amplified without certainty in the same way the 1.34 eV optimal energy bandgap E_g [254] is determined by the Shockley-Queisser limit [255], with quasi-exponential drop in power conversion efficiency upon divergences away from that value. The effects of neutral defects hosted by CZTS on the physics and photovoltaic performance of kesterite solar cells are given in **Table 2.2**.

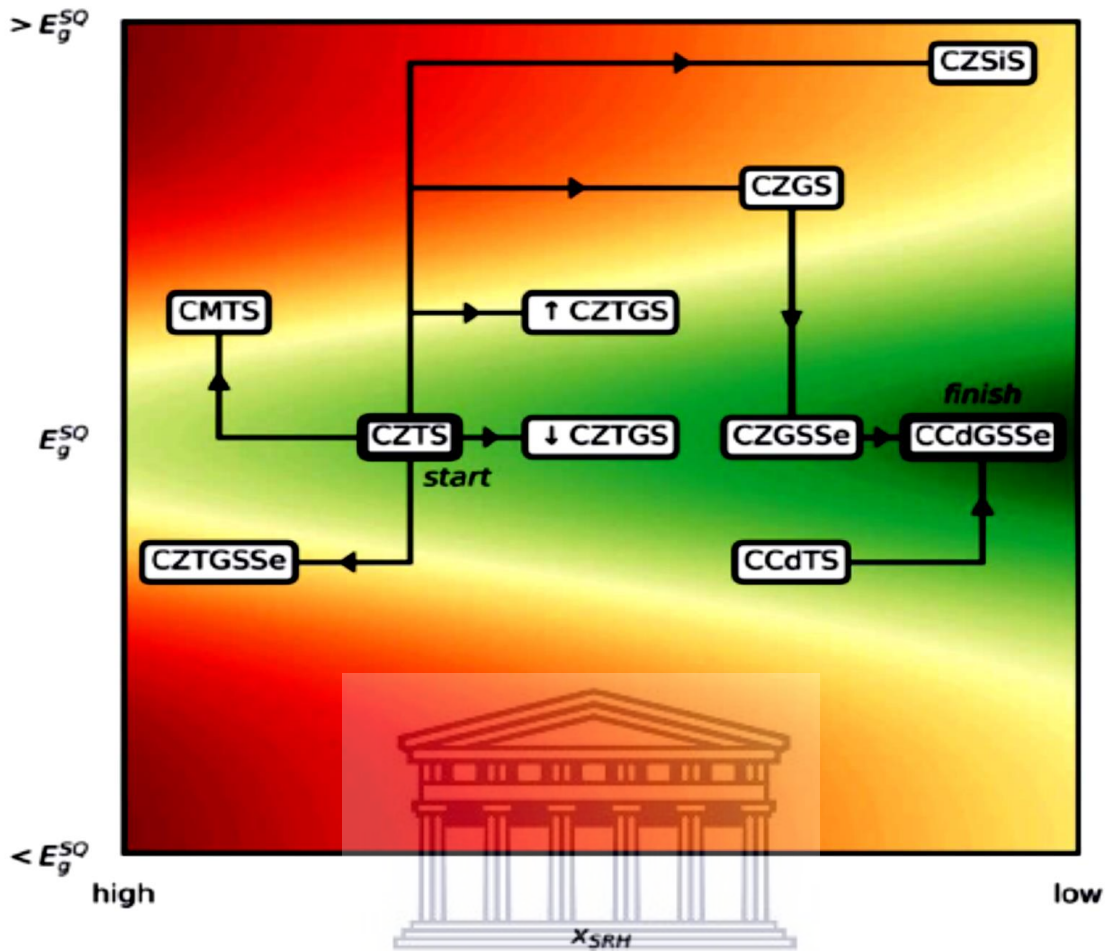


Figure 2.7: Schematic road map of substitution strategies considered, from $\text{Cu}_2\text{ZnSnS}_4$ (CZTS) to $\text{Cu}_2\text{CdGeS}_3\text{Se}$ (CCdGSSe), where C is Cu^{1+} , Z is Zn^{2+} , M is Mg^{2+} , T is Sn^{4+} , G is Ge^{4+} , $\downarrow\text{CZTGS}$ is $\text{Cu}_2\text{ZnSn}_{0.875}\text{Ge}_{0.125}\text{S}_4$, and $\uparrow\text{CZTGS}$ is $\text{Cu}_2\text{ZnSn}_{0.5}\text{Ge}_{0.5}\text{S}_4$. The horizontal and vertical axes correspond, respectively, to the concentration of Shockley-Read-Hall recombination centers (x_{SRH}) [250,251] and the energy bandgap (E_g), where E_g^{SQ} is the energy bandgap that maximizes the Shockley-Queisser (SQ) limit [254,255]. Red and green contours indicate regions of lower and higher solar cell efficiency, respectively. Reproduced with permission from Ref. [256]. Copyright 2021, The Royal Society of Chemistry.

The defects are labelled using a simplified Kroger-Vink notation M_S (in **Table 2.2** and thereafter), where M represents the point defect species, which can either be an atom (*e.g.*, Cu) or a vacancy (V), and S represents the lattice site occupied by the species. In place of $\text{Cu}_x + X_{\text{Cu}}$, Cu^+ and X^{2+} cations exchange sites leading to the growth of shallow donor (X_{Cu}) and acceptor (Cu_x) levels within the energy bandgap, causing conduction and valence band edges spatial fluctuations.

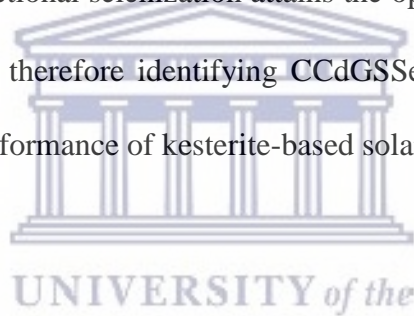
Table 2.2. Defects considered and their effects on the physics of kesterite solar cells and solar cell parameters. X is Zn, Cd, or Mg; Y is Sn, Ge, or Si; E_g is the bandgap; V_{OC} is the open-circuit voltage; and I_{SC} is the short-circuit current.

Defect	Effect on the physics of kesterite solar cells	Primary effect on solar cell parameters
$Cu_X + X_{Cu}$	Causes electrostatic potential fluctuations	Decreases V_{OC}
V_{Cu}	Mitigates potential fluctuations along valence band edge	Increases V_{OC}
$2Cu_X + Y_X$	Causes Shockley-Read-Hall recombination	Decreases I_{SC}

These spatial fluctuations results in the effective energy bandgap reduction, consequently reducing the V_{OC} of the kesterite absorber material [248,257–262]. It has been predicted by quantum mechanics simulations that the potential spatial fluctuations along the valence band edge can be reduced by Cu vacancies, which can lessen any energy bandgap reduction induced by $Cu_X + X_{Cu}$ clusters [248]. As a result, V_{Cu} is inclined to lessen any potential reduction in V_{OC} , in coherence with the Cu-poor preparation conditions that are normally employed to attain the optimum power conversion efficiency [246,263,264]. Lastly, in place of $2Cu_X + Y_X$, two Cu^+ and one Y^{4+} supplant the three X^{2+} , leading to the deficient X^{2+} -crystal and rich Cu^+/Y^{4+} . It has been revealed by previous quantum mechanics studies that the localized trap states proximate to energy bandgap center are produced by $2Cu_{Zn} + Sn_{Zn}$, which advance SRH recombination and thus decreasing the I_{SC} of CZT [253,265,266]. It has also been observed that the interface recombination can lower the open circuit voltage V_{OC} [267,268]. Nevertheless, Wexler *et al.* [256], focused their work on repressing the growth of well-known detrimental bulk defects to kesterite solar cell power conversion efficiency, via both experimental and theoretical studies. Wexler *et al.* [256], used density functional theory (DFT) and thermodynamic analyses to better understand how to manage the growth of defects and to ascertain doping strategies with potential to reduce the growth of detrimental

bulk defects and ultimately advance the solar cell photovoltaic performance. For instance, it has been inferred from both theoretical studies [269] and experimental studies [270–272] that phases incorporating Ag are more well-arranged in the $1+$ and Zn^{2+} sub-lattices (*i.e.*, lower content of $Cu_x + X_{Cu}$ defects) owing to the anisotropic enlargement of the unit cell induced by the substitution of Cu by Ag [270]. Advance photovoltaic performance can be anticipated via theoretical studies specifically for $Ag_2ZnSnSe_4$ than Cu_2ZnSnS_4 , in coherence with experimental studies [273–280]. Theoretical studies have demonstrated that $< 25\%$ Na-doping in CZTS represses the growth of $Cu_{Zn} + Zn_{Cu}$ defects [281] presenting alkali metals as another promising group of isovalent substitution for Cu [273–283]. Moreover to the Cu^+ site, a number of investigations ascertain isovalent doping on the Zn^{2+} site as a potential strategy to advance the photovoltaic performance of CZTS-based kesterite solar cells as well. Both theory [269] and experiment [284] have demonstrated Cd as one of the most helpful $2+$ cation at diminishing $1+/2+$ and $2+/4+$ cation chaos among the considered $2+$ cations which include the alkaline earth [281,285,286] and transition metals [269,284,287]. Lastly, several experimental studies have reported Ge as an outstanding candidate for substitution on the $4+$ site, whereby the fractional mixture of Ge- and Se-alloying optimized the energy bandgap, leading to a remarkable boost in both the V_{OC} and I_{SC} and as a result the solar cell power conversion efficiency. Nevertheless, the impact of these dopants on the growth of defects has not yet been thoroughly unravelled for better understanding and consequently there is still much uncertainty with regard to potential routes for the optimization of material design. **Table 2.2** gives likelihoods of bulk stability, energy bandgap, and the formation energies for the key defects to provide an insight of the mechanical effects that rule defect growth but also gives the practical approach for improving the photovoltaic performance of kesterite solar cell technologies in the previous six years [288]. Wexler *et al.* [256] sketched the route from CZTS to their suggested novel quinary chalcogenide, Cu_2CdGeS_3Se (CCdGSSe), to present a

clear depiction of the ion substitution schemes they adopted, see **Figure 2.7**. The first finding made was that the substitution of Mg and Si for Zn and Sn, respectively, widens the energy bandgap E_g and also increases recombination χ_{SRH} for Mg-substitution, and thus leading to solar cell devices with poor photovoltaic performance (*i.e.*, inefficient solar cells). The second finding made was that the 100% Ge-substitution (CZGS) reduces χ_{SRH} but widens the energy bandgap E_g . Although fractional Ge-substitution (CZTGS) widens the energy bandgap E_g to a lesser degree, this approach was found to not have the same potential as the fractional selenization (CZGSSe). Motivated by the recent research on Cu_2CdSnS_4 (CCdTS) [269,284], the third finding that was made is that the 100% Cd-substitution, alongside Ge-substitution in tandem with fractional selenization attains the optimal energy bandgap E_g and remarkably reduces χ_{SRH} , and therefore identifying CCdGSSe as a potential candidate for optimizing the photovoltaic performance of kesterite-based solar cells.



2.2.2 DOPING MECHANISMS IN KESTERITE MATERIALS

Several elements have been tested as potential candidates for doping and alloying inspired by the tunability, complexity and richness of the kesterite structure. The far most investigated elements for intrinsic doping is a variation of: Cu, Zn, & Sn, and for the extrinsic doping is a variation of alkaline elements which include: Li, Na, K, Rb and Cs, respectively. The potential dopants and alloying candidates are demonstrated in **Figure 2.8**. With regard to alloying, the substitution of cations is preferable done utilizing isoelectronic elements from the same column, for example, substitution of Cu by Ag, Zn by Cd, and Sn by Ge or Si, even though other unconventional doping alternatives such as Mg, Mn, and Fe have been reported.

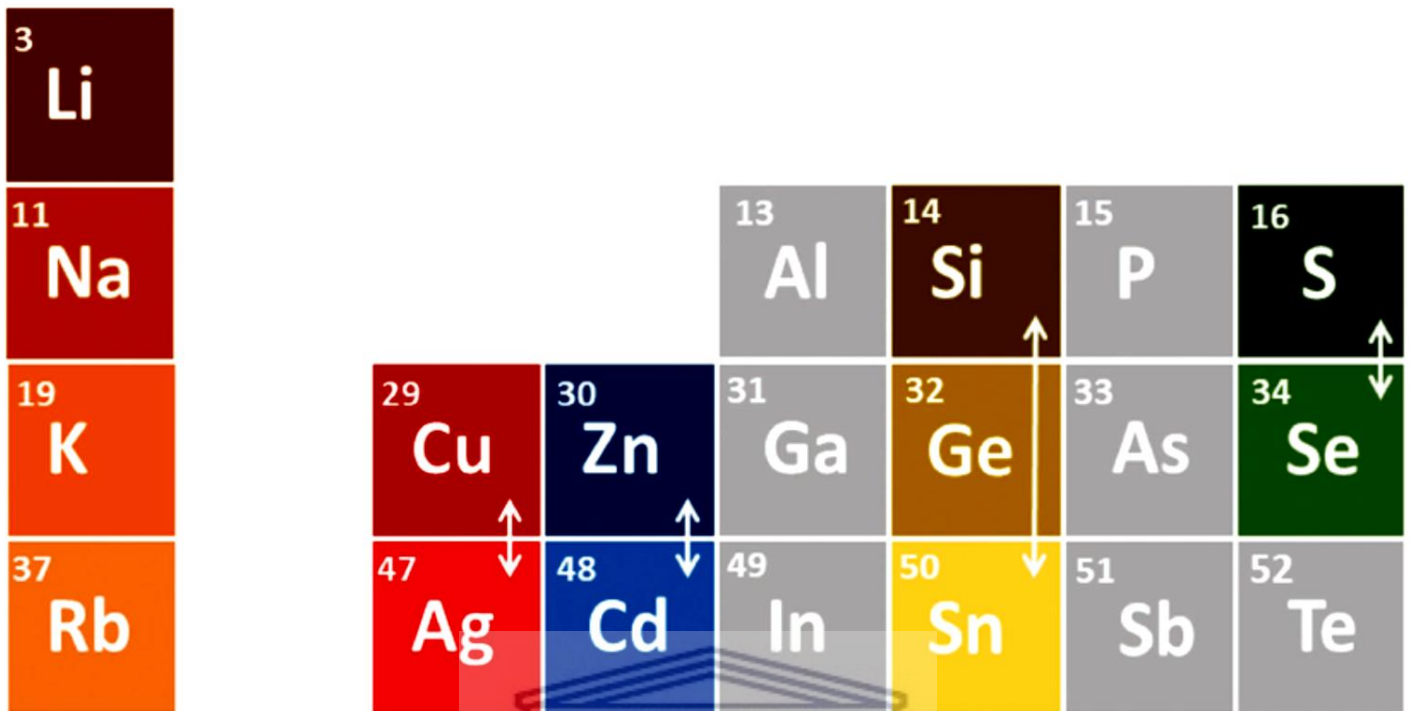
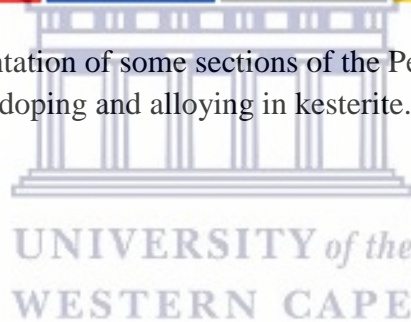


Figure 2.8: Schematic representation of some sections of the Periodic Table, highlighting the most interesting candidates for doping and alloying in kesterite. Reproduced with permission from Ref. [289].



i. Intrinsic Doping

It has been well known since the early developmental stages of kesterite materials that an off-stoichiometric elemental composition is required to attain kesterite solar cell devices with high power conversion efficiency [241,290]. The Cu-poor, stoichiometric Sn, and Zn-rich stoichiometry has produced kesterite devices with high photovoltaic performance [241,291,292], while poor performing devices haven been produced by Zn-poor [293,294] and/or Cu-rich [294] conditions. The classification of compositional-type kesterite materials was first introduced by Lafond *et al.* [295] which were later extended by Gurieva *et al.* [296] owing to the significance of kesterite power conversion efficiency, and its intrinsic relationship with structural defects and the formation of secondary phases as illustrated in **Figure 2.9**. There were 12 compositional-type kesterites classified, each classification

parallel to the different cationic balances (merging all possible poor and rich areas for each cation) and also comprising the formation of the most probable secondary phases and intrinsic point defects [296,297]. Kesterite material has a flexible structure; it is capable of self-adapting from Cu-poor up to Cu-rich regime (composition) without major changes in the structure, this remarkable property was demonstrated by Valle Rios *et al.* [298].

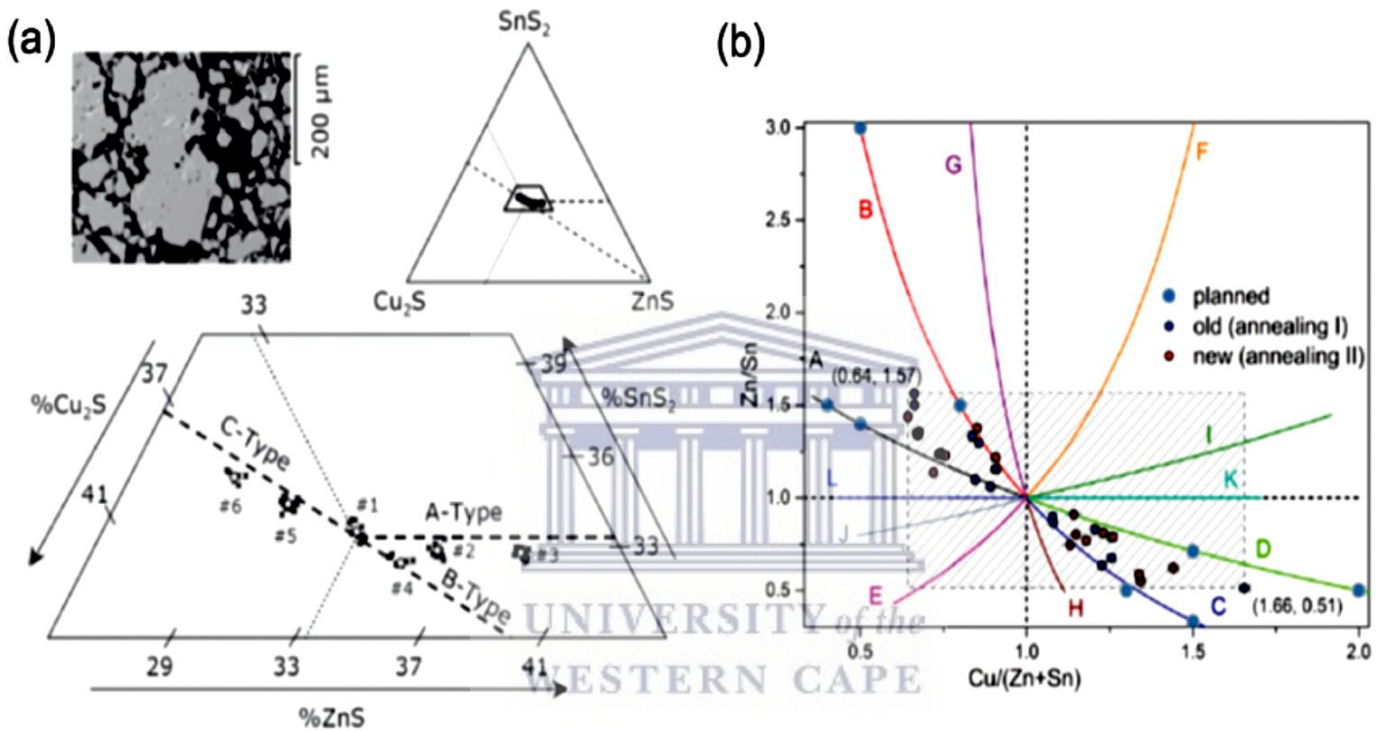
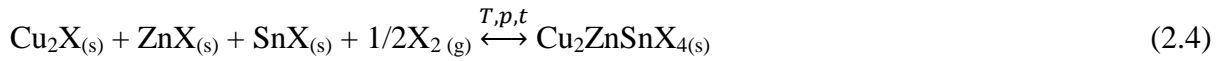


Figure 2.9: (a) First off-stoichiometric types kesterite (A-, B-, and C-type) proposed by Lafond *et al.* Reproduced with permission from Ref. [295]. Copyright 2012, Wiley-VCH. (b) Complete classification of off-stoichiometric kesterite presented by Gurieva *et al.* Reproduced with permission from Ref. [296]. Copyright 2018, Wiley-VCH.

The questions still remain: why Cu-poor and Zn-rich kesterites produce the highest power conversion efficiency devices and why the elemental composition follows the so called “A-line” (equivalent to Cu-poor, Zn-rich, and Sn-stoichiometric elemental composition)? The pathways through which the kesterite can be formed must be taken into consideration to address this question. The formation of the highest performing kesterites can take place either through direct reaction of elements or equivalent alloys, through the binaries (Equation 2.4), or following more complex molecules (Equation 2.5). It is impossible to form a kesterite

through a direct reaction between a metal and a chalcogen, since one binary phase (ZnX, where X = S and Se) is more stable [299] than the quaternary phase, and thus the simpler chalcogen species are expected to form first. The synthesis of the kesterite then takes place through the following equations (with X = S or Se).



The most probable pathways for kesterite material synthesis depending on the pressure and temperature of the system are illustrated by the two equations above. ZnX is the first species formed in this system irrespective of the succeeding pathway (equation 2.4 or 2.5) owing to high stability of these compounds. Subsequent to the formation of binary and ternary compounds, ZnX is then integrated into the structure forming the kesterite material [300,301]. This process indicates that the kesterite phase is Zn-poor at the initial stages of the reaction, which subsequently forms the basis of the associated point defects. Widespread Zn-rich conditions are essential to compensate for this detrimental effect to achieve a fully completed synthesis and to also reduce the risk of unfavourable remaining unreacted Cu-X, Sn-X, or Cu-Sn-X phases. This is the ultimate explanation for the requirement of Zn-rich conditions in the preparation (or synthesis) of high quality kesterite from an opto-electronic perspective, producing kesterite absorber films devoid of the detrimental secondary phases. The necessity of Cu-poor conditions is largely associated to the formation of intrinsic defects that control the doping level of the material [253]. The intrinsic doping in kesterite material is equally relevant to previously reported studies on other chalcogenides. Dimitrievska *et al.* [302] proved this clearly by performing a comprehensive experiment that demonstrated highest power conversion efficiency attained around the previously stated A compositional line as illustrated in **Figure 2.10 (a)** (amid the B- and L-lines). Based on the work reported by

Dimitrievska *et al.*; V_{Cu} , Cu_{Zn} , and Zn_{Cu} [297,302] are the most likely point defects which are all classified as shallow defects [253] (i.e. Zn_{Cu} is a shallow donor and V_{Cu} and Cu_{Zn} are shallow acceptors), which theoretically have a partial effect on recombination processes.

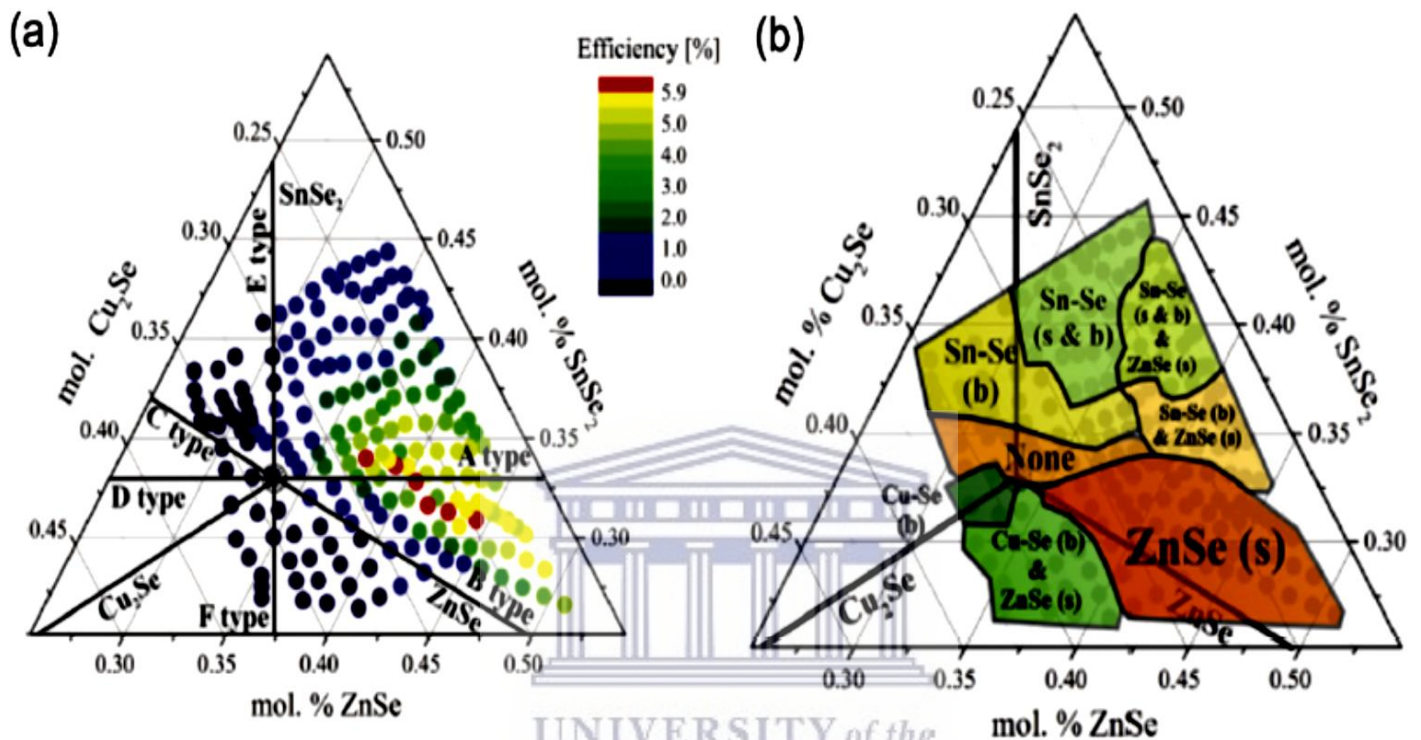


Figure 2.10: (a) Combinatorial experiment showing the relationship of conversion efficiency with composition. (b) Secondary phases composition (at the surface) as a function of the kesterite composition. (a,b) Reproduced with permission from Ref. [302]. Copyright 2016, Elsevier.

All of these theoretical estimates are founded on stoichiometric material, while high power conversion efficiency solar cell devices are constructed with Cu-poor based kesterite absorber material. This proposes that the shallow defect V_{Cu} (shallow acceptor) could play a greater role in intrinsic doping. Furthermore, a similar case is observed for CIGSSe [303] where the presence of V_{Cu} explained the intrinsic p-doping of the absorber material. However, no conclusive work has been reported for the intrinsic doping mechanism on kesterite materials so far.

ii. Extrinsic Doping

Owing to the intricacy of kesterite structure, there is always an expectation for intrinsic detrimental defects caused by compositional and/or processing problems. Extrinsic doping can be employed to reduce these intrinsic detrimental defects; however, since there is little knowledge published considering these deep defects, this remains a challenging task. However, numerous advantages of extrinsic doping of kesterite solar cell material have been reported in literature and this work has been mentioned as a “hot topic” of kesterite material. There are three types of possible extrinsic doping which include:

1. Nonconventional elements extrinsic doping: In [304], Bi [305,306], Sb [307–310], and Fe [311]
2. Isoelectronic elements extrinsic doping from the same family as Cu, Zn, and Sn: this includes Ag [269], Cd [269,311], and more extensively Ge [300,312–318]
3. Alkaline elements extrinsic doping: Li [274–276,319,320], Na [269,305,317,321–329,307,330,308–310,313–316], K [319,320,326,328,331,332], Rb [319,320], and Cs [319,320].

There is no work that has been reported on the exploitation of “nonconventional elements” mostly because they have shown a restrained effect on CIGSSe also, and only a small number of examples have been reported on literature. For example, it has been observed that solar cells based on kesterite can take a comparatively high In content without impacting much of the properties [304,333]. The resilience of kesterite to comparatively high content of In was demonstrated by the work done by Giraldo *et al.* [304], and in this study, the degradation for high In content was related to the formation of Sn-In-O conductive phase. Moreover, it was also observed by Hartnauer *et al.* [333] that a high In content can be housed by the kesterite, subduing ZnSe presence which is a by-product of the $\text{CuInZn}_2\text{Se}_4$ phase formation. These

works reported a significant finding because there is a presence of In in the buffer layer (In_2S_3) [334–337] and the window layer ($\text{In}_2\text{O}_3:\text{SnO}_2$, ITO), signifying that the possible interdiffusion will not negatively impact the properties of the kesterite absorber material. Studies have demonstrated interesting properties for Sb and Bi as potential crystallization flux agents, even though they also showed disadvantageous or no effect on the optoelectronic properties of the kesterite solar cell devices [305–309]. It was observed that there is a strong interaction between Sb with Na, and within the context of this co-doping, to significantly increase the grain size [310]. Ultimately, the doping of kesterite with Fe had disadvantageous effect [311], restricting the quasi-Fermi level splitting of the kesterite solar cell devices even when doping was done at very low content, and resultantly the V_{OC} of the devices. This observation emphasizes the absolute importance of controlling Fe contamination in kesterite solar cell devices fabricated on steel substrates [326]. However, more closely related elements have been utilized to improve success with extrinsic doping. At large, extrinsic doping has yielded more irrefutable and effective results by utilizing elements from the same group as Cu, Zn, and Sn. In that regard, the substitution of Cu by Ag has been widely explored. A theoretical analysis of Ag doping in CZTS presented by Gautam *et al.* [269] proposed that a low level substitution result to a large disorder suppression on kesterite, however, this only occur under Cu-rich and confined Cu-poor conditions. A different observation was made by Cherns *et al.*, reporting the opposite effect whereby a high level of disorder (significant amount of Cu and Ag species) was observed in crystals containing Ag [338]. Gautam *et al.* [269] also studied doping with Cd and found out that it could be a disadvantageous factor by stabilizing the narrower energy bandgap stannite structure, as a replacement for the kesterite counterpart. Further experimental work by other research groups will be vital to validate these conclusions. Moreover, a positive and advantageous effect of Cd dopant was observed by Collord *et al.* [311] through conducting a comprehensive

experimental study of Cd concentration (wide range concentrations from 0 – 10 000 ppm). Extrinsic doping utilizing isoelectronic elements (small Ge quantities) has recently been reported to yield significantly positive results. Giraldo *et al.* recently reported for the first time the advantageous outcome of utilizing Ge as a dopant in CZTSe [312], reporting advancements in power conversion efficiency (for small Ge quantities below 0.5%) chiefly ascribed to a significant increase of V_{OC} and FF [315], see **Figure 2.11 (a)** and **(b)**. The beneficial effects and advancements attained with Ge have been largely attributed to numerous advantageous effects on kesterite; a significant effect on the grain size has been observed, and significantly large grains are often attained [300,315,339]. Giraldo *et al.* proposed that this observation largely correlates to the formation of Ge-Se liquid phases at comparatively low temperature (380°C) and acting as crystallization flux [312]. Other advantageous outcomes of Ge dopants have been reported and include; Na interaction that explains its effect on the carrier's concentration [313], the alteration of formation pathways with less Sn losses and less formation of secondary phases [300], eradication or reduction of deep defects [318], and the passivation of recombination attributed to harmful grain boundary [340]. Thus, doping with Ge resulted in significantly positive results which include the reduction of the V_{OC} deficit of CZTSe solar cell devices to photovoltaic parameters analogous to the ones reported for CISE, see **Table 2.3**. In that regard, doping with Ge has demonstrated great potential for the advancement of kesterite solar cells device properties and photovoltaic device performance.

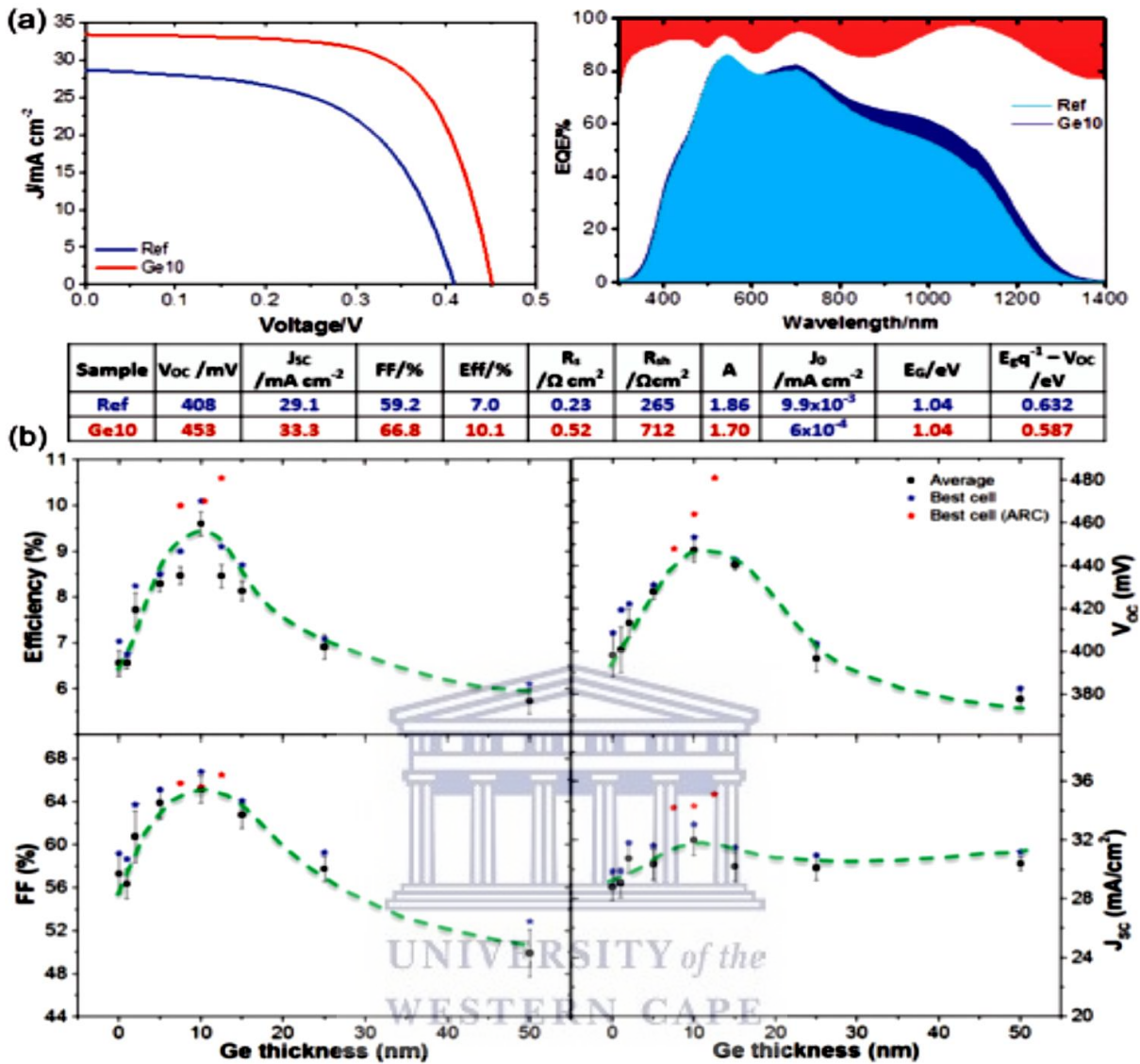


Figure 2.11: (a) Efficiency improvements of CZTSe solar cells with very small quantities of Ge. Reproduced with permission from Ref [312]. Copyright 2015, Wiley-VCH. (b) Effect of Ge doping on the different optoelectronic properties. Reproduced with permission from Ref. [315]. Copyright 2016, John Wiley and Sons.

Alkaline elements have also been explored as doping pathways and they have demonstrated significant positive impact on kesterite solar cells. Some of the widely explored alkaline elements include Li [274–276,319,320], Na [269,305,317,321–329,307,330,308–310,313–316], K [319,320,331,332], Rb [319,320] and Cs [319,320] and the effect of these dopants have been illuminated by recent studies. The large part of this body of work is derived from the CIGSSe family, where Na and K alkaline elements were the first dopants to be explored.

Generally, the grain size increase in kesterite was connected to Na [320,326,329] alongside alteration of the carrier's concentration [313,325,330]. It is still unclear why Na doping has such a strong impact on carrier concentration since Na fills Cu position in principle, and it is also iso-electronic to Cu, and thus no substantial effect on the electric properties should be anticipated. However, there are two potential mechanisms that impact the carrier concentration that can be theorized. Since A-type kesterites is used for these investigations, this result in Zn_{Cu} shallow donor defect formation [297]. In principle Na occupies the Cu-sites during doping, thus substituting Zn in the Zn_{Cu} defects, which result in the reduction in the concentration of shallow donor and subsequently improving the conductivity of the p-type semiconductor kesterite material. The second potential mechanism can be inferred to the analogous CIGSSe mechanism, since at substantially higher temperatures mandatory for the formation of kesterite absorber ($< 500^{\circ}C$), Na diffuses very well in the chalcogenide material [341], filling up Cu-sites. There is a significant decrease in the solubility of Na leading to diffusion towards the grain boundaries during the cooling-down process and this process leaves a higher number of Cu vacancies. The two above mechanisms can take place concurrently; however, they both still need to be confirmed. Moreover, advance crystalline quality and grain size in kesterite absorbers with increased carrier's concentrations [320,331,332] were distinctly demonstrated by K dopants, producing results parallel to those of Na. To date, there has never been any synergetic behaviour observed between K and Na on the kesterite absorber [331].

Table 2.3: Compilation of some of the most relevant devices reported in the literature which includes extrinsic doping. The V_{OC} deficit and V_{OC} gain are included for comparison of the different strategies. N/A: Not Available.

Material	Doping element	E_g [eV]	V_{OC} [mV]	V_{OC} deficit [mV]	V_{OC} gain [mV]	Eff. [%]	Ref.
CZTSe	Na	1.0	423	337	N/A	11.6	[342]
CZTSe	Na	1.07	425	401	17	9.6	[343]
CZTSe	Ge	1.04	453	345	45	10.1	[312]
CZTSe	Ge	1.05	463	344	46	10.0	[313]
CZTSe	Ge	1.05	473	334	72	10.6	[315]
CZTSe	Ge	1.04	463	335	37	11.8	[300]
CZTSSe	Li	1.04	449	349	22	11.8	[275]
CZTSSe	Li	1.11	496	368	N/A	11.5	[320]
CZTSe	K	1.03	350	438	58	5.6	[326]
CZTSe	Na+Ge	1.01	360	409	68	6.1	[326]
CZTSSe	Li	1.08	380	456	70	6.0	[344]
CZTSSe	Rb	1.08	360	476	50	6.4	[344]
CZTSSe	Na	1.12	378	496	68	6.2	[344]
CZTSe	Na	1.05	397	410	N/A	7.5	[328]
CZTSe	In	1.02	423	356	N/A	7.8	[304]
CZTSe	Na	1.0	N/A	N/A	36	N/A	[319]
CZTSe	K	1.0	N/A	N/A	28	N/A	[319]
CZTSe	Na+K	1.0	N/A	N/A	53	8.3	[319]
CZTSe	Na	1.05	409	398	79	7.9	[345]
CZTSe	K	1.05	364	443	34	5.4	[345]
CZTSe	Na+K	1.05	421	386	91	8.3	[345]
CZTS	Na	1.50	628	607	47	6.3	[346]

Furthermore, a significant effect on solar cell device properties based on kesterite absorber was demonstrated by Li dopant. A significant advance in the power conversion efficiency was observed through the addition of small amounts of Li to their molecular ink utilizing DMSO solvent by Collord *et al.* [311]. The advancements were largely in the J_{SC} and FF,

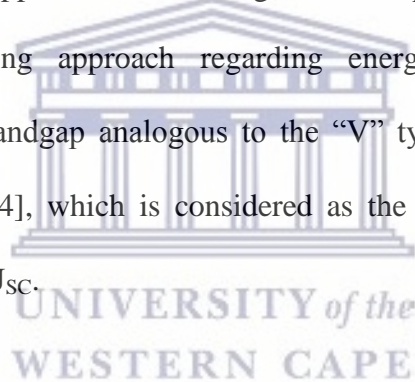
with a balanced effect on the V_{OC} . In this study, it was suggested by the authors that the inversion of the potential at the grain boundaries was attributed to the presence of Li dopant which then explained the improvement in power conversion efficiency; however, no impact was observed on the crystalline properties for Li dopant. Nevertheless, Yang *et al.* [274], reported that Li dopant helps facilitate the diffusion process of Na from soda lime glass substrate, while remaining efficiently integrated into the kesterite absorber material without the presence of Na. Outstanding results have been attained utilizing numerous doping elements; however, no agreement has been reached so far on which element within the family of alkaline elements represents the optimum option for the kesterite extrinsic doping from different studies by different authors suggesting their respective different pathways to alkalis doping as the best one [319,326,344,347].



2.2.3 OPTIMIZING THE ENERGY BANDGAP OF KESTERITE ABSORBER AND ENGINEERING ITS BANDGAP GRADING

The energy bandgap of the kesterite absorber material is a crucial factor and has a large effect on the V_{OC} deficit and the associated photovoltaic device performance. Hypothetically, the optimum energy bandgap of CZTSSe and CIGS required to attain the highest hypothetical power conversion efficiency is about 1.4 – 1.5 eV according to S – Q limit [255,348]. Nevertheless, the present practical optimal energy bandgap of CZTSSe solar cell devices is below (1.1 – 1.2 eV) [349,350]. It has been experimentally observed that CZTSSe solar cell devices with high concentration of S and wide energy bandgap near 1.5 eV result in poor photovoltaic performance than the narrow energy bandgap CZTSSe solar cell devices. The deterioration of the electronic properties of the kesterite absorber material should be taken into consideration when the energy bandgap is widened via the alteration of cation or anion

ratio. For instance, since the transition energy of Ga_{Cu} is deeper than that of In_{Cu} , the photovoltaic device performance will decline significantly if $\text{Ga}/(\text{Ga}+\text{In})$ ratio is too high (i.e. $\text{Ga}/(\text{Ga}+\text{In}) > 0.4$) [351]. Similarly, CZTS has transition energy level point defects (as well as the major Cu_{Zn} antisite defects) deeper than that of the narrow energy band CZTSe, which results in greater non-radiative recombination loss in the bulk and grain boundaries. The detrimental Conduction Band Offset (CBO) occurring at the CdS buffer layer/absorber interface is another impediment that constrains the practical optimal energy bandgap of the CZTSSe, particularly for the pure sulphide CZTS solar cell devices [352]. Nevertheless, the preparation of wider energy band gap kesterite absorber materials with outstanding electronic properties is a prospective approach to investigate more potential kesterite solar cell technology. Another promising approach regarding energy bandgap engineering, is fabricating a graded energy bandgap analogous to the “V” type energy bandgap of CIGS solar cell devices [349,353,354], which is considered as the best solution to equalise the compromise between V_{OC} and J_{SC} .



i. Engineering Absorber Bandgap and Conduction Band Offset at Junction Interface

For an ideal semiconductor absorber material (e.g. kesterite material), a spike-like Conduction Band Offset (CBO) ($\Delta E_C = E_{C \text{ buffer}} - E_{C \text{ absorber}} > 0$) is important in making sure that the space-charge-region (SCR) recombination barrier, Φ_b is virtually equivalent to the energy bandgap E_g of the semiconductor absorber material devoid of any band tailing. The open circuit voltage V_{OC} of the solar cell device is strongly determined by Φ_b using the following equation;

$$V_{OC} = \frac{\Phi_b}{q} - \frac{AkT}{q} \ln \left(\frac{J_{00}}{J_L} \right) \quad (2.6)$$

where q = unit charge, A = ideal diode quality factor, k = Boltzmann constant, T = temperature, J_{00} = reverse saturation diode current prefactor and J_L = light generated current density [355–357]. In the event of cliff-like CBO where $\Delta E_C < 0$, Φ_b is largely smaller than the energy bandgap E_g , unavoidably resulting in intense interface recombination and significantly large V_{OC} deficit. On the other side, excessively larger or wider CBO (ΔE_C) impedes the transportation of photo-generated electron current, and therefore results in the reduction of fill factor FF and the short-circuit current density (J_{SC}). Gloeckler *et al.* worked on solar cell device simulations and reported that the best value for CBO is between 0.1 – 0.3 eV for an ideal absorber material [358]. Thus the balance in conduction band edge between the CdS buffer layer and the kesterite absorber material plays a significant role in attaining solar cell devices with higher power conversion efficiency. For a CZTSSe kesterite absorber material, the optical energy bandgap E_g is greater than the effective electronic energy bandgap determined by photoluminescence (PL) measurements due to critical band tailing, chiefly for the S-rich CZTSSe with wider energy bandgap [342]. Thus, the optical energy bandgap E_g will inevitably be wider than the SCR recombination barrier Φ_b even though the interface recombination is not taking place. In this context, the Φ_b value should be almost equal to the electronic energy bandgap calculated from PL measurements. The pure selenide CZTSe and the pure sulphide CZTS kesterite absorbers have PL emission energies commonly in the range of 0.95 – 0.98 eV and 1.2 – 1.35 eV, respectively [342,359–361]. The recombination barrier Φ_b of CZTSe kesterite solar cell devices calculated from temperature-dependent V_{OC} measurements is around 0.90 – 0.97 eV [359], which is almost equal to the energy of the PL emission. Nevertheless, the PL emission energy of the pure sulphide CZTS is normally much greater than the Φ_b . It has been reported by Platzer-Bjorkman *et al.* [361]

that difference in energy gap between Φ_b and PL emission energy can be as wide as about 300 meV. The detrimental “cliff-like” CBO at the CdS buffer layer/CZTS kesterite absorber interface is the reason for the wide difference between the Φ_b and the PL emission energy of the CZTS kesterite absorber. The theoretical calculated energy bandgap structure has demonstrated that the CBO of CdS/CZTS is negative (-0.09 eV) while the CBO of CdS/CZTSe counterpart is positive ($+0.26$ eV) for the regular employed CdS buffer layer [362]. Several experimental results have confirmed analogous conclusion [363–365]. This challenge can be overcome by finding a substitute buffer layer with conduction band edge parallel to that of the wider energy bandgap CZTSSe with high concentration of sulfur. The substitute buffer layer materials with wider energy bandgap and higher conduction band edge such as In_2S_3 , $\text{Zn}(\text{O},\text{S})$, $(\text{Zn},\text{Sn})\text{O}$, $(\text{Zn},\text{Cd})\text{S}$ [366–371] are widely investigated. Significant developments of V_{OC} have been attained by using $(\text{Zn},\text{Sn})\text{O}$ and $(\text{Zn},\text{Cd})\text{S}$ buffer layer employing atomic layer deposition (ALD) followed by ionic layer adsorption and reaction (SILAR) techniques, respectively [366,367]. Nevertheless, more comprehensive research into interface junction is needed because the V_{OC} deficit of CZTS solar cells is too wide. On the other side, the CdS deposited by chemical bath method is still an appealing and predominant buffer layer employed and it produce solar cell devices with advanced photovoltaic performance owing to its smooth and compact coverage with insignificant discrepancy with kesterite absorber layer, although CdS has detrimental attributes of parasitic absorption of blue light and hazardous chemical constituents [288,349]. In this present context, optimizing the energy bandgap of the kesterite absorber layer for better band alignment with CdS buffer layer is an effective strategy to minimize the V_{OC} deficit caused by interface discrepancy. The ideal energy bandgap of the CZTSSe kesterite absorber must be in the range of 1.3 – 1.4 eV in order to attain a slightly positive value for CBO with the CdS buffer layer. The energy bandgap in the range of 1.3 – 1.4 eV can be attained through many

strategies since the energy bandgap of the CZTSSe kesterite absorber can be modulated by a continuous substitution of the cation and anion ratio. Nevertheless, the biggest challenge is in attaining a kesterite absorber material with an ideal energy bandgap without any detrimental effects on the electronic properties. One of the strategies to optimize the energy bandgap is by tuning the S/(S+Se) ratio in CZTSSe absorber material. A great deal of research input has been devoted to validate this concept [372–376]. Nevertheless, to date, the optimum performing kesterite solar cell device assume narrow energy bandgap (1.0 – 1.15 eV) or wider energy bandgap almost close to 1.5 eV [288,349,377]. Unparalleled result of optimum performing CZTSSe kesterite solar cell device with an average energy bandgap in the range 1.2 – 1.4 eV is published. The main issue confronted by this strategy is high level synthesis energy of CZTSSe kesterite materials with an average ratio of S/(S+Se), i.e., the solid solubility is low when the S and Se concentration is close [352,362,378]. Thus, the segregation phases of high-sulfur content and low-sulfur content are frequently observed in CZTSSe absorber film with an average S/(S+Se) ratio, therefore resulting in rigorous energy bandgap fluctuation and large V_{OC} deficit [249,379]. Another potential strategy for energy bandgap optimization of kesterite absorber materials is the cation substitution. Chen *et al.* investigated and reported the impact of cation types on the band edge [285,378,380,381]. It has been demonstrated by first-principle calculations that the conduction band minimum of CZTS(Se) is interconnected to the anti-bonding Sn s and anion p hybrid orbital whereas the hybridization of Cu d and anion p orbitals chiefly control the valence band maximum. Thus, Sn(IV) substitution by Ge(IV), and Cu(I) substitution by Ag(I) will optimize the conduction band edge and the valence band edge, respectively. **Table 2.4** gives a list of some of the Ge-doped kesterite absorber CZTSSe-based thin film.

Table 2.4: Energy bandgap (E_g) of CZTGeS and CZTGeSe absorber layers with different Ge/(Ge+Sn) ratio.

Material	Method	Ge/(Ge+Sn) [%]	E_g [eV]	Ref.
CZTGeS	Chemical vapour transport	10 – 50	1.59 – 1.94	[382]
CZTGeS	Spray-based deposition	0 – 100	1.51 – 1.91	[383]
CZTGeSe	Hydrazine processed	0 – 40	1.08 – 1.15	[384]
CZTGeSe	Solid solution powders	0 – 100	0.99 – 1.35	[385]
CZTGeSe	Spray-based deposition	0 – 100	1.07 – 1.44	[383]
CZTGeSe	Co-evaporating	0 – 100	1.0 – 1.4	[386]
CZTGeSe	Electrodeposition	40	1.15	[387]



2.2.4 Ge-ALLOYING IN KESTERITE MATERIALS

The substitution of Sn by Ge is one of the latest important substitution pathways worth mentioning. Although elemental Ge is counted a CRM, its utilization by partial substitution has potential sustainability. For instance, in the event of Sn substitution by 20% Ge, it is estimated that about less than 1 Ton of Ge is needed to yield 1 GW for a 15% efficient solar panel. This is equivalent to less than 1% of the total global production of Ge. However, the minimum use of Ge in the kesterite solar cell technology will be interesting. Ge has showed significant improvements on kesterite absorbers since from the early stages as in the incident of Ge-doping [300], Ge-alloying ($\text{Cu}_2\text{ZnGeS}_4$, CZGS; $\text{Cu}_2\text{ZnGeSe}_4$, CZGSe). The optimization of kesterite absorbers containing Ge for the sulfur-selenide material was first published by Hages *et al.* [339], attaining an outstanding power conversion efficiency of 9.4% for Sn substitution with 30% Ge, indicating 1% boost in comparison to pure kesterite

(no Ge content), interconnected to a direct upgrading of the V_{OC} . A significant improvement in the minority carrier lifetime was also pronounced, authenticating Ge as one of the candidates with great potential to improve the power conversion efficiency in solar cells based on kesterite absorber materials. These initial studies paved a way for gradual developments, and a kesterite solar cell device attaining over 10% power conversion efficiency was reported by Kim *et al.* [386] with higher content of Ge (39%), by adjusting the annealing profile accordingly. A synthesis of a graded kesterite sample with blending of Ge and Sn, including almost all possible Ge/(Sn+Ge) stoichiometric ratios was later on published by Collord and Hillhouse [388], attaining about 11% power conversion efficiency solar cell device with a well-adjusted 25% of Ge content and a significant V_{OC} -deficit decrease. A significant drop in power conversion efficiency results from further increase in Ge content attributed to both detrimental band alignment between the Ge-based kesterite and CdS buffer layer, and the deep defect formation situated at about 0.8 eV beyond the valence band shifting near mid-gap as the energy bandgap widens in direct proportion to the content of Ge. Last of all, Kim *et al.* [389], reported a 12.3% improvement in power conversion efficiency with a significant improvement of V_{OC} deficit attained by further optimization of Ge depth composition. This development in power conversion efficiency and V_{OC} deficit was correlated to band tailing reduction through the regulation of the Ge/(Sn + Ge) ratio. Moreover, an outstanding FF (73%) was reported, proposing a significant decrease in carrier recombination at the absorber/CdS buffer interface and/or in the space charge area. The authors also reported an enhancement on carrier lifetime, largely proposing a higher quality kesterite absorber. The fast developments in power conversion efficiency attained for Ge-alloyed kesterite absorber places it as one of the pathways with great potential to advance the kesterite power conversion efficiency. Recently, Gunder *et al.* [390] experimental results showed that CZGSe assumes a kesterite crystal structure, and the widespread Cu-rich

compound yields detrimental Cu_{Ge} defect but it is not preeminent in the general Cu-poor devices published in literature. The fast developments of Ge-alloying recently reported that a pure CZGSe-based kesterite solar cell produced 7.6% power conversion efficiency with the associated V_{OC} of 558 mV, attained via CdS buffer layer optimization [391]. Nevertheless, it has been observed that the interface recombination attributable to poor band alignment between the kesterite absorber and the CdS buffer layer largely restrains the V_{OC} , providing understanding for future developments utilizing unconventional buffer layers. Lastly, Marquez *et al.* [317], with the help of joint *in situ* energy-dispersive X-ray diffraction (EDXRD) synchrotron and high-resolution scanning electron microscopy/energy dispersive X-ray spectroscopy (SEM/EDX) characterization techniques demonstrated that elemental Ge is likely to accrue near the back contact in Sn-Ge alloys, analogous to Ga in CIGSSe, proposing a chance for back contact interface optimization studies.

Table 2.5: Compilation of some of the most relevant devices reported in the literature which includes alloying with Ge, Cd, and Ag.

Material	Alloying element	E_{g} [eV]	V_{oc} [mV]	V_{oc} deficit[mV]	Eff.[%]	Ref.
CZTGSe	Ge/(Ge+Sn) = 22%	1.11	527	337	12.3	[389]
CZTGSSe	Ge/(Ge+Sn) = 25%	1.2	583	367	11.0	[388]
CZCTS	Cd/(Cd+Zn) = 40%	1.38	650	470	11.5	[392]
CZCTS	Cd/(Cd+Zn) = 40%	1.36	581	421	9.2	[393]
ACZTSSe	Ag/(Ag+Cu) = 3%	1.07	448	378	10.4	[394]
ACZTSe	Ag/(Ag+Cu) = 10%	1.0	423	337	10.2	[395]
ACZCTS	Ag/(Ag+Cu) = 5% Cd/(Cd+Zn) = 25%	1.4	650	490	10.8	[396]

Table 2.5 outlines a summary of the most important experimental results achieved until now by employing the three different alloying pathways, emphasizing the prospects to further

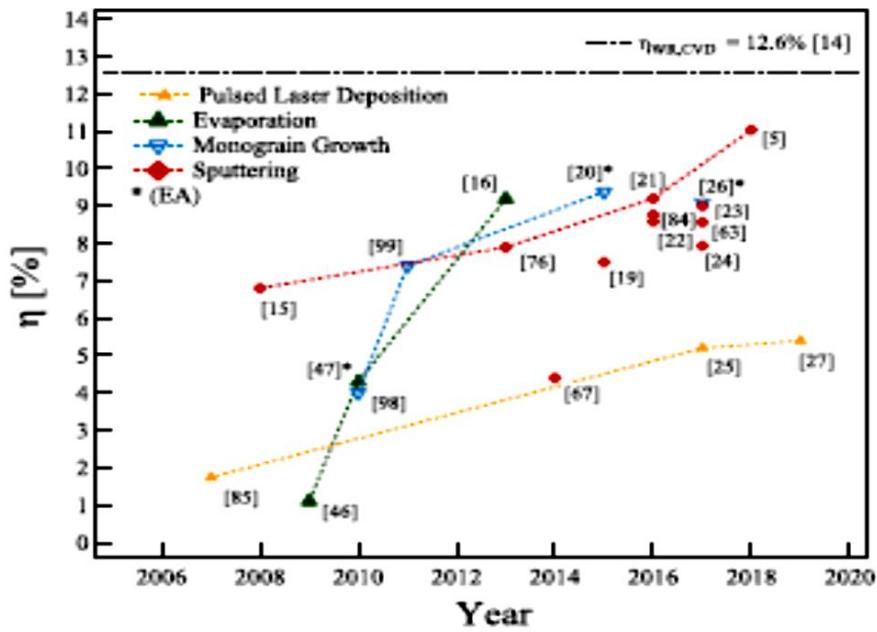
improve these promising alloying pathways in quest to advance the power conversion efficiency of solar cells based on kesterite absorber material. Alternative elements such as Mn [397,398], Mg [399], and Fe [400] have also been tested for alloying in kesterite absorber and they attained a power conversion efficiency still at a 7 – 8 level utilizing low Mn and Mg content (below 5%), or 2 – 3% power conversion efficiency attained through 100% complete substitution of Zn by Fe. Currently, these alloying substitutions still have not outperformed the previously reported ones. Kesterite absorber still suffers from significant V_{OC} deficit despite the impressive developments made in intrinsic and extrinsic doping as well as alloying approaches.

2.2.5 PHYSICAL ROUTES FOR THE SYNTHESIS OF KESTERITES

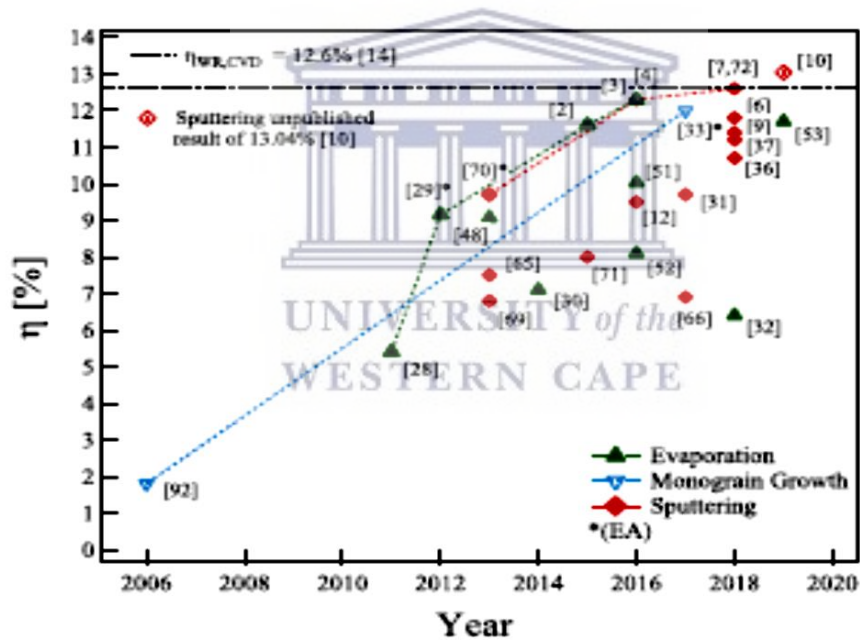
Owing to the parallels between kesterite and chalcopyrite compounds, the standard solar cell device archetype implemented for $Cu(In,Ga)(S,Se)_2$ (CIGSSe) was directly expanded to CZTSSe and this was achieved by a simple replacement of the CIGSSe absorber layer with a p-type CZTSSe kesterite thin film. Generally, a soda lime glass (SLG) substrate covered with a sputtered Mo layer functioning as a metallic back contact is utilized to fabricate the CZTSSe solar cells. The sputtered thickness of Mo layer on SLG is usually around 500 nm - $1\mu m$ [401]. The Mo layer then becomes the scaffold on which the kesterite absorber is deposited. The synthesis of the kesterite absorber material involves the deposition of a precursor layer through a physical or a chemical method, which is then followed by high temperature reactive annealing in a S (sulfurization) or Se (selenization) atmosphere. After a reactive annealing process, a thin $Mo(S,Se)_2$ layer forms at the CZTSSe/Mo interface as a result of partial selenization or sulfurization taking place at the rear Mo contact. Even in the CIG(S,Se) solar cell technology, this $Mo(S,Se)_2$ layer partially forms at the CIG(S,Se)/Mo

interface, and it has been reported that this p-doped layer aids in advancing the ohmic character of the rear Mo contact [401,402]. Subsequent to the deposition of the kesterite absorber, surface passivation of the absorber is performed by chemical bath treatment method to eliminate the detrimental secondary phases and/or to prepare the absorber for the succeeding construction of PN junction.

Generally, cadmium sulphide (CdS) is utilized as the n-type buffer layer of the PN junction. Chemical bath deposition technique is commonly employed to deposit the n-type buffer layer with usually 50 – 100 nm thickness order. The intrinsic ZnO (50 – 100 nm thick) and a transparent conducting oxide (TCO) layer (200 – 400 nm thick indium tin oxide or aluminium zinc oxide) form the window layer which is deposited by sputtering technique. Lastly, a front contact of the solar cell which consists of a metallic Al, Ni or Ni/Al grid is deposited. Finally, the entire configuration (structure) of the solar cell device is as follows; Al-Ni/TCO/ZnO/CdS/CdS/CZT(S,Se)/Mo(S,Se)₂/Mo/SLG. MgF₂, an anti-reflective (AR) covering is occasionally deposited on top of the solar cell device. A graphical representation of the evolution of the power conversion efficiency over the layers is summarized for each physical route using two graphs; one for solar cells based on CZTS (see **Figure 2.12(a)**) and the other for solar cells based on CZTSe (see **Figure 2.12(b)**). Remarkably, all the physical route techniques have made striking improvements over the last years despite the fact that chemical routes have attained record power conversion efficiency for kesterite solar cells which remained constant since 2012 [288].



(a) $\text{Cu}_2\text{ZnSnS}_4$



(b) $\text{Cu}_2\text{ZnSn}(\text{S},\text{Se})_4$

Figure 2.12: Evolution of the maximum efficiency η_{max} [%] for (a) CZTS-based and (b) CZT(S,Se)-based cells over the period of 2016 – 2019. In figure legend WR stand for world record and EA stands for effective area. Reproduced with permission from Ref. [403].

Bibliography

- [1] N.K. Noel, S.D. Stranks, A. Abate, C. Wehrenfennig, S. Guarnera, A.A. Haghighirad, A. Sadhanala, G.E. Eperon, S.K. Pathak, M.B. Johnston, A. Petrozza, L.M. Herz, H.J. Snaith, Lead-free organic-inorganic tin halide perovskites for photovoltaic applications, *Energy and Environmental Science*. 7 (2014) 3061–3068.
<https://doi.org/10.1039/c4ee01076k>.
- [2] Q. Tai, K.C. Tang, F. Yan, Recent progress of inorganic perovskite solar cells, *Energy and Environmental Science*. 12 (2019) 2375–2405.
<https://doi.org/10.1039/c9ee01479a>.
- [3] R. Wang, M. Mujahid, Y. Duan, Z.K. Wang, J. Xue, Y. Yang, A Review of Perovskites Solar Cell Stability, *Advanced Functional Materials*. 29 (2019) 1808843.
<https://doi.org/10.1002/adfm.201808843>.
- [4] X. Jiang, J. Zhang, S. Ahmad, D. Tu, X. Liu, G. Jia, X. Guo, C. Li, Dion-Jacobson 2D-3D perovskite solar cells with improved efficiency and stability, *Nano Energy*. 75 (2020) 104892. <https://doi.org/10.1016/j.nanoen.2020.104892>.
- [5] E.H. Jung, N.J. Jeon, E.Y. Park, C.S. Moon, T.J. Shin, T.Y. Yang, J.H. Noh, J. Seo, Efficient, stable and scalable perovskite solar cells using poly(3-hexylthiophene), *Nature*. 567 (2019) 511–515. <https://doi.org/10.1038/s41586-019-1036-3>.
- [6] Q. Jiang, Z. Ni, G. Xu, Y. Lin, P.N. Rudd, R. Xue, Y. Li, Y. Li, Y. Gao, J. Huang, Interfacial Molecular Doping of Metal Halide Perovskites for Highly Efficient Solar Cells, *Advanced Materials*. 32 (2020) 2001581.
<https://doi.org/10.1002/adma.202001581>.

- [7] M. Saliba, T. Matsui, K. Domanski, J.Y. Seo, A. Ummadisingu, S.M. Zakeeruddin, J.P. Correa-Baena, W.R. Tress, A. Abate, A. Hagfeldt, M. Grätzel, Incorporation of rubidium cations into perovskite solar cells improves photovoltaic performance, *Science*. 354 (2016) 206–209. <https://doi.org/10.1126/science.aah5557>.
- [8] M. Abdi-Jalebi, Z. Andaji-Garmaroudi, S. Cacovich, C. Stavrakas, B. Philippe, J.M. Richter, M. Alsari, E.P. Booker, E.M. Hutter, A.J. Pearson, S. Lilliu, T.J. Savenije, H. Rensmo, G. Divitini, C. Ducati, R.H. Friend, S.D. Stranks, Maximizing and stabilizing luminescence from halide perovskites with potassium passivation, *Nature*. 555 (2018) 497–501. <https://doi.org/10.1038/nature25989>.
- [9] H. Zhao, Y. Han, Z. Xu, C. Duan, S. Yang, S. Yuan, Z. Yang, Z. Liu, S. Liu, A Novel Anion Doping for Stable CsPbI₂Br Perovskite Solar Cells with an Efficiency of 15.56% and an Open Circuit Voltage of 1.30 V, *Advanced Energy Materials*. 9 (2019) 1902279. <https://doi.org/10.1002/aenm.201902279>.
- [10] T. Bu, J. Li, Q. Lin, D.P. McMeekin, J. Sun, M. Wang, W. Chen, X. Wen, W. Mao, C.R. McNeill, W. Huang, X.L. Zhang, J. Zhong, Y.B. Cheng, U. Bach, F. Huang, Structure engineering of hierarchical layered perovskite interface for efficient and stable wide bandgap photovoltaics, *Nano Energy*. 75 (2020) 104917. <https://doi.org/10.1016/j.nanoen.2020.104917>.
- [11] M.M. Lee, J. Teuscher, T. Miyasaka, T.N. Murakami, H.J. Snaith, Efficient hybrid solar cells based on meso-superstructured organometal halide perovskites, *Science*. 338 (2012) 643–647. <https://doi.org/10.1126/science.1228604>.

- [12] Z.K. Tang, Z.F. Xu, D.Y. Zhang, S.X. Hu, W.M. Lau, L.M. Liu, Enhanced optical absorption via cation doping hybrid lead iodine perovskites, *Scientific Reports*. 7 (2017) 7843. <https://doi.org/10.1038/s41598-017-08215-3>.
- [13] X.F. Zhang, C. Liu, J. Wu, B. Xu, Tetrabenzotriazacorrole and its derivatives as undoped hole transporting materials for perovskite solar cells: Synthesis, device fabrication, and device performance, *Journal of Energy Chemistry*. 43 (2020) 139–147. <https://doi.org/10.1016/j.jechem.2019.08.012>.
- [14] Q. Dong, Y. Fang, Y. Shao, P. Mulligan, J. Qiu, L. Cao, J. Huang, Electron-hole diffusion lengths > 175 μm in solution-grown $\text{CH}_3\text{NH}_3\text{PbI}_3$ single crystals, *Science*. 347 (2015) 967–970. <https://doi.org/10.1126/science.aaa5760>.
- [15] D.W. DeQuilettes, S.M. Vorpahl, S.D. Stranks, H. Nagaoka, G.E. Eperon, M.E. Ziffer, H.J. Snaith, D.S. Ginger, Impact of microstructure on local carrier lifetime in perovskite solar cells, *Science*. 348 (2015) 683–686. <https://doi.org/10.1126/science.aaa5333>.
- [16] J. Tong, Z. Song, D.H. Kim, X. Chen, C. Chen, A.F. Palmstrom, P.F. Ndione, M.O. Reese, S.P. Dunfield, O.G. Reid, J. Liu, F. Zhang, S.P. Harvey, Z. Li, S.T. Christensen, G. Teeter, D. Zhao, M.M. Al-Jassim, M.F.A.M. Van Hest, M.C. Beard, S.E. Shaheen, J.J. Berry, Y. Yan, K. Zhu, Carrier lifetimes of >1 ms in Sn-Pb perovskites enable efficient all-perovskite tandem solar cells, *Science*. 364 (2019) 475–479. <https://doi.org/10.1126/science.aav7911>.

- [17] C.C. Stoumpos, C.D. Malliakas, M.G. Kanatzidis, Semiconducting tin and lead iodide perovskites with organic cations: Phase transitions, high mobilities, and near-infrared photoluminescent properties, *Inorganic Chemistry*. 52 (2013) 9019–9038.
<https://doi.org/10.1021/ic401215x>.
- [18] L.M. Herz, Charge-Carrier Mobilities in Metal Halide Perovskites: Fundamental Mechanisms and Limits, *ACS Energy Letters*. 2 (2017) 1539–1548.
<https://doi.org/10.1021/acsenergylett.7b00276>.
- [19] G. Wu, Y. Zhang, R. Kaneko, Y. Kojima, A. Islam, K. Sugawa, J. Otsuki, S. Liu, Anthradithiophene based hole-transport material for efficient and stable perovskite solar cells, *Journal of Energy Chemistry*. 48 (2020) 293–298.
<https://doi.org/10.1016/j.jechem.2020.02.021>.
- [20] A. Wang, Z. Cao, J. Wang, S. Wang, C. Li, N. Li, L. Xie, Y. Xiang, T. Li, X. Niu, L. Ding, F. Hao, Vacancy defect modulation in hot-casted NiOx film for efficient inverted planar perovskite solar cells, *Journal of Energy Chemistry*. 48 (2020) 426–434. <https://doi.org/10.1016/j.jechem.2020.02.034>.
- [21] Y. Gao, K. Wang, M. Wang, J.I. Khan, A.H. Balawi, W. Liu, S. De Wolf, F. Laquai, Impact of Cesium/Rubidium Incorporation on the Photophysics of Multiple-Cation Lead Halide Perovskites, *Solar RRL*. 4 (2020) 2000072.
<https://doi.org/10.1002/solr.202000072>.
- [22] C. Bi, X. Zheng, B. Chen, H. Wei, J. Huang, Spontaneous Passivation of Hybrid Perovskite by Sodium Ions from Glass Substrates: Mysterious Enhancement of Device Efficiency Revealed, *ACS Energy Letters*. 2 (2017) 1400–1406.
<https://doi.org/10.1021/acsenergylett.7b00356>.

- [23] X. Wan, Z. Yu, W. Tian, F. Huang, S. Jin, X. Yang, Y.B. Cheng, A. Hagfeldt, L. Sun, Efficient and stable planar all-inorganic perovskite solar cells based on high-quality CsPbBr₃ films with controllable morphology, *Journal of Energy Chemistry*. 46 (2020) 8–15. <https://doi.org/10.1016/j.jechem.2019.10.017>.
- [24] J. Zhang, H. Yu, Multifunctional dopamine-assisted preparation of efficient and stable perovskite solar cells, *Journal of Energy Chemistry*. 54 (2021) 291–300. <https://doi.org/10.1016/j.jechem.2020.05.061>.
- [25] Y. Du, J. Wu, X. Zhang, Q. Zhu, M. Zhang, X. Liu, Y. Zou, S. Wang, W. Sun, Surface passivation using pyridinium iodide for highly efficient planar perovskite solar cells, *Journal of Energy Chemistry*. 52 (2021) 84–91. <https://doi.org/10.1016/j.jechem.2020.04.049>.
- [26] A. Kojima, K. Teshima, Y. Shirai, T. Miyasaka, Organometal halide perovskites as visible-light sensitizers for photovoltaic cells, *Journal of the American Chemical Society*. 131 (2009) 6050–6051. <https://doi.org/10.1021/ja809598r>.
- [27] NREL, Best Research-Cell Efficiency Chart. <https://www.nrel.gov/pv/cell-efficiency.html>.
- [28] L. Gao, S. Huang, L. Chen, X. Li, B. Ding, S. Huang, G. Yang, Excellent Stability of Perovskite Solar Cells by Passivation Engineering, *Solar RRL*. 2 (2018) 1800088. <https://doi.org/10.1002/solr.201800088>.
- [29] H. Zhu, Y. Liu, F.T. Eickemeyer, L. Pan, D. Ren, M.A. Ruiz-Preciado, B. Carlsen, B. Yang, X. Dong, Z. Wang, H. Liu, S. Wang, S.M. Zakeeruddin, A. Hagfeldt, M.I. Dar, X. Li, M. Grätzel, Tailored Amphiphilic Molecular Mitigators for Stable Perovskite Solar Cells with 23.5% Efficiency, *Advanced Materials*. 32 (2020) 1907757.

<https://doi.org/10.1002/adma.201907757>.

- [30] S. Zhang, X. Yan, Z. Liu, H. Zhu, Z. Yang, Y. Huang, S. Liu, D. Wu, M. Pan, W. Chen, Evaporated potassium chloride for double-sided interfacial passivation in inverted planar perovskite solar cells, *Journal of Energy Chemistry*. 54 (2021) 493–500. <https://doi.org/10.1016/j.jechem.2020.06.019>.
- [31] Y. Wang, M. Ibrahim Dar, L.K. Ono, T. Zhang, M. Kan, Y. Li, L. Zhang, X. Wang, Y. Yang, X. Gao, Y. Qi, M. Grätzel, Y. Zhao, Thermodynamically stabilized b-CsPbI₃-based perovskite solar cells with efficiencies >18%, *Science*. 365 (2019) 591–595. <https://doi.org/10.1126/science.aav8680>.
- [32] M. Saliba, T. Matsui, J.Y. Seo, K. Domanski, J.P. Correa-Baena, M.K. Nazeeruddin, S.M. Zakeeruddin, W. Tress, A. Abate, A. Hagfeldt, M. Grätzel, Cesium-containing triple cation perovskite solar cells: Improved stability, reproducibility and high efficiency, *Energy and Environmental Science*. 9 (2016) 1989–1997. <https://doi.org/10.1039/c5ee03874j>.
- [33] Z. Wu, M. Zhang, Y. Liu, Y. Dou, Y. Kong, L. Gao, W. Han, G. Liang, X.L. Zhang, F. Huang, Y.B. Cheng, J. Zhong, Groups-dependent phosphines as the organic redox for point defects elimination in hybrid perovskite solar cells, *Journal of Energy Chemistry*. 54 (2020) 23–29. <https://doi.org/10.1016/j.jechem.2020.05.047>.
- [34] Y. Hu, M.F. Aygüler, M.L. Petrus, T. Bein, P. Docampo, Impact of Rubidium and Cesium Cations on the Moisture Stability of Multiple-Cation Mixed-Halide Perovskites, *ACS Energy Letters*. 2 (2017) 2212–2218. <https://doi.org/10.1021/acsenergylett.7b00731>.

- [35] M. Que, Z. Dai, H. Yang, H. Zhu, Y. Zong, W. Que, N.P. Padture, Y. Zhou, O. Chen, Quantum-Dot-Induced Cesium-Rich Surface Imparts Enhanced Stability to Formamidinium Lead Iodide Perovskite Solar Cells, *ACS Energy Letters*. 4 (2019) 1970–1975. <https://doi.org/10.1021/acsenergylett.9b01262>.
- [36] Q. Zhou, J. Duan, Y. Wang, X. Yang, Q. Tang, Tri-functionalized $\text{TiO}_x\text{Cl}_{4-2x}$ accessory layer to boost efficiency of hole-free, all-inorganic perovskite solar cells, *Journal of Energy Chemistry*. 50 (2020) 1–8. <https://doi.org/10.1016/j.jechem.2020.03.004>.
- [37] S. Xiong, T. Hao, Y. Sun, J. Yang, R. Ma, J. Wang, S. Gong, X. Liu, L. Ding, M. Fahlman, Q. Bao, Defect passivation by nontoxic biomaterial yields 21% efficiency perovskite solar cells, *Journal of Energy Chemistry*. 55 (2021) 265–271. <https://doi.org/10.1016/j.jechem.2020.06.061>.
- [38] D.P. McMeekin, G. Sadoughi, W. Rehman, G.E. Eperon, M. Saliba, M.T. Hörantner, A. Haghighirad, N. Sakai, L. Korte, B. Rech, M.B. Johnston, L.M. Herz, H.J. Snaith, A mixed-cation lead mixed-halide perovskite absorber for tandem solar cells, *Science*. 351 (2016) 151–155. <https://doi.org/10.1126/science.aad5845>.
- [39] W. Tress, N. Marinova, T. Moehl, S.M. Zakeeruddin, M.K. Nazeeruddin, M. Grätzel, Understanding the rate-dependent J-V hysteresis, slow time component, and aging in $\text{CH}_3\text{NH}_3\text{PbI}_3$ perovskite solar cells: The role of a compensated electric field, *Energy and Environmental Science*. 8 (2015) 995–1004. <https://doi.org/10.1039/c4ee03664f>.
- [40] Y. Hu, E.M. Hutter, P. Rieder, I. Grill, J. Hanisch, M.F. Aygüler, A.G. Hufnagel, M. Handloser, T. Bein, A. Hartschuh, K. Tvingstedt, V. Dyakonov, A. Baumann, T.J. Savenije, M.L. Petrus, P. Docampo, Understanding the Role of Cesium and Rubidium Additives in Perovskite Solar Cells: Trap States, Charge Transport, and

- Recombination, *Advanced Energy Materials*. 8 (2018) 1703057.
<https://doi.org/10.1002/aenm.201703057>.
- [41] J. V. Patil, S.S. Mali, C.K. Hong, A-Site Rubidium Cation-Incorporated CsPbI₂Br All-Inorganic Perovskite Solar Cells Exceeding 17% Efficiency, *Solar RRL*. 4 (2020) 2000164. <https://doi.org/10.1002/solr.202000164>.
- [42] H. Ren, S. Yu, L. Chao, Y. Xia, Y. Sun, S. Zuo, F. Li, T. Niu, Y. Yang, H. Ju, B. Li, H. Du, X. Gao, J. Zhang, J. Wang, L. Zhang, Y. Chen, W. Huang, Efficient and stable Ruddlesden–Popper perovskite solar cell with tailored interlayer molecular interaction, *Nature Photonics*. 14 (2020) 154–163. <https://doi.org/10.1038/s41566-019-0572-6>.
- [43] M. Chen, P. Li, C. Liang, H. Gu, W. Tong, S. Cheng, W. Li, G. Zhao, G. Shao, Enhanced efficiency and stability of perovskite solar cells by 2D perovskite vapor-assisted interface optimization, *Journal of Energy Chemistry*. 45 (2020) 103–109. <https://doi.org/10.1016/j.jechem.2019.10.006>.
- [44] F. Matteocci, L. Cinà, E. Lamanna, S. Cacovich, G. Divitini, P.A. Midgley, C. Ducati, A. Di Carlo, Encapsulation for long-term stability enhancement of perovskite solar cells, *Nano Energy*. 30 (2016) 162–172. <https://doi.org/10.1016/j.nanoen.2016.09.041>.
- [45] R. Cheacharoen, C.C. Boyd, G.F. Burkhard, T. Leijtens, J.A. Raiford, K.A. Bush, S.F. Bent, M.D. McGehee, Encapsulating perovskite solar cells to withstand damp heat and thermal cycling, *Sustainable Energy and Fuels*. 2 (2018) 2398–2406.
<https://doi.org/10.1039/c8se00250a>.
- [46] A.K. Jena, A. Kulkarni, T. Miyasaka, Halide Perovskite Photovoltaics: Background, Status, and Future Prospects, *Chemical Reviews*. 119 (2019) 3036–3103.
<https://doi.org/10.1021/acs.chemrev.8b00539>.

- [47] J. Luo, H. Bin Yang, M. Zhuang, S. Liu, L. Wang, B. Liu, Making fully printed perovskite solar cells stable outdoor with inorganic superhydrophobic coating, *Journal of Energy Chemistry*. 50 (2020) 332–338. <https://doi.org/10.1016/j.jechem.2020.03.082>.
- [48] Z. Shi, S. Li, Y. Li, H. Ji, X. Li, D. Wu, T. Xu, Y. Chen, Y. Tian, Y. Zhang, C. Shan, G. Du, Strategy of Solution-Processed All-Inorganic Heterostructure for Humidity/Temperature-Stable Perovskite Quantum Dot Light-Emitting Diodes, *ACS Nano*. 12 (2018) 1462–1472. <https://doi.org/10.1021/acsnano.7b07856>.
- [49] J. Duan, Y. Wang, X. Yang, Q. Tang, Alkyl-Chain-Regulated Charge Transfer in Fluorescent Inorganic CsPbBr₃ Perovskite Solar Cells, *Angewandte Chemie - International Edition*. 59 (2020) 4391–4395. <https://doi.org/10.1002/anie.202000199>.
- [50] L. Shi, M.P. Bucknall, T.L. Young, M. Zhang, L. Hu, J. Bing, D.S. Lee, J. Kim, T. Wu, N. Takamure, D.R. McKenzie, S. Huang, M.A. Green, A.W.Y. Ho-Baillie, Gas chromatography-mass spectrometry analyses of encapsulated stable perovskite solar cells, *Science*. 368 (2020) 6497. <https://doi.org/10.1126/science.aba2412>.
- [51] M. Grätzel, The light and shade of perovskite solar cells, *Nature Materials*. 13 (2014) 838–842. <https://doi.org/10.1038/nmat4065>.
- [52] X. Li, F. Zhang, H. He, J.J. Berry, K. Zhu, T. Xu, On-device lead sequestration for perovskite solar cells, *Nature*. 578 (2020) 555–558. <https://doi.org/10.1038/s41586-020-2001-x>.
- [53] R. Wang, J. Wang, S. Tan, Y. Duan, Z.K. Wang, Y. Yang, Opportunities and Challenges of Lead-Free Perovskite Optoelectronic Devices, *Trends in Chemistry*. 1 (2019) 368–379. <https://doi.org/10.1016/j.trechm.2019.04.004>.

- [54] Y. Jiang, L. Qiu, E.J. Juarez-Perez, L.K. Ono, Z. Hu, Z. Liu, Z. Wu, L. Meng, Q. Wang, Y. Qi, Reduction of lead leakage from damaged lead halide perovskite solar modules using self-healing polymer-based encapsulation, *Nature Energy*. 4 (2019) 585–593. <https://doi.org/10.1038/s41560-019-0406-2>.
- [55] A.H. Slavney, T. Hu, A.M. Lindenberg, H.I. Karunadasa, A Bismuth-Halide Double Perovskite with Long Carrier Recombination Lifetime for Photovoltaic Applications, *Journal of the American Chemical Society*. 138 (2016) 2138–2141. <https://doi.org/10.1021/jacs.5b13294>.
- [56] J. Su, Y. qiang Huang, H. Chen, J. Huang, Solution Growth and Performance Study of Cs₂AgBiBr₆ Single Crystal, *Crystal Research and Technology*. 55 (2020) 1900222. <https://doi.org/10.1002/crat.201900222>.
- [57] T. Jiang, Z. Chen, X. Chen, T. Liu, X. Chen, W.E.I. Sha, H. Zhu, Y. Yang, Realizing High Efficiency over 20% of Low-Bandgap Pb–Sn-Alloyed Perovskite Solar Cells by In Situ Reduction of Sn⁴⁺, *Solar RRL*. 4 (2020) 1900467. <https://doi.org/10.1002/solr.201900467>.
- [58] X. Zhou, L. Zhang, X. Wang, C. Liu, S. Chen, M. Zhang, X. Li, W. Yi, B. Xu, Highly Efficient and Stable GABr-Modified Ideal-Bandgap (1.35 eV) Sn/Pb Perovskite Solar Cells Achieve 20.63% Efficiency with a Record Small Voc Deficit of 0.33 V, *Advanced Materials*. 32 (2020) 1908107. <https://doi.org/10.1002/adma.201908107>.
- [59] C. Li, R. Ma, X. He, T. Yang, Z. Zhou, S. Yang, Y. Liang, X.W. Sun, J. Wang, Y. Yan, W.C.H. Choy, In Situ Tin(II) Complex Antisolvent Process Featuring Simultaneous Quasi-Core–Shell Structure and Heterojunction for Improving Efficiency and Stability of Low-Bandgap Perovskite Solar Cells, *Advanced Energy*

- Materials. 10 (2020) 1903013. <https://doi.org/10.1002/aenm.201903013>.
- [60] L.J. Chen, C.R. Lee, Y.J. Chuang, Z.H. Wu, C. Chen, Synthesis and Optical Properties of Lead-Free Cesium Tin Halide Perovskite Quantum Rods with High-Performance Solar Cell Application, *Journal of Physical Chemistry Letters*. 7 (2016) 5028–5035. <https://doi.org/10.1021/acs.jpcclett.6b02344>.
- [61] H. Chen, S. Xiang, W. Li, H. Liu, L. Zhu, S. Yang, Inorganic Perovskite Solar Cells: A Rapidly Growing Field, *Solar RRL*. 2 (2018) 1700188. <https://doi.org/10.1002/solr.201700188>.
- [62] B. Lee, C.C. Stoumpos, N. Zhou, F. Hao, C. Malliakas, C.Y. Yeh, T.J. Marks, M.G. Kanatzidis, R.P.H. Chang, Air-stable molecular semiconducting iodosalts for solar cell applications: Cs_2SnI_6 as a hole conductor, *Journal of the American Chemical Society*. 136 (2014) 15379–15385. <https://doi.org/10.1021/ja508464w>.
- [63] M. Chen, M.G. Ju, A.D. Carl, Y. Zong, R.L. Grimm, J. Gu, X.C. Zeng, Y. Zhou, N.P. Padture, Cesium Titanium(IV) Bromide Thin Films Based Stable Lead-free Perovskite Solar Cells, *Joule*. 2 (2018) 558–570. <https://doi.org/10.1016/j.joule.2018.01.009>.
- [64] K. Dave, M.H. Fang, Z. Bao, H.T. Fu, R.S. Liu, Recent Developments in Lead-Free Double Perovskites: Structure, Doping, and Applications, *Chemistry - An Asian Journal*. 15 (2020) 242–252. <https://doi.org/10.1002/asia.201901510>.
- [65] P. Han, X. Mao, S. Yang, F. Zhang, B. Yang, D. Wei, W. Deng, K. Han, Lead-Free Sodium–Indium Double Perovskite Nanocrystals through Doping Silver Cations for Bright Yellow Emission, *Angewandte Chemie*. 131 (2019) 17391–17395. <https://doi.org/10.1002/ange.201909525>.

- [66] F. Igbari, Z.K. Wang, L.S. Liao, Progress of Lead-Free Halide Double Perovskites, *Advanced Energy Materials*. 9 (2019) 1803150.
<https://doi.org/10.1002/aenm.201803150>.
- [67] W. Ning, F. Gao, Structural and Functional Diversity in Lead-Free Halide Perovskite Materials, *Advanced Materials*. 31 (2019) 1900326.
<https://doi.org/10.1002/adma.201900326>.
- [68] E.T. McClure, M.R. Ball, W. Windl, P.M. Woodward, Cs₂AgBiX₆ (X = Br, Cl): New Visible Light Absorbing, Lead-Free Halide Perovskite Semiconductors, *Chemistry of Materials*. 28 (2016) 1348–1354. <https://doi.org/10.1021/acs.chemmater.5b04231>.
- [69] M.R. Filip, S. Hillman, A.A. Haghighirad, H.J. Snaith, F. Giustino, Band Gaps of the Lead-Free Halide Double Perovskites Cs₂BiAgCl₆ and Cs₂BiAgBr₆ from Theory and Experiment, *Journal of Physical Chemistry Letters*. 7 (2016) 2579–2585.
<https://doi.org/10.1021/acs.jpcclett.6b01041>.
- [70] E. Greul, M.L. Petrus, A. Binek, P. Docampo, T. Bein, Highly stable, phase pure Cs₂AgBiBr₆ double perovskite thin films for optoelectronic applications, *Journal of Materials Chemistry A*. 5 (2017) 19972–19981. <https://doi.org/10.1039/c7ta06816f>.
- [71] W. Gao, C. Ran, J. Xi, B. Jiao, W. Zhang, M. Wu, X. Hou, Z. Wu, High-Quality Cs₂AgBiBr₆ Double Perovskite Film for Lead-Free Inverted Planar Heterojunction Solar Cells with 2.2 % Efficiency, *ChemPhysChem*. 19 (2018) 1696–1700.
<https://doi.org/10.1002/cphc.201800346>.
- [72] X. Yang, Y. Chen, P. Liu, H. Xiang, W. Wang, R. Ran, W. Zhou, Z. Shao, Simultaneous Power Conversion Efficiency and Stability Enhancement of Cs₂AgBiBr₆ Lead-Free Inorganic Perovskite Solar Cell through Adopting a Multifunctional Dye

- Interlayer, *Advanced Functional Materials*. 30 (2020) 2001557.
<https://doi.org/10.1002/adfm.202001557>.
- [73] G. Liu, C. Wu, Z. Zhang, Z. Chen, L. Xiao, B. Qu, Ultraviolet-Protective Transparent Photovoltaics Based on Lead-Free Double Perovskites, *Solar RRL*. 4 (2020) 2000056.
<https://doi.org/10.1002/solr.202000056>.
- [74] K. Nishimura, M.A. Kamarudin, D. Hirotani, K. Hamada, Q. Shen, S. Iikubo, T. Minemoto, K. Yoshino, S. Hayase, Lead-free tin-halide perovskite solar cells with 13% efficiency, *Nano Energy*. 74 (2020) 104850.
<https://doi.org/10.1016/j.nanoen.2020.104858>.
- [75] W. Ning, F. Wang, B. Wu, J. Lu, Z. Yan, X. Liu, Y. Tao, J.M. Liu, W. Huang, M. Fahlman, L. Hultman, T.C. Sum, F. Gao, Long Electron–Hole Diffusion Length in High-Quality Lead-Free Double Perovskite Films, *Advanced Materials*. 30 (2018) 1706246. <https://doi.org/10.1002/adma.201706246>.
- [76] S.E. Creutz, E.N. Crites, M.C. De Siena, D.R. Gamelin, Colloidal Nanocrystals of Lead-Free Double-Perovskite (Elpasolite) Semiconductors: Synthesis and Anion Exchange to Access New Materials, *Nano Letters*. 18 (2018) 1118–1123.
<https://doi.org/10.1021/acs.nanolett.7b04659>.
- [77] M. Wang, P. Zeng, S. Bai, J. Gu, F. Li, Z. Yang, M. Liu, High-Quality Sequential-Vapor-Deposited Cs₂AgBiBr₆ Thin Films for Lead-Free Perovskite Solar Cells, *Solar RRL*. 2 (2018) 1800217. <https://doi.org/10.1002/solr.201800217>.
- [78] C. Wu, Q. Zhang, Y. Liu, W. Luo, X. Guo, Z. Huang, H. Ting, W. Sun, X. Zhong, S. Wei, S. Wang, Z. Chen, L. Xiao, The Dawn of Lead-Free Perovskite Solar Cell: Highly Stable Double Perovskite Cs₂AgBiBr₆ Film, *Advanced Science*. 5 (2018)

1700759. <https://doi.org/10.1002/advs.201700759>.
- [79] A.S. Bhalla, R. Guo, R. Roy, The perovskite structure - A review of its role in ceramic science and technology, *Materials Research Innovations*. 4 (2000) 3–26.
<https://doi.org/10.1007/s100190000062>.
- [80] C. Li, K.C.K. Soh, P. Wu, Formability of ABO_3 perovskites, *Journal of Alloys and Compounds*. 372 (2004) 40–48. <https://doi.org/10.1016/j.jallcom.2003.10.017>.
- [81] E. Grabowska, Selected perovskite oxides: Characterization, preparation and photocatalytic properties-A review, *Applied Catalysis B: Environmental*. 186 (2016) 97–126. <https://doi.org/10.1016/j.apcatb.2015.12.035>.
- [82] A. Hossain, P. Bandyopadhyay, S. Roy, An overview of double perovskites $A_2B'B''O_6$ with small ions at A site: Synthesis, structure and magnetic properties, *Journal of Alloys and Compounds*. 740 (2018) 414–427.
<https://doi.org/10.1016/j.jallcom.2017.12.282>.
- [83] A. Waleed, M.M. Tavakoli, L. Gu, S. Hussain, D. Zhang, S. Poddar, Z. Wang, R. Zhang, Z. Fan, All inorganic cesium lead iodide perovskite nanowires with stabilized cubic phase at room temperature and nanowire array-based photodetectors, *Nano Letters*. 17 (2017) 4951–4957. <https://doi.org/10.1021/acs.nanolett.7b02101>.
- [84] H.-Y. Ye, Y. Zhang, D.-W. Fu, R.-G. Xiong, An Above-Room-Temperature Ferroelectric Organo-Metal Halide Perovskite: $(3\text{-Pyrrolinium})(\text{CdCl}_3)$, *Angewandte Chemie*. 126 (2014) 11424–11429. <https://doi.org/10.1002/ange.201406810>.
- [85] J.H. Im, I.H. Jang, N. Pellet, M. Grätzel, N.G. Park, Growth of $\text{CH}_3\text{NH}_3\text{PbI}_3$ cuboids with controlled size for high-efficiency perovskite solar cells, *Nature Nanotechnology*. 9 (2014) 927–932. <https://doi.org/10.1038/nnano.2014.181>.

- [86] J. Chen, S. Zhou, S. Jin, H. Li, T. Zhai, Crystal organometal halide perovskites with promising optoelectronic applications, *Journal of Materials Chemistry C*. 4 (2015) 11–27. <https://doi.org/10.1039/c5tc03417e>.
- [87] X. Zhang, S. Chen, X. Wang, A. Pan, Controlled Synthesis and Photonics Applications of Metal Halide Perovskite Nanowires, *Small Methods*. 3 (2019) 1800294. <https://doi.org/10.1002/smt.201800294>.
- [88] H. Fu, Colloidal metal halide perovskite nanocrystals: A promising juggernaut in photovoltaic applications, *Journal of Materials Chemistry A*. 7 (2019) 14357–14379. <https://doi.org/10.1039/c8ta12509k>.
- [89] R. Babu, L. Giribabu, S.P. Singh, Recent Advances in Halide-Based Perovskite Crystals and Their Optoelectronic Applications, *Crystal Growth and Design*. 18 (2018) 2645–2664. <https://doi.org/10.1021/acs.cgd.7b01767>.
- [90] Z. Zhu, Q. Sun, Z. Zhang, J. Dai, G. Xing, S. Li, X. Huang, W. Huang, Metal halide perovskites: stability and sensing-ability, *Journal of Materials Chemistry C*. 6 (2018) 10121–10137. <https://doi.org/10.1039/C8TC03164A>.
- [91] S. Gonzalez-Carrero, R.E. Galian, J. Pérez-Prieto, Organic-inorganic and all-inorganic lead halide nanoparticles [Invited], *Optics Express*. 24 (2016) A285. <https://doi.org/10.1364/oe.24.00a285>.
- [92] L. Protesescu, S. Yakunin, M.I. Bodnarchuk, F. Krieg, R. Caputo, C.H. Hendon, R.X. Yang, A. Walsh, M. V. Kovalenko, Nanocrystals of Cesium Lead Halide Perovskites (CsPbX₃, X = Cl, Br, and I): Novel Optoelectronic Materials Showing Bright Emission with Wide Color Gamut, *Nano Letters*. 15 (2015) 3692–3696. <https://doi.org/10.1021/nl5048779>.

- [93] F. Zhang, H. Zhong, C. Chen, X.G. Wu, X. Hu, H. Huang, J. Han, B. Zou, Y. Dong, Brightly luminescent and color-tunable colloidal $\text{CH}_3\text{NH}_3\text{PbX}_3$ ($X = \text{Br}, \text{I}, \text{Cl}$) quantum dots: Potential alternatives for display technology, *ACS Nano*. 9 (2015) 4533–4542. <https://doi.org/10.1021/acsnano.5b01154>.
- [94] A. Perumal, S. Shendre, M. Li, Y.K.E. Tay, V.K. Sharma, S. Chen, Z. Wei, Q. Liu, Y. Gao, P.J.S. Buenconsejo, S.T. Tan, C.L. Gan, Q. Xiong, T.C. Sum, H.V. Demir, High brightness formamidinium lead bromide perovskite nanocrystal light emitting devices, *Scientific Reports*. 6 (2016) 36733. <https://doi.org/10.1038/srep36733>.
- [95] L.C. Schmidt, A. Pertegás, S. González-Carrero, O. Malinkiewicz, S. Agouram, G. Mínguez Espallargas, H.J. Bolink, R.E. Galian, J. Pérez-Prieto, Nontemplate synthesis of $\text{CH}_3\text{NH}_3\text{PbBr}_3$ perovskite nanoparticles, *Journal of the American Chemical Society*. 136 (2014) 850–853. <https://doi.org/10.1021/ja4109209>.
- [96] A. Maity, A.K. Raychaudhuri, B. Ghosh, High sensitivity NH_3 gas sensor with electrical readout made on paper with perovskite halide as sensor material, *Scientific Reports*. 9 (2019) 7777. <https://doi.org/10.1038/s41598-019-43961-6>.
- [97] A. Nur'aini, I. Oh, Volatile organic compound gas sensors based on methylammonium lead iodide perovskite operating at room temperature, *RSC Advances*. 10 (2020) 12982–12987. <https://doi.org/10.1039/c9ra10703g>.
- [98] E. Kymakis, A. Panagiotopoulos, M.M. Stylianakis, K. Petridis, Organometallic hybrid perovskites for humidity and gas sensing applications, in: *2D Nanomaterials for Energy Applications: Graphene and Beyond*, Elsevier, 2019: pp. 131–147. <https://doi.org/10.1016/B978-0-12-816723-6.00005-8>.

- [99] X. Shan, S. Zhang, M. Zhou, T. Geske, M. Davis, A. Hao, H. Wang, Z. Yu, Porous Halide Perovskite–Polymer Nanocomposites for Explosive Detection with a High Sensitivity, *Advanced Materials Interfaces*. 6 (2019) 1801686. <https://doi.org/10.1002/admi.201801686>.
- [100] M.A. Haque, A. Syed, F.H. Akhtar, R. Shevate, S. Singh, K.V. Peinemann, D. Baran, T. Wu, Giant Humidity Effect on Hybrid Halide Perovskite Microstrips: Reversibility and Sensing Mechanism, *ACS Applied Materials and Interfaces*. 11 (2019) 29821–29829. <https://doi.org/10.1021/acsami.9b07751>.
- [101] M.A. Stoeckel, M. Gobbi, S. Bonacchi, F. Liscio, L. Ferlauto, E. Orgiu, P. Samorì, Reversible, Fast, and Wide-Range Oxygen Sensor Based on Nanostructured Organometal Halide Perovskite, *Advanced Materials*. 29 (2017) 1702469. <https://doi.org/10.1002/adma.201702469>.
- [102] C. Bao, J. Yang, W. Zhu, X. Zhou, H. Gao, F. Li, G. Fu, T. Yu, Z. Zou, A resistance change effect in perovskite $\text{CH}_3\text{NH}_3\text{PbI}_3$ films induced by ammonia, *Chemical Communications*. 51 (2015) 15426–15429. <https://doi.org/10.1039/c5cc06060e>.
- [103] Y. Zhao, K. Zhu, Optical bleaching of perovskite $(\text{CH}_3\text{NH}_3)\text{PbI}_3$ through room-temperature phase transformation induced by ammonia, *Chemical Communications*. 50 (2014) 1605–1607. <https://doi.org/10.1039/c3cc48522f>.
- [104] G. Li, W. Zhang, C. She, S. Jia, S. Liu, F. Yue, C. Jing, Y. Cheng, J. Chu, Stable fluorescent NH_3 sensor based on MAPbBr_3 encapsulated by tetrabutylammonium cations, *Journal of Alloys and Compounds*. 835 (2020) 155386. <https://doi.org/10.1016/j.jallcom.2020.155386>.

- [105] W. Jiao, J. He, L. Zhang, Synthesis and high ammonia gas sensitivity of $(\text{CH}_3\text{NH}_3)\text{PbBr}_{3-x}\text{I}_x$ perovskite thin film at room temperature, *Sensors and Actuators, B: Chemical*. 309 (2020) 127786. <https://doi.org/10.1016/j.snb.2020.127786>.
- [106] K. Brintakis, E. Gagaoudakis, A. Kostopoulou, V. Faka, A. Argyrou, V. Binas, G. Kiriakidis, E. Stratakis, Ligand-free all-inorganic metal halide nanocubes for fast, ultra-sensitive and self-powered ozone sensors, *Nanoscale Advances*. 1 (2019) 2699–2706. <https://doi.org/10.1039/c9na00219g>.
- [107] A. Kostopoulou, K. Brintakis, N.K. Nasikas, E. Stratakis, Perovskite nanocrystals for energy conversion and storage, *Nanophotonics*. 8 (2019) 1607–1640. <https://doi.org/10.1515/nanoph-2019-0119>.
- [108] G. King, P.M. Woodward, Cation ordering in perovskites, *Journal of Materials Chemistry*. 20 (2010) 5785–5796. <https://doi.org/10.1039/b926757c>.
- [109] Y. Cao, B. Lin, Y. Sun, H. Yang, X. Zhang, Synthesis, structure and electrochemical properties of lanthanum manganese nanofibers doped with Sr and Cu, *Journal of Alloys and Compounds*. 638 (2015) 204–213. <https://doi.org/10.1016/j.jallcom.2015.03.054>.
- [110] Y. Zhou, J. Chen, O.M. Bakr, H.T. Sun, Metal-Doped Lead Halide Perovskites: Synthesis, Properties, and Optoelectronic Applications, *Chemistry of Materials*. 30 (2018) 6589–6613. <https://doi.org/10.1021/acs.chemmater.8b02989>.
- [111] M. Berkowski, J. Fink-Finowicki, W. Piekarczyk, L. Perchuć, P. Byszewski, L.O. Vasylechko, D.I. Savytskij, K. Mazur, J. Sass, E. Kowalska, J. Kapuśniak, Czochralski growth and structural investigations of $\text{La}_{1-x}\text{Nd}_x\text{GaO}_3$ solid solution single crystals, *Journal of Crystal Growth*. 209 (2000) 75–80. <https://doi.org/10.1016/S0022->

0248(99)00594-1.

- [112] R.S. Kalubarme, G.-E. Park, K.-N. Jung, K.-H. Shin, W.-H. Ryu, C.-J. Park, $\text{LaNi}_x\text{Co}_{1-x}\text{O}_{3-\delta}$ Perovskites as Catalyst Material for Non-Aqueous Lithium-Oxygen Batteries, *Journal of The Electrochemical Society*. 161 (2014) A880–A889.
<https://doi.org/10.1149/2.012406jes>.
- [113] C. Zhang, B. Wang, W. Li, S. Huang, L. Kong, Z. Li, L. Li, Conversion of invisible metal-organic frameworks to luminescent perovskite nanocrystals for confidential information encryption and decryption, *Nature Communications*. 8 (2017) 1138.
<https://doi.org/10.1038/s41467-017-01248-2>.
- [114] L. Vasylechko, M. Berkowski, A. Matkovski, D. Savytskii, J. Fink-Finowicki, Crystal structure of $\text{La}_{1-x}\text{Nd}_x\text{GaO}_3$ single crystals ($0 < x < 0.2$), *Materials Research Bulletin*. 35 (2000) 333–340. [https://doi.org/10.1016/S0025-5408\(00\)00231-2](https://doi.org/10.1016/S0025-5408(00)00231-2).
- [115] X. Zhu, X. Pan, Y. Wu, W. Wan, T. Chen, Y. Wang, X. Ji, Z. Lü, Layered perovskite oxide $\text{PrBaCo}_2\text{O}_{5+\delta}$ as a potential cathode for lithium–oxygen batteries: High-performance bi-functional electrocatalysts, *Materials Letters*. 237 (2019) 200–203.
<https://doi.org/10.1016/j.matlet.2018.11.113>.
- [116] Q. Huang, A. Santoro, J. Lynn, Structure and magnetic order, *Physical Review B - Condensed Matter and Materials Physics*. 58 (1998) 2684–2691.
<https://doi.org/10.1103/PhysRevB.58.2684>.
- [117] M. Prabu, P. Ramakrishnan, P. Ganesan, A. Manthiram, S. Shanmugam, $\text{LaTi}_{0.65}\text{Fe}_{0.35}\text{O}_{3-\delta}$ nanoparticle-decorated nitrogen-doped carbon nanorods as an advanced hierarchical air electrode for rechargeable metal-air batteries, *Nano Energy*. 15 (2015) 92–103. <https://doi.org/10.1016/j.nanoen.2015.04.005>.

- [118] Y. Cao, B. Lin, Y. Sun, H. Yang, X. Zhang, Symmetric/Asymmetric Supercapacitor Based on the Perovskite-type Lanthanum Cobaltate Nanofibers with Sr-substitution, *Electrochimica Acta*. 178 (2015) 398–406.
<https://doi.org/10.1016/j.electacta.2015.08.033>.
- [119] B. Huang, S.R. Wang, R.Z. Liu, X.F. Ye, H.W. Nie, X.F. Sun, T.L. Wen, Performance of $\text{La}_{0.75}\text{Sr}_{0.25}\text{Cr}_{0.5}\text{Mn}_{0.5}\text{O}_{3-\delta}$ perovskite-structure anode material at lanthanum gallate electrolyte for IT-SOFC running on ethanol fuel, *Journal of Power Sources*. 167 (2007) 39–46. <https://doi.org/10.1016/j.jpowsour.2007.02.022>.
- [120] J. Liu, E. Sheha, S.I. El-Dek, D. Goonetilleke, M. Harguindeguy, N. Sharma, SmFeO_3 and Bi-doped SmFeO_3 perovskites as an alternative class of electrodes in lithium-ion batteries, *CrystEngComm*. 20 (2018) 6165–6172. <https://doi.org/10.1039/c8ce00780b>.
- [121] F. Lu, T. Xia, Q. Li, J. Wang, L. Huo, H. Zhao, Heterostructured simple perovskite nanorod-decorated double perovskite cathode for solid oxide fuel cells: Highly catalytic activity, stability and CO_2 -durability for oxygen reduction reaction, *Applied Catalysis B: Environmental*. 249 (2019) 19–31.
<https://doi.org/10.1016/j.apcatb.2019.02.056>.
- [122] G. Liu, H. Chen, L. Xia, S. Wang, L.X. Ding, D. Li, K. Xiao, S. Dai, H. Wang, Hierarchical Mesoporous/Macroporous Perovskite $\text{La}_{0.5}\text{Sr}_{0.5}\text{CoO}_{3-x}$ Nanotubes: A Bifunctional Catalyst with Enhanced Activity and Cycle Stability for Rechargeable Lithium Oxygen Batteries, *ACS Applied Materials and Interfaces*. 7 (2015) 22478–22486. <https://doi.org/10.1021/acsami.5b06587>.

- [123] F. Hao, C.C. Stoumpos, D.H. Cao, R.P.H. Chang, M.G. Kanatzidis, Lead-free solid-state organic-inorganic halide perovskite solar cells, *Nature Photonics*. 8 (2014) 489–494. <https://doi.org/10.1038/nphoton.2014.82>.
- [124] W. Sun, H. Wei, L. yang An, C. Jin, H. Wu, Z. ang Xiong, C. Pu, C. Sun, Oxygen vacancy mediated $\text{La}_{1-x}\text{Ce}_x\text{FeO}_{3-\Delta}$ perovskite oxides as efficient catalysts for CWAO of acrylic acid by A-site Ce doping, *Applied Catalysis B: Environmental*. 245 (2019) 20–28. <https://doi.org/10.1016/j.apcatb.2018.12.024>.
- [125] W.J. Mir, M. Jagadeeswararao, S. Das, A. Nag, Colloidal Mn-doped cesium lead halide perovskite nanoplatelets, *ACS Energy Letters*. 2 (2017) 537–543. <https://doi.org/10.1021/acsenergylett.6b00741>.
- [126] C. Zhou, Y. Tian, O. Khabou, M. Worku, Y. Zhou, J. Hurley, H. Lin, B. Ma, Manganese-Doped One-Dimensional Organic Lead Bromide Perovskites with Bright White Emissions, *ACS Applied Materials and Interfaces*. 9 (2017) 40446–40451. <https://doi.org/10.1021/acsami.7b12456>.
- [127] H. Yang, W. Fan, K. Hills-Kimball, O. Chen, L.Q. Wang, Introducing Manganese-Doped Lead Halide Perovskite Quantum Dots: A Simple Synthesis Illustrating Optoelectronic Properties of Semiconductors, *Journal of Chemical Education*. 96 (2019) 2300–2307. <https://doi.org/10.1021/acs.jchemed.8b00735>.
- [128] W.J. Mir, T. Sheikh, H. Arfin, Z. Xia, A. Nag, Lanthanide doping in metal halide perovskite nanocrystals: spectral shifting, quantum cutting and optoelectronic applications, *NPG Asia Materials*. 12 (2020) 9. <https://doi.org/10.1038/s41427-019-0192-0>.

- [129] Z. Xiao, Z. Song, Y. Yan, From Lead Halide Perovskites to Lead-Free Metal Halide Perovskites and Perovskite Derivatives, *Advanced Materials*. 31 (2019) 1803792.
<https://doi.org/10.1002/adma.201803792>.
- [130] F. Li, Z. Xia, Y. Gong, L. Gu, Q. Liu, Optical properties of Mn²⁺ doped cesium lead halide perovskite nanocrystals: Via a cation-anion co-substitution exchange reaction, *Journal of Materials Chemistry C*. 5 (2017) 9281–9287.
<https://doi.org/10.1039/c7tc03575f>.
- [131] J. Zhu, X. Yang, Y. Zhu, Y. Wang, J. Cai, J. Shen, L. Sun, C. Li, Room-Temperature Synthesis of Mn-Doped Cesium Lead Halide Quantum Dots with High Mn Substitution Ratio, *Journal of Physical Chemistry Letters*. 8 (2017) 4167–4171.
<https://doi.org/10.1021/acs.jpcclett.7b01820>.
- [132] F. Lin, F. Li, Z. Lai, Z. Cai, Y. Wang, O.S. Wolfbeis, X. Chen, MnII-Doped Cesium Lead Chloride Perovskite Nanocrystals: Demonstration of Oxygen Sensing Capability Based on Luminescent Dopants and Host-Dopant Energy Transfer, *ACS Applied Materials and Interfaces*. 10 (2018) 23335–23343.
<https://doi.org/10.1021/acsami.8b06329>.
- [133] Y. Li, K.S. Moon, C.P. Wong, Electronics without lead, *Science*. 308 (2005) 1419–1420. <https://doi.org/10.1126/science.1110168>.
- [134] R.A. Goyer, Lead toxicity: Current concerns, *Environmental Health Perspectives*. 100 (1993) 177–187. <https://doi.org/10.1289/ehp.93100177>.
- [135] V.I. Slaveykova, K.J. Wilkinson, Physicochemical aspects of lead bioaccumulation by *Chlorella vulgaris*, *Environmental Science and Technology*. 36 (2002) 969–975.
<https://doi.org/10.1021/es0101577>.

- [136] R. Asadpour, R.V.K. Chavali, M. Ryyan Khan, M.A. Alam, Bifacial Si heterojunction-perovskite organic-inorganic tandem to produce highly efficient ($\eta T^* \sim 33\%$) solar cell, *Applied Physics Letters*. 106 (2015) 243902. <https://doi.org/10.1063/1.4922375>.
- [137] L. Whitzling, M. Wander, E. Phillips, Testing and educating on urban soil lead: A case of Chicago community gardens, *Journal of Agriculture, Food Systems, and Community Development*. 1(2010) 167–185.
<https://doi.org/10.5304/jafscd.2010.012.015>.
- [138] F.R. Stoddard, A.D. Brooks, B.A. Eskin, G.J. Johannes, Iodine alters gene expression in the MCF7 breast cancer cell line: Evidence for an anti-estrogen effect of iodine, *International Journal of Medical Sciences*. 5 (2008) 189–196.
<https://doi.org/10.7150/ijms.5.189>.
- [139] T.T. Sherer, K.D. Thrall, R.J. Bull, Comparison of toxicity induced by iodine and iodide in male and female rats, *Journal of Toxicology and Environmental Health*. 32 (1991) 89–101. <https://doi.org/10.1080/15287399109531467>.
- [140] M. Mayer, G. Schaaf, I. Mouro, C. Lopez, Y. Colin, P. Neumann, J.P. Cartron, U. Ludewig, Different transport mechanisms in plant and human AMT/Rh-type ammonium transporters, *Journal of General Physiology*. 127 (2006) 133–144.
<https://doi.org/10.1085/jgp.200509369>.
- [141] H. Needleman, Lead poisoning, *Annual Review of Medicine*. 55 (2004) 209–222.
<https://doi.org/10.1146/annurev.med.55.091902.103653>.
- [142] D. Cortecchia, H.A. Dewi, J. Yin, A. Bruno, S. Chen, T. Baikie, P.P. Boix, M. Grätzel, S. Mhaisalkar, C. Soci, N. Mathews, Lead-Free $MA_2CuCl_xBr_{4-x}$ Hybrid Perovskites, *Inorganic Chemistry*. 55 (2016) 1044–1052.

<https://doi.org/10.1021/acs.inorgchem.5b01896>.

- [143] T. Yokoyama, T. Bin Song, D.H. Cao, C.C. Stoumpos, S. Aramaki, M.G. Kanatzidis, The Origin of Lower Hole Carrier Concentration in Methylammonium Tin Halide Films Grown by a Vapor-Assisted Solution Process, *ACS Energy Letters*. 2 (2017) 22–28. <https://doi.org/10.1021/acsenergylett.6b00513>.
- [144] C.M. Tsai, H.P. Wu, S.T. Chang, C.F. Huang, C.H. Wang, S. Narra, Y.W. Yang, C.L. Wang, C.H. Hung, E.W.G. Diau, Role of Tin Chloride in Tin-Rich Mixed-Halide Perovskites Applied as Mesoscopic Solar Cells with a Carbon Counter Electrode, *ACS Energy Letters*. 1 (2016) 1086–1093. <https://doi.org/10.1021/acsenergylett.6b00514>.
- [145] A. Wang, X. Yan, M. Zhang, S. Sun, M. Yang, W. Shen, X. Pan, P. Wang, Z. Deng, Controlled synthesis of lead-free and stable perovskite derivative Cs_2SnI_6 nanocrystals via a facile hot-injection process, *Chemistry of Materials*. 28 (2016) 8132–8140. <https://doi.org/10.1021/acs.chemmater.6b01329>.
- [146] S. Gupta, T. Bendikov, G. Hodes, D. Cahen, CsSnBr_3 , A Lead-Free Halide Perovskite for Long-Term Solar Cell Application: Insights on SnF_2 Addition, *ACS Energy Letters*. 1 (2016) 1028–1033. <https://doi.org/10.1021/acsenergylett.6b00402>.
- [147] W. Zhang, X. Liu, L. Li, Z. Sun, S. Han, Z. Wu, J. Luo, Triiodide-induced band-edge reconstruction of a lead-free perovskite-derivative hybrid for strong light absorption, *Chemistry of Materials*. 30 (2018) 4081–4088. <https://doi.org/10.1021/acs.chemmater.8b01200>.
- [148] T. Yokoyama, D.H. Cao, C.C. Stoumpos, T. Bin Song, Y. Sato, S. Aramaki, M.G. Kanatzidis, Overcoming Short-Circuit in Lead-Free $\text{CH}_3\text{NH}_3\text{SnI}_3$ Perovskite Solar Cells via Kinetically Controlled Gas-Solid Reaction Film Fabrication Process, *Journal*

- of Physical Chemistry Letters. 7 (2016) 776–782.
<https://doi.org/10.1021/acs.jpcllett.6b00118>.
- [149] G. Volonakis, M.R. Filip, A.A. Haghighirad, N. Sakai, B. Wenger, H.J. Snaith, F. Giustino, Lead-Free Halide Double Perovskites via Heterovalent Substitution of Noble Metals, *Journal of Physical Chemistry Letters*. 7 (2016) 1254–1259.
<https://doi.org/10.1021/acs.jpcllett.6b00376>.
- [150] G. Volonakis, A.A. Haghighirad, R.L. Milot, W.H. Sio, M.R. Filip, B. Wenger, M.B. Johnston, L.M. Herz, H.J. Snaith, F. Giustino, Cs₂InAgCl₆: A New Lead-Free Halide Double Perovskite with Direct Band Gap, *Journal of Physical Chemistry Letters*. 8 (2017) 772–778. <https://doi.org/10.1021/acs.jpcllett.6b02682>.
- [151] F. Wei, Z. Deng, S. Sun, F. Zhang, D.M. Evans, G. Kieslich, S. Tominaka, M.A. Carpenter, J. Zhang, P.D. Bristowe, A.K. Cheetham, Synthesis and Properties of a Lead-Free Hybrid Double Perovskite: (CH₃NH₃)₂AgBiBr₆, *Chemistry of Materials*. 29 (2017) 1089–1094. <https://doi.org/10.1021/acs.chemmater.6b03944>.
- [152] H.C. Sansom, G.F.S. Whitehead, M.S. Dyer, M. Zanella, T.D. Manning, M.J. Pitcher, T.J. Whittles, V.R. Dhanak, J. Alaria, J.B. Claridge, M.J. Rosseinsky, AgBiI₄ as a Lead-Free Solar Absorber with Potential Application in Photovoltaics, *Chemistry of Materials*. 29 (2017) 1538–1549. <https://doi.org/10.1021/acs.chemmater.6b04135>.
- [153] T. Umebayashi, K. Asai, T. Umebayashi, K. Asai, T. Kondo, T. Kondo, A. Nakao, Electronic structures of lead iodide based low-dimensional crystals, *Physical Review B - Condensed Matter and Materials Physics*. 67 (2003) 155405.
<https://doi.org/10.1103/PhysRevB.67.155405>.

- [154] C. Yu, Y. Ren, Z. Chen, K. Shum, First-principles study of structural phase transitions in CsSnI₃, *Journal of Applied Physics*. 114 (2013) 163505.
<https://doi.org/10.1063/1.4826068>.
- [155] A.K. Deb, V. Kumar, Ab initio design of CsSn(X_xY_{1-x})₃ (X and y = Cl, Br, and I) perovskites for photovoltaics, *AIP Advances*. 5 (2015) 077158.
<https://doi.org/10.1063/1.4927503>.
- [156] Z. Chen, J.J. Wang, Y. Ren, C. Yu, K. Shum, Schottky solar cells based on CsSnI₃ thin-films, *Applied Physics Letters*. 101 (2012) 093901.
<https://doi.org/10.1063/1.4748888>.
- [157] C.C. Stoumpos, L. Frazer, D.J. Clark, Y.S. Kim, S.H. Rhim, A.J. Freeman, J.B. Ketterson, J.I. Jang, M.G. Kanatzidis, Hybrid germanium iodide perovskite semiconductors: Active lone pairs, structural distortions, direct and indirect energy gaps, and strong nonlinear optical properties, *Journal of the American Chemical Society*. 137 (2015) 6804–6819. <https://doi.org/10.1021/jacs.5b01025>.
- [158] P.P. Sun, Q.S. Li, L.N. Yang, Z.S. Li, Theoretical insights into a potential lead-free hybrid perovskite: Substituting Pb²⁺ with Ge²⁺, *Nanoscale*. 8 (2016) 1503–1512.
<https://doi.org/10.1039/c5nr05337d>.
- [159] W. Ming, H. Shi, M.H. Du, Large dielectric constant, high acceptor density, and deep electron traps in perovskite solar cell material CsGeI₃, *Journal of Materials Chemistry A*. 4 (2016) 13852–13858. <https://doi.org/10.1039/c6ta04685a>.
- [160] T. Krishnamoorthy, H. Ding, C. Yan, W.L. Leong, T. Baikie, Z. Zhang, M. Sherburne, S. Li, M. Asta, N. Mathews, S.G. Mhaisalkar, Lead-free germanium iodide perovskite materials for photovoltaic applications, *Journal of Materials Chemistry A*. 3 (2015)

23829–23832. <https://doi.org/10.1039/c5ta05741h>.

- [161] M.G. Ju, J. Dai, L. Ma, X.C. Zeng, Lead-Free Mixed Tin and Germanium Perovskites for Photovoltaic Application, *Journal of the American Chemical Society*. 139 (2017) 8038–8043. <https://doi.org/10.1021/jacs.7b04219>.
- [162] S. Nagane, D. Ghosh, R.L.Z. Hoye, B. Zhao, S. Ahmad, A.B. Walker, M. Saiful Islam, S. Ogale, A. Sadhanala, Lead-Free Perovskite Semiconductors Based on Germanium-Tin Solid Solutions: Structural and Optoelectronic Properties, *Journal of Physical Chemistry C*. 122 (2018) 5940–5947. <https://doi.org/10.1021/acs.jpcc.8b00480>.
- [163] N. Ito, M.A. Kamarudin, D. Hirotani, Y. Zhang, Q. Shen, Y. Ogomi, S. Iikubo, T. Minemoto, K. Yoshino, S. Hayase, Mixed Sn-Ge Perovskite for Enhanced Perovskite Solar Cell Performance in Air, *Journal of Physical Chemistry Letters*. 9 (2018) 1682–1688. <https://doi.org/10.1021/acs.jpcclett.8b00275>.
- [164] C.H. Ng, K. Nishimura, N. Ito, K. Hamada, D. Hirotani, Z. Wang, F. Yang, S. Iikubo, Q. Shen, K. Yoshino, T. Minemoto, S. Hayase, Role of GeI₂ and SnF₂ additives for SnGe perovskite solar cells, *Nano Energy*. 58 (2019) 130–137. <https://doi.org/10.1016/j.nanoen.2019.01.026>.
- [165] T. Miyasaka, A. Kulkarni, G.M. Kim, S. Öz, A.K. Jena, Perovskite Solar Cells: Can We Go Organic-Free, Lead-Free, and Dopant-Free?, *Advanced Energy Materials*. 10 (2020) 1902500. <https://doi.org/10.1002/aenm.201902500>.
- [166] M. Lyu, J.H. Yun, P. Chen, M. Hao, L. Wang, Addressing Toxicity of Lead: Progress and Applications of Low-Toxic Metal Halide Perovskites and Their Derivatives, *Advanced Energy Materials*. 7 (2017) 1602512. <https://doi.org/10.1002/aenm.201602512>.

- [167] M.B. Johansson, B. Philippe, A. Banerjee, D. Phuyal, S. Mukherjee, S. Chakraborty, M. Cameau, H. Zhu, R. Ahuja, G. Boschloo, H. Rensmo, E.M.J. Johansson, Cesium Bismuth Iodide Solar Cells from Systematic Molar Ratio Variation of CsI and BiI₃, *Inorganic Chemistry*. 58 (2019) 12040–12052.
<https://doi.org/10.1021/acs.inorgchem.9b01233>.
- [168] K. Eckhardt, V. Bon, J. Getzschmann, J. Grothe, F.M. Wisser, S. Kaskel, Crystallographic insights into (CH₃NH₃)₃(Bi₂I₉): A new lead-free hybrid organic-inorganic material as a potential absorber for photovoltaics, *Chemical Communications*. 52 (2016) 3058–3060. <https://doi.org/10.1039/c5cc10455f>.
- [169] B.W. Park, B. Philippe, X. Zhang, H. Rensmo, G. Boschloo, E.M.J. Johansson, Bismuth Based Hybrid Perovskites A₃Bi₂I₉ (A: Methylammonium or Cesium) for Solar Cell Application, *Advanced Materials*. 27 (2015) 6806–6813.
<https://doi.org/10.1002/adma.201501978>.
- [170] S. Öz, J.C. Hebig, E. Jung, T. Singh, A. Lepcha, S. Olthof, F. Jan, Y. Gao, R. German, P.H.M. van Loosdrecht, K. Meerholz, T. Kirchartz, S. Mathur, Zero-dimensional (CH₃NH₃)₃Bi₂I₉ perovskite for optoelectronic applications, *Solar Energy Materials and Solar Cells*. 158 (2016) 195–201. <https://doi.org/10.1016/j.solmat.2016.01.035>.
- [171] M. Vigneshwaran, T. Ohta, S. Iikubo, G. Kapil, T.S. Ripolles, Y. Ogomi, T. Ma, S.S. Pandey, Q. Shen, T. Toyoda, K. Yoshino, T. Minemoto, S. Hayase, Facile synthesis and characterization of sulfur doped low bandgap bismuth based perovskites by soluble precursor route, *Chemistry of Materials*. 28 (2016) 6436–6440.
<https://doi.org/10.1021/acs.chemmater.6b02315>.

- [172] A. Maiti, G. Paul, H. Bhunia, A.J. Pal, Band-edges of bismuth-based ternary halide perovskites ($A_3Bi_2I_9$) through scanning tunneling spectroscopy vis-à-vis impact of defects in limiting the performance of solar cells, *Solar Energy Materials and Solar Cells*. 200 (2019) 109941. <https://doi.org/10.1016/j.solmat.2019.109941>.
- [173] H. Hu, B. Dong, W. Zhang, Low-toxic metal halide perovskites: Opportunities and future challenges, *Journal of Materials Chemistry A*. 5 (2017) 11436–11449. <https://doi.org/10.1039/c7ta00269f>.
- [174] J.C. Hebig, I. Kühn, J. Flohre, T. Kirchartz, Optoelectronic Properties of $(CH_3NH_3)_3Sb_2I_9$ Thin Films for Photovoltaic Applications, *ACS Energy Letters*. 1 (2016) 309–314. <https://doi.org/10.1021/acsenergylett.6b00170>.
- [175] K.M. Boopathi, P. Karuppuswamy, A. Singh, C. Hanmandlu, L. Lin, S.A. Abbas, C.C. Chang, P.C. Wang, G. Li, C.W. Chu, Solution-processable antimony-based light-absorbing materials beyond lead halide perovskites, *Journal of Materials Chemistry A*. 5 (2017) 20843–20850. <https://doi.org/10.1039/c7ta06679a>.
- [176] K. Ahmad, P. Kumar, S.M. Mobin, A Two-Step Modified Sequential Deposition Method-based Pb-Free $(CH_3NH_3)_3Sb_2I_9$ Perovskite with Improved Open Circuit Voltage and Performance, *ChemElectroChem*. 7 (2020) 946–950. <https://doi.org/10.1002/celec.201902107>.
- [177] F. Jiang, D. Yang, Y. Jiang, T. Liu, X. Zhao, Y. Ming, B. Luo, F. Qin, J. Fan, H. Han, L. Zhang, Y. Zhou, Chlorine-Incorporation-Induced Formation of the Layered Phase for Antimony-Based Lead-Free Perovskite Solar Cells, *Journal of the American Chemical Society*. 140 (2018) 1019–1027. <https://doi.org/10.1021/jacs.7b10739>.

- [178] A. Dubey, N. Adhikari, S. Mabrouk, F. Wu, K. Chen, S. Yang, Q. Qiao, A strategic review on processing routes towards highly efficient perovskite solar cells, *Journal of Materials Chemistry A*. 6 (2018) 2406–2431. <https://doi.org/10.1039/c7ta08277k>.
- [179] J.H. Im, H.S. Kim, N.G. Park, Morphology-photovoltaic property correlation in perovskite solar cells: One-step versus two-step deposition of $\text{CH}_3\text{NH}_3\text{PbI}_3$, *APL Materials*. 2 (2014) 081510. <https://doi.org/10.1063/1.4891275>.
- [180] J.H. Heo, D.H. Song, S.H. Im, Planar $\text{CH}_3\text{NH}_3\text{PbBr}_3$ hybrid solar cells with 10.4% power conversion efficiency, fabricated by controlled crystallization in the spin-coating process, *Advanced Materials*. 26 (2014) 8179–8183. <https://doi.org/10.1002/adma.201403140>.
- [181] H.S. Kim, C.R. Lee, J.H. Im, K.B. Lee, T. Moehl, A. Marchioro, S.J. Moon, R. Humphry-Baker, J.H. Yum, J.E. Moser, M. Grätzel, N.G. Park, Lead iodide perovskite sensitized all-solid-state submicron thin film mesoscopic solar cell with efficiency exceeding 9%, *Scientific Reports*. 2 (2012) 591. <https://doi.org/10.1038/srep00591>.
- [182] P.W. Liang, C.Y. Liao, C.C. Chueh, F. Zuo, S.T. Williams, X.K. Xin, J. Lin, A.K.Y. Jen, Additive enhanced crystallization of solution-processed perovskite for highly efficient planar-heterojunction solar cells, *Advanced Materials*. 26 (2014) 3748–3754. <https://doi.org/10.1002/adma.201400231>.
- [183] D.T. Moore, H. Sai, K.W. Tan, D.M. Smilgies, W. Zhang, H.J. Snaith, U. Wiesner, L.A. Estroff, Crystallization kinetics of organic-inorganic trihalide perovskites and the role of the lead anion in crystal growth, *Journal of the American Chemical Society*. 137 (2015) 2350–2358. <https://doi.org/10.1021/ja512117e>.

- [184] J. Burschka, N. Pellet, S.J. Moon, R. Humphry-Baker, P. Gao, M.K. Nazeeruddin, M. Grätzel, Sequential deposition as a route to high-performance perovskite-sensitized solar cells, *Nature*. 499 (2013) 316–319. <https://doi.org/10.1038/nature12340>.
- [185] D.H. Cao, C.C. Stoumpos, C.D. Malliakas, M.J. Katz, O.K. Farha, J.T. Hupp, M.G. Kanatzidis, Remnant PbI₂, an unforeseen necessity in high-efficiency hybrid perovskite-based solar cells?, *APL Materials*. 2 (2014) 091101. <https://doi.org/10.1063/1.4895038>.
- [186] M. Liu, M.B. Johnston, H.J. Snaith, Efficient planar heterojunction perovskite solar cells by vapour deposition, *Nature*. 501 (2013) 395–398. <https://doi.org/10.1038/nature12509>.
- [187] Q. Chen, H. Zhou, Z. Hong, S. Luo, H.S. Duan, H.H. Wang, Y. Liu, G. Li, Y. Yang, Planar heterojunction perovskite solar cells via vapor-assisted solution process, *Journal of the American Chemical Society*. 136 (2014) 622–625. <https://doi.org/10.1021/ja411509g>.
- [188] C.J. Brabec, J.R. Durrant, Solution-processed organic solar cells, *MRS Bulletin*. 33 (2008) 670–675. <https://doi.org/10.1557/mrs2008.138>.
- [189] M. Graetzel, R.A.J. Janssen, D.B. Mitzi, E.H. Sargent, Materials interface engineering for solution-processed photovoltaics, *Nature*. 488 (2012) 304–312. <https://doi.org/10.1038/nature11476>.
- [190] H.C. Liao, P. Guo, C.P. Hsu, M. Lin, B. Wang, L. Zeng, W. Huang, C.M.M. Soe, W.F. Su, M.J. Bedzyk, M.R. Wasielewski, A. Facchetti, R.P.H. Chang, M.G. Kanatzidis, T.J. Marks, Enhanced Efficiency of Hot-Cast Large-Area Planar Perovskite Solar Cells/Modules Having Controlled Chloride Incorporation, *Advanced Energy*

- Materials. 7 (2017) 1601660. <https://doi.org/10.1002/aenm.201601660>.
- [191] W. Nie, H. Tsai, R. Asadpour, J.C. Blancon, A.J. Neukirch, G. Gupta, J.J. Crochet, M. Chhowalla, S. Tretiak, M.A. Alam, H.L. Wang, A.D. Mohite, High-efficiency solution-processed perovskite solar cells with millimeter-scale grains, *Science*. 347 (2015) 522–525. <https://doi.org/10.1126/science.aaa0472>.
- [192] K. Hwang, Y.S. Jung, Y.J. Heo, F.H. Scholes, S.E. Watkins, J. Subbiah, D.J. Jones, D.Y. Kim, D. Vak, Toward large scale roll-to-roll production of fully printed perovskite solar cells, *Advanced Materials*. 27 (2015) 1241–1247. <https://doi.org/10.1002/adma.201404598>.
- [193] D. Vak, K. Hwang, A. Faulks, Y.S. Jung, N. Clark, D.Y. Kim, G.J. Wilson, S.E. Watkins, 3D printer based slot-die coater as a lab-to-fab translation tool for solution-processed solar cells, *Advanced Energy Materials*. 5 (2015) 1401539. <https://doi.org/10.1002/aenm.201401539>.
- [194] R.R. Søndergaard, M. Hösel, F.C. Krebs, Roll-to-Roll fabrication of large area functional organic materials, *Journal of Polymer Science, Part B: Polymer Physics*. 51 (2013) 16–34. <https://doi.org/10.1002/polb.23192>.
- [195] A.T. Barrows, A.J. Pearson, C.K. Kwak, A.D.F. Dunbar, A.R. Buckley, D.G. Lidzey, Efficient planar heterojunction mixed-halide perovskite solar cells deposited via spray-deposition, *Energy and Environmental Science*. 7 (2014) 2944–2950. <https://doi.org/10.1039/c4ee01546k>.
- [196] S. Das, B. Yang, G. Gu, P.C. Joshi, I.N. Ivanov, C.M. Rouleau, T. Aytug, D.B. Geohegan, K. Xiao, High-Performance Flexible Perovskite Solar Cells by Using a Combination of Ultrasonic Spray-Coating and Low Thermal Budget Photonic Curing,

- ACS Photonics. 2 (2015) 680–686. <https://doi.org/10.1021/acsp Photonics.5b00119>.
- [197] Z. Wang, Z. Shi, T. Li, Y. Chen, W. Huang, Stability of Perovskite Solar Cells: A Prospective on the Substitution of the A Cation and X Anion, *Angewandte Chemie - International Edition*. 56 (2017) 1190–1212. <https://doi.org/10.1002/anie.201603694>.
- [198] Z. Wei, H. Chen, K. Yan, S. Yang, Inkjet Printing and Instant Chemical Transformation of a $\text{CH}_3\text{NH}_3\text{PbI}_3$ /Nanocarbon Electrode and Interface for Planar Perovskite Solar Cells , *Angewandte Chemie*. 126 (2014) 13455–13459. <https://doi.org/10.1002/ange.201408638>.
- [199] J.H. Kim, S.T. Williams, N. Cho, C.C. Chueh, A.K.Y. Jen, Enhanced Environmental Stability of Planar Heterojunction Perovskite Solar Cells Based on Blade-Coating, *Advanced Energy Materials*. 5 (2015) 1401229. <https://doi.org/10.1002/aenm.201401229>.
- [200] H.C. Yeh, H.F. Meng, H.W. Lin, T.C. Chao, M.R. Tseng, H.W. Zan, All-small-molecule efficient white organic light-emitting diodes by multi-layer blade coating, *Organic Electronics*. 13 (2012) 914–918. <https://doi.org/10.1016/j.orgel.2012.02.001>.
- [201] C.Y. Chen, H.W. Chang, Y.F. Chang, B.J. Chang, Y.S. Lin, P.S. Jian, H.C. Yeh, H.T. Chien, E.C. Chen, Y.C. Chao, H.F. Meng, H.W. Zan, H.W. Lin, S.F. Horng, Y.J. Cheng, F.W. Yen, I.F. Lin, H.Y. Yang, K.J. Huang, M.R. Tseng, Continuous blade coating for multi-layer large-area organic light-emitting diode and solar cell, *Journal of Applied Physics*. 110 (2011) 094501. <https://doi.org/10.1063/1.3636398>.
- [202] T.M. Schmidt, T.T. Larsen-Olsen, J.E. Carlé, D. Angmo, F.C. Krebs, Upscaling of Perovskite Solar Cells: Fully Ambient Roll Processing of Flexible Perovskite Solar Cells with Printed Back Electrodes, *Advanced Energy Materials*. 5 (2015) 1500569.

<https://doi.org/10.1002/aenm.201500569>.

- [203] Z. Gu, L. Zuo, T.T. Larsen-Olsen, T. Ye, G. Wu, F.C. Krebs, H. Chen, Interfacial engineering of self-assembled monolayer modified semi-roll-to-roll planar heterojunction perovskite solar cells on flexible substrates, *Journal of Materials Chemistry A*. 3 (2015) 24254–24260. <https://doi.org/10.1039/c5ta07008b>.
- [204] S. Kumar, A. Dhar, Accelerated Thermal-Aging-Induced Degradation of Organometal Triiodide Perovskite on ZnO Nanostructures and Its Effect on Hybrid Photovoltaic Devices, *ACS Applied Materials and Interfaces*. 8 (2016) 18309–18320. <https://doi.org/10.1021/acsami.6b06878>.
- [205] O. Haillant, Accelerated weathering testing principles to estimate the service life of organic PV modules, *Solar Energy Materials and Solar Cells*. 95 (2011) 1284–1292. <https://doi.org/10.1016/j.solmat.2010.08.033>.
- [206] B. Conings, J. Drijkoningen, N. Gauquelin, A. Babayigit, J. D’Haen, L. D’Olieslaeger, A. Ethirajan, J. Verbeeck, J. Manca, E. Mosconi, F. De Angelis, H.G. Boyen, Intrinsic Thermal Instability of Methylammonium Lead Trihalide Perovskite, *Advanced Energy Materials*. 5 (2015) 1500477. <https://doi.org/10.1002/aenm.201500477>.
- [207] A.M.A. Leguy, Y. Hu, M. Campoy-Quiles, M.I. Alonso, O.J. Weber, P. Azarhoosh, M. Van Schilfgaarde, M.T. Weller, T. Bein, J. Nelson, P. Docampo, P.R.F. Barnes, Reversible hydration of $\text{CH}_3\text{NH}_3\text{PbI}_3$ in films, single crystals, and solar cells, *Chemistry of Materials*. 27 (2015) 3397–3407. <https://doi.org/10.1021/acs.chemmater.5b00660>.

- [208] Z. Yang, A. Rajagopal, S.B. Jo, C.C. Chueh, S. Williams, C.C. Huang, J.K. Katahara, H.W. Hillhouse, A.K.Y. Jen, Stabilized Wide Bandgap Perovskite Solar Cells by Tin Substitution, *Nano Letters*. 16 (2016) 7739–7747.
<https://doi.org/10.1021/acs.nanolett.6b03857>.
- [209] W. Qiu, T. Merckx, M. Jaysankar, C. Masse De La Huerta, L. Rakocevic, W. Zhang, U.W. Paetzold, R. Gehlhaar, L. Froyen, J. Poortmans, D. Cheyns, H.J. Snaith, P. Heremans, Pinhole-free perovskite films for efficient solar modules, *Energy and Environmental Science*. 9 (2016) 484–489. <https://doi.org/10.1039/c5ee03703d>.
- [210] A. Baumann, K. Tvingstedt, M.C. Heiber, S. V  th, C. Momblona, H.J. Bolink, V. Dyakonov, Persistent photovoltage in methylammonium lead iodide perovskite solar cells, *APL Materials*. 2 (2014) 081501. <https://doi.org/10.1063/1.4885255>.
- [211] M. J  rgensen, K. Norrman, S.A. Gevorgyan, T. Tromholt, B. Andreasen, F.C. Krebs, Stability of polymer solar cells, *Advanced Materials*. 24 (2012) 580–612.
<https://doi.org/10.1002/adma.201104187>.
- [212] R. Peleg, Aalto team finds significant shortcomings in aging tests performed on Perovskite-based solar cells, 07 Feb 2018. (2018). <https://www.perovskite-info.com/aalto-team-finds-significant-shortcomings-aging-tests-performed-perovskite-based-solar-cells>.
- [213] D. Bi, C. Yi, J. Luo, J.D. D  coppet, F. Zhang, S.M. Zakeeruddin, X. Li, A. Hagfeldt, M. Gr  tzel, Polymer-templated nucleation and crystal growth of perovskite films for solar cells with efficiency greater than 21%, *Nature Energy*. 1 (2016) 16142.
<https://doi.org/10.1038/nenergy.2016.142>.

- [214] J. Jean, P.R. Brown, R.L. Jaffe, T. Buonassisi, V. Bulović, Pathways for solar photovoltaics, *Energy and Environmental Science*. 8 (2015) 1200–1219.
<https://doi.org/10.1039/c4ee04073b>.
- [215] F. Haase, C. Hollemann, S. Schäfer, A. Merkle, M. Rienäcker, J. Krügener, R. Brendel, R. Peibst, Laser contact openings for local poly-Si-metal contacts enabling 26.1%-efficient POLO-IBC solar cells, *Solar Energy Materials and Solar Cells*. 186 (2018) 184–193. <https://doi.org/10.1016/j.solmat.2018.06.020>.
- [216] K. Yoshikawa, H. Kawasaki, W. Yoshida, T. Irie, K. Konishi, K. Nakano, T. Uto, D. Adachi, M. Kanematsu, H. Uzu, K. Yamamoto, Silicon heterojunction solar cell with interdigitated back contacts for a photoconversion efficiency over 26%, *Nature Energy*. 2 (2017) 1732. <https://doi.org/10.1038/nenergy.2017.32>.
- [217] C. Battaglia, A. Cuevas, S. De Wolf, High-efficiency crystalline silicon solar cells: Status and perspectives, *Energy and Environmental Science*. 9 (2016) 1552–1576.
<https://doi.org/10.1039/c5ee03380b>.
- [218] K. Peng, Y. Xu, Y. Wu, Y. Yan, S.T. Lee, J. Zhu, Aligned single-crystalline Si nanowire arrays for photovoltaic applications, *Small*. 1 (2005) 1062–1067.
<https://doi.org/10.1002/sml.200500137>.
- [219] S.G. Kumar, K.S.R.K. Rao, Physics and chemistry of CdTe/CdS thin film heterojunction photovoltaic devices: Fundamental and critical aspects, *Energy and Environmental Science*. 7 (2014) 45–102. <https://doi.org/10.1039/c3ee41981a>.
- [220] X. Wu, High-efficiency polycrystalline CdTe thin-film solar cells, *Solar Energy*. 77 (2004) 803–814. <https://doi.org/10.1016/j.solener.2004.06.006>.

- [221] J. Ma, S.H. Wei, Origin of novel diffusions of Cu and Ag in semiconductors: The case of CdTe, *Physical Review Letters*. 110 (2013) 235901.
<https://doi.org/10.1103/PhysRevLett.110.235901>.
- [222] M. Nakamura, K. Yamaguchi, Y. Kimoto, Y. Yasaki, T. Kato, H. Sugimoto, Cd-Free Cu(In,Ga)(Se,S)₂ thin-film solar cell with record efficiency of 23.35%, *IEEE Journal of Photovoltaics*. 9 (2019) 1863–1867.
<https://doi.org/10.1109/JPHOTOV.2019.2937218>.
- [223] J. Ramanujam, U.P. Singh, Copper indium gallium selenide based solar cells - A review, *Energy and Environmental Science*. 10 (2017) 1306–1319.
<https://doi.org/10.1039/c7ee00826k>.
- [224] S. Siebentritt, M. Igalson, C. Persson, S. Lany, The electronic structure of chalcopyrites - Bands, point defects and grain boundaries, *Progress in Photovoltaics: Research and Applications*. 18 (2010) 390–410. <https://doi.org/10.1002/pip.936>.
- [225] B.M. Kayes, H. Nie, R. Twist, S.G. Spruytte, F. Reinhardt, I.C. Kizilyalli, G.S. Higashi, 27.6% Conversion efficiency, a new record for single-junction solar cells under 1 sun illumination, in: *Conference Record of the IEEE Photovoltaic Specialists Conference, IEEE, 2011*: pp. 000004–000008.
<https://doi.org/10.1109/PVSC.2011.6185831>.
- [226] P. Dutta, M. Rathi, D. Khatiwada, S. Sun, Y. Yao, B. Yu, S. Reed, M. Kacharia, J. Martinez, A.P. Litvinchuk, Z. Pasala, S. Pouladi, B. Eslami, J.H. Ryou, H. Ghasemi, P. Ahrenkiel, S. Hubbard, V. Selvamanickam, Flexible GaAs solar cells on roll-to-roll processed epitaxial Ge films on metal foils: A route towards low-cost and high-performance III-V photovoltaics, *Energy and Environmental Science*. 12 (2019) 756–

766. <https://doi.org/10.1039/c8ee02553c>.
- [227] A.J. Ritenour, J.W. Boucher, R. Delancey, A.L. Greenaway, S. Aloni, S.W. Boettcher, Doping and electronic properties of GaAs grown by close-spaced vapor transport from powder sources for scalable III-V photovoltaics, *Energy and Environmental Science*. 8 (2015) 278–285. <https://doi.org/10.1039/c4ee01943a>.
- [228] S.D. Stranks, G.E. Eperon, G. Grancini, C. Menelaou, M.J.P. Alcocer, T. Leijtens, L.M. Herz, A. Petrozza, H.J. Snaith, Electron-hole diffusion lengths exceeding 1 micrometer in an organometal trihalide perovskite absorber, *Science*. 342 (2013) 341–344. <https://doi.org/10.1126/science.1243982>.
- [229] W.J. Yin, J.H. Yang, J. Kang, Y. Yan, S.H. Wei, Halide perovskite materials for solar cells: A theoretical review, *Journal of Materials Chemistry A*. 3 (2015) 8926–8942. <https://doi.org/10.1039/c4ta05033a>.
- [230] H.L. Yip, A.K.Y. Jen, Recent advances in solution-processed interfacial materials for efficient and stable polymer solar cells, *Energy and Environmental Science*. 5 (2012) 5994–6011. <https://doi.org/10.1039/c2ee02806a>.
- [231] Y. Li, Molecular design of photovoltaic materials for polymer solar cells: Toward suitable electronic energy levels and broad absorption, *Accounts of Chemical Research*. 45 (2012) 723–733. <https://doi.org/10.1021/ar2002446>.
- [232] Y. Lin, J. Wang, Z.G. Zhang, H. Bai, Y. Li, D. Zhu, X. Zhan, An electron acceptor challenging fullerenes for efficient polymer solar cells, *Advanced Materials*. 27 (2015) 1170–1174. <https://doi.org/10.1002/adma.201404317>.

- [233] B. O'Regan, M. Grätzel, A low-cost, high-efficiency solar cell based on dye-sensitized colloidal TiO₂ films, *Nature*. 353 (1991) 737–740. <https://doi.org/10.1038/353737a0>.
- [234] Z. Ning, Y. Fu, H. Tian, Improvement of dye-sensitized solar cells: What we know and what we need to know, *Energy and Environmental Science*. 3 (2010) 1170–1181. <https://doi.org/10.1039/c003841e>.
- [235] A. Hagfeldt, G. Boschloo, L. Sun, L. Kloo, H. Pettersson, Dye-sensitized solar cells, *Chemical Reviews*. 110 (2010) 6595–6663. <https://doi.org/10.1021/cr900356p>.
- [236] L. Ye, Y. Xiong, Q. Zhang, S. Li, C. Wang, Z. Jiang, J. Hou, W. You, H. Ade, Surpassing 10% Efficiency Benchmark for Nonfullerene Organic Solar Cells by Scalable Coating in Air from Single Nonhalogenated Solvent, *Advanced Materials*. 30 (2018) 1705485. <https://doi.org/10.1002/adma.201705485>.
- [237] W. Zhao, Y. Zhang, S. Zhang, S. Li, C. He, J. Hou, Vacuum-assisted annealing method for high efficiency printable large-area polymer solar cell modules, *Journal of Materials Chemistry C*. 7 (2019) 3206–3211. <https://doi.org/10.1039/c8tc06513f>.
- [238] A. Kakekhani, R.N. Katti, A.M. Rappe, Water in hybrid perovskites: Bulk MAPbI₃ degradation via super-hydrous state, *APL Materials*. 7 (2019) 041112. <https://doi.org/10.1063/1.5087290>.
- [239] S.K. Wallace, J.M. Frost, A. Walsh, Atomistic insights into the order-disorder transition in Cu₂ZnSnS₄ solar cells from Monte Carlo simulations, *Journal of Materials Chemistry A*. 7 (2019) 312–321. <https://doi.org/10.1039/c8ta04812f>.

- [240] F. Ye, H. Wu, M. Qin, S. Yang, G. Niu, X. Lu, J. Wang, D.B. Mitzi, W.C.H. Choy, High-Quality MAPbBr₃ Cuboid Film with Promising Optoelectronic Properties Prepared by a Hot Methylamine Precursor Approach, *ACS Applied Materials and Interfaces*. 12 (2020) 24498–24504. <https://doi.org/10.1021/acsami.0c04516>.
- [241] S. Delbos, Kesterite thin films for photovoltaics: A review, *EPJ Photovoltaics*. 3 (2012) 12008. <https://doi.org/10.1051/epjpv/2012008>.
- [242] H. Azimi, Y. Hou, C.J. Brabec, Towards low-cost, environmentally friendly printed chalcopyrite and kesterite solar cells, *Energy and Environmental Science*. 7 (2014) 1829–1849. <https://doi.org/10.1039/c3ee43865a>.
- [243] H. Zhou, H.S. Duan, W. Yang, Q. Chen, C.J. Hsu, W.C. Hsu, C.C. Chen, Y. Yang, Facile single-component precursor for Cu₂ZnSnS₄ with enhanced phase and composition controllability, *Energy and Environmental Science*. 7 (2014) 998–1005. <https://doi.org/10.1039/c3ee43101k>.
- [244] H. Zhou, W.C. Hsu, H.S. Duan, B. Bob, W. Yang, T. Bin Song, C.J. Hsu, Y. Yang, CZTS nanocrystals: A promising approach for next generation thin film photovoltaics, *Energy and Environmental Science*. 6 (2013) 2822–2838. <https://doi.org/10.1039/c3ee41627e>.
- [245] K. Woo, Y. Kim, J. Moon, A non-toxic, solution-processed, earth abundant absorbing layer for thin-film solar cells, *Energy and Environmental Science*. 5 (2012) 5340–5345. <https://doi.org/10.1039/c1ee02314d>.
- [246] A. Redinger, D.M. Berg, P.J. Dale, S. Siebentritt, The consequences of kesterite equilibria for efficient solar cells, *Journal of the American Chemical Society*. 133 (2011) 3320–3323. <https://doi.org/10.1021/ja111713g>.

- [247] G. Wang, W. Zhao, Y. Cui, Q. Tian, S. Gao, L. Huang, D. Pan, Fabrication of a $\text{Cu}_2\text{ZnSn}(\text{S},\text{Se})_4$ photovoltaic device by a low-toxicity ethanol solution process, *ACS Applied Materials and Interfaces*. 5 (2013) 10042–10047.
<https://doi.org/10.1021/am402558a>.
- [248] K. Yu, E.A. Carter, Elucidating Structural Disorder and the Effects of Cu Vacancies on the Electronic Properties of $\text{Cu}_2\text{ZnSnS}_4$, *Chemistry of Materials*. 28 (2016) 864–869.
<https://doi.org/10.1021/acs.chemmater.5b04351>.
- [249] J.J. Scragg, T. Ericson, T. Kubart, M. Edoff, C. Platzer-Björkman, Chemical insights into the instability of $\text{Cu}_2\text{ZnSnS}_4$ films during annealing, *Chemistry of Materials*. 23 (2011) 4625–4633. <https://doi.org/10.1021/cm202379s>.
- [250] W. Shockley, W.T. Read, Statistics of the recombinations of holes and electrons, *Physical Review*. 87 (1952) 835–842. <https://doi.org/10.1103/PhysRev.87.835>.
- [251] R.N. Hall, Electron-hole recombination in germanium [21], *Physical Review*. 87 (1952) 387. <https://doi.org/10.1103/PhysRev.87.387>.
- [252] K. Yu, E.A. Carter, A strategy to stabilize kesterite CZTS for high-performance solar cells, *Chemistry of Materials*. 27 (2015) 2920–2927.
<https://doi.org/10.1021/acs.chemmater.5b00172>.
- [253] S. Chen, J.H. Yang, X.G. Gong, A. Walsh, S.H. Wei, Intrinsic point defects and complexes in the quaternary kesterite semiconductor $\text{Cu}_2\text{ZnSnS}_4$, *Physical Review B - Condensed Matter and Materials Physics*. 81 (2010) 245204.
<https://doi.org/10.1103/PhysRevB.81.245204>.

- [254] S. Rühle, Tabulated values of the Shockley-Queisser limit for single junction solar cells, *Solar Energy*. 130 (2016) 139–147.
<https://doi.org/10.1016/j.solener.2016.02.015>.
- [255] W. Shockley, H.J. Queisser, Detailed balance limit of efficiency of p-n junction solar cells, *Journal of Applied Physics*. 32 (1961) 510–519.
<https://doi.org/10.1063/1.1736034>.
- [256] R.B. Wexler, G.S. Gautam, E.A. Carter, Optimizing kesterite solar cells from $\text{Cu}_2\text{ZnSnS}_4$ to $\text{Cu}_2\text{CdGe}(\text{S},\text{Se})_4$, *Journal of Materials Chemistry A*. 9 (2021) 9882–9897. <https://doi.org/10.1039/d0ta11603c>.
- [257] J.J.S. Scragg, L. Choubrac, A. Lafond, T. Ericson, C. Platzer-Björkman, A low-temperature order-disorder transition in $\text{Cu}_2\text{ZnSnS}_4$ thin films, *Applied Physics Letters*. 104 (2014) 041911. <https://doi.org/10.1063/1.4863685>.
- [258] S. Schorr, The crystal structure of kesterite type compounds: A neutron and X-ray diffraction study, *Solar Energy Materials and Solar Cells*. 95 (2011) 1482–1488.
<https://doi.org/10.1016/j.solmat.2011.01.002>.
- [259] B.G. Mendis, M.D. Shannon, M.C. Goodman, J.D. Major, R. Claridge, D.P. Halliday, K. Durose, Direct observation of Cu, Zn cation disorder in $\text{Cu}_2\text{ZnSnS}_4$ solar cell absorber material using aberration corrected scanning transmission electron microscopy, *Progress in Photovoltaics: Research and Applications*. 22 (2014) 24–34.
<https://doi.org/10.1002/pip.2279>.
- [260] D.P. Halliday, R. Claridge, M.C.J. Goodman, B.G. Mendis, K. Durose, J.D. Major, Luminescence of $\text{Cu}_2\text{ZnSnS}_4$ polycrystals described by the fluctuating potential model, *Journal of Applied Physics*. 113 (2013) 223503. <https://doi.org/10.1063/1.4810846>.

- [261] G. Rey, A. Redinger, J. Sendler, T.P. Weiss, M. Thevenin, M. Guennou, B. El Adib, S. Siebentritt, The band gap of $\text{Cu}_2\text{ZnSnSe}_4$: Effect of order-disorder, *Applied Physics Letters*. 105 (2014) 112106. <https://doi.org/10.1063/1.4896315>.
- [262] J.J.S. Scragg, J.K. Larsen, M. Kumar, C. Persson, J. Sendler, S. Siebentritt, C. Platzer Björkman, Cu-Zn disorder and band gap fluctuations in $\text{Cu}_2\text{ZnSn}(\text{S},\text{Se})_4$: Theoretical and experimental investigations, *Physica Status Solidi (B) Basic Research*. 253 (2016) 247–254. <https://doi.org/10.1002/pssb.201552530>.
- [263] S. Chen, A. Walsh, X.G. Gong, S.H. Wei, Classification of lattice defects in the kesterite $\text{Cu}_2\text{ZnSnS}_4$ and $\text{Cu}_2\text{ZnSnSe}_4$ earth-abundant solar cell absorbers, *Advanced Materials*. 25 (2013) 1522–1539. <https://doi.org/10.1002/adma.201203146>.
- [264] K. Yu, E.A. Carter, Determining and Controlling the Stoichiometry of $\text{Cu}_2\text{ZnSnS}_4$ Photovoltaics: The Physics and Its Implications, *Chemistry of Materials*. 28 (2016) 4415–4420. <https://doi.org/10.1021/acs.chemmater.6b01612>.
- [265] S. Chen, L.W. Wang, A. Walsh, X.G. Gong, S.H. Wei, Abundance of $\text{CuZn} + \text{SnZn}$ and $2\text{CuZn} + \text{SnZn}$ defect clusters in kesterite solar cells, *Applied Physics Letters*. 101 (2012) 223901. <https://doi.org/10.1063/1.4768215>.
- [266] Y.S. Yee, B. Magyari-Köpe, Y. Nishi, S.F. Bent, B.M. Clemens, Deep recombination centers in $\text{Cu}_2\text{ZnSnSe}_4$ revealed by screened-exchange hybrid density functional theory, *Physical Review B - Condensed Matter and Materials Physics*. 92 (2015) 195201. <https://doi.org/10.1103/PhysRevB.92.195201>.
- [267] C. Frisk, T. Ericson, S.Y. Li, P. Szaniawski, J. Olsson, C. Platzer-Björkman, Combining strong interface recombination with bandgap narrowing and short diffusion length in $\text{Cu}_2\text{ZnSnS}_4$ device modeling, *Solar Energy Materials and Solar Cells*. 144

- (2016) 364–370. <https://doi.org/10.1016/j.solmat.2015.09.019>.
- [268] M. Courel, J.A. Andrade-Arvizu, O. Vigil-Galán, The role of buffer/kesterite interface recombination and minority carrier lifetime on kesterite thin film solar cells, *Materials Research Express*. 3 (2016) 095501. <https://doi.org/10.1088/2053-1591/3/9/095501>.
- [269] G. Sai Gautam, T.P. Senftle, E.A. Carter, Understanding the Effects of Cd and Ag Doping in $\text{Cu}_2\text{ZnSnS}_4$ Solar Cells, *Chemistry of Materials*. 30 (2018) 4543–4555. <https://doi.org/10.1021/acs.chemmater.8b00677>.
- [270] P. Mangelis, A. Aziz, I. Da Silva, R. Grau-Crespo, P. Vaqueiro, A. V. Powell, Understanding the origin of disorder in kesterite-type chalcogenides A_2ZnBQ_4 (A = Cu, Ag; B = Sn, Ge; Q = S, Se): The influence of inter-layer interactions, *Physical Chemistry Chemical Physics*. 21 (2019) 19311–19317. <https://doi.org/10.1039/c9cp03630j>.
- [271] C. Ma, H. Guo, K. Zhang, N. Yuan, J. Ding, Fabrication of p-type kesterite $\text{Ag}_2\text{ZnSnS}_4$ thin films with a high hole mobility, *Materials Letters*. 186 (2017) 390–393. <https://doi.org/10.1016/j.matlet.2016.10.013>.
- [272] Z. Xu, Z. Guan, J. Yang, Q. Li, Band Positions and Photoelectrochemical Properties of Solution-Processed Silver-Substituted $\text{Cu}_2\text{ZnSnS}_4$ Photocathode, *ACS Applied Energy Materials*. 2 (2019) 2779–2785. <https://doi.org/10.1021/acs.aem.9b00116>.
- [273] V. Cappello, L. Marchetti, P. Parlanti, S. Landi, I. Tonazzini, M. Cecchini, V. Piazza, M. Gemmi, Ultrastructural characterization of the lower motor system in a mouse model of krabbe disease, *Scientific Reports*. 6 (2016) 1. <https://doi.org/10.1038/s41598-016-0001-8>.

- [274] Y. Yang, L. Huang, D. Pan, New Insight of Li-Doped $\text{Cu}_2\text{ZnSn}(\text{S},\text{Se})_4$ Thin Films: Li-Induced Na Diffusion from Soda Lime Glass by a Cation-Exchange Reaction, *ACS Applied Materials and Interfaces*. 9 (2017) 23878–23883.
<https://doi.org/10.1021/acsami.7b07796>.
- [275] H. Xin, S.M. Vorpahl, A.D. Collord, I.L. Braly, A.R. Uhl, B.W. Krueger, D.S. Ginger, H.W. Hillhouse, Lithium-doping inverts the nanoscale electric field at the grain boundaries in $\text{Cu}_2\text{ZnSn}(\text{S},\text{Se})_4$ and increases photovoltaic efficiency, *Physical Chemistry Chemical Physics*. 17 (2015) 23859–23866.
<https://doi.org/10.1039/c5cp04707b>.
- [276] Z. Wang, N. Brodusch, R. Gauvin, G.P. Demopoulos, Lithium-doped $\text{Cu}_2\text{ZnSnS}_4$ superstrate solar cells with 5% efficiency – An alternative to thin film kesterite photovoltaics, *Nano Energy*. 53 (2018) 130–134.
<https://doi.org/10.1016/j.nanoen.2018.08.049>.
- [277] B. Liu, J. Guo, R. Hao, L. Wang, K. Gu, S. Sun, A. Aierken, Effect of Na doping on the performance and the band alignment of CZTS/CdS thin film solar cell, *Solar Energy*. 201 (2020) 219–226. <https://doi.org/10.1016/j.solener.2020.02.088>.
- [278] S. Grini, K. V. Sopiha, N. Ross, X. Liu, T.S. Bjørheim, C. Platzer-Björkman, C. Persson, L. Vines, Strong Interplay between Sodium and Oxygen in Kesterite Absorbers: Complex Formation, Incorporation, and Tailoring Depth Distributions, *Advanced Energy Materials*. 9 (2019) 1900740.
<https://doi.org/10.1002/aenm.201900740>.

- [279] A. Mondal, C. Scheinert, J.G. Radich, Carrier lifetime and charge separation in K⁺-doped CZTS nanocrystals, *ACS Applied Energy Materials*. 2 (2019) 250–259.
<https://doi.org/10.1021/acsaem.8b01168>.
- [280] J. Kim, G.Y. Kim, T.T.T. Nguyen, S. Yoon, Y.K. Kim, S.Y. Lee, M. Kim, D.H. Cho, Y.D. Chung, J.H. Lee, M.J. Seong, W. Jo, Sodium-Assisted passivation of grain boundaries and defects in Cu₂ZnSnSe₄ thin films, *Physical Chemistry Chemical Physics*. 22 (2020) 7597–7605. <https://doi.org/10.1039/c9cp06537g>.
- [281] S. Berman, G. Sai Gautam, E.A. Carter, Role of Na and Ca as Isovalent Dopants in Cu₂ZnSnS₄ Solar Cells, *ACS Sustainable Chemistry and Engineering*. 7 (2019) 5792–5800. <https://doi.org/10.1021/acssuschemeng.8b05348>.
- [282] M. Johnson, S. V. Baryshev, E. Thimsen, M. Manno, X. Zhang, I. V. Veryovkin, C. Leighton, E.S. Aydil, Alkali-metal-enhanced grain growth in Cu₂ZnSnS₄ thin films, *Energy and Environmental Science*. 7 (2014) 1931–1938.
<https://doi.org/10.1039/c3ee44130j>.
- [283] W. Xiao, J.N. Wang, X.S. Zhao, J.W. Wang, G.J. Huang, L. Cheng, L.J. Jiang, L.G. Wang, Intrinsic defects and Na doping in Cu₂ZnSnS₄: A density-functional theory study, *Solar Energy*. 116 (2015) 125–132.
<https://doi.org/10.1016/j.solener.2015.04.005>.
- [284] S. Hadke, S. Levchenko, G. Sai Gautam, C.J. Hages, J.A. Márquez, V. Izquierdo-Roca, E.A. Carter, T. Unold, L.H. Wong, Suppressed Deep Traps and Bandgap Fluctuations in Cu₂CdSnS₄ Solar Cells with ≈8% Efficiency, *Advanced Energy Materials*. 9 (2019) 1902509. <https://doi.org/10.1002/aenm.201902509>.

- [285] R. Chen, C. Persson, Electronic and optical properties of Cu_2XSnS_4 (X = Be, Mg, Ca, Mn, Fe, and Ni) and the impact of native defect pairs, *Journal of Applied Physics*. 121 (2017) 203104 1REVIEW. <https://doi.org/10.1063/1.4984115>.
- [286] L. Weston, C. Stampfl, Machine learning the band gap properties of kesterite $\text{I}_2\text{-II-IV-V}_4$ quaternary compounds for photovoltaics applications, *Physical Review Materials*. 2 (2018) 085407. <https://doi.org/10.1103/PhysRevMaterials.2.085407>.
- [287] A. Karabulut, A. Sarilmaz, F. Ozel, İ. Orak, M.A. Şahinkaya, A novel device fabricated with $\text{Cu}_2\text{NiSnS}_4$ chalcogenide: Morphological and temperature-dependent electrical characterizations, *Current Applied Physics*. 20 (2020) 58–64. <https://doi.org/10.1016/j.cap.2019.10.011>.
- [288] W. Wang, M.T. Winkler, O. Gunawan, T. Gokmen, T.K. Todorov, Y. Zhu, D.B. Mitzi, Device characteristics of CZTSSe thin-film solar cells with 12.6% efficiency, *Advanced Energy Materials*. 4 (2014) 1301465. <https://doi.org/10.1002/aenm.201301465>.
- [289] S. Giraldo, Z. Jehl, M. Placidi, V. Izquierdo-Roca, A. Pérez-Rodríguez, E. Saucedo, Progress and Perspectives of Thin Film Kesterite Photovoltaic Technology: A Critical Review, *Advanced Materials*. 31 (2019) 1806692. <https://doi.org/10.1002/adma.201806692>.
- [290] H. Katagiri, N. Sasaguchi, S. Hando, S. Hoshino, J. Ohashi, T. Yokota, Preparation and evaluation of $\text{Cu}_2\text{ZnSnS}_4$ thin films by sulfurization of E-B evaporated precursors, *Solar Energy Materials and Solar Cells*. 49 (1997) 407–414. [https://doi.org/10.1016/S0927-0248\(97\)00119-0](https://doi.org/10.1016/S0927-0248(97)00119-0).

- [291] J. Márquez, M. Neuschitzer, M. Dimitrievska, R. Gunder, S. Haass, M. Werner, Y.E. Romanyuk, S. Schorr, N.M. Pearsall, I. Forbes, Systematic compositional changes and their influence on lattice and optoelectronic properties of $\text{Cu}_2\text{ZnSnSe}_4$ kesterite solar cells, *Solar Energy Materials and Solar Cells*. 144 (2016) 579–585.
<https://doi.org/10.1016/j.solmat.2015.10.004>.
- [292] F.A. Pulgarín-Agudelo, O. Vigil-Galán, J.A. Andrade-Arvizu, J.R. González-Castillo, E. Rodríguez-González, M. Courel, Y. Sánchez, E. Saucedo, Cu content dependence of $\text{Cu}_2\text{Zn}(\text{SnGe})\text{Se}_4$ solar cells prepared by using sequential thermal evaporation technique of Cu/Sn/Cu/Zn/Ge stacked layers, *Journal of Materials Science: Materials in Electronics*. 29 (2018) 15363–15368. <https://doi.org/10.1007/s10854-018-8915-5>.
- [293] A. Fairbrother, M. Neuschitzer, E. Saucedo, A. Pérez-Rodríguez, Zn-poor $\text{Cu}_2\text{ZnSnSe}_4$ thin films and solar cell devices, *Physica Status Solidi (A) Applications and Materials Science*. 212 (2015) 109–115. <https://doi.org/10.1002/pssa.201431408>.
- [294] A. Fairbrother, M. Dimitrievska, Y. Sánchez, V. Izquierdo-Roca, A. Pérez-Rodríguez, E. Saucedo, Compositional paradigms in multinary compound systems for photovoltaic applications: A case study of kesterites, *Journal of Materials Chemistry A*. 3 (2015) 9451–9455. <https://doi.org/10.1039/c5ta02000j>.
- [295] A. Lafond, L. Choubrac, C. Guillot-Deudon, P. Deniard, S. Jobic, Crystal structures of photovoltaic chalcogenides, an intricate puzzle to solve: The cases of CIGSe and CZTS materials, *Zeitschrift Fur Anorganische Und Allgemeine Chemie*. 638 (2012) 2571–2577. <https://doi.org/10.1002/zaac.201200279>.



- [296] G. Gurieva, R. Ferreira, P. Knoll, S. Schorr, $\text{Cu}_2\text{ZnSnSe}_4$: How Far Does Off-Stoichiometry Go?, *Physica Status Solidi (A) Applications and Materials Science*. 215 (2018) 1700957. <https://doi.org/10.1002/pssa.201700957>.
- [297] G. Gurieva, L.E. Valle Rios, A. Franz, P. Whitfield, S. Schorr, Intrinsic point defects in off-stoichiometric $\text{Cu}_2\text{ZnSnSe}_4$: A neutron diffraction study, *Journal of Applied Physics*. 123 (2018) 161519. <https://doi.org/10.1063/1.4997402>.
- [298] L.E. Valle Rios, K. Neldner, G. Gurieva, S. Schorr, Existence of off-stoichiometric single phase kesterite, *Journal of Alloys and Compounds*. 657 (2016) 408–413. <https://doi.org/10.1016/j.jallcom.2015.09.198>.
- [299] S. Chen, X.G. Gong, A. Walsh, S.H. Wei, Defect physics of the kesterite thin-film solar cell absorber $\text{Cu}_2\text{ZnSnS}_4$, *Applied Physics Letters*. 96 (2010) 021902. <https://doi.org/10.1063/1.3275796>.
- [300] S. Giraldo, E. Saucedo, M. Neuschitzer, F. Oliva, M. Placidi, X. Alcobé, V. Izquierdo-Roca, S. Kim, H. Tampo, H. Shibata, A. Pérez-Rodríguez, P. Pistor, How small amounts of Ge modify the formation pathways and crystallization of kesterites, *Energy and Environmental Science*. 11 (2018) 582–593. <https://doi.org/10.1039/c7ee02318a>.
- [301] A. Hernández-Martínez, M. Placidi, L. Arqués, S. Giraldo, Y. Sánchez, V. Izquierdo-Roca, P. Pistor, M. Valentini, C. Malerba, E. Saucedo, Insights into the Formation Pathways of $\text{Cu}_2\text{ZnSnSe}_4$ Using Rapid Thermal Processes, *ACS Applied Energy Materials*. 1 (2018) 1981–1989. <https://doi.org/10.1021/acsaem.8b00089>.
- [302] M. Dimitrievska, A. Fairbrother, E. Saucedo, A. Pérez-Rodríguez, V. Izquierdo-Roca, Secondary phase and Cu substitutional defect dynamics in kesterite solar cells: Impact on optoelectronic properties, *Solar Energy Materials and Solar Cells*. 149 (2016) 304–

309. <https://doi.org/10.1016/j.solmat.2016.01.029>.
- [303] T. Nishimura, H. Sugiura, K. Nakada, A. Yamada, Characterization of Interface Between Accurately Controlled Cu-Deficient Layer and Cu(In,Ga)Se₂ Absorber for Cu(In,Ga)Se₂ Solar Cells, *Physica Status Solidi - Rapid Research Letters*. 12 (2018) 1800129. <https://doi.org/10.1002/pssr.201800129>.
- [304] S. Giraldo, C.M. Ruiz, M. Espíndola-Rodríguez, Y. Sánchez, M. Placidi, D. Cozza, D. Barakel, L. Escoubas, A. Pérez-Rodríguez, E. Saucedo, Optical and electrical properties of In-doped Cu₂ZnSnSe₄, *Solar Energy Materials and Solar Cells*. 151 (2016) 44–51. <https://doi.org/10.1016/j.solmat.2016.02.024>.
- [305] K. Rawat, P.K. Shishodia, Enhancement of photosensitivity in bismuth doped Cu₂ZnSnS₄ thin films, *Physica Status Solidi - Rapid Research Letters*. 10 (2016) 890–894. <https://doi.org/10.1002/pssr.201600335>.
- [306] Z. Tong, K. Zhang, K. Sun, C. Yan, F. Liu, L. Jiang, Y. Lai, X. Hao, J. Li, Modification of absorber quality and Mo-back contact by a thin Bi intermediate layer for kesterite Cu₂ZnSnS₄ solar cells, *Solar Energy Materials and Solar Cells*. 144 (2016) 537–543. <https://doi.org/10.1016/j.solmat.2015.09.066>.
- [307] A. Carrete, A. Shavel, X. Fontané, J. Montserrat, J. Fan, M. Ibáñez, E. Saucedo, A. Pérez-Rodríguez, A. Cabot, Antimony-based ligand exchange to promote crystallization in spray-deposited Cu₂ZnSnSe₄ solar cells, *Journal of the American Chemical Society*. 135 (2013) 15982–15985. <https://doi.org/10.1021/ja4068639>.
- [308] D. Tiwari, T. Koehler, X. Lin, R. Harniman, I. Griffiths, L. Wang, D. Cherns, R. Klenk, D.J. Fermin, Cu₂ZnSnS₄ Thin Films Generated from a Single Solution Based Precursor: The Effect of Na and Sb Doping, *Chemistry of Materials*. 28 (2016) 4991–

4997. <https://doi.org/10.1021/acs.chemmater.6b01499>.
- [309] K.F. Tai, D. Fu, S.Y. Chiam, C.H.A. Huan, S.K. Batabyal, L.H. Wong, Antimony Doping in Solution-processed $\text{Cu}_2\text{ZnSn}(\text{S},\text{Se})_4$ Solar Cells, *ChemSusChem*. 8 (2015) 3504–3511. <https://doi.org/10.1002/cssc.201500433>.
- [310] D. Tiwari, M. Cattelan, R.L. Harniman, A. Sarua, N. Fox, T. Koehler, R. Klenk, D.J. Fermin, Impact of Sb and Na Doping on the Surface Electronic Landscape of $\text{Cu}_2\text{ZnSnS}_4$ Thin Films, *ACS Energy Letters*. 3 (2018) 2977–2982. <https://doi.org/10.1021/acsenergylett.8b02081>.
- [311] A.D. Collord, H. Xin, H.W. Hillhouse, Combinatorial exploration of the effects of intrinsic and extrinsic defects in $\text{Cu}_2\text{ZnSn}(\text{S},\text{Se})_4$, *IEEE Journal of Photovoltaics*. 5 (2015) 288–298. <https://doi.org/10.1109/JPHOTOV.2014.2361053>.
- [312] S. Giraldo, M. Neuschitzer, T. Thersleff, S. López-Marino, Y. Sánchez, H. Xie, M. Colina, M. Placidi, P. Pistor, V. Izquierdo-Roca, K. Leifer, A. Pérez-Rodríguez, E. Saucedo, Large Efficiency Improvement in $\text{Cu}_2\text{ZnSnSe}_4$ Solar Cells by Introducing a Superficial Ge Nanolayer, *Advanced Energy Materials*. 5 (2015) 1501070. <https://doi.org/10.1002/aenm.201501070>.
- [313] S. Giraldo, M. Neuschitzer, M. Placidi, P. Pistor, A. Perez-Rodriguez, E. Saucedo, $\text{Cu}_2\text{ZnSnSe}_4$ -Based Solar Cells with Efficiency Exceeding 10% by Adding a Superficial Ge Nanolayer: The Interaction between Ge and Na, *IEEE Journal of Photovoltaics*. 6 (2016) 754–759. <https://doi.org/10.1109/JPHOTOV.2016.2535236>.
- [314] S. Lee, K.J. Price, E. Saucedo, S. Giraldo, Improved quantum efficiency models of CZTSe: GE nanolayer solar cells with a linear electric field, *Nanoscale*. 10 (2018) 2990–2997. <https://doi.org/10.1039/c7nr08824h>.

- [315] S. Giraldo, T. Thersleff, G. Larramona, M. Neuschitzer, P. Pistor, K. Leifer, A. Pérez-Rodríguez, C. Moisan, G. Dennler, E. Saucedo, $\text{Cu}_2\text{ZnSnSe}_4$ solar cells with 10.6% efficiency through innovative absorber engineering with Ge superficial nanolayer, *Progress in Photovoltaics: Research and Applications*. 24 (2016) 1359–1367.
<https://doi.org/10.1002/pip.2797>.
- [316] M. Neuschitzer, J. Marquez, S. Giraldo, M. Dimitrievska, M. Placidi, I. Forbes, V. Izquierdo-Roca, A. Pérez-Rodríguez, E. Saucedo, Voc Boosting and Grain Growth Enhancing Ge-Doping Strategy for $\text{Cu}_2\text{ZnSnSe}_4$ Photovoltaic Absorbers, *Journal of Physical Chemistry C*. 120 (2016) 9661–9670.
<https://doi.org/10.1021/acs.jpcc.6b02315>.
- [317] J. Márquez, H. Stange, C.J. Hages, N. Schaefer, S. Levchenko, S. Giraldo, E. Saucedo, K. Schwarzburg, D. Abou-Ras, A. Redinger, M. Klaus, C. Genzel, T. Unold, R. Mainz, Chemistry and Dynamics of Ge in Kesterite: Toward Band-Gap-Graded Absorbers, *Chemistry of Materials*. 29 (2017) 9399–9406.
<https://doi.org/10.1021/acs.chemmater.7b03416>.
- [318] M. Neuschitzer, M.E. Rodriguez, M. Guc, J.A. Marquez, S. Giraldo, I. Forbes, A. Perez-Rodríguez, E. Saucedo, Revealing the beneficial effects of Ge doping on $\text{Cu}_2\text{ZnSnSe}_4$ thin film solar cells, *Journal of Materials Chemistry A*. 6 (2018) 11759–11772. <https://doi.org/10.1039/c8ta02551g>.
- [319] A. Mule, B. Vermang, M. Sylvester, G. Brammertz, S. Ranjbar, T. Schnabel, N. Gampa, M. Meuris, J. Poortmans, Effect of different alkali (Li, Na, K, Rb, Cs) metals on $\text{Cu}_2\text{ZnSnSe}_4$ solar cells, *Thin Solid Films*. 633 (2017) 156–161.
<https://doi.org/10.1016/j.tsf.2016.11.027>.

- [320] S.G. Haass, C. Andres, R. Figi, C. Schreiner, M. Bürki, Y.E. Romanyuk, A.N. Tiwari, Complex Interplay between Absorber Composition and Alkali Doping in High-Efficiency Kesterite Solar Cells, *Advanced Energy Materials*. 8 (2018) 1701760. <https://doi.org/10.1002/aenm.201701760>.
- [321] A. Redinger, K. Hönes, X. Fontañ, V. Izquierdo-Roca, E. Saucedo, N. Valle, A. Pérez-Rodríguez, S. Siebentritt, Detection of a ZnSe secondary phase in coevaporated $\text{Cu}_2\text{ZnSnSe}_4$ thin films, *Applied Physics Letters*. 98 (2011) 101907. <https://doi.org/10.1063/1.3558706>.
- [322] A. Fairbrother, E. García-Hemme, V. Izquierdo-Roca, X. Fontané, F.A. Pulgarín-Agudelo, O. Vigil-Galán, A. Pérez-Rodríguez, E. Saucedo, Development of a selective chemical Etch to improve the conversion efficiency of Zn-rich $\text{Cu}_2\text{ZnSnS}_4$ solar cells, *Journal of the American Chemical Society*. 134 (2012) 8018–8021. <https://doi.org/10.1021/ja301373e>.
- [323] Y. Zhang, J. Han, C. Liao, Investigation of the role of sodium in $\text{Cu}_2\text{ZnSnS}_4$ films and the resulting phase evolution during sulfurization, *CrystEngComm*. 18 (2016) 9026–9032. <https://doi.org/10.1039/c6ce02041k>.
- [324] Z.Y. Zhao, X. Zhao, First-principles study on doping effects of sodium in kesterite $\text{Cu}_2\text{ZnSnS}_4$, *Inorganic Chemistry*. 53 (2014) 9235–9241. <https://doi.org/10.1021/ic5013268>.
- [325] H. Xie, S. López-Marino, T. Olar, Y. Sánchez, M. Neuschitzer, F. Oliva, S. Giraldo, V. Izquierdo-Roca, I. Lauermann, A. Pérez-Rodríguez, E. Saucedo, Impact of Na Dynamics at the $\text{Cu}_2\text{ZnSn}(\text{S},\text{Se})_4/\text{CdS}$ Interface during Post Low Temperature Treatment of Absorbers, *ACS Applied Materials and Interfaces*. 8 (2016) 5017–5024.

<https://doi.org/10.1021/acsami.5b12243>.

- [326] S. López-Marino, Y. Sánchez, M. Espíndola-Rodríguez, X. Alcobé, H. Xie, M. Neuschitzer, I. Becerril, S. Giraldo, M. Dimitrievska, M. Placidi, L. Fourdrinier, V. Izquierdo-Roca, A. Pérez-Rodríguez, E. Saucedo, Alkali doping strategies for flexible and light-weight $\text{Cu}_2\text{ZnSnSe}_4$ solar cells, *Journal of Materials Chemistry A*. 4 (2016) 1895–1907. <https://doi.org/10.1039/c5ta09640e>.
- [327] I. Becerril-Romero, L. Acebo, F. Oliva, V. Izquierdo-Roca, S. López-Marino, M. Espíndola-Rodríguez, M. Neuschitzer, Y. Sánchez, M. Placidi, A. Pérez-Rodríguez, E. Saucedo, P. Pistor, CZTSe solar cells developed on polymer substrates: Effects of low-temperature processing, *Progress in Photovoltaics: Research and Applications*. 26 (2018) 55–68. <https://doi.org/10.1002/pip.2945>.
- [328] I. Becerril-Romero, S. Giraldo, S. López-Marino, M. Placidi, Y. Sánchez, D. Sylla, A. Pérez-Rodríguez, E. Saucedo, P. Pistor, Vitreous enamel as sodium source for efficient kesterite solar cells on commercial ceramic tiles, *Solar Energy Materials and Solar Cells*. 154 (2016) 11–17. <https://doi.org/10.1016/j.solmat.2016.04.035>.
- [329] K.S. Gour, O.P. Singh, A.K. Yadav, R. Parmar, V.N. Singh, Effect of NaF evaporation on morphological and structural properties of $\text{Cu}_2\text{ZnSnSe}_4$ (CZTSe) thin film deposited by sputtering from a single compound target, *Journal of Alloys and Compounds*. 718 (2017) 231–235. <https://doi.org/10.1016/j.jallcom.2017.05.098>.
- [330] T. Abzieher, T. Schnabel, M. Hetterich, M. Powalla, E. Ahlswede, Source and effects of sodium in solution-processed kesterite solar cells, *Physica Status Solidi (A) Applications and Materials Science*. 213 (2016) 1039–1049. <https://doi.org/10.1002/pssa.201532619>.

- [331] S.G. Haass, C. Andres, R. Figi, C. Schreiner, M. Bürki, A.N. Tiwari, Y.E. Romanyuk, Effects of potassium on kesterite solar cells: Similarities, differences and synergies with sodium, *AIP Advances*. 8 (2018) 015133. <https://doi.org/10.1063/1.5013114>.
- [332] Z. Tong, C. Yan, Z. Su, F. Zeng, J. Yang, Y. Li, L. Jiang, Y. Lai, F. Liu, Effects of potassium doping on solution processed kesterite $\text{Cu}_2\text{ZnSnS}_4$ thin film solar cells, *Applied Physics Letters*. 105 (2014) 223903. <https://doi.org/10.1063/1.4903500>.
- [333] S. Hartnauer, L.A. Wägele, E. Jarzembowski, R. Scheer, In-situ XRD study of alloyed $\text{Cu}_2\text{ZnSnSe}_4$ - CuInSe_2 thin films for solar cells, *Thin Solid Films*. 582 (2015) 272–275. <https://doi.org/10.1016/j.tsf.2014.11.061>.
- [334] F. Jiang, Gunawan, T. Harada, Y. Kuang, T. Minegishi, K. Domen, S. Ikeda, Pt/ In_2S_3 / $\text{CdS}/\text{Cu}_2\text{ZnSnS}_4$ Thin Film as an Efficient and Stable Photocathode for Water Reduction under Sunlight Radiation, *Journal of the American Chemical Society*. 137 (2015) 13691–13697. <https://doi.org/10.1021/jacs.5b09015>.
- [335] D.A.R. Barkhouse, R. Haight, N. Sakai, H. Hiroi, H. Sugimoto, D.B. Mitzi, Cd-free buffer layer materials on $\text{Cu}_2\text{ZnSn}(\text{S}_x\text{Se}_{1-x})_4$: Band alignments with ZnO , ZnS , and In_2S_3 , *Applied Physics Letters*. 100 (2012) 193904. <https://doi.org/10.1063/1.4714737>.
- [336] B. Asenjo, C. Guilln, A.M. Chaparro, E. Saucedo, V. Bermudez, D. Lincot, J. Herrero, M.T. Gutierrez, Properties of In_2S_3 thin films deposited onto ITO/glass substrates by chemical bath deposition, *Journal of Physics and Chemistry of Solids*. 71 (2010) 1629–1633. <https://doi.org/10.1016/j.jpcs.2010.09.011>.
- [337] C. Yan, F. Liu, K. Sun, N. Song, J.A. Stride, F. Zhou, X. Hao, M. Green, Boosting the efficiency of pure sulfide CZTS solar cells using the In/Cd-based hybrid buffers, *Solar Energy Materials and Solar Cells*. 144 (2016) 700–706.

<https://doi.org/10.1016/j.solmat.2015.10.019>.

- [338] D. Cherns, I.J. Griffiths, L. Jones, D.M. Bishop, M.A. Lloyd, B.E. McCandless, Direct Observation of High Densities of Antisite Defects in $\text{Ag}_2\text{ZnSnSe}_4$, *ACS Applied Energy Materials*. 1 (2018) 6260–6267. <https://doi.org/10.1021/acsaem.8b01274>.
- [339] C.J. Hages, S. Levenco, C.K. Miskin, J.H. Alsmeier, D. Abou-Ras, R.G. Wilks, M. Bär, T. Unold, R. Agrawal, Improved performance of Ge-alloyed CZTGeSSe thin-film solar cells through control of elemental losses, *Progress in Photovoltaics: Research and Applications*. 23 (2015) 376–384. <https://doi.org/10.1002/pip.2442>.
- [340] T. Thersleff, S. Giraldo, M. Neuschitzer, P. Pistor, E. Saucedo, K. Leifer, Chemically and morphologically distinct grain boundaries in Ge-doped $\text{Cu}_2\text{ZnSnSe}_4$ solar cells revealed with STEM-EELS, *Materials and Design*. 122 (2017) 102–109. <https://doi.org/10.1016/j.matdes.2017.02.077>.
- [341] Z.K. Yuan, S. Chen, Y. Xie, J.S. Park, H. Xiang, X.G. Gong, S.H. Wei, Na-Diffusion Enhanced p-type Conductivity in $\text{Cu}(\text{In,Ga})\text{Se}_2$: A New Mechanism for Efficient Doping in Semiconductors, *Advanced Energy Materials*. 6 (2016) 1601191. <https://doi.org/10.1002/aenm.201601191>.
- [342] Y.S. Lee, T. Gershon, O. Gunawan, T.K. Todorov, T. Gokmen, Y. Virgus, S. Guha, $\text{Cu}_2\text{ZnSnSe}_4$ thin-film solar cells by thermal co-evaporation with 11.6% efficiency and improved minority carrier diffusion length, *Advanced Energy Materials*. 5 (2015) 1401372. <https://doi.org/10.1002/aenm.201401372>.
- [343] H. Tampo, K.M. Kim, S. Kim, H. Shibata, S. Niki, Improvement of minority carrier lifetime and conversion efficiency by Na incorporation in $\text{Cu}_2\text{ZnSnSe}_4$ solar cells, *Journal of Applied Physics*. 122 (2017) 023106. <https://doi.org/10.1063/1.4993288>.

- [344] G. Altamura, M. Wang, K.L. Choy, Influence of alkali metals (Na, Li, Rb) on the performance of electrostatic spray-assisted vapor deposited $\text{Cu}_2\text{ZnSn}(\text{S,Se})_4$ solar cells, *Scientific Reports*. 6 (2016) 22109. <https://doi.org/10.1038/srep22109>.
- [345] S. Sahayaraj, G. Brammertz, B. Vermang, A. Mule, T. Schnabel, M. Meuris, J. Vleugels, J. Poortmans, Doping of $\text{Cu}_2\text{ZnSnSe}_4$ solar cells with Na^+ or K^+ alkali ions, *Journal of Materials Chemistry A*. 6 (2018) 2653–2663. <https://doi.org/10.1039/c7ta05415g>.
- [346] K. Sun, F. Liu, J. Huang, C. Yan, N. Song, H. Sun, C. Xue, Y. Zhang, A. Pu, Y. Shen, J.A. Stride, M. Green, X. Hao, Flexible kesterite $\text{Cu}_2\text{ZnSnS}_4$ solar cells with sodium-doped molybdenum back contacts on stainless steel substrates, *Solar Energy Materials and Solar Cells*. 182 (2018) 14–20. <https://doi.org/10.1016/j.solmat.2018.02.036>.
- [347] Y.T. Hsieh, Q. Han, C. Jiang, T. Bin Song, H. Chen, L. Meng, H. Zhou, Y. Yang, Efficiency Enhancement of $\text{Cu}_2\text{ZnSn}(\text{S,Se})_4$ Solar Cells via Alkali Metals Doping, *Advanced Energy Materials*. 6 (2016) 1502386. <https://doi.org/10.1002/aenm.201502386>.
- [348] M. Gloeckler, J.R. Sites, Band-gap grading in $\text{Cu}(\text{In,Ga})\text{Se}_2$ solar cells, *Journal of Physics and Chemistry of Solids*. 66 (2005) 1891–1894. <https://doi.org/10.1016/j.jpcs.2005.09.087>.
- [349] P. Jackson, R. Wuerz, D. Hariskos, E. Lotter, W. Witte, M. Powalla, Effects of heavy alkali elements in $\text{Cu}(\text{In,Ga})\text{Se}_2$ solar cells with efficiencies up to 22.6%, *Physica Status Solidi - Rapid Research Letters*. 10 (2016) 583–586. <https://doi.org/10.1002/pssr.201600199>.

- [350] M.T. Winkler, W. Wang, O. Gunawan, H.J. Hovel, T.K. Todorov, D.B. Mitzi, Optical designs that improve the efficiency of $\text{Cu}_2\text{ZnSn}(\text{S},\text{Se})_4$ solar cells, *Energy and Environmental Science*. 7 (2014) 1029–1036. <https://doi.org/10.1039/c3ee42541j>.
- [351] S.H. Wei, S.B. Zhang, A. Zunger, Effects of Ga addition to CuInSe_2 on its electronic, structural, and defect properties, *Applied Physics Letters*. 72 (1998) 3199–3201. <https://doi.org/10.1063/1.121548>.
- [352] A. Walsh, S. Chen, S.H. Wei, X.G. Gong, Kesterite thin-film solar cells: Advances in materials modelling of $\text{Cu}_2\text{ZnSnS}_4$, *Advanced Energy Materials*. 2 (2012) 400–409. <https://doi.org/10.1002/aenm.201100630>.
- [353] A. Chirilă, P. Reinhard, F. Pianezzi, P. Bloesch, A.R. Uhl, C. Fella, L. Kranz, D. Keller, C. Gretener, H. Hagendorfer, D. Jaeger, R. Erni, S. Nishiwaki, S. Buecheler, A.N. Tiwari, Potassium-induced surface modification of $\text{Cu}(\text{In},\text{Ga})\text{Se}_2$ thin films for high-efficiency solar cells, *Nature Materials*. 12 (2013) 1107–1111. <https://doi.org/10.1038/nmat3789>.
- [354] P. Jackson, D. Hariskos, R. Wuerz, O. Kiowski, A. Bauer, T.M. Friedlmeier, M. Powalla, Properties of $\text{Cu}(\text{In},\text{Ga})\text{Se}_2$ solar cells with new record efficiencies up to 21.7%, *Physica Status Solidi - Rapid Research Letters*. 9 (2015) 28–31. <https://doi.org/10.1002/pssr.201409520>.
- [355] M.A. Contreras, K. Ramanathan, J. Abushama, F. Hasoon, D.L. Young, B. Egaas, R. Noufi, Diode characteristics in state-of-the-art $\text{ZnO}/\text{CdS}/\text{Cu}(\text{In}_{1-x}\text{Ga}_x)\text{Se}_2$ solar cells, *Progress in Photovoltaics: Research and Applications*. 13 (2005) 209–216. <https://doi.org/10.1002/pip.626>.

- [356] M. Courel, F.A. Pulgarín-Agudelo, J.A. Andrade-Arvizu, O. Vigil-Galán, Open-circuit voltage enhancement in CdS/Cu₂ZnSnSe₄-based thin film solar cells: A metal-insulator-semiconductor (MIS) performance, *Solar Energy Materials and Solar Cells*. 149 (2016) 204–212. <https://doi.org/10.1016/j.solmat.2016.01.027>.
- [357] O. Gunawan, T.K. Todorov, D.B. Mitzi, Loss mechanisms in hydrazine-processed Cu₂ZnSn(Se,S)₄ solar cells, *Applied Physics Letters*. 97 (2010) 233506. <https://doi.org/10.1063/1.3522884>.
- [358] M. Gloeckler, J.R. Sites, Efficiency limitations for wide-band-gap chalcopyrite solar cells, *Thin Solid Films*. 480–481 (2005) 241–245. <https://doi.org/10.1016/j.tsf.2004.11.018>.
- [359] J. Li, S.Y. Kim, D. Nam, X. Liu, J.H. Kim, H. Cheong, W. Liu, H. Li, Y. Sun, Y. Zhang, Tailoring the defects and carrier density for beyond 10% efficient CZTSe thin film solar cells, *Solar Energy Materials and Solar Cells*. 159 (2017) 447–455. <https://doi.org/10.1016/j.solmat.2016.09.034>.
- [360] B.T. Gershon, Y.S. Lee, R. Mankad, O. Gunawan, T. Gokmen, D. Bishop, B. McCandless, S. Guha, The impact of sodium on the sub-bandgap states in CZTSe and CZTS, *Applied Physics Letters*. 106 (2015) 123905. <https://doi.org/10.1063/1.4916635>.
- [361] C. Platzer-Björkman, C. Frisk, J.K. Larsen, T. Ericson, S.Y. Li, J.J.S. Scragg, J. Keller, F. Larsson, T. Törndahl, Reduced interface recombination in Cu₂ZnSnS₄ solar cells with atomic layer deposition Zn_{1-x}Sn_xO_y buffer layers, *Applied Physics Letters*. 107 (2015) 243904. <https://doi.org/10.1063/1.4937998>.

- [362] S. Chen, A. Walsh, J.H. Yang, X.G. Gong, L. Sun, P.X. Yang, J.H. Chu, S.H. Wei, Compositional dependence of structural and electronic properties of $\text{Cu}_2\text{ZnSn}(\text{S},\text{Se})_4$ alloys for thin film solar cells, *Physical Review B - Condensed Matter and Materials Physics*. 83 (2011) 125201. <https://doi.org/10.1103/PhysRevB.83.125201>.
- [363] J. Li, M. Wei, Q. Du, W. Liu, G. Jiang, C. Zhu, The band alignment at $\text{CdS}/\text{Cu}_2\text{ZnSnSe}_4$ heterojunction interface, *Surface and Interface Analysis*. 45 (2013) 682–684. <https://doi.org/10.1002/sia.5095>.
- [364] S. Tajima, K. Kataoka, N. Takahashi, Y. Kimoto, T. Fukano, M. Hasegawa, H. Hazama, Direct measurement of band offset at the interface between CdS and $\text{Cu}_2\text{ZnSnS}_4$ using hard X-ray photoelectron spectroscopy, *Applied Physics Letters*. 103 (2013) 243906. <https://doi.org/10.1063/1.4850235>.
- [365] R. Haight, A. Barkhouse, O. Gunawan, B. Shin, M. Copel, M. Hopstaken, D.B. Mitzi, Band alignment at the $\text{Cu}_2\text{ZnSn}(\text{S}_x\text{Se}_{1-x})_4/\text{CdS}$ interface, *Applied Physics Letters*. 98 (2011) 253502. <https://doi.org/10.1063/1.3600776>.
- [366] K. Sun, C. Yan, F. Liu, J. Huang, F. Zhou, J.A. Stride, M. Green, X. Hao, Over 9% Efficient Kesterite $\text{Cu}_2\text{ZnSnS}_4$ Solar Cell Fabricated by Using $\text{Zn}_{1-x}\text{Cd}_x\text{S}$ Buffer Layer, *Advanced Energy Materials*. 6 (2016) 1600046. <https://doi.org/10.1002/aenm.201600046>.
- [367] P.M.P. Salomé, J. Keller, T. Törndahl, J.P. Teixeira, N. Nicoara, R.R. Andrade, D.G. Stroppa, J.C. González, M. Edoff, J.P. Leitão, S. Sadewasser, CdS and $\text{Zn}_{1-x}\text{Sn}_x\text{O}_y$ buffer layers for CIGS solar cells, *Solar Energy Materials and Solar Cells*. 159 (2017) 272–281. <https://doi.org/10.1016/j.solmat.2016.09.023>.

- [368] C. Yan, F. Liu, N. Song, B.K. Ng, J.A. Stride, A. Tadich, X. Hao, Band alignments of different buffer layers (CdS, Zn(O,S), and In₂S₃) on Cu₂ZnSnS₄, *Applied Physics Letters*. 104 (2014) 173901. <https://doi.org/10.1063/1.4873715>.
- [369] X. Li, Z. Su, S. Venkataraj, S.K. Batabyal, L.H. Wong, 8.6% Efficiency CZTSSe solar cell with atomic layer deposited Zn-Sn-O buffer layer, *Solar Energy Materials and Solar Cells*. 157 (2016) 101–107. <https://doi.org/10.1016/j.solmat.2016.05.032>.
- [370] K.X. Steirer, R.L. Garris, J. V. Li, M.J. Dzara, P.F. Ndione, K. Ramanathan, I. Repins, G. Teeter, C.L. Perkins, Co-solvent enhanced zinc oxysulfide buffer layers in Kesterite copper zinc tin selenide solar cells, *Physical Chemistry Chemical Physics*. 17 (2015) 15355–15364. <https://doi.org/10.1039/c5cp01607j>.
- [371] J. Li, X. Liu, W. Liu, L. Wu, B. Ge, S. Lin, S. Gao, Z. Zhou, F. Liu, Y. Sun, J. Ao, H. Zhu, Y. Mai, Y. Zhang, Restraining the Band Fluctuation of CBD-Zn(O,S) Layer: Modifying the Hetero-Junction Interface for High Performance Cu₂ZnSnSe₄ Solar Cells With Cd-Free Buffer Layer, *Solar RRL*. 1 (2017) 1700075. <https://doi.org/10.1002/solr.201700075>.
- [372] H.S. Duan, W. Yang, B. Bob, C.J. Hsu, B. Lei, Y. Yang, The role of sulfur in solution-processed Cu₂ZnSn(S,Se)₄ and its effect on defect properties, *Advanced Functional Materials*. 23 (2013) 1466–1471. <https://doi.org/10.1002/adfm.201201732>.
- [373] R. Sun, M. Zhao, D. Zhuang, Q. Gong, L. Guo, L. Ouyang, Y. Wei, High-sulfur Cu₂ZnSn(S,Se)₄ films by sulfurizing as-deposited CZTSe film: The evolutions of phase, crystallinity and S/(S+Se) ratio, *Journal of Alloys and Compounds*. 695 (2017) 3139–3145. <https://doi.org/10.1016/j.jallcom.2016.11.335>.

- [374] M. Dimitrievska, A. Fairbrother, R. Gunder, G. Gurieva, H. Xie, E. Saucedo, A. Pérez-Rodríguez, V. Izquierdo-Roca, S. Schorr, Role of S and Se atoms on the microstructural properties of kesterite $\text{Cu}_2\text{ZnSn}(\text{S}_x\text{Se}_{1-x})_4$ thin film solar cells, *Physical Chemistry Chemical Physics*. 18 (2016) 8692–8700.
<https://doi.org/10.1039/c5cp07577g>.
- [375] A. Redinger, M. Mousel, M.H. Wolter, N. Valle, S. Siebentritt, Influence of S/Se ratio on series resistance and on dominant recombination pathway in $\text{Cu}_2\text{ZnSn}(\text{SSe})_4$ thin film solar cells, *Thin Solid Films*. 535 (2013) 291–295.
<https://doi.org/10.1016/j.tsf.2012.11.111>.
- [376] P.M.P. Salomé, J. Malaquias, P.A. Fernandes, M.S. Ferreira, A.F. Da Cunha, J.P. Leitão, J.C. González, F.M. Martinaga, Growth and characterization of $\text{Cu}_2\text{ZnSn}(\text{S},\text{Se})_4$ thin films for solar cells, *Solar Energy Materials and Solar Cells*. 101 (2012) 147–153.
<https://doi.org/10.1016/j.solmat.2012.02.031>.
- [377] T.K. Todorov, K.B. Reuter, D.B. Mitzi, High-efficiency solar cell with earth-abundant liquid-processed absorber, *Advanced Materials*. 22 (2010) 0904155.
<https://doi.org/10.1002/adma.200904155>.
- [378] S. Chen, X.G. Gong, A. Walsh, S.H. Wei, Electronic structure and stability of quaternary chalcogenide semiconductors derived from cation cross-substitution of II-VI and I-III-VI₂ compounds, *Physical Review B - Condensed Matter and Materials Physics*. 79 (2009) 165211. <https://doi.org/10.1103/PhysRevB.79.165211>.
- [379] G. Altamura, J. Vidal, Impact of Minor Phases on the Performances of CZTSSe Thin-Film Solar Cells, *Chemistry of Materials*. 28 (2016) 3540–3563.
<https://doi.org/10.1021/acs.chemmater.6b00069>.

- [380] S. Chen, X.G. Gong, A. Walsh, S.H. Wei, Crystal and electronic band structure of $\text{Cu}_2\text{ZnSnX}_4$ ($X = \text{S}$ and Se) photovoltaic absorbers: First-principles insights, *Applied Physics Letters*. 94 (2009) 041903. <https://doi.org/10.1063/1.3074499>.
- [381] Z.K. Yuan, S. Chen, H. Xiang, X.G. Gong, A. Walsh, J.S. Park, I. Repins, S.H. Wei, Engineering Solar Cell Absorbers by Exploring the Band Alignment and Defect Disparity: The Case of Cu- and Ag-Based Kesterite Compounds, *Advanced Functional Materials*. 25 (2015) 6733–6743. <https://doi.org/10.1002/adfm.201502272>.
- [382] R. Caballero, I. Victorov, R. Serna, J.M. Cano-Torres, C. Maffiotte, E. Garcia-Llamas, J.M. Merino, M. Valakh, I. Bodnar, M. León, Band-gap engineering of $\text{Cu}_2\text{ZnSn}_{1-x}\text{Ge}_x\text{S}_4$ single crystals and influence of the surface properties, *Acta Materialia*. 79 (2014) 181–187. <https://doi.org/10.1016/j.actamat.2014.06.040>.
- [383] D.B. Khadka, J.H. Kim, Band gap engineering of alloyed $\text{Cu}_2\text{ZnGe}_x\text{Sn}_{1-x}\text{Q}_4$ ($Q = \text{S, Se}$) films for solar cell, *Journal of Physical Chemistry C*. 119 (2015) 1706–1713. <https://doi.org/10.1021/jp510877g>.
- [384] S. Bag, O. Gunawan, T. Gokmen, Y. Zhu, D.B. Mitzi, Hydrazine-processed Ge-substituted CZTSe solar cells, *Chemistry of Materials*. 24 (2012) 4588–4593. <https://doi.org/10.1021/cm302881g>.
- [385] M. Morihama, F. Gao, T. Maeda, T. Wada, Crystallographic and optical properties of $\text{Cu}_2\text{Zn}(\text{Sn}_{1-x}\text{Ge}_x)\text{Se}_4$ solid solution, *Japanese Journal of Applied Physics*. 53 (2014) 4S. <https://doi.org/10.7567/JJAP.53.04ER09>.
- [386] S. Kim, K.M. Kim, H. Tampo, H. Shibata, K. Matsubara, S. Niki, Ge-incorporated $\text{Cu}_2\text{ZnSnSe}_4$ thin-film solar cells with efficiency greater than 10%, *Solar Energy Materials and Solar Cells*. 144 (2016) 488–492.

<https://doi.org/10.1016/j.solmat.2015.09.039>.

- [387] K. Clauwaert, M. Goossens, J. De Wild, D. Colombara, P.J. Dale, K. Binnemans, E. Matthijs, J. Fransaer, Electrodeposition and selenization of brass/tin/germanium multilayers for $\text{Cu}_2\text{Zn}(\text{Sn}_{1-x}\text{Ge}_x)\text{Se}_4$ thin film photovoltaic devices, *Electrochimica Acta*. 198 (2016) 104–114. <https://doi.org/10.1016/j.electacta.2016.03.048>.
- [388] A.D. Collord, H.W. Hillhouse, Germanium Alloyed Kesterite Solar Cells with Low Voltage Deficits, *Chemistry of Materials*. 28 (2016) 2067–2073. <https://doi.org/10.1021/acs.chemmater.5b04806>.
- [389] S. Kim, K.M. Kim, H. Tampo, H. Shibata, S. Niki, Improvement of voltage deficit of Ge-incorporated kesterite solar cell with 12.3% conversion efficiency, *Applied Physics Express*. 9 (2016) 102301. <https://doi.org/10.7567/APEX.9.102301>.
- [390] R. Gunder, J.A. Márquez-Prieto, G. Gurieva, T. Unold, S. Schorr, Structural characterization of off-stoichiometric kesterite-type $\text{Cu}_2\text{ZnGeSe}_4$ compound semiconductors: From cation distribution to intrinsic point defect density, *CrystEngComm*. 20 (2018) 1491–1498. <https://doi.org/10.1039/c7ce02090b>.
- [391] L. Choubrac, G. Brammertz, N. Barreau, L. Arzel, S. Harel, M. Meuris, B. Vermang, 7.6% CZGSe Solar Cells Thanks to Optimized CdS Chemical Bath Deposition, *Physica Status Solidi (A) Applications and Materials Science*. 215 (2018) 1800043. <https://doi.org/10.1002/pssa.201800043>.
- [392] C. Yan, K. Sun, J. Huang, S. Johnston, F. Liu, B.P. Veetil, K. Sun, A. Pu, F. Zhou, J.A. Stride, M.A. Green, X. Hao, Beyond 11% Efficient Sulfide Kesterite $\text{Cu}_2\text{Zn}_x\text{Cd}_{1-x}\text{SnS}_4$ Solar Cell: Effects of Cadmium Alloying, *ACS Energy Letters*. 2 (2017) 930–936. <https://doi.org/10.1021/acsenergylett.7b00129>.

- [393] Z. Su, J.M.R. Tan, X. Li, X. Zeng, S.K. Batabyal, L.H. Wong, Cation Substitution of Solution-Processed $\text{Cu}_2\text{ZnSnS}_4$ Thin Film Solar Cell with over 9% Efficiency, *Advanced Energy Materials*. 5 (2015) 1500682.
<https://doi.org/10.1002/aenm.201500682>.
- [394] Y. Qi, Q. Tian, Y. Meng, D. Kou, Z. Zhou, W. Zhou, S. Wu, Elemental Precursor Solution Processed $(\text{Cu}_{1-x}\text{Ag}_x)_2\text{ZnSn}(\text{S},\text{Se})_4$ Photovoltaic Devices with over 10% Efficiency, *ACS Applied Materials and Interfaces*. 9 (2017) 21243–21250.
<https://doi.org/10.1021/acsami.7b03944>.
- [395] T. Gershon, Y.S. Lee, P. Antunez, R. Mankad, S. Singh, D. Bishop, O. Gunawan, M. Hopstaken, R. Haight, Photovoltaic materials and devices based on the alloyed kesterite absorber $(\text{Ag}_x\text{Cu}_{1-x})_2\text{ZnSnSe}_4$, *Advanced Energy Materials*. 6 (2016) 1502468. <https://doi.org/10.1002/aenm.201502468>.
- [396] S.H. Hadke, S. Levchenko, S. Lie, C.J. Hages, J.A. Márquez, T. Unold, L.H. Wong, Synergistic Effects of Double Cation Substitution in Solution-Processed CZTS Solar Cells with over 10% Efficiency, *Advanced Energy Materials*. 8 (2018) 1802540.
<https://doi.org/10.1002/aenm.201802540>.
- [397] S. Lie, J.M.R. Tan, W. Li, S.W. Leow, Y.F. Tay, D.M. Bishop, O. Gunawan, L.H. Wong, Reducing the interfacial defect density of CZTSSe solar cells by Mn substitution, *Journal of Materials Chemistry A*. 6 (2018) 1540–1550.
<https://doi.org/10.1039/c7ta09668b>.
- [398] R.R. Prabhakar, S. Zhenghua, Z. Xin, T. Baikie, L.S. Woei, S. Shukla, S.K. Batabyal, O. Gunawan, L.H. Wong, Photovoltaic effect in earth abundant solution processed $\text{Cu}_2\text{MnSnS}_4$ and $\text{Cu}_2\text{MnSn}(\text{S},\text{Se})_4$ thin films, *Solar Energy Materials and Solar Cells*.

- 157 (2016) 867–873. <https://doi.org/10.1016/j.solmat.2016.07.006>.
- [399] R. Caballero, S.G. Haass, C. Andres, L. Arques, F. Oliva, V. Izquierdo-Roca, Y.E. Romanyuk, Effect of magnesium incorporation on solution-processed kesterite solar cells, *Frontiers in Chemistry*. 6 (2018) 00005. <https://doi.org/10.3389/fchem.2018.00005>.
- [400] S. Chatterjee, A.J. Pal, A solution approach to p-type $\text{Cu}_2\text{FeSnS}_4$ thin-films and pn-junction solar cells: Role of electron selective materials on their performance, *Solar Energy Materials and Solar Cells*. 160 (2017) 233–240. <https://doi.org/10.1016/j.solmat.2016.10.037>.
- [401] S. Lopez-Marino, M. Espíndola-Rodríguez, Y. Sánchez, X. Alcobé, F. Oliva, H. Xie, M. Neuschitzer, S. Giraldo, M. Placidi, R. Caballero, V. Izquierdo-Roca, A. Pérez-Rodríguez, E. Saucedo, The importance of back contact modification in $\text{Cu}_2\text{ZnSnSe}_4$ solar cells: The role of a thin MoO_2 layer, *Nano Energy*. 26 (2016) 708–721. <https://doi.org/10.1016/j.nanoen.2016.06.034>.
- [402] T. Wada, N. Kohara, S. Nishiwaki, T. Negami, Characterization of the $\text{Cu}(\text{In,Ga})\text{Se}_2/\text{Mo}$ interface in CIGS solar cells, *Thin Solid Films*. 387 (2001) 118–122. [https://doi.org/10.1016/S0040-6090\(00\)01846-0](https://doi.org/10.1016/S0040-6090(00)01846-0).
- [403] T. Ratz, G. Brammertz, R. Caballero, M. León, S. Canulescu, J. Schou, L. Gütay, D. Pareek, T. Taskesen, D.H. Kim, J.K. Kang, C. Malerba, A. Redinger, E. Saucedo, B. Shin, H. Tampo, K. Timmo, N.D. Nguyen, B. Vermang, Physical routes for the synthesis of kesterite, *JPhys Energy*. 1 (2019) 042003. <https://doi.org/10.1088/2515-7655/ab281c>.

CHAPTER 3

Experimental Details

3.1 INTRODUCTION

In this study, two distinct types of photovoltaic materials were explored, namely; NiCuZn hybrid perovskite thin film materials and the inorganic Ge kesterite absorber material: CZGSe. This chapter discusses the experimental details which include; reagents, solution processing's, indium tin oxide (ITO) glass & soda lime glass (SLG) substrate cleaning, thin film deposition technique that was followed to produce hybrid perovskite thin films and the sputtering deposition technique that was followed to prepare the kesterite absorber films. Characterization techniques/instruments that were employed to interrogate the structural, optical, microscopic properties and the photovoltaic parameters of hybrid perovskite thin films and kesterite absorber film materials under investigation are also discussed.

Owing to the continuous development towards the commercialization of perovskite solar cells, the quest for lead-free hybrid perovskite materials has become a cutting edge research topic due to the eco-toxicity posed by elemental Pb in Pb-containing perovskite solar cells generating serious concern towards environmental pollution [1–4]. These environmental concerns inspired the course of this study; doping of the traditional $\text{CH}_3\text{NH}_3\text{PbI}_3$ with transition metals; Ni, Cu & Zn, as a strategy to address this challenge. It has already been mentioned in chapter 2 (literature review) that one of the major shortcomings of hybrid perovskite materials has been the display of instability against moisture, ultra-violet radiation,

oxygen, heat and electrical biases [5–14]. In 2020 – 2021, the main focus of research undertakings on hybrid perovskite layers has been directed towards stabilizing the formamidinium lead iodide (FAPbI₃) perovskite phase with wide-range absorption and improved carrier lifetime to advance the short-circuit current density (J_{SC}) and open-circuit voltage (V_{OC}) of hybrid perovskite solar cells [15,16]. Hybrid perovskites are ionic materials and have a tolerable amount of non-coordinated ions, mainly the I⁻ anions which are able to simply drift into the perovskite grains [17] and out of the perovskite layer and oxidize the metal electrode, subsequently leading to the formation of defects in the perovskite layer and thus speeding up the disintegration of the hybrid perovskite film layer [18]. The formation of these defects easily occur at the surface and grain boundaries of hybrid perovskite thin film and they act as non-radiative recombination cores, decreasing the charge carrier lifetime and consequently diminishing the power conversion efficiency of hybrid perovskite solar cell devices [19]. The defect-formed areas and grain boundaries are vulnerable to eroding moisture (humidity) or oxygen which furthers the decomposition of hybrid perovskite thin film [20,21]. Therefore, these challenges call for the development of low to non-toxic hybrid perovskite thin film materials with outstanding optoelectronic properties, full surface coverage, large grain size and less grain boundaries (for lower bulk defect density and less carrier recombination) to produce stable hybrid perovskite solar cells with high power conversion efficiency. In this study, terephthalic acid (TPA) was used as an additive to produce air stable thin films since hybrid perovskite materials have been reported to deteriorate (degrade/decompose) under ambient conditions (i.e. upon exposure to air (oxygen) and humidity/moisture) [22]. The addition of terephthalic acid additive was inspired by the work reported by X. Hou *et al.* for the construction of efficient and stable perovskites via interconnecting perovskite grains [22]. A solution deposition technique was followed to produce all thin films under investigation which include CH₃NH₃PbI₃ (pristine

hybrid perovskite thin film for comparison purposes) and the novel NiCuZn transition metal doped hybrid perovskite thin films; $\text{CH}_3\text{NH}_3\text{PbI}_3\cdot\text{Ni}$, $\text{CH}_3\text{NH}_3\text{PbI}_3\cdot\text{Cu}$, $\text{CH}_3\text{NH}_3\text{PbI}_3\cdot\text{Zn}$ (doped from 1 to 10% with Ni/Cu/Zn), respectively. There are two types of solution deposition techniques that exist, namely: one step solution deposition technique and two step solution deposition technique. In this study, a two-step solution deposition technique proposed by Burschka *et al.* [23] and later modified by Xiao *et al.* [24] was followed to produce all the hybrid perovskite thin films under investigation. In Xiao *et al.* [24] modified two step solution deposition technique; a layer of PbI_2 was first deposited on the glass substrate by spin coating, which was then followed by an annealing treatment. Instead of immersing the PbI_2 thin film into a $\text{CH}_3\text{NH}_3\text{I}$ solvent, $\text{CH}_3\text{NH}_3\text{I}$ was deposited by spin coating also followed by an annealing treatment and this yielded a good quality hybrid perovskite thin film

For Ge kesterite absorber materials; CZGSe, a sputtering deposition technique was followed to produce absorber materials under investigation; CZGSe. It has already been mentioned in literature review (see chapter 2) that the low open circuit voltage (V_{OC}) is the common constraint restricting the performance in kesterite-based solar cells chiefly when compared to the highest possible V_{OC} value ruled by the Shockley-Queisser radiative limit ($V_{\text{OC,SQ}}$) [25], and this challenge inspired the course of this study; development of Ge kesterite solar cells. A two-step process was employed to produce CZGSe absorber materials under investigation. Two-step processes are extensively employed for the development of kesterite absorber materials. The first part of the process involves a deposition of a precursor film incorporating all (or part of) the chemical elements that constitute the kesterite phase formation. The second part of the process involves the reactive thermal annealing treatment under S (sulfurization) or Se (selenization) enclosing atmosphere, essential to transform the precursor into a kesterite absorber and to advance the grain growth. There are two types of two-step processes that

exist for the synthesis of kesterite absorbers, namely: sequential evaporation/co-evaporation and sequential sputtering/co-sputtering. In this study, a sequential sputtering/co-sputtering two-step process was followed. The developments achieved in these methods demonstrated that the utilization of metallic stacks yield improved power conversion efficiencies at least for selenide compounds, with University of Oldenburg (EHF/LCP group) reporting 11.4% [26], IREC 11.8% [27] and DGIST a 12.6% power conversion efficiency solar cell device [28].

3.2 REAGENTS

Lead (II) iodide (99, 99% trace metals), Dimethyl formamide (DMF) (99,8%), Terephthalic Acid (98%), Methylammonium Iodide (0.42 M in 2-propanol), Nickel (II) Iodide (99.99% trace metal basis), Copper (I) Iodide (99.99% trace metal basis), Zinc (II) Iodide (98%), Indium Tin doped Oxide (ITO) glass substrates (14 Ω /square, 1.1 mm thick). All reagents were obtained from Sigma Aldrich and were used without further purification. ITO glass substrates were obtained from Ossilla.

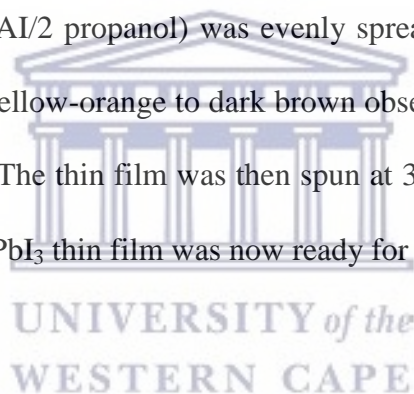
3.3 PROCEDURE FOR HYBRID PEROVSKITE THIN FILMS

3.3.1 Preparation of pure $\text{CH}_3\text{NH}_3\text{PbI}_3$ thin films

Solution Processing: Firstly, a standard solution of terephthalic acid (8 mg/L) was prepared by dissolving terephthalic acid powder (80 mg) in dimethylformamide solvent (10 mL) and the reaction mixture was stirred for 30 minutes at room temperature to attain a homogeneous solution. Secondly, PbI_2 (461 mg) was dissolved in 1mL of terephthalic acid (8 mg/L) solution prepared above. The reaction mixture was then stirred overnight at 70°C to attain a homogeneous yellow-to-orange solution.

ITO glass substrates cleaning: Firstly, the ITO glass substrates (1 cm × 1 cm) were washed with soap for 5 minutes using a sponge and rinsed with distilled water. Secondly, the glass substrates were sonicated for 30 minutes in a solution mixture of acetone and isopropanol in volume ratio of 1:1. Lastly, the substrates were dried by blow-drying with Nitrogen gas and stored in a vacuum desiccator, ready for use.

Two-step solution deposition of CH₃NH₃PbI₃ thin films: Firstly, 60 μL of PbI₂ solution prepared in (I) was deposited (evenly spread) on a clean ITO glass substrate by a micropipette and spin coated at 3000 rpm for 30 s. A yellow-to-orange homogeneous layer was observed. The PbI₂ layer was then annealed at 100°C for 1 hour. Secondly, a 60 μL of methylammonium solution (MAI/2 propanol) was evenly spread on the annealed PbI₂ layer above. A colour change from yellow-orange to dark brown observed indicating the formation of CH₃NH₃PbI₃ nanoparticles. The thin film was then spun at 3000 rpm for 30 s and dried at 70°C for 20 min. The CH₃NH₃PbI₃ thin film was now ready for characterization.



3.3.2 Preparation of Ni doped CH₃NH₃PbI₃•Ni thin films

Solution Processing: A similar procedure followed above for the preparation of CH₃NH₃PbI₃ thin films was also followed for the preparation of Ni doped perovskite CH₃NH₃PbI₃•Ni thin films. Transition metal Ni was introduced into the CH₃NH₃PbI₃ crystal structure by mixing 4.7, 23.5 and 47.1 mg of NiI₂ reagent (for 1%, 5% and 10% Ni content, respectively) together with PbI₂ (461 mg in 8 mg/L terephthalic acid solution) and the reaction mixture was stirred overnight at 70°C. A homogeneous orange-to-yellow solution was also observed for all the reaction mixtures.

Two-step solution deposition of $\text{CH}_3\text{NH}_3\text{PbI}_3\cdot\text{Ni}$ thin films: Firstly, 60 μL of $\text{PbI}_2 + \text{NiI}_2$ homogenous solution prepared above was deposited (evenly spread) on a clean ITO glass substrate by a micropipette and spin coated at 3000 rpm for 30 s. A yellow-to-orange homogeneous layer was observed. The $\text{PbI}_2 + \text{NiI}_2$ layer was then annealed at 100°C for 1 hour. Secondly, a 60 μL of methylammonium solution (MAI/2 propanol) was evenly spread on the annealed $\text{PbI}_2 + \text{NiI}_2$ layer above. A colour change from yellow-orange to dark brown was observed indicating the formation of $\text{CH}_3\text{NH}_3\text{PbI}_3\cdot\text{Ni}$ nanoparticles. The thin film was then spun at 3000 rpm for 30 s and dried at 70°C for 20 min. The $\text{CH}_3\text{NH}_3\text{PbI}_3\cdot\text{Ni}$ thin films were now ready for characterization.

3.3.3 Preparation of Cu doped $\text{CH}_3\text{NH}_3\text{PbI}_3\cdot\text{Cu}$ thin films

Solution Processing: A similar procedure followed above for the preparation of $\text{CH}_3\text{NH}_3\text{PbI}_3$ thin films was also followed for the preparation of Cu doped perovskite $\text{CH}_3\text{NH}_3\text{PbI}_3\cdot\text{Cu}$ thin films. Transition metal Cu was introduced into the $\text{CH}_3\text{NH}_3\text{PbI}_3$ crystal structure by mixing 4.7, 23.5 and 47.1 mg of CuI reagent (for 1%, 5% and 10% Cu content, respectively) together with PbI_2 (461 mg in 8 mg/L terephthalic acid solution) and the reaction mixture was stirred overnight at 70°C . A homogeneous orange-to-yellow solution was also observed for all the reaction mixtures.

Two-step solution deposition of $\text{CH}_3\text{NH}_3\text{PbI}_3\cdot\text{Cu}$ thin films: Firstly, 60 μL of $\text{PbI}_2 + \text{CuI}$ homogenous solution prepared above was deposited (evenly spread) on a clean ITO glass substrate by a micropipette and spin coated at 3000 rpm for 30 s. A yellow-to-orange homogeneous layer was observed. The $\text{PbI}_2 + \text{CuI}$ layer was then annealed at 100°C for 1 hour. Secondly, a 60 μL of methylammonium solution (MAI/2 propanol) was evenly spread on the annealed $\text{PbI}_2 + \text{CuI}$ layer above. A colour change from yellow-orange to dark brown

was observed indicating the formation of $\text{CH}_3\text{NH}_3\text{PbI}_3\cdot\text{Cu}$ nanoparticles. The thin films were then spun at 3000 rpm for 30 s and dried at 70°C for 20 min. The $\text{CH}_3\text{NH}_3\text{PbI}_3\cdot\text{Cu}$ thin films were now ready for characterization.

3.3.4 Preparation of Zn doped $\text{CH}_3\text{NH}_3\text{PbI}_3\cdot\text{Zn}$ thin films

Solution Processing: A similar procedure followed above for the preparation of $\text{CH}_3\text{NH}_3\text{PbI}_3$ thin films was also followed for the preparation of Zn doped perovskite $\text{CH}_3\text{NH}_3\text{PbI}_3\cdot\text{Zn}$ thin films. Transition metal Zn was introduced into the $\text{CH}_3\text{NH}_3\text{PbI}_3$ crystal structure by mixing 4.7, 23.5 and 47.1 mg of ZnI_2 reagent (for 1%, 5% and 10% ZnI_2 content, respectively) together with PbI_2 (461 mg in 8 mg/L terephthalic acid solution) and the reaction mixture was stirred overnight at 70°C . A homogeneous orange-to-yellow solution was also observed for all the reaction mixtures.

Two-step solution deposition of $\text{CH}_3\text{NH}_3\text{PbI}_3\cdot\text{Zn}$ thin films: Firstly, 60 μL of $\text{PbI}_2 + \text{ZnI}_2$ homogenous solution prepared above was deposited (evenly spread) on a clean ITO glass substrate by a micropipette and spin coated at 3000 rpm for 30 s. A yellow-to-orange homogeneous layer was observed. The $\text{PbI}_2 + \text{ZnI}_2$ layer was then annealed at 100°C for 1 hour. Secondly, a 60 μL of methylammonium solution (MAI/2 propanol) was evenly spread on the annealed $\text{PbI}_2 + \text{ZnI}_2$ layer above. A colour change from yellow-orange to dark brown was observed indicating the formation of $\text{CH}_3\text{NH}_3\text{PbI}_3\cdot\text{Zn}$ nanoparticles. The thin films were then spun at 3000 rpm for 30 s and dried at 70°C for 20 min. The $\text{CH}_3\text{NH}_3\text{PbI}_3\cdot\text{Zn}$ thin films were now ready for characterization.

3.3.5 Hybrid perovskite thin films characterization/analyses

Structural Validation and Structural Defects: The X-ray diffraction (XRD) patterns for all the perovskite thin films under investigation were recorded by utilising a Bruker D8-Discover advanced diffractometer using CuK α source operate at accelerating voltage and electrical current of 40 kV and 40 mA, respectively. The measurements were taken at a stepwise of 0.01° and acquisition time of 40 min from 10° to 65° for 2 θ .

Surface Analysis/Chemical Composition Studies: The elemental composition, chemical state and electronic state of elements that exists in perovskite thin film materials under investigation were measured using PHI 5000 Versa Probe II Scanning XPS Microprobe. The XPS surveys were done with 100 μ m, 25 W, and 15 kV x-rays monochromatic beam (source: aluminium K α line of 1486.6 eV energy) positioned perpendicular to the axis of the analyser. The x-ray source was calibrated using the 3d $_{5/2}$ Ag line with 0.8 eV full width at half maximum (FWHM). The area analysed was a circle with a diameter of 0.8 mm. The survey spectra were measured using a resolution of 187.5 eV pass energy (selected resolution) at a stepwise of 0.8 eV. The spectra of different elements were carried out with pass energy of 23.5 eV at a stepwise of 0.1 eV. The depth profiling measurements were collected with 2 kV, 2 μ A, and 1 \times 1 mm raster – Ar ion gun, with sputter rate of about 170 Å/m. All the above mentioned measurements were carried out in an ultra-high vacuum (UHV) chamber pressure at about 5 \times 10 $^{-9}$ torr.

Photo-physics Studies: Absorption measurements of all the perovskite thin film samples were collected using a Perkin Elmer Lamb 950 UV-vis spectrometer. Photoluminescence (PL) excitation and emission measurements of all the perovskite thin films under investigation were conducted at room temperature employing Jobin-Yvon Horiba Fluorolog 3 equipped with He-Cd laser system with an excitation wavelength of 325 nm.

Microscopic Studies: High Resolution (HR-SEM) top view images of all the perovskite thin films under investigation were collected using Hitachi X-650 SEM technique at an accelerating voltage of 25 keV, tilt angle of 0°, aperture of 0.4 mm, resolution of 3, working distance of 10 mm at different magnifications (e.g. 100, 200 nm to 1µm). The surface topography measurements of all perovskite thin films under investigation were collected using a Veeco NanoMan V model (Cambridge, USA) at a resonance frequency of 60 – 100 kHz, spring constant of 1 – 5 M.m⁻¹. A silicon tip was used and the measurements were collected at a room temperature.

3.4 PROCEDURE FOR DEVELOPMENT OF Ge-KESTERITE SOLAR CELLS

The development of CZGSe-based kesterite solar cells explored in this study involves a series of optimization experiments with the goal of attaining high quality Ge kesterite absorber material that yield solar cell devices with optimum photovoltaic performance. The experiments involved (in sequence) (i) stack order and reactive annealing pressure variations, (ii) reactive annealing temperature variations at a constant pressure, (iii) chemical bath etching (CBE) studies with different solutions and lastly (iv) CdS buffer layer optimization studies.

3.4.1 Stack Order and Reactive Annealing Pressure Variations

B.H. Lee *et al.* recently published a study focusing on the effect of Ge nanolayer stacking order on the photovoltaic performance of CZTSSe thin film solar cells and the experimental results indicated that the ideal Ge nanolayer content and the respective ideal position (stack order) has the capability to advance the optoelectronic properties of kesterite CZTSSe

absorber layer which will resultantly attain high power conversion efficiency in kesterite based solar cells [29]. The aim of these experiments was to determine the optimal metal stack order (sequence of metals and germanium deposition) and the optimal reactive annealing profile (optimal pressure) for the synthesis of pure germanium kesterite in the regime $\text{Cu}_{1.8}\text{Zn}_{1.2}\text{GeSe}_4$ at a constant reactive annealing temperature of 480 °C. Three precursors with different stack orders were prepared;

Stack Order A: Mo(\approx 700nm) /Cu(4nm) /Zn(168nm) /Cu(206nm) /Ge(194nm)

Stack Order B: Mo(\approx 700nm) /Zn(162nm) /Cu(199nm) /Ge(196nm)

Stack Order C: Mo(\approx 700nm) /Cu(200nm) /Zn(166nm) /Ge(197nm)

The precursors were subjected to one step annealing profile with Se (100 mg, Alfa-Aesar powder, 99.999%) and GeSe_2 (50 mg, Alfa-Aesar powder, 99.999%) at a heating rate of 20 °C/min, dwelling time of 15 minutes and annealing temperature of 480 °C. The reactive annealing process was carried out at two different pressures; 700 mbar and 1bar pressure. The selenized absorbers; CZGSe, were then subjected to wet-chemical etching/passivation stage in NH_4S (22% v/v, Alfa-Aesar, for 2 min) [30] to remove the ZnSe secondary phases.

3.4.2 Annealing Temperature Variation Studies

The aim of these experiments was to determine the optimal reactive annealing temperature to improve the quality of the CZGSe absorber. The precursor with stack order; Mo(\approx 700nm) /Cu(4nm) /Zn(168nm) /Cu(206nm) /Ge(219nm), was prepared by sequential deposition. For the sake of fair comparisons, the precursor was divided into four pieces (same composition) and subjected to one step reactive annealing process with Se (100 mg, Alfa-Aesar powder, 99.999%) and GeSe_2 (50 mg, Alfa-Aesar powder, 99.999%) at a heating rate of 20 °C/min,

dwelling time of 15 minutes at various annealing temperatures; 500, 525, 535 and 550 °C. All the reactive annealing processes were performed at a constant pressure of 1bar. The selenized absorbers; CZGSe, were then subjected to wet-chemical etching/passivation stage in NH_4S (22% v/v, Alfa-Aesar, for 2 min) [30] to remove the ZnSe secondary phases.

3.4.3 Chemical Bath Etching (CBE) studies with different solutions

The aim of these experiments was to explore different solutions prepared under different conditions as an attempt to completely remove the ZnSe secondary from the surface of the absorber. The same precursor stack order; Mo(\approx 700nm) /Cu(4nm) /Zn(168nm) /Cu(206nm) /Ge(220nm), was prepared during the absorber synthesis and it was subjected to the same annealing treatment following one step annealing profile, at pressure: 1000 mbar, for 15 minutes, at 535 °C using Se(100 mg, Alfa-Aesar powder, 99.999%) and GeSe_2 (50 mg, Alfa-Aesar powder, 99.999%). The selenized absorbers; CZGSe, were then subjected to wet-chemical etching/passivation stage in the following etching solutions as an attempt to completely remove the ZnSe secondary phases:

Cell A: KCN (0.01 M for 40s) + NH_4S (22% v/v, Alfa-Aesar, for 2 min) [31]

Cell B: NH_4S (22% v/v, Alfa-Aesar, for 2 min) [30]

Cell C: HCl (5% at 80°C for 40s) [32]

Cell D: [KMnO_4 (0.01 M) + H_2SO_4 (1M)] for 40 s + NH_4S (22% v/v, Alfa-Aesar, for 2 min) [33]

3.4.4 CdS buffer layer optimization

A specific optimization of the CdS buffer layer for CZGSe absorber appears to be critical for the improvement of the solar cell devices performance since the absorber/CdS heterojunction

characteristics rule the solar cell operation. The aim of these experiments was to adapt the optimal CdS buffer layer parameters employed by Leo Choubrac *et al.* [34] to revamp the power conversion efficiency of the devices fabricated from absorbers etched/passivated following;

Cell A: $(\text{NH}_4)_2\text{S}$ (22% v/v, Alfa-Aesar, for 2 min) [30] and

Cell B: $[\text{KMnO}_4$ (0.1M) + H_2SO_4 (1M)] for 40s + $(\text{NH}_4)_2\text{S}$ (22% v/v, Alfa-Aesar, for 2 min) [33].

The same precursor stack order; Mo(\approx 700nm) /Cu(4nm) /Zn(168nm) /Cu(205nm) /Ge(219nm), was prepared during the absorber synthesis and it was subjected to the same annealing treatment following the same profile, i.e., one step annealing profile, at pressure: 1000 mbar, for 15 minutes, at 535 °C using Se(100 mg, Alfa-Aesar powder, 99.999%) and GeSe_2 (50 mg, Alfa-Aesar powder, 99.999%). For the CdS buffer layer chemical bath deposition (CBD), the following parameters were adapted [34]:

Concentrations of reagents: Ammonia: [1M], Cadmium Acetate: [2.6 mM], Thiourea: [0.1 M]

Chemical bath deposition parameters: Deposition Temperature: $T = 52$ °C, Deposition time $t = 5$ min.

3.4.5 General sample fabrication procedure

This part summarizes the general synthesis route followed to produce all the Ge-kesterite absorber films and the corresponding solar cell devices explored under different optimization parameters as outlined above. The details regarding metal stacks (stack orders and deposited

film thickness), reactive annealing profiles and the wet-chemical bath etching (CBE) solutions are already given in the descriptions of optimization experiments above.

Soda lime glass (SLG) substrate cleaning: Firstly, the SLG glass substrates ($10 \times 10 \text{ cm}^2$) were washed with soap for 10 min using a sponge and rinsed with distilled water. Secondly, the substrates were sequentially sonicated in acetone, isopropanol and deionised water. Each ultrasonic treatment was carried out for 30 min at a temperature of 55°C . The substrates were then dried with an argon flux. Prior to Mo back contact deposition, the substrates were finally submitted to an additional surface treatment employing radiofrequency (RF) plasma (100 W, 2×10^{-2} mbar Ar pressure, room temperature, for 5 min).

CZGSe Absorber Synthesis: Firstly, a Mo back-contact layer ($\approx 700 \text{ nm}$, $0.13 \text{ } \Omega/\text{sq}$) was deposited onto a clean $10 \times 10 \text{ cm}^2$ soda-lime glass (SLG) substrate employing (DC) magnetron sputtering system (Ac450 Alliance Concepts, Annecy, France). Different Ge-kesterite absorber films; CZGSe, with different content compositions were synthesized by a sequential sputtering deposition of constituent elements Cu/Zn/Ge (precursor stack) by direct current (DC) magnetron sputtering technique (Ac450 Alliance Concepts, Annecy, France), as reported elsewhere[35]. The precursor stacks ($2.5 \times 2.5 \text{ cm}^2$) were subsequently selenized following one-step reactive annealing processes described under optimization experiments above in order to obtain CZGSe absorber films. The duration of the entire reactive annealing process (ramp, dwell and cooling) was 3h in all optimization experiments. The reactive annealing processes were carried out in a Se + GeSe₂ environment created by 100 mg of Se (Alfa-Aesar powder, 99.999%) and 50 mg of GeSe₂ (Alfa-Aesar powder, 99.9999%) in a conventional tubular furnace, for all the CZGSe absorber films under investigation. During reactive annealing, the precursor stacks were held in a square shaped graphite box (69 cm^3 in volume) with provision to place Se and GeSe₂ on the sides of the box. The purpose of GeSe₂ was to compensate for the anticipated Ge loss during the reactive annealing process. The

CZGSe absorbers (selenized precursor stacks) were then immersed in different etching solutions (see optimization experiment descriptions) to remove secondary phases, elemental selenium and native oxides from the absorber surface after reactive annealing process.

CdS buffer layer deposition: A standard baseline routine established at Catalonia Institute for Energy Research (IREC) was adopted for CdS buffer layer deposition via chemical bath deposition (CBD) technique [36]. The CBD was carried out in aqueous bath (pH = 9.5) with the chemical concentrations: cadmium acetate [0.12M], and thiourea [0.3M]. During CBD process, the reactants, reactor, and samples (CZGSe absorber films) were held at room temperature whilst the temperature of the thermostatic bath was stabilized at a temperature of 70°C. The process took 5 min to deposit a CdS layer with thickness of 50 ± 8 nm.

Solar Cell Fabrication: To complete CZGSe solar cell devices, a 50 nm thick CdS layer was deposited via chemical bath deposition (CBD) technique followed by DC-pulsed sputtering deposition of i-ZnO (50 nm) and In₂O₃-SnO₂ (ITO, 350 nm, 90/10 wt.%) as transparent conductive window layer employing (Alliance CT100, Grenoble, France) system. Individual cells with an area 3×3 mm² were laterally isolated by mechanical scribing using a manual microdiamond scribe MR200 OEG (OEG Gesellschaft für Optik, Elektronik & Gerätetechnik mbH, Frankfurt, Germany) with a 20 μm line width. Neither antireflective coating nor metallic grids were used for the optoelectronic characterization of the devices.

3.4.6 CZGSe sample characterization/analyses

Physical Analysis: The chemical compositions of precursor stacks (Cu/Zn/Ge) and CZGSe absorbers were determined by a calibrated X-ray fluorescence system XRF (Fischercope XVD, Maharashtra, India). The images for top view (of the absorber films) and cross

sectional morphology (of the solar cell devices) were obtained utilising Scanning Electron Microscope (SEM) ZEISS Series Auriga microscope (New York, U.S.) using 5 kV accelerating voltage. Raman spectra were obtained using a Horiba Jobin Yvon LabRam HR800-UV coupled with an Olympus metallographic microscope. All Raman measurements were carried out in an area of $30 \times 30 \mu\text{m}^2$ in a dual scan mode and the laser spot diameter was about $1 \mu\text{m}$. The power density was kept below 16 kW cm^{-2} in order to avoid the possible thermal effects in the Raman measurements. Si mono-crystal reference was utilized to calibrate the Raman spectra and imposing the Raman shift for the main Si band at 520 cm^{-1} . A number of experiments were performed on the same spot of the samples in order to evaluate the Raman shift and FWHM errors.

Electrical and Optical Analyses: The photovoltaic parameters were measured using a calibrated Sun 3000 class AAA solar simulator (Abet Technologies Inc., Milford, Connecticut, USA; uniform illumination area of $15 \times 15 \text{ cm}^2$), starting from the negative to positive voltage. The measurements were carried out at 25°C under illumination. The intensity of the solar simulator was calibrated to 1 SUN AM 1.5 utilising a Si reference cell prior to measuring the irradiance. External Quantum Efficiency (EQE) measurements were carried out employing a Bentham PVE300 system (Bentham Instruments Ltd, Berkshire, U.K.) calibrated with a Si and Ge photodiode. The system was operated at a voltage of 300 kV.

Bibliography

- [1] T. Wu, X. Liu, X. Luo, X. Lin, D. Cui, Y. Wang, H. Segawa, Y. Zhang, L. Han, Lead-free tin perovskite solar cells, *Joule*. 5 (2021) 863–886.
<https://doi.org/10.1016/j.joule.2021.03.001>.
- [2] K. Nishimura, M.A. Kamarudin, D. Hirotani, K. Hamada, Q. Shen, S. Iikubo, T. Minemoto, K. Yoshino, S. Hayase, Lead-free tin-halide perovskite solar cells with 13% efficiency, *Nano Energy*. 74 (2020) 104858.
<https://doi.org/10.1016/j.nanoen.2020.104858>.
- [3] C. Wang, Y. Zhang, F. Gu, Z. Zhao, H. Li, H. Jiang, Z. Bian, Z. Liu, Illumination Durability and High-Efficiency Sn-Based Perovskite Solar Cell under Coordinated Control of Phenylhydrazine and Halogen Ions, *Matter*. 4 (2021) 709–721.
<https://doi.org/10.1016/j.matt.2020.11.012>.
- [4] X. Li, F. Zhang, H. He, J.J. Berry, K. Zhu, T. Xu, On-device lead sequestration for perovskite solar cells, *Nature*. 578 (2020) 555–558. <https://doi.org/10.1038/s41586-020-2001-x>.
- [5] N. Rajamanickam, S. Kumari, V.K. Vendra, B.W. Lavery, J. Spurgeon, T. Druffel, M.K. Sunkara, Stable and durable $\text{CH}_3\text{NH}_3\text{PbI}_3$ perovskite solar cells at ambient conditions, *Nanotechnology*. 27 (2016) 235404. <https://doi.org/10.1088/0957-4484/27/23/235404>.
- [6] C.G. Wu, C.H. Chiang, Z.L. Tseng, M.K. Nazeeruddin, A. Hagfeldt, M. Grätzel, High efficiency stable inverted perovskite solar cells without current hysteresis, *Energy and Environmental Science*. 8 (2015) 2725–2733. <https://doi.org/10.1039/c5ee00645g>.

- [7] S.N. Habisreutinger, D.P. McMeekin, H.J. Snaith, R.J. Nicholas, Research Update: Strategies for improving the stability of perovskite solar cells, *APL Materials*. 4 (2016) 091503. <https://doi.org/10.1063/1.4961210>.
- [8] T. Leijtens, G.E. Eperon, S. Pathak, A. Abate, M.M. Lee, H.J. Snaith, Overcoming ultraviolet light instability of sensitized TiO₂ with meso-superstructured organometal tri-halide perovskite solar cells, *Nature Communications*. 4 (2013) 3885. <https://doi.org/10.1038/ncomms3885>.
- [9] D. Bryant, N. Aristidou, S. Pont, I. Sanchez-Molina, T. Chotchunangatchaval, S. Wheeler, J.R. Durrant, S.A. Haque, Light and oxygen induced degradation limits the operational stability of methylammonium lead triiodide perovskite solar cells, *Energy and Environmental Science*. 9 (2016) 1655–1660. <https://doi.org/10.1039/c6ee00409a>.
- [10] J.A. Christians, P.A. Miranda Herrera, P. V. Kamat, Transformation of the excited state and photovoltaic efficiency of CH₃NH₃PbI₃ perovskite upon controlled exposure to humidified air, *Journal of the American Chemical Society*. 137 (2015) 1530–1538. <https://doi.org/10.1021/ja511132a>.
- [11] J. Yang, B.D. Siempelkamp, D. Liu, T.L. Kelly, Investigation of CH₃NH₃PbI₃ degradation rates and mechanisms in controlled humidity environments using in situ techniques, *ACS Nano*. 9 (2015) 1955–1963. <https://doi.org/10.1021/nn506864k>.
- [12] B.R. Vincent, K.N. Robertson, T.S. Cameron, O. Knop, Alkylammonium lead halides. Part 1. Isolated PbI₆⁴⁻ ions in (CH₃NH₃)₄PbI₆·2H₂O, *Canadian Journal of Chemistry*. 65 (1987) 1042–1046. <https://doi.org/10.1139/v87-176>.

- [13] A.M.A. Leguy, Y. Hu, M. Campoy-Quiles, M.I. Alonso, O.J. Weber, P. Azarhoosh, M. Van Schilfgaarde, M.T. Weller, T. Bein, J. Nelson, P. Docampo, P.R.F. Barnes, Reversible hydration of $\text{CH}_3\text{NH}_3\text{PbI}_3$ in films, single crystals, and solar cells, *Chemistry of Materials*. 27 (2015) 3397–3407.
<https://doi.org/10.1021/acs.chemmater.5b00660>.
- [14] A. Wakamiya, M. Endo, T. Sasamori, N. Tokitoh, Y. Ogomi, S. Hayase, Y. Murata, Reproducible fabrication of efficient perovskite-based solar cells: X-ray crystallographic studies on the formation of $\text{CH}_3\text{NH}_3\text{PbI}_3$ layers, *Chemistry Letters*. 43 (2014) 711–713. <https://doi.org/10.1246/cl.140074>.
- [15] C. Zhang, Y. Wang, X. Lin, T. Wu, Q. Han, Y. Zhang, L. Han, Effects of A site doping on the crystallization of perovskite films, *Journal of Materials Chemistry A*. 9 (2021) 1372–1394. <https://doi.org/10.1039/d0ta08656h>.
- [16] C. Shen, Y. Wu, S. Zhang, T. Wu, H. Tian, W.H. Zhu, L. Han, Stabilizing Formamidinium Lead Iodide Perovskite by Sulfonyl-Functionalized Phenethylammonium Salt via Crystallization Control and Surface Passivation, *Solar RRL*. 4 (2020) 2000069. <https://doi.org/10.1002/solr.202000069>.
- [17] Y. Zhao, W. Zhou, W. Ma, S. Meng, H. Li, J. Wei, R. Fu, K. Liu, D. Yu, Q. Zhao, Correlations between Immobilizing Ions and Suppressing Hysteresis in Perovskite Solar Cells, *ACS Energy Letters*. 1 (2016) 266–272.
<https://doi.org/10.1021/acsenergylett.6b00060>.
- [18] C. Besleaga, L.E. Abramiuc, V. Stancu, A.G. Tomulescu, M. Sima, L. Trinca, N. Plugaru, L. Pintilie, G.A. Nemnes, M. Iliescu, H.G. Svavarsson, A. Manolescu, I. Pintilie, Iodine Migration and Degradation of Perovskite Solar Cells Enhanced by

- Metallic Electrodes, *Journal of Physical Chemistry Letters*. 7 (2016) 5168–5175.
<https://doi.org/10.1021/acs.jpcllett.6b02375>.
- [19] W. Nie, H. Tsai, R. Asadpour, J.C. Blancon, A.J. Neukirch, G. Gupta, J.J. Crochet, M. Chhowalla, S. Tretiak, M.A. Alam, H.L. Wang, A.D. Mohite, High-efficiency solution-processed perovskite solar cells with millimeter-scale grains, *Science*. 347 (2015) 522–525. <https://doi.org/10.1126/science.aaa0472>.
- [20] D. Li, P. Liao, X. Shai, W. Huang, S. Liu, H. Li, Y. Shen, M. Wang, Recent progress on stability issues of organic-inorganic hybrid lead perovskite-based solar cells, *RSC Advances*. 6 (2016) 89356–89366. <https://doi.org/10.1039/c6ra19801e>.
- [21] J. You, Z. Hong, T. Bin Song, L. Meng, Y. Liu, C. Jiang, H. Zhou, W.H. Chang, G. Li, Y. Yang, Moisture assisted perovskite film growth for high performance solar cells, *Applied Physics Letters*. 105 (2014) 183902. <https://doi.org/10.1063/1.4901510>.
- [22] X. Hou, S. Huang, W. Ou-Yang, L. Pan, Z. Sun, X. Chen, Constructing Efficient and Stable Perovskite Solar Cells via Interconnecting Perovskite Grains, *ACS Applied Materials and Interfaces*. 9 (2017) 35200–35208.
<https://doi.org/10.1021/acsami.7b08488>.
- [23] J. Burschka, N. Pellet, S.J. Moon, R. Humphry-Baker, P. Gao, M.K. Nazeeruddin, M. Grätzel, Sequential deposition as a route to high-performance perovskite-sensitized solar cells, *Nature*. 499 (2013) 316–319. <https://doi.org/10.1038/nature12340>.
- [24] Z. Xiao, C. Bi, Y. Shao, Q. Dong, Q. Wang, Y. Yuan, C. Wang, Y. Gao, J. Huang, Efficient, high yield perovskite photovoltaic devices grown by interdiffusion of solution-processed precursor stacking layers, *Energy and Environmental Science*. 7 (2014) 2619–2623. <https://doi.org/10.1039/c4ee01138d>.

- [25] W. Shockley, H.J. Queisser, Detailed balance limit of efficiency of p-n junction solar cells, *Journal of Applied Physics*. 32 (1961) 510–519.
<https://doi.org/10.1063/1.1736034>.
- [26] T. Taskesen, J. Neerken, J. Schoneberg, D. Pareek, V. Steininger, J. Parisi, L. Gütay, Device Characteristics of an 11.4% CZTSe Solar Cell Fabricated from Sputtered Precursors, *Advanced Energy Materials*. 8 (2018) 03295.
<https://doi.org/10.1002/aenm.201703295>.
- [27] S. Giraldo, E. Saucedo, M. Neuschitzer, F. Oliva, M. Placidi, X. Alcobé, V. Izquierdo-Roca, S. Kim, H. Tampo, H. Shibata, A. Pérez-Rodríguez, P. Pistor, How small amounts of Ge modify the formation pathways and crystallization of kesterites, *Energy and Environmental Science*. 11 (2018) 582–593. <https://doi.org/10.1039/c7ee02318a>.
- [28] M.A. Green, Y. Hishikawa, E.D. Dunlop, D.H. Levi, J. Hohl-Ebinger, M. Yoshita, A.W.Y. Ho-Baillie, Solar cell efficiency tables (Version 53), *Progress in Photovoltaics: Research and Applications*. 27 (2019) 3–12.
<https://doi.org/10.1002/pip.3102>.
- [29] B.H. Lee, K.S. Gour, V. Karade, J.S. Jang, J. Kim, E. Jo, M.G. Gang, D.M. Lee, I.J. Lee, J. Park, J.H. Kim, Effect of Ge nanolayer stacking order on performance of CZTSSe thin film solar cells, *Materials Letters*. 284 (2021) 12891.
<https://doi.org/10.1016/j.matlet.2020.128981>.
- [30] A. Osinsky, Y. Qiu, J. Mahan, H. Temkin, S.A. Gurevich, S.I. Nesterov, E.M. Tanklevskaia, V. Tretyakov, O.A. Lavrova, V.I. Skopina, Novel wet chemical etch for nanostructures based on II-VI compounds, *Applied Physics Letters*. 71 (1997) 509–511. <https://doi.org/10.1063/1.119593>.

- [31] M. Mousel, A. Redinger, R. Djemour, M. Arasimowicz, N. Valle, P. Dale, S. Siebentritt, HCl and Br₂-MeOH etching of Cu₂ZnSnSe₄ polycrystalline absorbers, *Thin Solid Films*. 535 (2013) 83–87. <https://doi.org/10.1016/j.tsf.2012.12.095>.
- [32] A. Fairbrother, E. García-Hemme, V. Izquierdo-Roca, X. Fontané, F.A. Pulgarín-Agudelo, O. Vigil-Galán, A. Pérez-Rodríguez, E. Saucedo, Development of a selective chemical Etch to improve the conversion efficiency of Zn-rich Cu₂ZnSnS₄ solar cells, *Journal of the American Chemical Society*. 134 (2012) 8018–8021. <https://doi.org/10.1021/ja301373e>.
- [33] S. López-Marino, Y. Sánchez, M. Placidi, A. Fairbrother, M. Espindola-Rodríguez, X. Fontané, V. Izquierdo-Roca, J. López-García, L. Calvo-Barrio, A. Pérez-Rodríguez, E. Saucedo, ZnSe etching of Zn-Rich Cu₂ZnSnSe₄: An oxidation route for improved solar-cell efficiency, *Chemistry - A European Journal*. 19 (2013) 14814–14822. <https://doi.org/10.1002/chem.201302589>.
- [34] L. Choubrac, G. Brammertz, N. Barreau, L. Arzel, S. Harel, M. Meuris, B. Vermang, 7.6% CZGSe Solar Cells Thanks to Optimized CdS Chemical Bath Deposition, *Physica Status Solidi (A) Applications and Materials Science*. 215 (2018) 00043. <https://doi.org/10.1002/pssa.201800043>.
- [35] A. Fairbrother, X. Fontané, V. Izquierdo-Roca, M. Placidi, D. Sylla, M. Espindola-Rodríguez, S. López-Mariño, F.A. Pulgarín, O. Vigil-Galán, A. Pérez-Rodríguez, E. Saucedo, Secondary phase formation in Zn-rich Cu₂ZnSnSe₄-based solar cells annealed in low pressure and temperature conditions, *Progress in Photovoltaics: Research and Applications*. 22 (2014) 479–487. <https://doi.org/10.1002/pip.2473>.

- [36] M. Neuschitzer, Y. Sanchez, S. L3pez-Marino, H. Xie, A. Fairbrother, M. Placidi, S. Haass, V. Izquierdo-Roca, A. Perez-Rodriguez, E. Saucedo, Optimization of CdS buffer layer for high-performance $\text{Cu}_2\text{ZnSnSe}_4$ solar cells and the effects of light soaking: Elimination of crossover and red kink, *Progress in Photovoltaics: Research and Applications*. 23 (2015) 1660–1667. <https://doi.org/10.1002/pip.2589>.



CHAPTER 4

Experimental Results and Discussion

4.1 INTRODUCTION

Eco-toxicity posed by metal Pb and the poor stability against humidity remain to be the two most serious challenges hindering the practical industrial application in spite of the remarkable achievements and potentials of hybrid perovskite materials (see chapter 1 and 2). The eco-toxicity of metal Pb stems from the fact that Pb is highly soluble in water and can have harmful effects in the human anatomy and the environment [1–6]. The utilization of heavy and toxic materials (as well as the metal Pb) for application in optoelectronic devices is currently regulated by the European Union and the maximum Pb content in air and water has been agreed to be $0.15 \mu\text{gL}^{-1}$ and $15 \mu\text{gL}^{-1}$, respectively, established by the U.S. EPA [7,8]. Owing to the continuous development towards the commercialization of hybrid perovskite solar cells, the quest for lead-free hybrid perovskite materials has become a cutting edge research topic due to the eco-toxicity posed by elemental Pb in Pb-containing hybrid perovskite; i.e. $\text{CH}_3\text{NH}_3\text{PbI}_3$, solar cells generating serious concern towards environmental pollution [9–12]. Moreover, the poor stability against humidity (oxygen/moisture) [3–5], heat [2], and ultraviolet (UV) electromagnetic radiation [3,6] remains to be another impediment for industrial application of hybrid perovskite based optoelectronic devices. In 2020 – 2021, the main focus of research undertakings on hybrid perovskite layers has been directed towards stabilizing the formamidinium lead iodide (FAPbI₃) perovskite phase [13,14].

Therefore, these challenges call for the development of hybrid perovskite materials with outstanding optoelectronic properties, high eco-stability and low to non-toxicity. The chief aim of this study is to synthesize and characterize new air-stable hybrid perovskite thin film materials incorporating earth abundant and non-toxic transition metals which include Ni, Cu & Zn to address the issue of eco-toxicity posed by metal Pb.

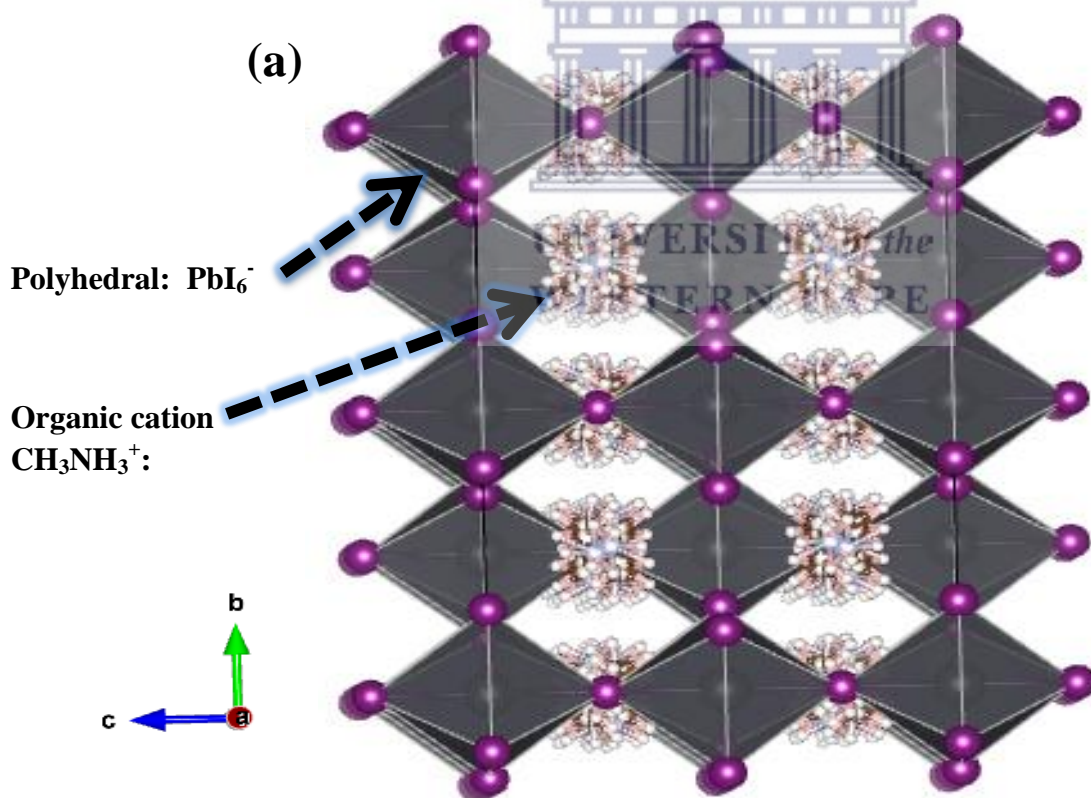
Kesterite based solar cell technology has been extensively explored in the last years and significant advances and fundamental understanding have been attained, however, only a record power conversion efficiency of 13% (on a laboratory scale) has been attained to date and it has since remained stagnant at this value [15]. The stagnation of the record power conversion efficiency is primarily related to elemental Sn, largely to the volatile $\text{Sn}(\text{S},\text{Se})_x$ species [16] that results in morphological and compositional issues [17], and the unstable oxidation state (i.e. $\text{Sn}^{2+} \leftrightarrow \text{Sn}^{4+}$) that results in the growth of deep defects [18,19] that ultimately generate high V_{OC} deficit in CZTSSe-based solar cell devices. It has already been mentioned that the low open circuit voltage (V_{OC}) is the common constraint restricting the performance in kesterite based solar cells chiefly when compared to the highest possible V_{OC} value ruled by the Shockley-Queisser radiative limit ($V_{\text{OC,SQ}}$) [20]. Currently, the replacement of Sn by elemental Ge is considered a potential strategy to advance the kesterite based solar cell technology and this challenge inspired the course of this study; development of Ge kesterite solar cells. B.H. Lee *et al.* [21] recently published a study focusing on the effect of Ge nanolayer stacking order on the photovoltaic performance of CZTSSe thin film solar cells and the experimental results indicated that the ideal Ge nanolayer content and the respective ideal position (stack order) has the capability to advance the optoelectronic properties of kesterite CZTSSe absorber layer which will resultantly attain high power conversion efficiency in kesterite based solar cells.

4.2 NiCuZn HYBRID PEROVSKITE THIN FILMS

4.2.1 Structural Analysis by X-ray Diffraction (XRD)

The X-Ray diffraction patterns of all the compounds investigated in this study were collected to confirm the purity of the perovskite phase for all the compounds investigated in this study. From these XRD patterns, other information concerning the structural properties of the materials was extracted to further probe the structures. The Visualization for Electronic and Structural Analysis (VESTA) software was utilized to visualize the electronic structures of the compounds.

i. Purity and Degree of Crystallinity (peak to noise ratio)



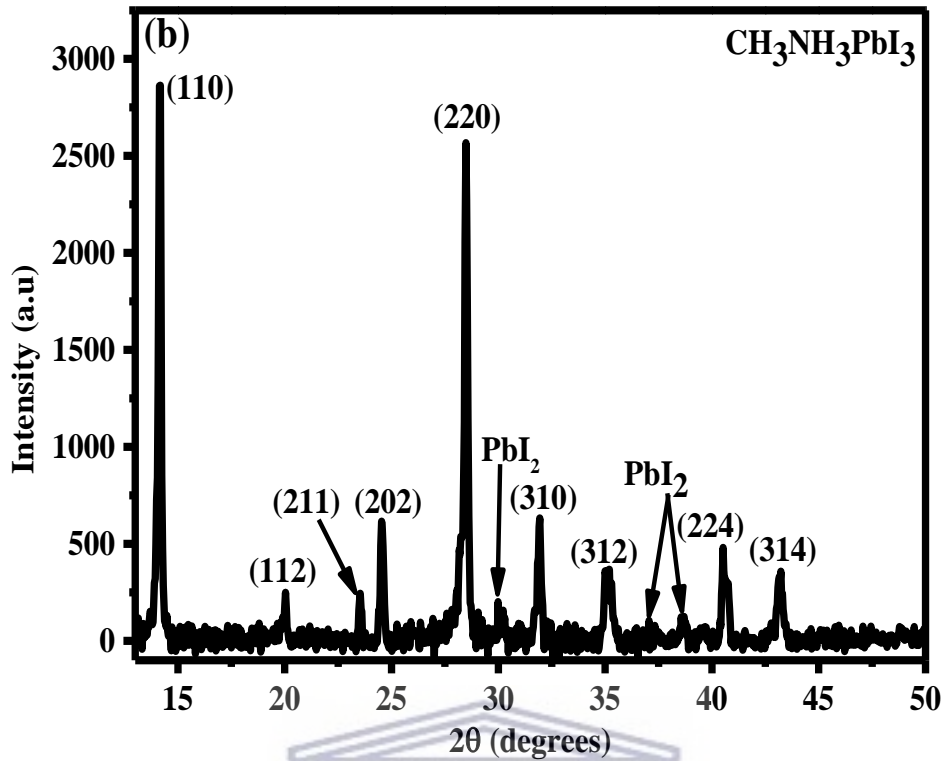


Figure 4.1: Simulated crystal structure of tetragonal $\text{CH}_3\text{NH}_3\text{PbI}_3$ by VESTA (a). XRD patterns of pure traditional $\text{CH}_3\text{NH}_3\text{PbI}_3$ perovskite (b).

X-ray diffraction patterns in **Figure 4.1** are for $\text{CH}_3\text{NH}_3\text{PbI}_3$ thin film deposited on ITO coated glass substrate via two-step deposition technique which was employed in this study. The preferential orientation of prominent peaks is illustrated towards (110), (112), (211), (202), (220), (310), (312), (224), and (314) which perfectly fits the pure phase tetragonal crystal system (space group $I4/mcm$) with lattice parameters; $a = b = 8.8390 \text{ \AA}$, $c = 12.6950 \text{ \AA}$, $\alpha = \beta = \gamma = 90^\circ$, (Volume of cell (10^6 pm^3): 991.83) [22–26]. The strong diffraction peaks observed at crystal planes of (110) and (220) compare very well with the ones previously reported in literature [27–29]. The presence of these two strong peaks confirmed the formation of tetragonal perovskite structure [30–32]. **Table 4.1** shows the lattice parameters determined from the XRD patterns using the following equations:

$$n\lambda = 2d \sin \theta, (n = 1), \text{ Bragg's Law,} \quad (1)$$

$$d = \frac{1}{\sqrt{\frac{h^2+k^2}{a^2} + \frac{l^2}{c^2}}} \quad (2)$$

where d is the interplanar distance (taken from the JSCDPS card number: 96-412-4389), a and c are lattice parameters and h , k and l are miller indices (taken from the XRD patterns). The lattice parameters were determined to be $a = b = 8.865\text{\AA}$ and $c = 12.6950\text{\AA}$ which compared very well with the ones reported in literature for pure tetragonal perovskite $\text{CH}_3\text{NH}_3\text{PbI}_3$ with $I4/mcm$ space group [22–25]. Remarkably, the tetragonal $\text{CH}_3\text{NH}_3\text{PbI}_3$ has been demonstrated to be centrosymmetric at room temperature with $I4/mcm$ space group using first principle calculations by Frohna *et al.* [26].

Table 4.1. Lattice parameters for crystal structure simulations by VESTA software.

Compound	a (Å)	b (Å)	c (Å)	α (°)	β (°)	γ (°)	Space group
$\text{CH}_3\text{NH}_3\text{PbI}_3$	8.8390	8.8390	12.6950	90.0000	90.0000	90.0000	$I4/mcm$

The degree of the crystallinity (peak to noise ratio) of the $\text{CH}_3\text{NH}_3\text{PbI}_3$ thin film was determined using the equation;

$$\text{Degree of crystallinity} = \frac{\text{Area of crystalline peaks}}{\text{Area of all peaks (crystalline+amorphous)}} \times 100\% \quad (3)$$

where area of crystalline peaks and the area of all peaks (crystalline + amorphous) were determined using Origin 9 software and the results are summarised in **Table 4.2**.

Table 4.2. Determination of the degree of crystallinity (peak to noise ratio).

Compound	Area of crystalline peaks	Area of all peaks (crystalline + amorphous)	Degree of Crystallinity
$\text{CH}_3\text{NH}_3\text{PbI}_3$	1691.49	2246.4	75.30

An impressive degree of crystallinity of 75.30% was observed for the pure perovskite $\text{CH}_3\text{NH}_3\text{PbI}_3$ thin film.

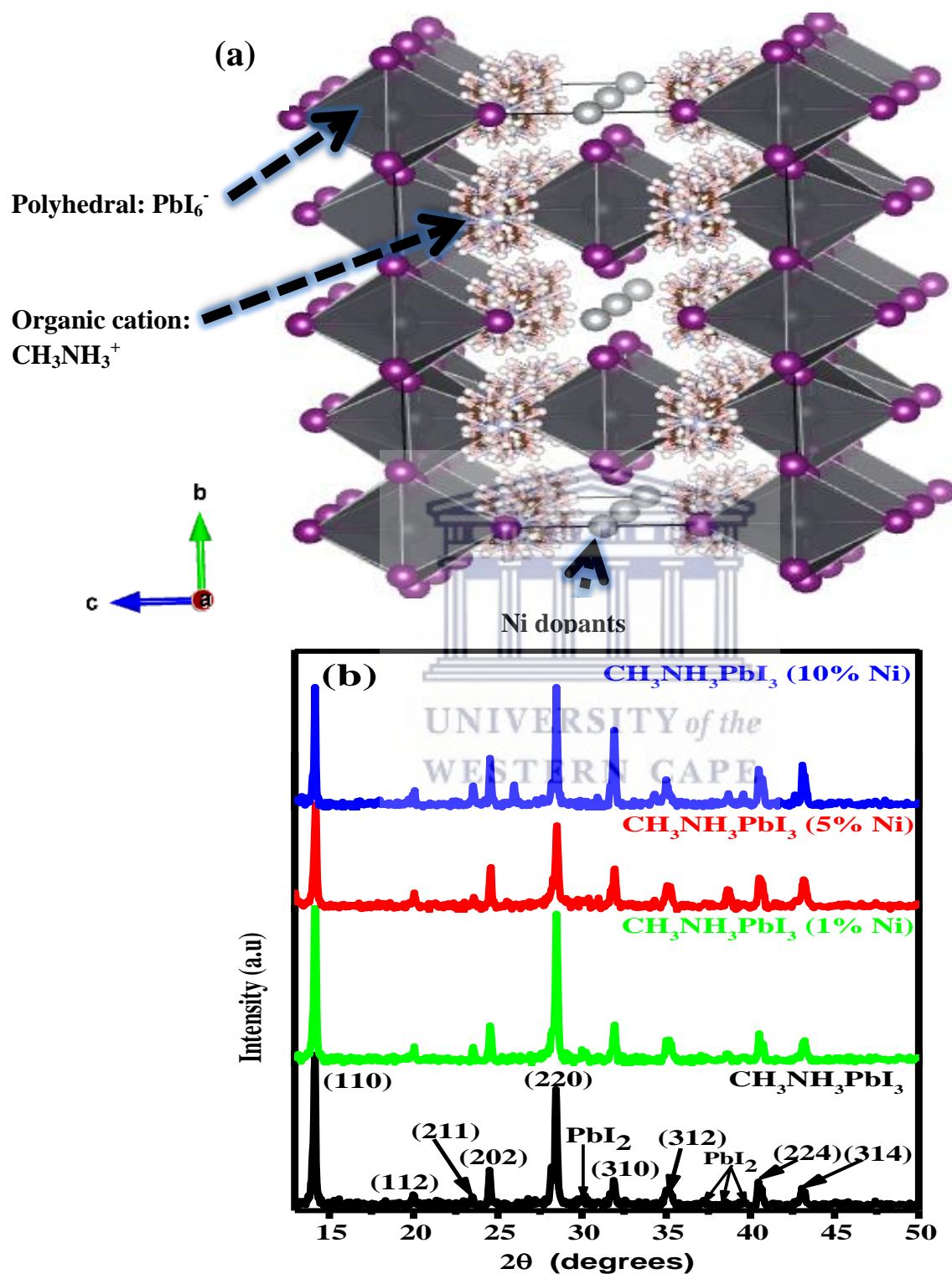


Figure 4.2: Simulated crystal structure of tetragonal Ni doped $\text{CH}_3\text{NH}_3\text{PbI}_3 \cdot \text{Ni}$ by VESTA (a). XRD patterns of pure and Zn doped $\text{CH}_3\text{NH}_3\text{PbI}_3$ (1, 5 and 10% Ni) perovskite thin films (b).

X-ray diffraction patterns in **Figure 4.2** are for $\text{CH}_3\text{NH}_3\text{PbI}_3\cdot\text{Ni}$ thin films deposited on ITO coated glass substrates via two-step deposition technique which was employed in this study. The preferential orientation of prominent peaks is illustrated towards (110), (112), (211), (202), (220), (310), (312), (224), and (314) which also perfectly fits the pure phase tetragonal crystal system (space group *I4/mcm*) with lattice parameters; $a = b = 8.8390 \text{ \AA}$, $c = 12.6950 \text{ \AA}$, $\alpha = \beta = \gamma = 90^\circ$, (Volume of cell (10^6 pm^3): 991.83) [22–25]. The strong diffraction peaks observed at crystal planes of (110) and (220) were also observed for Ni doped hybrid perovskite $\text{CH}_3\text{NH}_3\text{PbI}_3\cdot\text{Ni}$ thin films which also compare very well with the ones previously reported in literature [27–29]. The presence of these two strong peaks confirmed the formation of tetragonal perovskite structure [30–32]. **Table 4.3** shows the lattice parameters for $\text{CH}_3\text{NH}_3\text{PbI}_3\cdot\text{Ni}$ thin films determined from the XRD patterns using equation 1 & 2. The calculated lattice parameters for $\text{CH}_3\text{NH}_3\text{PbI}_3\cdot\text{Ni}$ thin films compared very well with the ones reported in literature for pure tetragonal perovskite $\text{CH}_3\text{NH}_3\text{PbI}_3$ with *I4/mcm* space group [22–25].

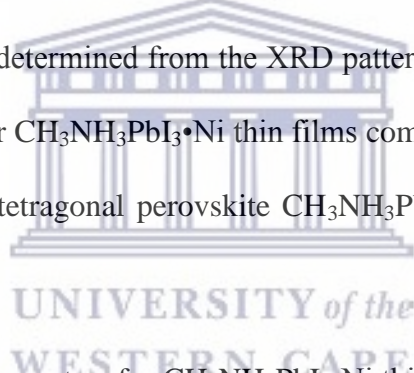
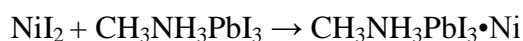


Table 4.3. Calculated lattice parameters for $\text{CH}_3\text{NH}_3\text{PbI}_3\cdot\text{Ni}$ thin films.

Compound	a (Å)	b (Å)	c (Å)	α (°)	γ (°)	β (°)	Space group
$\text{CH}_3\text{NH}_3\text{PbI}_3\cdot\text{Ni}$ (simulated)	8.8390	8.8390	12.6950	90.0000	90.0000	90.0000	I4/mcm
$\text{CH}_3\text{NH}_3\text{PbI}_3\cdot 1\%\text{Ni}$	8.8461	8.8461	12.6950	90.000	90.0000	90.0000	I4/mcm
$\text{CH}_3\text{NH}_3\text{PbI}_3\cdot 5\%\text{Ni}$	8.8391	8.8391	12.6950	90.000	90.0000	90.0000	I4/mcm
$\text{CH}_3\text{NH}_3\text{PbI}_3\cdot 10\%\text{Ni}$	8.8510	8.8510	12.6950	90.000	90.0000	90.0000	I4/mcm

The content of Ni dopant in CH₃NH₃PbI₃•Ni thin films was determined using Vergad's law which states that the unit cell parameter (and unit cell volume) vary linearly from end member to the other as a function of composition;



$$a(\text{CH}_3\text{NH}_3\text{PbI}_3 \cdot \text{Ni}) = xa(\text{NiI}_2) + (1 - x)a(\text{CH}_3\text{NH}_3\text{PbI}_3)$$

where x = dopant concentration, $a(\text{NiI}_2) = 3.91\text{\AA}$, $a(\text{CH}_3\text{NH}_3\text{PbI}_3) = 8.8390\text{\AA}$, $a(\text{CH}_3\text{NH}_3\text{PbI}_3 \cdot \text{Ni})$ is taken from **Table 4.3**. The results are summarized in **Table 4.4** below.

Table 4.4. Ni content in CH₃NH₃PbI₃•Ni determined using Vergad's Law.

Compound	Ni(%)
CH ₃ NH ₃ PbI ₃ •1%Ni	0.14
CH ₃ NH ₃ PbI ₃ •5%Ni	0.002
CH ₃ NH ₃ PbI ₃ •10%Ni	0.24

The results for the degree of crystallinity are summarized in **Table 4.5** below.

Table 4.5. Determination of the degree of crystallinity (peak to noise ratio).

Compound	Area of crystalline peaks	Area of all peaks (crystalline + amorphous)	Degree of Crystallinity
CH ₃ NH ₃ PbI ₃ •1%Ni	2314.1300	3193.977	72.45
CH ₃ NH ₃ PbI ₃ •5%Ni	2798.5189	3460.019	80.88
CH ₃ NH ₃ PbI ₃ •10%Ni	2527.3800	3085.600	81.90

A slight increase in degree of crystallinity from 72.45% to 80.88% to 81.90% (average = 78.41%) for CH₃NH₃PbI₃•1%Ni, CH₃NH₃PbI₃•5%Ni, CH₃NH₃PbI₃•10%Ni, respectively, was observed for Ni doped CH₃NH₃PbI₃•Ni perovskites as observed from **Table 4.5**

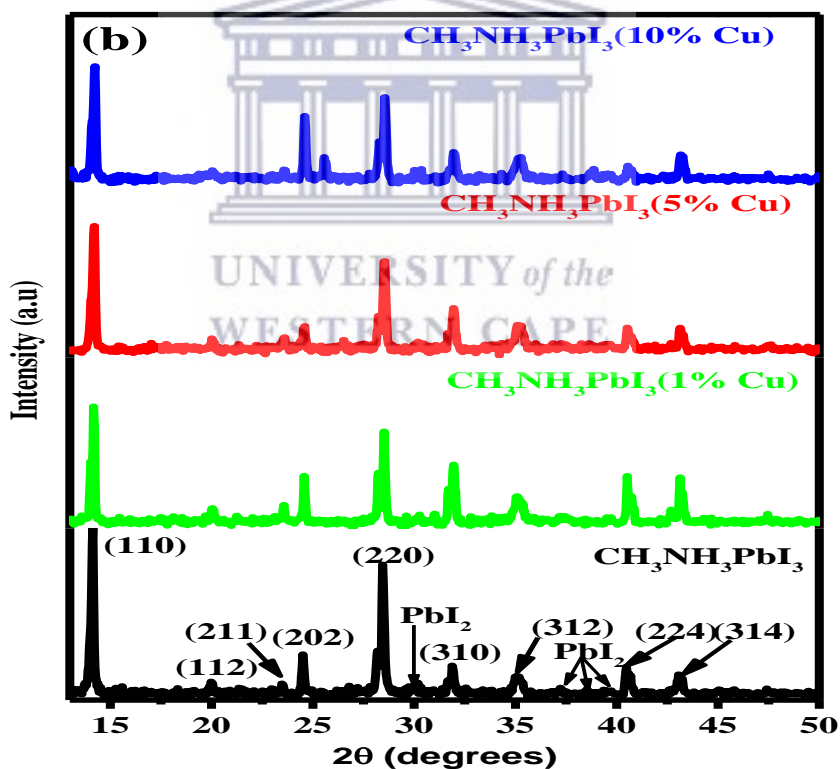
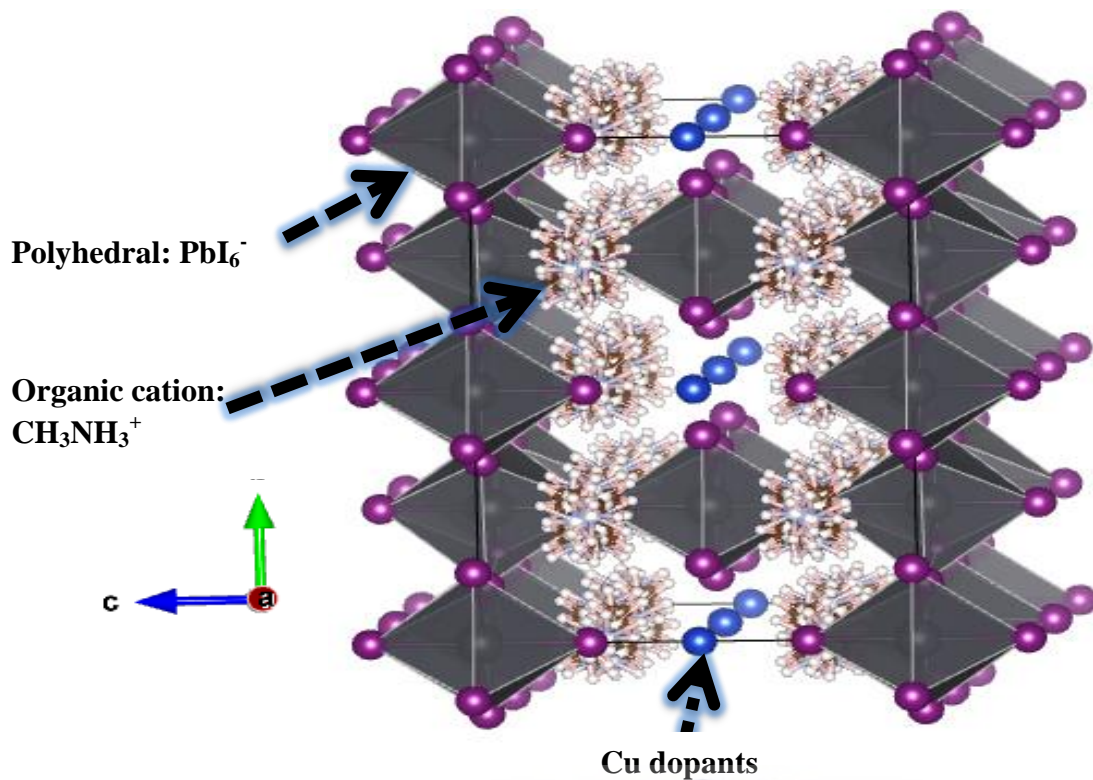


Figure 4.3: Simulated crystal structure of tetragonal Cu doped $\text{CH}_3\text{NH}_3\text{PbI}_3 \cdot \text{Cu}$ by VESTA (a). XRD patterns of pure and Cu doped $\text{CH}_3\text{NH}_3\text{PbI}_3$ (1, 5 and 10% Cu) perovskite thin films (b).

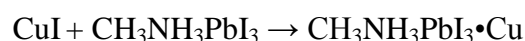
X-ray diffraction patterns in **Figure 4.3** are for $\text{CH}_3\text{NH}_3\text{PbI}_3 \cdot \text{Cu}$ thin films deposited on ITO coated glass substrates via two-step deposition technique which was employed in this study.

The preferential orientation of prominent peaks is illustrated towards (110), (112), (211), (202), (220), (310), (312), (224), and (314) which also perfectly fits the pure phase tetragonal crystal system (space group *I4/mcm*) with lattice parameters; $a = b = 8.8390 \text{ \AA}$, $c = 12.6950 \text{ \AA}$, $\alpha = \beta = \gamma = 90^\circ$, (Volume of cell (10^6 pm^3): 991.83). [22–25]. The strong diffraction peaks observed at crystal planes of (110) and (220) were also observed for Cu doped hybrid perovskite $\text{CH}_3\text{NH}_3\text{PbI}_3 \cdot \text{Cu}$ thin films which also compare very well with the ones previously reported in literature [27–29]. The presence of these two strong peaks confirmed the formation of tetragonal perovskite structure [30–32]. **Table 4.6** shows the lattice parameters for $\text{CH}_3\text{NH}_3\text{PbI}_3 \cdot \text{Cu}$ thin films determined from the XRD patterns using equation 1 & 2. The calculated lattice parameters for $\text{CH}_3\text{NH}_3\text{PbI}_3 \cdot \text{Cu}$ thin films compared very well with the ones reported in literature for pure tetragonal perovskite $\text{CH}_3\text{NH}_3\text{PbI}_3$ with *I4/mcm* space group [22–25].

Table 4.6. Calculated lattice parameters for $\text{CH}_3\text{NH}_3\text{PbI}_3 \cdot \text{Cu}$ thin films.

Compound	a (Å)	b (Å)	c (Å)	α (°)	γ (°)	β (°)	Space group
$\text{CH}_3\text{NH}_3\text{PbI}_3 \cdot \text{Cu}$ (simulated)	8.8390	8.8390	12.6950	90.0000	90.0000	90.0000	<i>I4/mcm</i>
$\text{CH}_3\text{NH}_3\text{PbI}_3 \cdot 1\% \text{Cu}$	8.8468	8.8468	12.6950	90.000	90.0000	90.0000	<i>I4/mcm</i>
$\text{CH}_3\text{NH}_3\text{PbI}_3 \cdot 5\% \text{Cu}$	8.8468	8.8468	12.6950	90.000	90.0000	90.0000	<i>I4/mcm</i>
$\text{CH}_3\text{NH}_3\text{PbI}_3 \cdot 10\% \text{Cu}$	8.8135	8.8135	12.6950	90.000	90.0000	90.0000	<i>I4/mcm</i>

The content of Cu dopant in $\text{CH}_3\text{NH}_3\text{PbI}_3 \cdot \text{Cu}$ thin films was determined using Vergad's law which states that the unit cell parameter (and unit cell volume) vary linearly from end member to the other as a function of composition;



$$a(\text{CH}_3\text{NH}_3\text{PbI}_3\cdot\text{Cu}) = xa(\text{CuI}) + (1 - x)a(\text{CH}_3\text{NH}_3\text{PbI}_3)$$

where x = dopant concentration, $a(\text{CuI}) = 6.0427\text{Å}$, $a(\text{CH}_3\text{NH}_3\text{PbI}_3) = 8.8390\text{Å}$, $a(\text{CH}_3\text{NH}_3\text{PbI}_3\cdot\text{Cu})$ is taken from **Table 4.6**. The results are summarized in **Table 4.7** below.

Table 4.7. Cu content in $\text{CH}_3\text{NH}_3\text{PbI}_3\cdot\text{Cu}$ determined using Vergad's Law.

Compound	Cu(%)
$\text{CH}_3\text{NH}_3\text{PbI}_3\cdot 1\%\text{Cu}$	0.26
$\text{CH}_3\text{NH}_3\text{PbI}_3\cdot 5\%\text{Cu}$	0.26
$\text{CH}_3\text{NH}_3\text{PbI}_3\cdot 10\%\text{Cu}$	0.911

The results for the degree of crystallinity are summarized in **Table 4.8** below.

Table 4.8. Determination of the degree of crystallinity (peak to noise ratio).

Compound	Area of crystalline peaks	Area of all peaks (crystalline + amorphous)	Degree of Crystallinity
$\text{CH}_3\text{NH}_3\text{PbI}_3\cdot 1\%\text{Cu}$	2099.55	3012.566	69.69
$\text{CH}_3\text{NH}_3\text{PbI}_3\cdot 5\%\text{Cu}$	2371.12	3692.58	64.21
$\text{CH}_3\text{NH}_3\text{PbI}_3\cdot 10\%\text{Cu}$	2242.08	3220,76	69.61

An average degree of crystallinity of 67.84% was observed for Cu doped $\text{CH}_3\text{NH}_3\text{PbI}_3\cdot\text{Cu}$ perovskites as seen from **Table 4.8**.

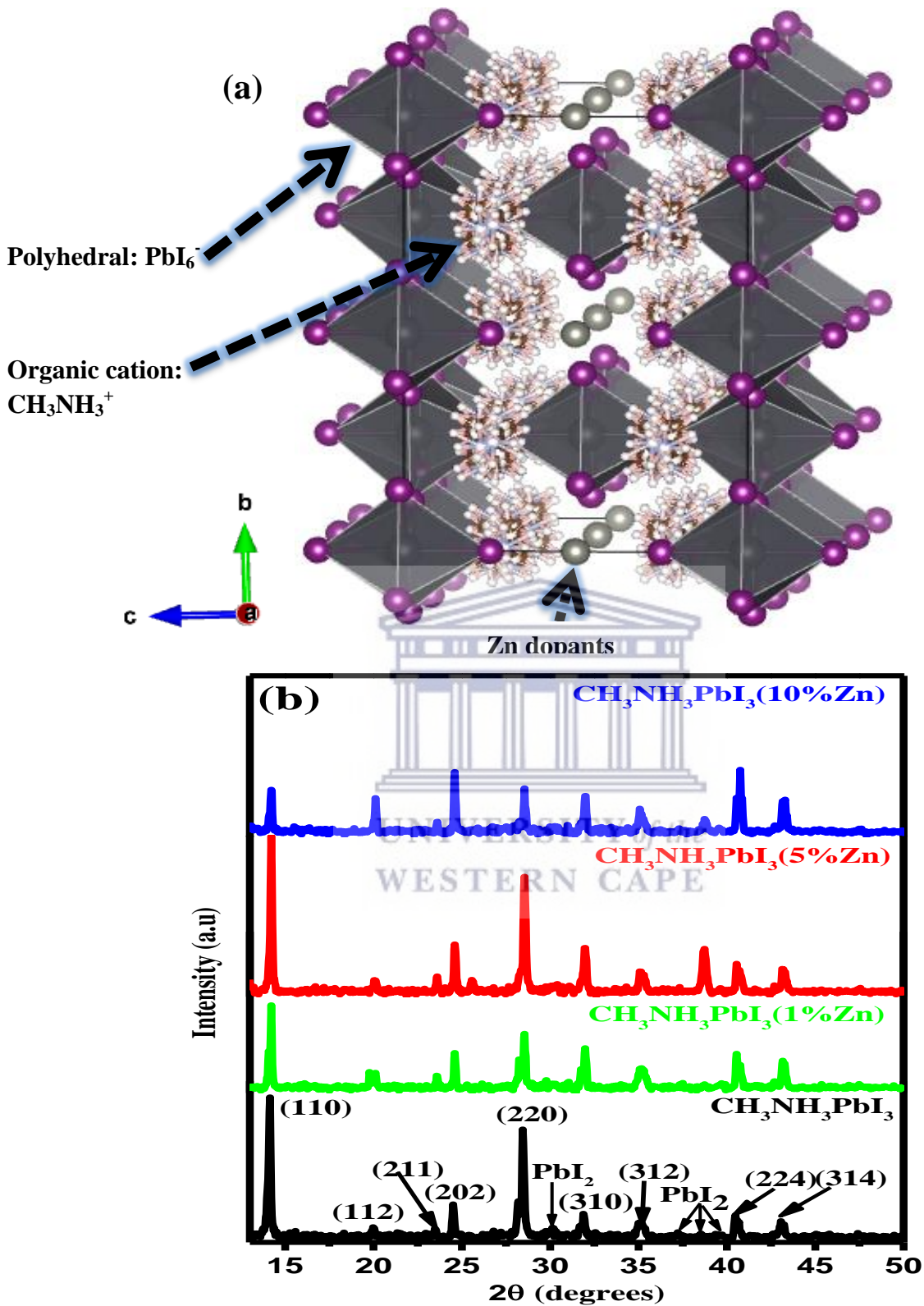


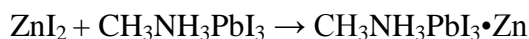
Figure 4.4: Simulated crystal structure of tetragonal Zn doped $\text{CH}_3\text{NH}_3\text{PbI}_3 \cdot \text{Zn}$ by VESTA (a). XRD patterns of pure and Zn doped $\text{CH}_3\text{NH}_3\text{PbI}_3$ (1, 5 and 10% Zn) perovskite thin films (b).

X-ray diffraction patterns in **Figure 4.4** are for Zn doped perovskites $\text{CH}_3\text{NH}_3\text{PbI}_3 \cdot \text{Zn}$ thin films deposited on ITO coated glass substrate via two-step deposition technique which was employed in this study. The preferential orientation of prominent peaks is illustrated towards (110), (112), (211), (202), (220), (310), (312), (224), and (314) which also perfectly fits the pure phase tetragonal crystal system (space group $I4/mcm$) with lattice parameters; $a = b = 8.8390 \text{ \AA}$, $c = 12.6950 \text{ \AA}$, $\alpha = \beta = \gamma = 90^\circ$, (Volume of cell (10^6 pm^3): 991.83) [22–25]. The strong diffraction peaks observed at crystal planes of (110) and (220) were also observed for Zn doped hybrid perovskite $\text{CH}_3\text{NH}_3\text{PbI}_3 \cdot \text{Zn}$ thin films which also compare very well with the ones previously reported in literature [27–29]. The presence of these two strong peaks confirmed the formation of tetragonal perovskite structure [30–32]. **Table 4.9** shows the lattice parameters for $\text{CH}_3\text{NH}_3\text{PbI}_3 \cdot \text{Zn}$ thin films determined from the XRD patterns using equation 1 & 2 and the results are summarized in **Table 4.9**. The calculated lattice parameters for $\text{CH}_3\text{NH}_3\text{PbI}_3 \cdot \text{Zn}$ thin films compared very well with the ones reported in literature for pure tetragonal perovskite $\text{CH}_3\text{NH}_3\text{PbI}_3$ with $I4/mcm$ space group [22–25]. **Table 4.9** shows the lattice parameters for $\text{CH}_3\text{NH}_3\text{PbI}_3 \cdot \text{Zn}$ thin films determined from the XRD patterns using equation 1 & 2.

Table 4.9. Calculated lattice parameters for $\text{CH}_3\text{NH}_3\text{PbI}_3 \cdot \text{Zn}$ thin films.

Compound	a (Å)	b (Å)	c (Å)	α (°)	γ (°)	β (°)	Space group
$\text{CH}_3\text{NH}_3\text{PbI}_3 \cdot \text{Zn}$ (simulated)	8.8390	8.8390	12.6950	90.0000	90.0000	90.0000	$I4/mcm$
$\text{CH}_3\text{NH}_3\text{PbI}_3 \cdot 1\% \text{Zn}$	8.8236	8.8236	12.6950	90.0000	90.0000	90.0000	$I4/mcm$
$\text{CH}_3\text{NH}_3\text{PbI}_3 \cdot 5\% \text{Zn}$	8.8073	8.8073	12.6950	90.0000	90.0000	90.0000	$I4/mcm$
$\text{CH}_3\text{NH}_3\text{PbI}_3 \cdot 10\% \text{Zn}$	8.8125	8.8125	12.6950	90.0000	90.0000	90.0000	$I4/mcm$

The content of Zn dopant in $\text{CH}_3\text{NH}_3\text{PbI}_3 \cdot \text{Zn}$ thin films was determined using Vergad's law which states that the unit cell parameter (and unit cell volume) vary linearly from end member to the other as a function of composition;



$$a(\text{CH}_3\text{NH}_3\text{PbI}_3 \cdot \text{Zn}) = xa(\text{ZnI}_2) + (1 - x)a(\text{CH}_3\text{NH}_3\text{PbI}_3)$$

where x = dopant concentration, $a(\text{ZnI}_2) = 12.284 \text{ \AA}$, $a(\text{CH}_3\text{NH}_3\text{PbI}_3) = 8.8390 \text{ \AA}$, $a(\text{CH}_3\text{NH}_3\text{PbI}_3 \cdot \text{Zn})$ is taken from **Table 4.9**. The results are summarized in **Table 4.10** below.

Table 4.10. Zn content in $\text{CH}_3\text{NH}_3\text{PbI}_3 \cdot \text{Zn}$ determined using Vergad's Law.

Compound	Zn(%)
$\text{CH}_3\text{NH}_3\text{PbI}_3 \cdot 1\% \text{Zn}$	0.14
$\text{CH}_3\text{NH}_3\text{PbI}_3 \cdot 5\% \text{Zn}$	0.002
$\text{CH}_3\text{NH}_3\text{PbI}_3 \cdot 10\% \text{Zn}$	0.24

The results for the degree of crystallinity are summarized in **Table 4.11** below.

Table 4.11. Determination of the degree of crystallinity (peak to noise ratio).

Compound	Area of crystalline peaks	Area of all peaks (crystalline + amorphous)	Degree of Crystallinity
$\text{CH}_3\text{NH}_3\text{PbI}_3 \cdot 1\% \text{Zn}$	1691.49	2246.40	75.30
$\text{CH}_3\text{NH}_3\text{PbI}_3 \cdot 5\% \text{Zn}$	3437.54	3920.42	87.68
$\text{CH}_3\text{NH}_3\text{PbI}_3 \cdot 10\% \text{Zn}$	2151.09	2680.50	80.25

An average degree of crystallinity of 81.08% was observed for Zn doped $\text{CH}_3\text{NH}_3\text{PbI}_3 \cdot \text{Zn}$ perovskites as observed from **Table 4.11**.

All thin films materials in this study confirmed a pure perovskite phase in the tetragonal crystal system which was in agreement with the results of the previous works for methylammonium lead triiodide [33]. There was no significant impact induced by transition metals on the lattice parameters and space group. This shows that the transition metals Ni, Cu and Zn did not shrink or expand the crystal structure of the traditional pure phase $\text{CH}_3\text{NH}_3\text{PbI}_3$ perovskite. This observation could be attributed to the atomic radiuses of the transition metals; Ni (1.15Å), Cu (1.17Å) and Zn (1.24Å) in close proximity to Pb (1.75Å). The other reason could be the fact that the transition metals were incorporated into the structure at a very low doping level (see **Table 4.4, 4.7 and 4.10**) and hence almost no impact on the lattice parameters. The ultimate reason for transition metals Ni, Cu and Zn not altering/perturbing the tetragonal crystal structure of the pure phase $\text{CH}_3\text{NH}_3\text{PbI}_3$ could be due to the fact that the calculated tolerance factors 1.02, 0.99, 1.00, for Ni, Cu and Zn, respectively, were within the accepted range of $0.76 < t < 1.13$ for perovskite formation and stabilization [34]. The tolerance factor calculations were done using the equation below;

$$t = \frac{(r_A + r_X)}{\sqrt{2}(r_B + r_X)} \quad (4)$$

where r_A is the ionic radii of the organic cation ($\text{CH}_3\text{NH}_3^+ = 180$ pm), r_B is the ionic radii of the metal cation ($\text{Ni}^{2+} = 70$ ppm, $\text{Cu}^+ = 77$ ppm and $\text{Zn}^{2+} = 74$ ppm), and r_X is the ionic radii of the halide anions ($\text{I}^- = 181$ ppm). Nonetheless, the degree of crystallinity (peak-to-noise-ratio) analysis demonstrated an effect induced by transition metals on the degree of crystallinity of the materials. On average; the degree of crystallinity for $\text{CH}_3\text{NH}_3\text{PbI}_3$, $\text{CH}_3\text{NH}_3\text{PbI}_3 \cdot \text{Ni}$, $\text{CH}_3\text{NH}_3\text{PbI}_3 \cdot \text{Cu}$ and $\text{CH}_3\text{NH}_3\text{PbI}_3 \cdot \text{Zn}$ were determined to be 75.30%, 78.41%, 67.84% and 81.08%, respectively. Ni^{2+} and Zn^{2+} doped perovskites demonstrated good crystallinity properties which is beneficial for enhancing the photo-physical properties [35] and for optimum solar cell device performance [36–38].

ii. Crystallite (grain) size

The crystallite (grain) sizes of all the compounds under investigation were calculated using the Scherrer equation below;

$$D = \frac{k\lambda}{\beta \cos\theta} \quad (5)$$

where, D = crystallite (grain) size (nm), $K = 0.9$ (Scherrer constant), $\lambda = 0.15406$ nm (wavelength of the x-ray sources), β = FWHM (radians) (determined using Origin 9.0 software for each and every crystalline peak), θ = peak positions (radians). The average crystallite (grain) size for traditional pure phase $\text{CH}_3\text{NH}_3\text{PbI}_3$ was determined to be 33.71 nm. The crystallite size for Ni, Cu, and Zn doped perovskites are summarized in **Table 4.12**.

Table 4.12. Crystallite (grain) sizes of Ni, Cu, and Zn doped perovskites.

Compound	Average Crystallite (grain) size; D (nm)
$\text{CH}_3\text{NH}_3\text{PbI}_3 \cdot \text{Ni}$	
$\text{CH}_3\text{NH}_3\text{PbI}_3 \cdot 1\% \text{Ni}$	36.12
$\text{CH}_3\text{NH}_3\text{PbI}_3 \cdot 5\% \text{Ni}$	32.02
$\text{CH}_3\text{NH}_3\text{PbI}_3 \cdot 10\% \text{Ni}$	36.42
$\text{CH}_3\text{NH}_3\text{PbI}_3 \cdot \text{Cu}$	
$\text{CH}_3\text{NH}_3\text{PbI}_3 \cdot 1\% \text{Cu}$	37.14
$\text{CH}_3\text{NH}_3\text{PbI}_3 \cdot 5\% \text{Cu}$	32.78
$\text{CH}_3\text{NH}_3\text{PbI}_3 \cdot 10\% \text{Cu}$	32.82
$\text{CH}_3\text{NH}_3\text{PbI}_3 \cdot \text{Zn}$	
$\text{CH}_3\text{NH}_3\text{PbI}_3 \cdot 1\% \text{Zn}$	35.72
$\text{CH}_3\text{NH}_3\text{PbI}_3 \cdot 5\% \text{Zn}$	40.22
$\text{CH}_3\text{NH}_3\text{PbI}_3 \cdot 10\% \text{Zn}$	42.68

The graphical representation of the impact of transition metals on the crystallite (grain) size at different doping content is illustrated below.

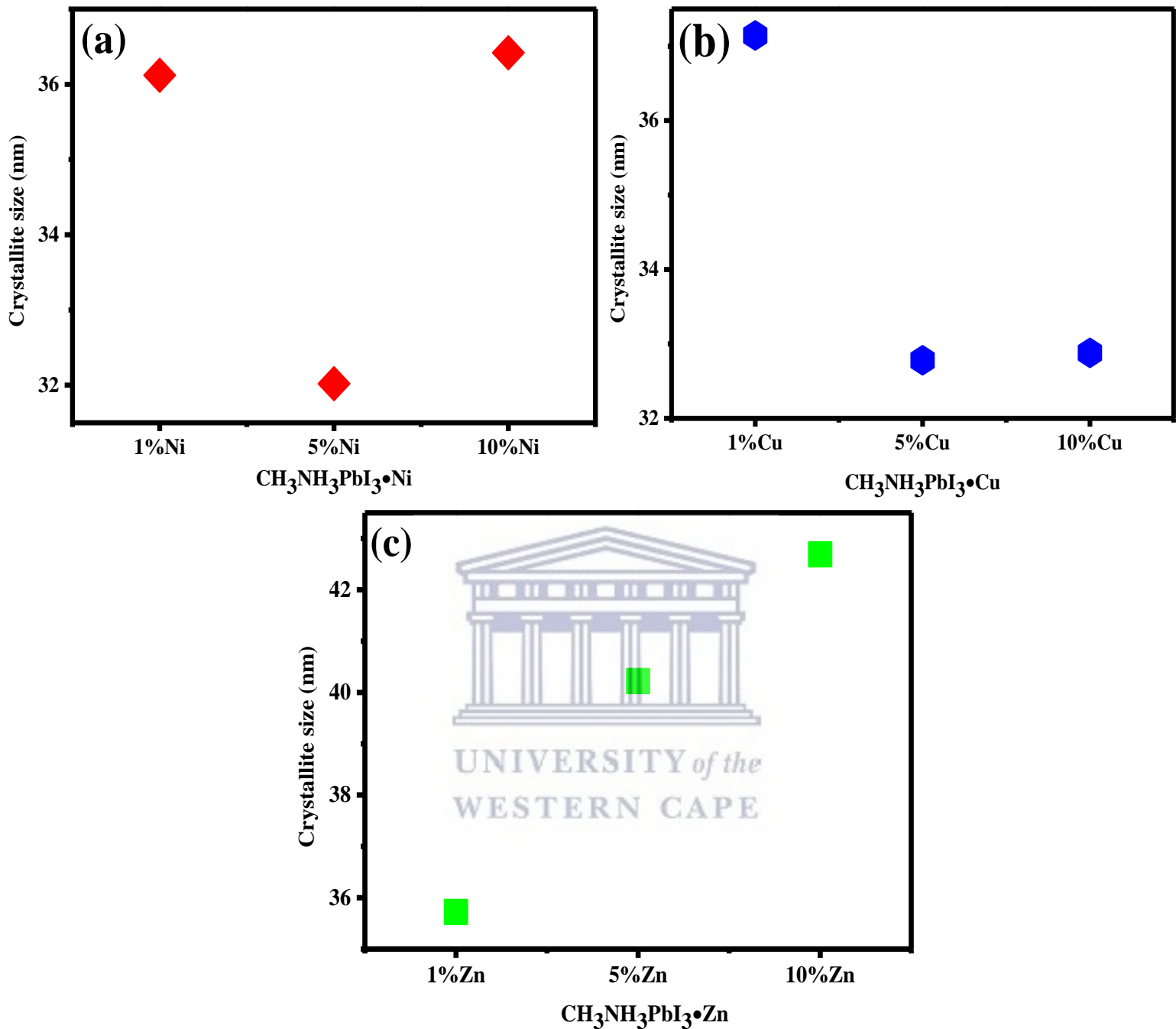


Figure 4.5: Crystallite size of transition metal perovskites; CH₃NH₃PbI₃•Ni (a), CH₃NH₃PbI₃•Cu (b), and CH₃NH₃PbI₃•Zn (c).

The crystallite sizes for all thin films material under investigation were determined to be CH₃NH₃PbI₃ (33.71 nm), CH₃NH₃PbI₃•Ni (32 to 36 nm), CH₃NH₃PbI₃•Cu (32 to 37 nm) and CH₃NH₃PbI₃•Zn (35 to 42 nm). These results were in close proximity to each other demonstrating that there was no significant increase or decrease in the crystallite size induced

by the transitional metal dopants; Ni, Cu and Zn, on the traditional $\text{CH}_3\text{NH}_3\text{PbI}_3$. The expansion and compression of the whole crystal lattice is dependent upon the size of the organic cation A (i.e. CH_3NH_3^+ in this study). The utilization of bigger organic cations, e.g. formamidinium cation ($\text{HC}(\text{NH}_2)_2^+$, FA^+), has demonstrated a higher symmetry to the perovskite structure corroborated by the observed reduction in energy bandgap [39].

iii. Micro-strain

J. Zhao *et al.* reported for the first time a detailed study on strained hybrid perovskite thin films and their impact on the intrinsic stability of perovskite solar cell [40]. J. Zhao *et al.* found out that the existing methods for the fabrication of hybrid perovskite thin films results in strained thin films and that strain is caused by mismatched thermal expansion of perovskite films and substrates during the thermal annealing (high temperature annealing) process. It was ultimately found that this strain accelerates degradation of perovskite thin films under illumination which could be explained by increased ion migration in strained hybrid perovskite thin films. The accelerated ion migration in strained perovskite films explains the faster degradation of hybrid perovskite because CH_3NH_3^+ and I^- ions can easily migrate from the $\text{CH}_3\text{NH}_3\text{PbI}_3$ thin films, producing PbI_2 .

In this study, a two-step deposition technique, with first annealing temperature $T_1 = 100^\circ\text{C}$ and final annealing temperature $T_2 = 70^\circ\text{C}$, was employed to produce all the thin films under investigation on ITO glass substrates. The strain analysis of these materials will be based on the impact of transition metals (dopants) on pure $\text{CH}_3\text{NH}_3\text{PbI}_3$ thin film. The micro-strain was calculated using the equation below;

$$\varepsilon = \frac{\beta}{4\tan\theta} \quad (6)$$

where, ε = micro-strain, β = FWHM (radians) (determined using Origin 9.0 software for each and every crystalline peak), θ = peak positions (radians). The average micro-strain for pure $\text{CH}_3\text{NH}_3\text{PbI}_3$ thin film was determined to be 4.14×10^{-3} .

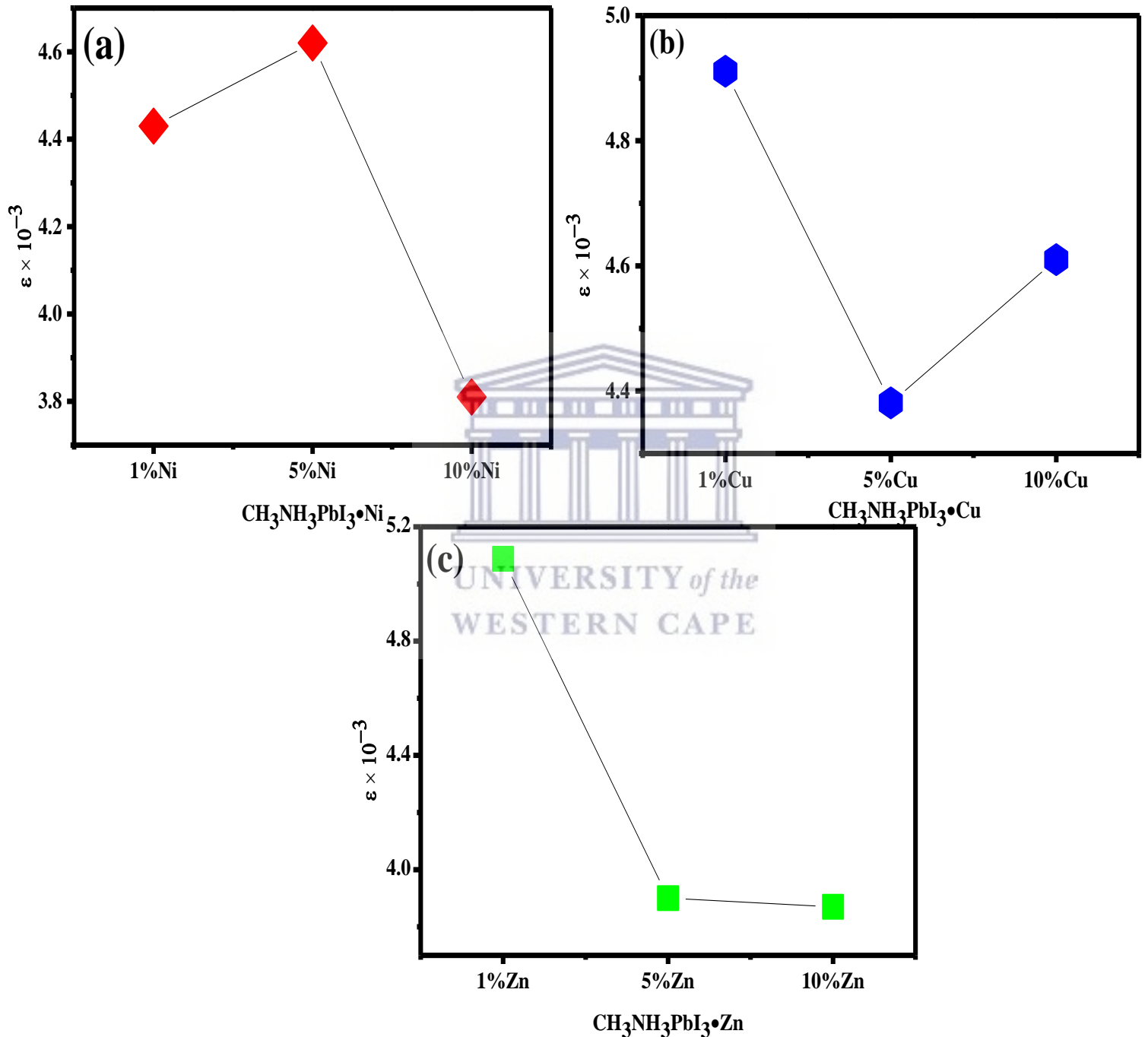
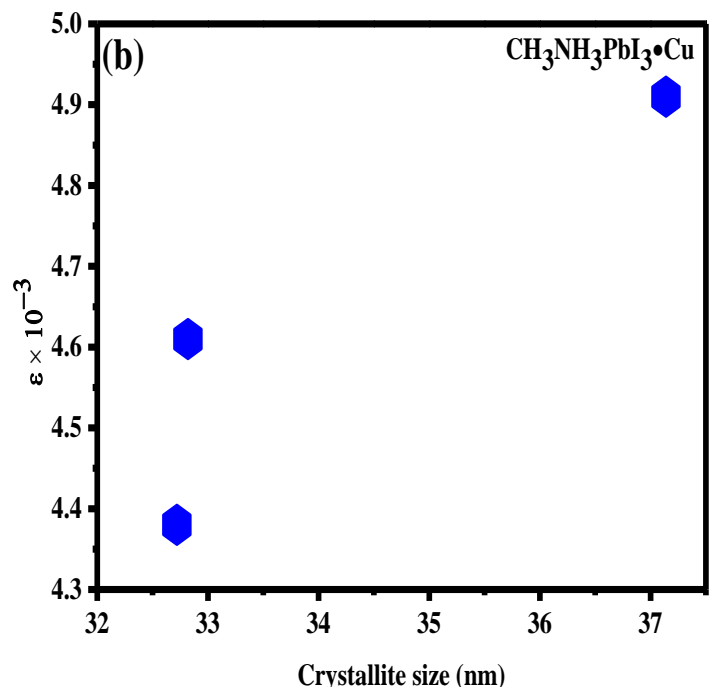
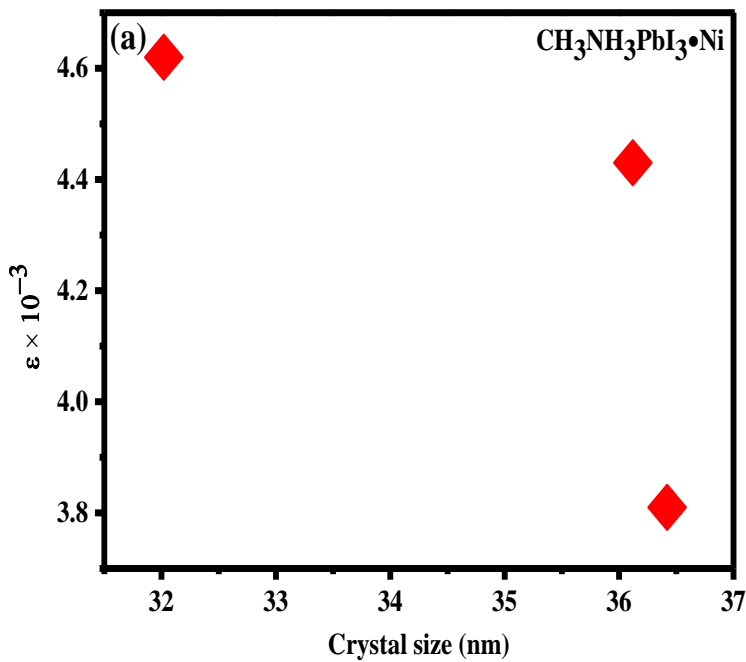


Figure 4.6: Impact of transition metals content on macrostrain for $\text{CH}_3\text{NH}_3\text{PbI}_3 \cdot \text{Ni}$ (a), $\text{CH}_3\text{NH}_3\text{PbI}_3 \cdot \text{Cu}$ (b) and $\text{CH}_3\text{NH}_3\text{PbI}_3 \cdot \text{Zn}$ (c).

For $\text{CH}_3\text{NH}_3\text{PbI}_3 \cdot \text{Ni}$ thin films, the $\text{CH}_3\text{NH}_3\text{PbI}_3 \cdot 10\% \text{Ni}$ with micro strain of 4.14×10^{-3} was the least strained. For $\text{CH}_3\text{NH}_3\text{PbI}_3 \cdot \text{Cu}$ thin films, the $\text{CH}_3\text{NH}_3\text{PbI}_3 \cdot 5\% \text{Cu}$ with micro

strain of 4.38×10^{-3} was the least strained. For $\text{CH}_3\text{NH}_3\text{PbI}_3 \cdot \text{Zn}$ thin films, $\text{CH}_3\text{NH}_3\text{PbI}_3 \cdot 10\% \text{Zn}$ with micro strain of 3.87×10^{-3} was the least strained. These results show that Zn transition metal has the potential/capacity for strain relaxation of strained $\text{CH}_3\text{NH}_3\text{PbI}_3$ (micro-strain of 4.14×10^{-3}) thin films. Therefore Zn showed better potential/capacity for the intrinsic stability of $\text{CH}_3\text{NH}_3\text{PbI}_3 \cdot \text{Zn}$ thin films. Zhao *et al.* [40] reported that hybrid perovskite materials with lower degree of micro-strain exhibit superior hole extraction capacity at the perovskite/hole transport layer boundary by levelling the valence band. Moreover, they also observed that as the micro-strains are eliminated, the carrier mobility increased.



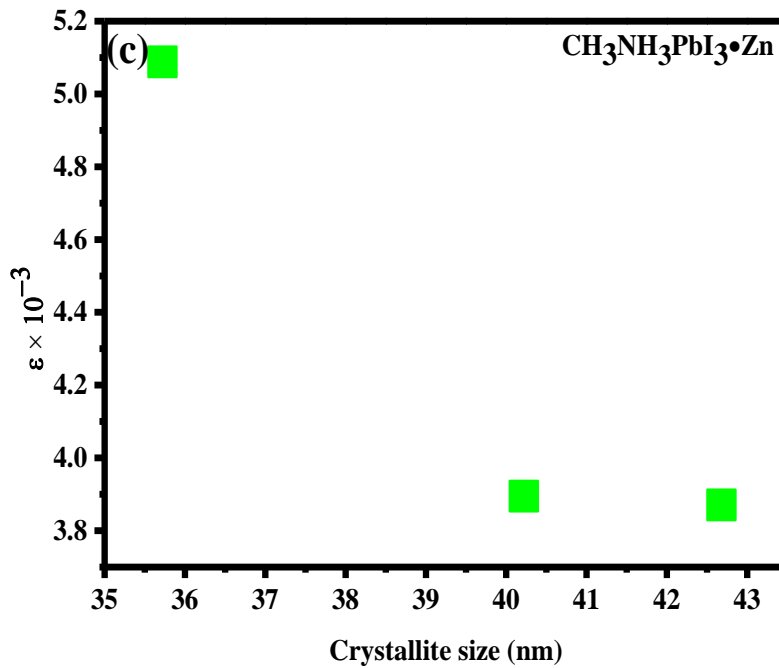


Figure 4.7: The relationship between micro-strain and crystallite size for $\text{CH}_3\text{NH}_3\text{PbI}_3\cdot\text{Ni}$ (a), $\text{CH}_3\text{NH}_3\text{PbI}_3\cdot\text{Cu}$ (b) and $\text{CH}_3\text{NH}_3\text{PbI}_3\cdot\text{Zn}$ (c).

The relationship between micro-strain and crystallite size is illustrated in **Figure 4.7** above. It was observed that the micro-strain and crystallite size are in an inverse proportion with each other (i.e. as the crystallite size increases, the micro-strain decreases). The Ni doped perovskite $\text{CH}_3\text{NH}_3\text{PbI}_3\cdot\text{Ni}$ thin films and the Zn doped perovskite $\text{CH}_3\text{NH}_3\text{PbI}_3\cdot\text{Zn}$ thin films best demonstrate this phenomena as seen from **Figure 4.7**.

iv. Dislocation density

The dislocation density magnitude represents the degree of structural imperfections of a material. An inversely proportional relationship between the dislocation density and the photovoltaic performance of cesium lead tri-iodide perovskite (CsPbI_3) solar cells was demonstrated by Haque *et al.* [41]. This means that solar cell devices with the lowest dislocation density had the best power conversion efficiency, and vice-versa [41,42]. The

dislocation density of all thin film materials under investigation was calculated using the following equation [43];

$$\delta = \frac{1}{D^2} \quad (7)$$

where, δ is the dislocation density (nm^{-2}), D = crystallite size (nm).

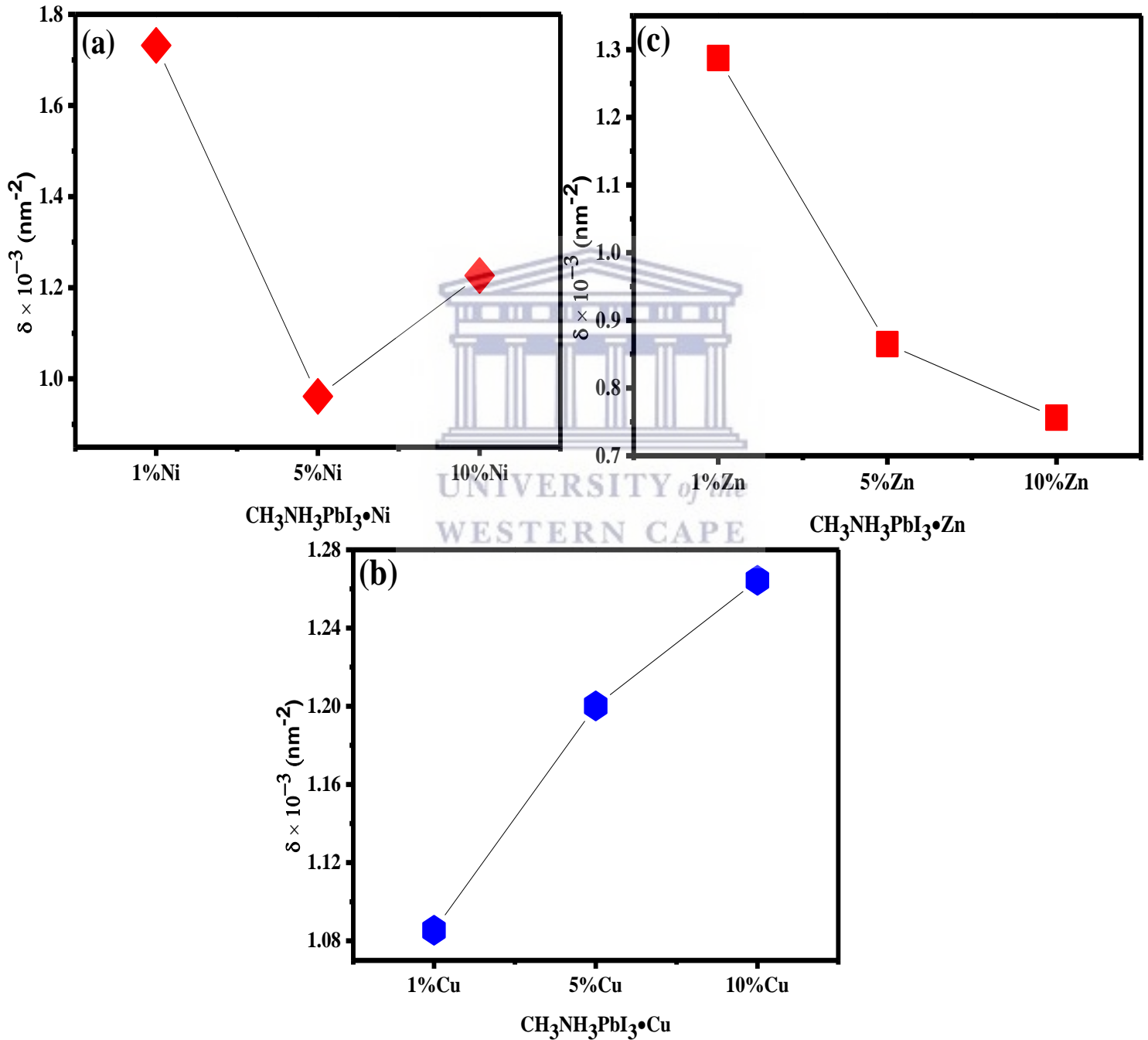
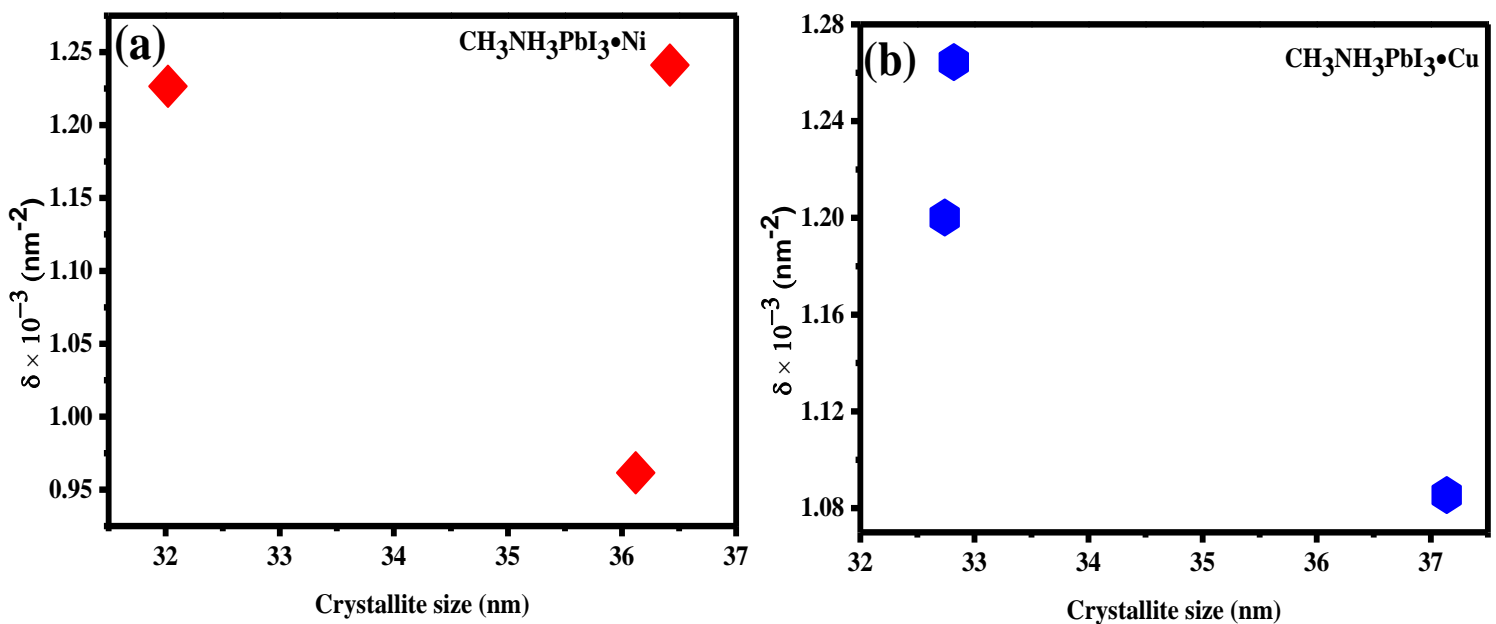


Figure 4.8: Impact of transition metals content on dislocation density for $\text{CH}_3\text{NH}_3\text{PbI}_3 \cdot \text{Ni}$ (a), $\text{CH}_3\text{NH}_3\text{PbI}_3 \cdot \text{Cu}$ (b) and $\text{CH}_3\text{NH}_3\text{PbI}_3 \cdot \text{Zn}$ (c).

The dislocation density for pure $\text{CH}_3\text{NH}_3\text{PbI}_3$ was determined to be $1.173 \times 10^{-3} \text{nm}^{-2}$. For $\text{CH}_3\text{NH}_3\text{PbI}_3 \cdot \text{Ni}$ thin films, the $\text{CH}_3\text{NH}_3\text{PbI}_3 \cdot 5\% \text{Ni}$ thin film with dislocation density of $1.223 \times 10^{-3} \text{nm}^{-2}$ was the material with the least dislocation density. For $\text{CH}_3\text{NH}_3\text{PbI}_3 \cdot \text{Cu}$ thin films, the $\text{CH}_3\text{NH}_3\text{PbI}_3 \cdot 1\% \text{Cu}$ thin film with dislocation density of $1.0833 \times 10^{-3} \text{nm}^{-2}$ was the material with the least dislocation density. For $\text{CH}_3\text{NH}_3\text{PbI}_3 \cdot \text{Zn}$ thin films, $\text{CH}_3\text{NH}_3\text{PbI}_3 \cdot 10\% \text{Zn}$ with dislocation density of $0.7563 \times 10^{-3} \text{nm}^{-2}$ was the material with the least dislocation density. This was in agreement with the results reported by Jones *et al.* [44] which demonstrated that the presence of micro-strains in $\text{CH}_3\text{NH}_3\text{PbI}_3$ raises the defect concentration in $\text{CH}_3\text{NH}_3\text{PbI}_3$ and yields non-radiative recombination. Thus, the reduction of (or total elimination of) micro-strain will yield hybrid perovskite material with less defect concentration and less non-radiative recombination. These results show that Zn transition metal has the potential/capacity for the reduction/elimination of dislocation density (degree of structural imperfections) for $\text{CH}_3\text{NH}_3\text{PbI}_3$ (dislocation density of $1.173 \times 10^{-3} \text{nm}^{-2}$) thin films. Therefore, Zn showed better potential/capacity for advanced photovoltaic performance of $\text{CH}_3\text{NH}_3\text{PbI}_3 \cdot \text{Zn}$ thin films.



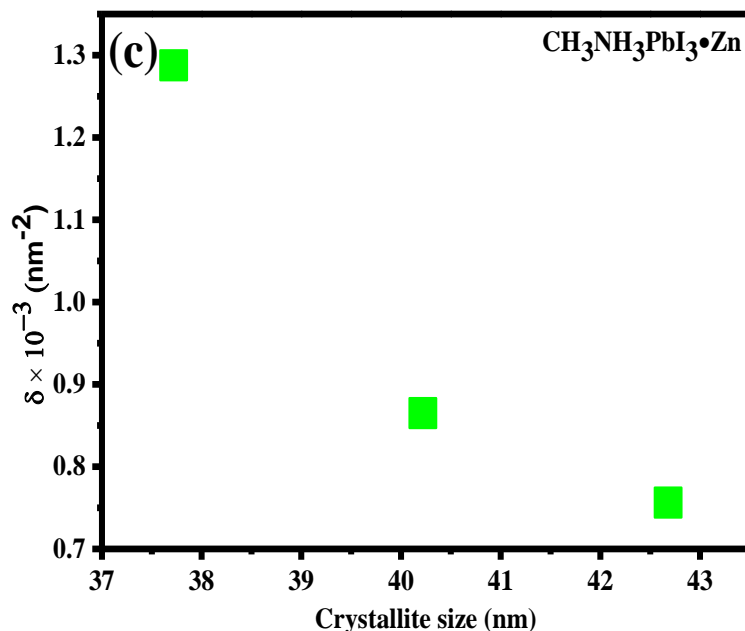
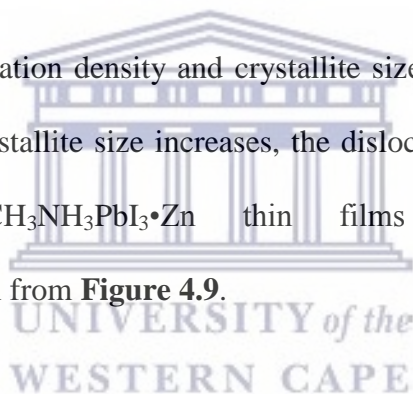


Figure 4.9: The relationship between dislocation density and crystallite size for $\text{CH}_3\text{NH}_3\text{PbI}_3\cdot\text{Ni}$ (a), $\text{CH}_3\text{NH}_3\text{PbI}_3\cdot\text{Cu}$ (b) and $\text{CH}_3\text{NH}_3\text{PbI}_3\cdot\text{Zn}$ (c).

It was observed that the dislocation density and crystallite size are in an inverse proportion with each other (i.e. as the crystallite size increases, the dislocation density decreases). The Zn doped perovskite $\text{CH}_3\text{NH}_3\text{PbI}_3\cdot\text{Zn}$ thin films best demonstrate this relationship/phenomena as seen from **Figure 4.9**.



4.2.2 Surface analysis by X-ray Photoelectron Spectroscopy (XPS)

The elemental composition of the perovskite thin films under investigation was analysed using the XPS surface analysis technique. During the XPS experiment, high energy x-rays are used to emit core-level electrons into the energy analyser of the photo-electron spectroscopy. Since the binding energy of the core-level electrons is to a certain degree unique to their parent atom, elemental identification can easily be done by assigning the atom to the corresponding binding energy peak as shown in the wide scan survey of pure $\text{CH}_3\text{NH}_3\text{PbI}_3$ in **Figure 4.10** below.

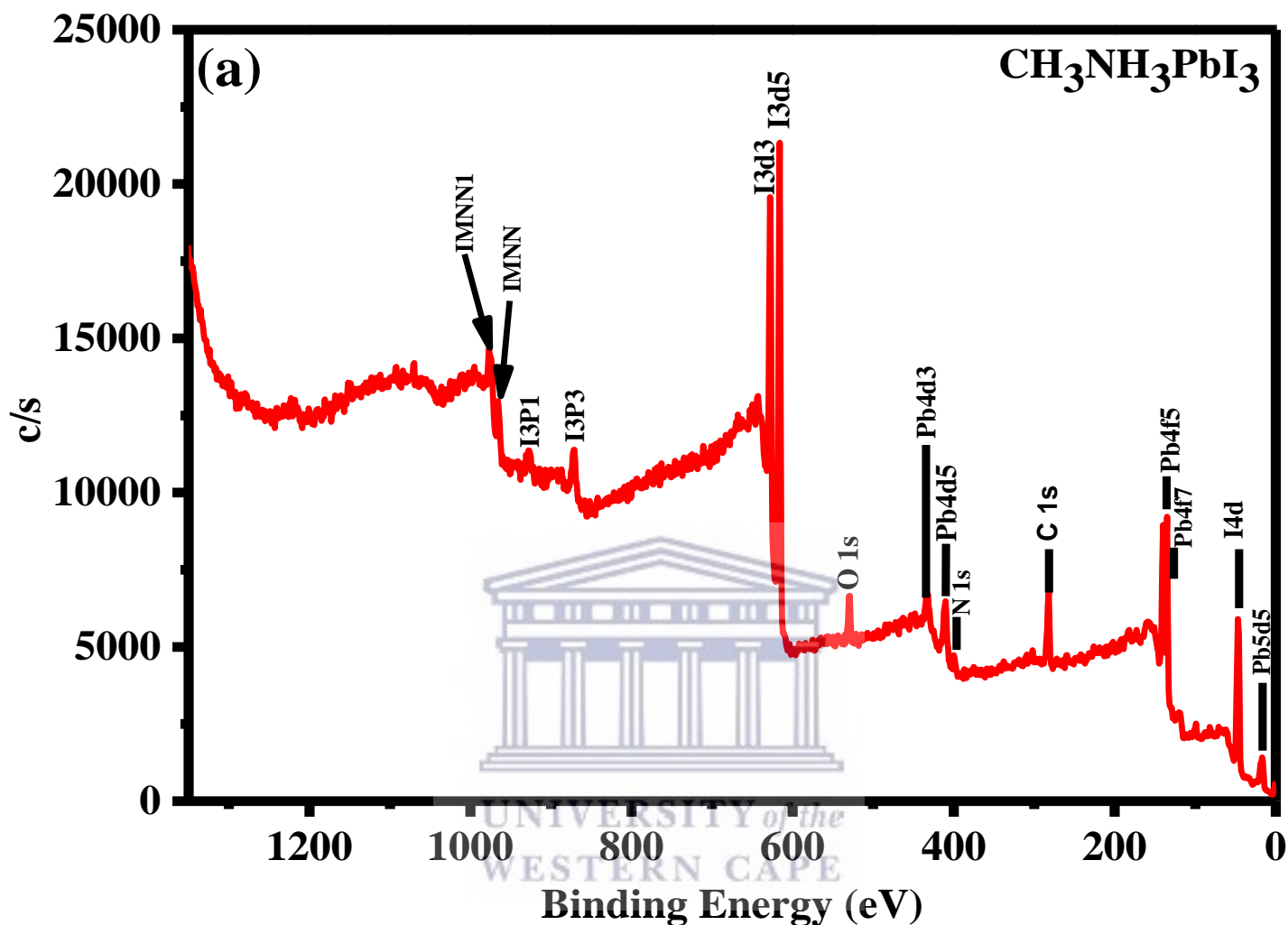


Figure 4.10: XPS survey spectrum of a pure $\text{CH}_3\text{NH}_3\text{PbI}_3$ thin film. Most represents unique electronic atomic orbitals allowing for elemental identification.

It was observed from the survey spectrum that Pb 4f, I 3d, C 1s, and N 1s signals exist on the surface of the pure tetragonal $\text{CH}_3\text{NH}_3\text{PbI}_3$ perovskite thin film. The presence of the oxygen atom is due to the fact that the thin film samples were not sputtered during the measurements. After running a wide survey scan on the surface of the pure tetragonal $\text{CH}_3\text{NH}_3\text{PbI}_3$ thin film, high resolution core level spectra for Pb 4f, I 3d, C 1s, and N 1s were taken.

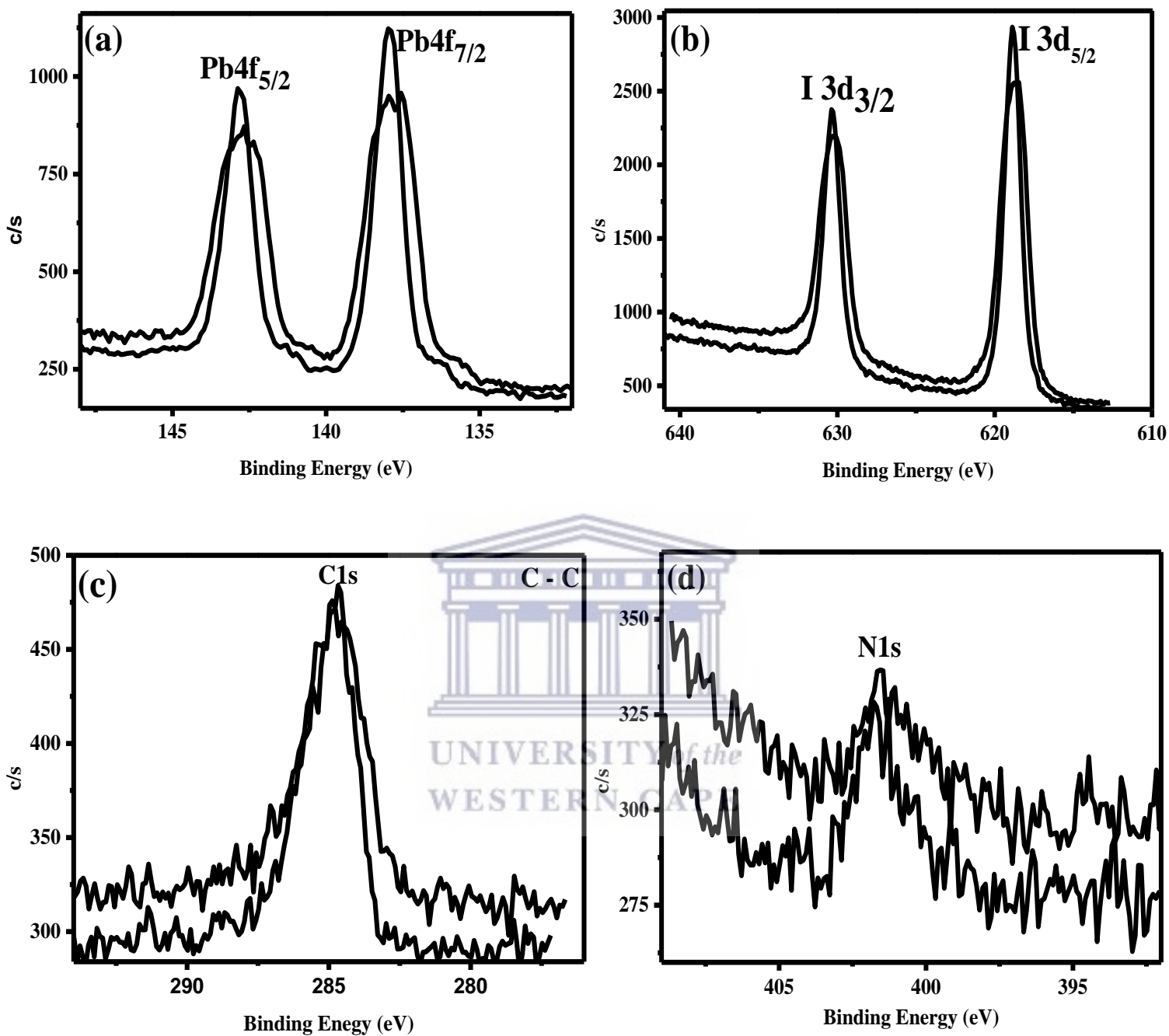


Figure 4.11: XPS high resolution scan for Pb4f (a), I_{3d} (b), C1s (d), N1s (c).

The Pb4f and I3d doublets displaying spin-orbit splitting into Pb4f_{5/2} & Pb4f_{7/2} and I3d_{5/2} & I3d_{3/2} were observed as shown from the high resolution core level spectra in **Figure 4.11**. The summary of the elemental binding energies is given in **Table 4.13**.

Table 4.13. Summary of the elemental binding energies.

Element	Orbital	Binding Energies (eV)
Pb	4f _{7/2} ; 4f _{5/2}	138.5 ; 143.5
I	3d _{5/2} ; 3d _{3/2}	619.3 ; 630.8
C	1s	284.8
N	1s	401.5

The first Pb4f_{5/2} peak located at 138.5 eV is characteristic of Pb²⁺ and the second Pb4f_{5/2} peak located at 143.5 eV is related to high Pb oxidation states; i.e. Pb⁴⁺. The Pb4f spin orbit splitting was determined to be 5 eV. Iodine at an oxidation state of -1; i.e. I⁻¹, was confirmed by I3d doublet at I3d_{5/2} (619.3 eV) & I3d_{3/2} (630.8 eV). The I3d spin orbit splitting was determined to be 11.5 eV comparing very well with the one reported in literature for iodine anions [45]. The difference in binding energy between Pb4f_{7/2} and I3d_{5/2} was determined to be 480.8 eV and it compared very well with the value reported in literature [46]. The C1s peak at 248.48 eV corresponds to C-C/C-H functional groups and the N1s peak at 401.5 eV corresponds to N-H functional group.

The XPS survey spectra for CH₃NH₃PbI₃•Ni, CH₃NH₃PbI₃•Cu and CH₃NH₃PbI₃•Zn also showed Pb4f, I3d, C1s, and N1s signals exist on the surface of the transition metals doped perovskite thin films. The XPS survey spectra are given in the **supporting information** at the end of the chapter. High resolution core level spectra for Ni, Cu and Zn are discussed below.

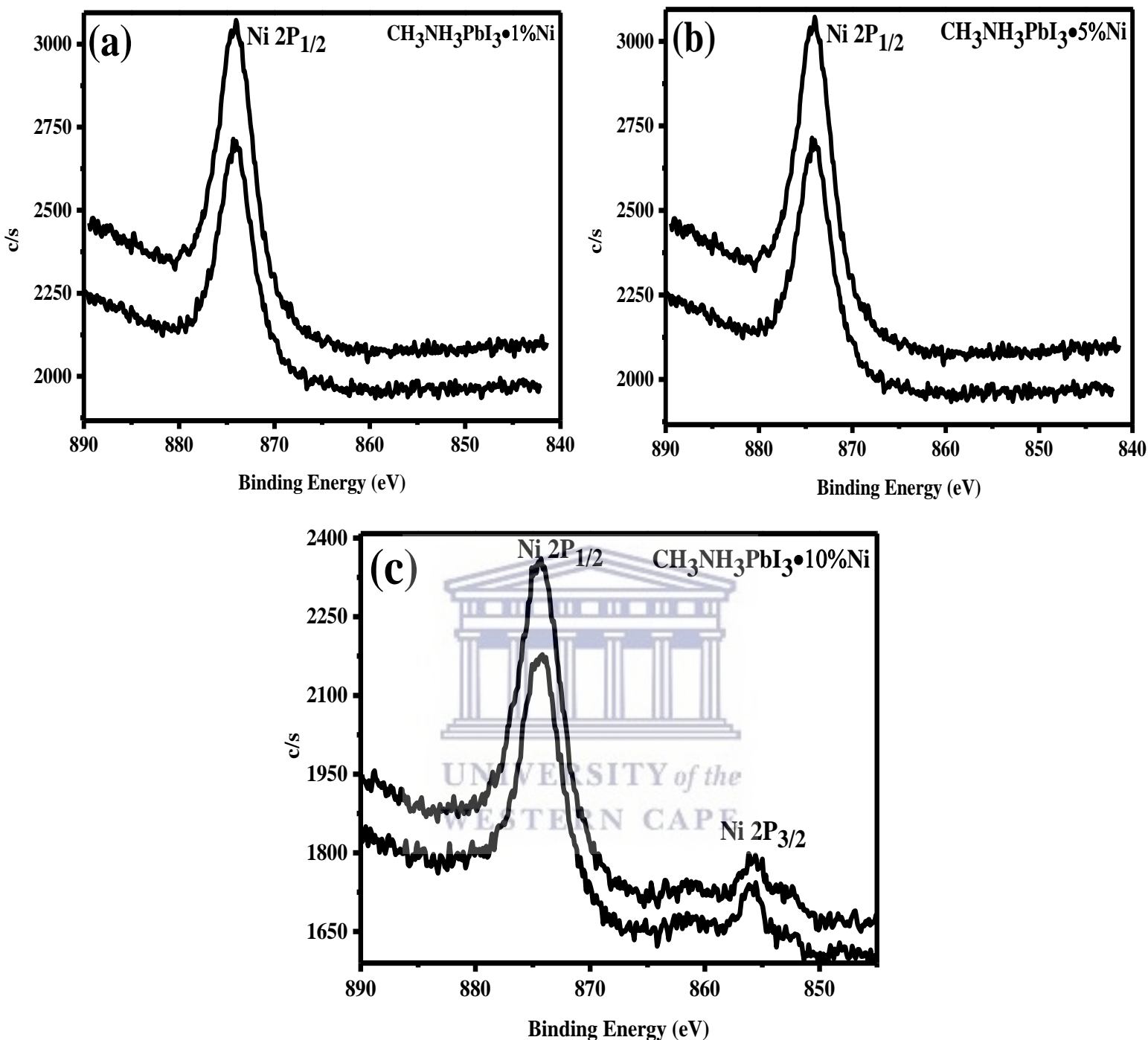


Figure 4.12: XPS high resolution scan for Ni $2P_{1/2}$ and Ni $2P_{3/2}$ for Ni doped $\text{CH}_3\text{NH}_3\text{PbI}_3\cdot\text{Ni}$ perovskite thin films (a, b and c).

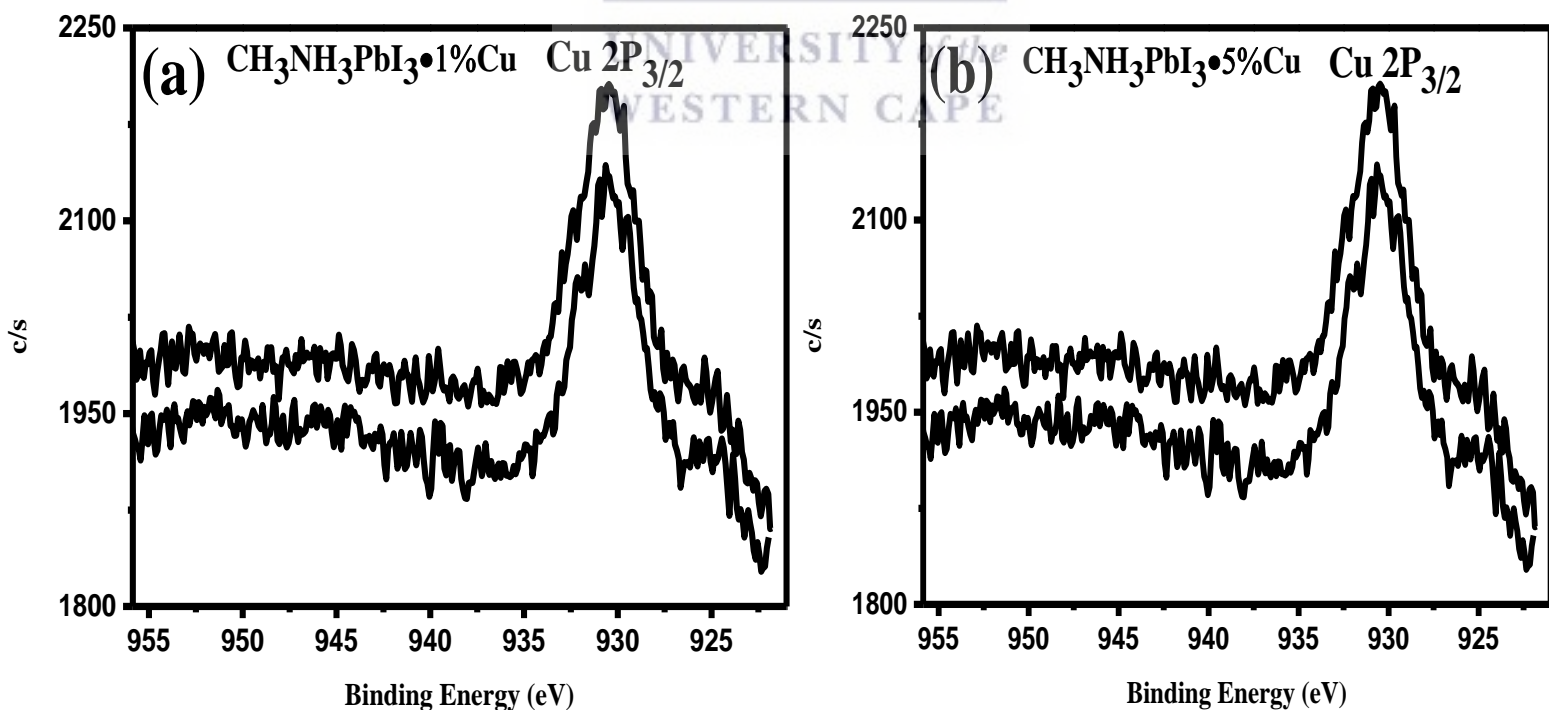
From **Figure 4.12**, the presence of Ni^{2+} was observed for all Ni doped $\text{CH}_3\text{NH}_3\text{PbI}_3\cdot\text{Ni}$ perovskite thin films. The Ni 2P doublet displaying spin-orbit splitting into Ni $2P_{1/2}$ & Ni $2P_{3/2}$ was observed from **Figure 4.12** for $\text{CH}_3\text{NH}_3\text{PbI}_3\cdot 10\%\text{Ni}$ (high content of Ni, i.e. 10%Ni) indicating the existence of Ni^{2+} at different microenvironments. The corresponding binding energies are given in **Table 4.14** below.

Table 4.14. Summary of the Ni binding energies.

Element	Orbital	Binding Energy (eV)
Ni	$2P_{1/2}$; $2P_{3/2}$	874.32 ; 855.77

The first $Ni2P_{1/2}$ peak located at 874.32 eV is characteristic of Ni^{2+} and the second $Ni2P_{3/2}$ peak located at 855.77 eV is related to high Ni oxidation states; i.e. Ni^{4+} . The $Ni2P$ spin orbit splitting was determined to be 18.55 eV.

From **Figure 4.13**, the presence of Cu^{2+} was observed for all Cu doped $CH_3NH_3PbI_3 \cdot Cu$ perovskite thin films. The $Cu2P$ doublet displaying spin-orbit splitting into $Cu2P_{1/2}$ & $Cu2P_{3/2}$ was observed from **Figure 4.13 (c)** for $CH_3NH_3PbI_3 \cdot 10\%Cu$ (high content of Cu, i.e. 10%Cu) indicating the existence of Cu^{2+} at different microenvironments.



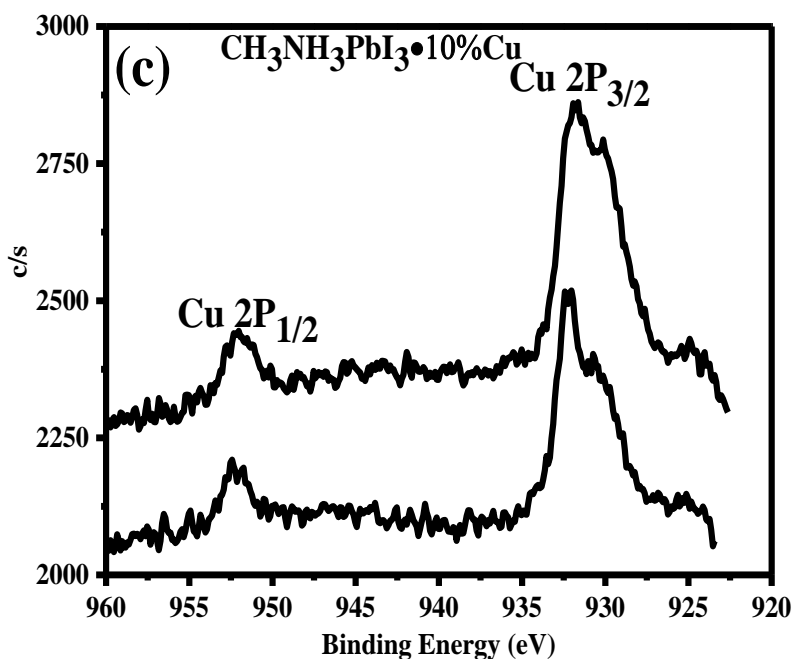


Figure 4.13: XPS high resolution scan for Cu $2P_{1/2}$ and Cu $2P_{3/2}$ for Cu doped CH₃NH₃PbI₃•Cu perovskite thin films.

The first Cu $2P_{1/2}$ peak located at 930.64 eV is characteristic of Cu and the second Cu $2P_{3/2}$ peak located at 951.92 eV is related to high Cu oxidation states; i.e. Cu²⁺. The Cu $2P$ spin orbit splitting was determined to be 21.28 eV. The corresponding Cu binding energies are given in **Table 4.15** below.

Table 4.15. Summary of the Cu binding energies.

Element	Orbital	Binding Energy (eV)
Cu	2P _{1/2} ; 2P _{3/2}	930.64 ; 951.92

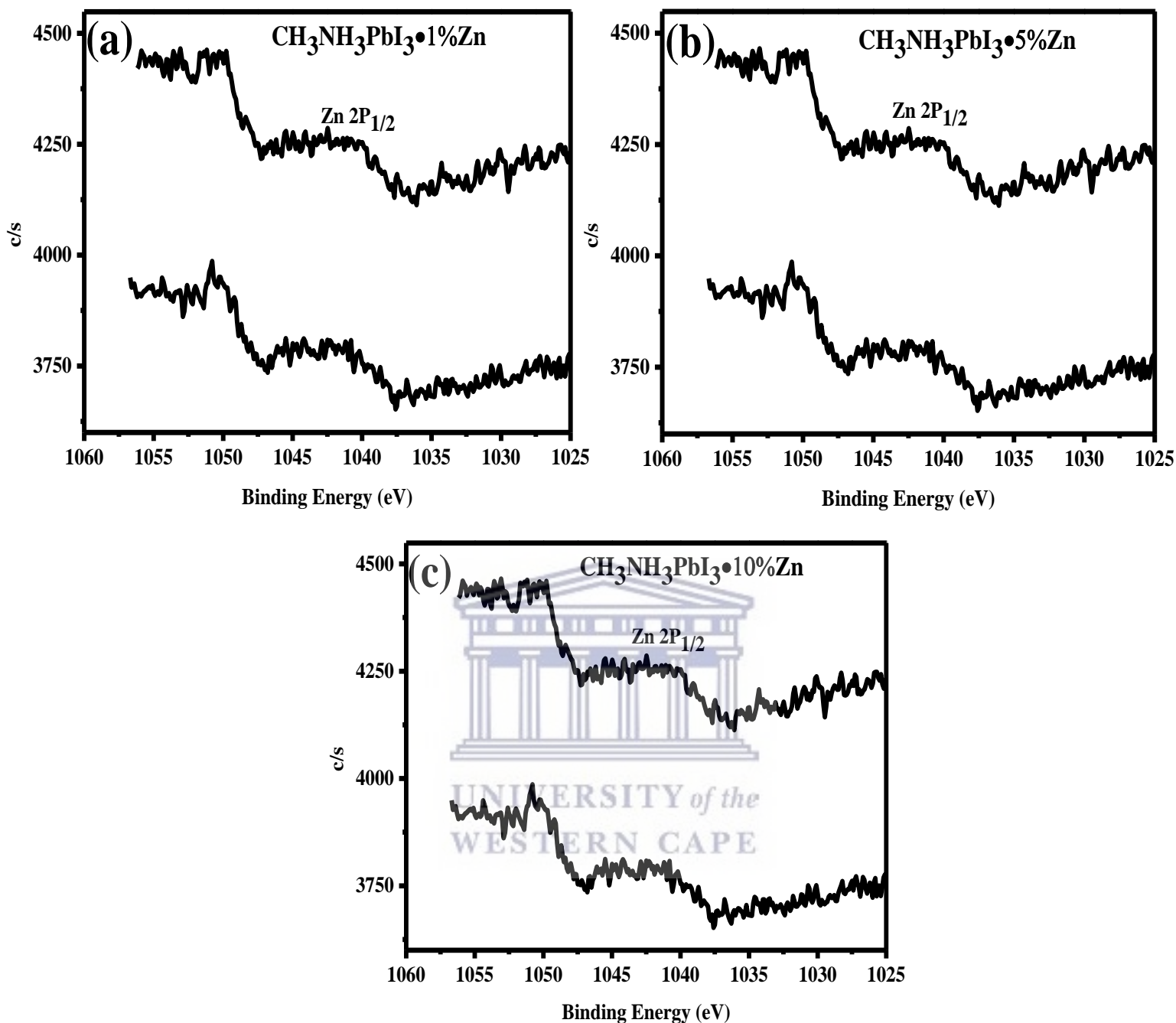


Figure 4.14: XPS high resolution scan for $Zn2P_{1/2}$ for Zn doped $CH_3NH_3PbI_3 \cdot Zn$ perovskite thin films.

From **Figure 4.14**, the presence of Zn^{2+} was observed for all Zn doped $CH_3NH_3PbI_3 \cdot Zn$ perovskite thin films. The $Zn2P_{1/2}$ peak located at 1044.09 eV is characteristic of Zn^{2+} . The corresponding binding energy is given in **Table 16** below.

Table 4.16. Summary of the Zn binding energy.

Element	Orbital	Binding Energy (eV)
Zn	2P _{1/2}	1044.09

The XPS measurements in this study confirmed the presence of the transition metals mainly in the +2 (and +4 at other microenvironments) oxidation states, i.e. Pb²⁺, Ni²⁺, Cu²⁺ and Zn²⁺. Thus, this qualitative analysis confirmed the successful incorporation of transition metals i.e. Ni, Cu and Zn into the hybrid perovskite structure.

4.2.3 Photo-physics studies by Ultra-violet visible (UV-vis) & Photoluminescence (PL)

The optical/electronic properties of all the materials under investigation were characterized by Ultra-violet (UV-vis) and photoluminescence spectroscopy techniques. For UV-vis spectroscopy, the characterization technique measures the amount of light absorbed or transmitted by a sample at a given wavelength. As the incident light (photons) passes through the material, its intensity is expressed by the Lambert-Beer-Bouguer law and the absorption coefficient is determined by the equation below;

$$\alpha = -\frac{1}{d} \ln\left(\frac{I}{I_0}\right) \quad (8)$$

where d is the film's thickness. The absorption coefficient α is dependent on the energy $h\nu$ of the incident light (photons). When the energy of the incident light is less than the energy bandgap of the material; i.e. $h\nu < E_g$ (direct), electron hole pairs cannot be generated, implying that the material is transparent. When the energy of the incident light is greater than the energy bandgap of the material; i.e. $h\nu \geq E_g$ (direct), electron hole pairs can be generated

and the absorption manifest. The dependence of absorption coefficient (α) on the frequency ν can be estimated by the following equation;

$$\alpha h\nu = A(h\nu - E_g)^{\frac{1}{2}} \quad (9)$$

where A is a proportional constant, h is Planck's constant and E_g is the bandgap energy. The optical energy bandgaps of hybrid perovskite materials under investigation were determined employing the Beer's law by plotting $(\alpha h\nu)^2$ vs $h\nu$ followed by the extrapolation of the linear part of the plot to the x-intercept that gives the optical energy bandgap [47,48].

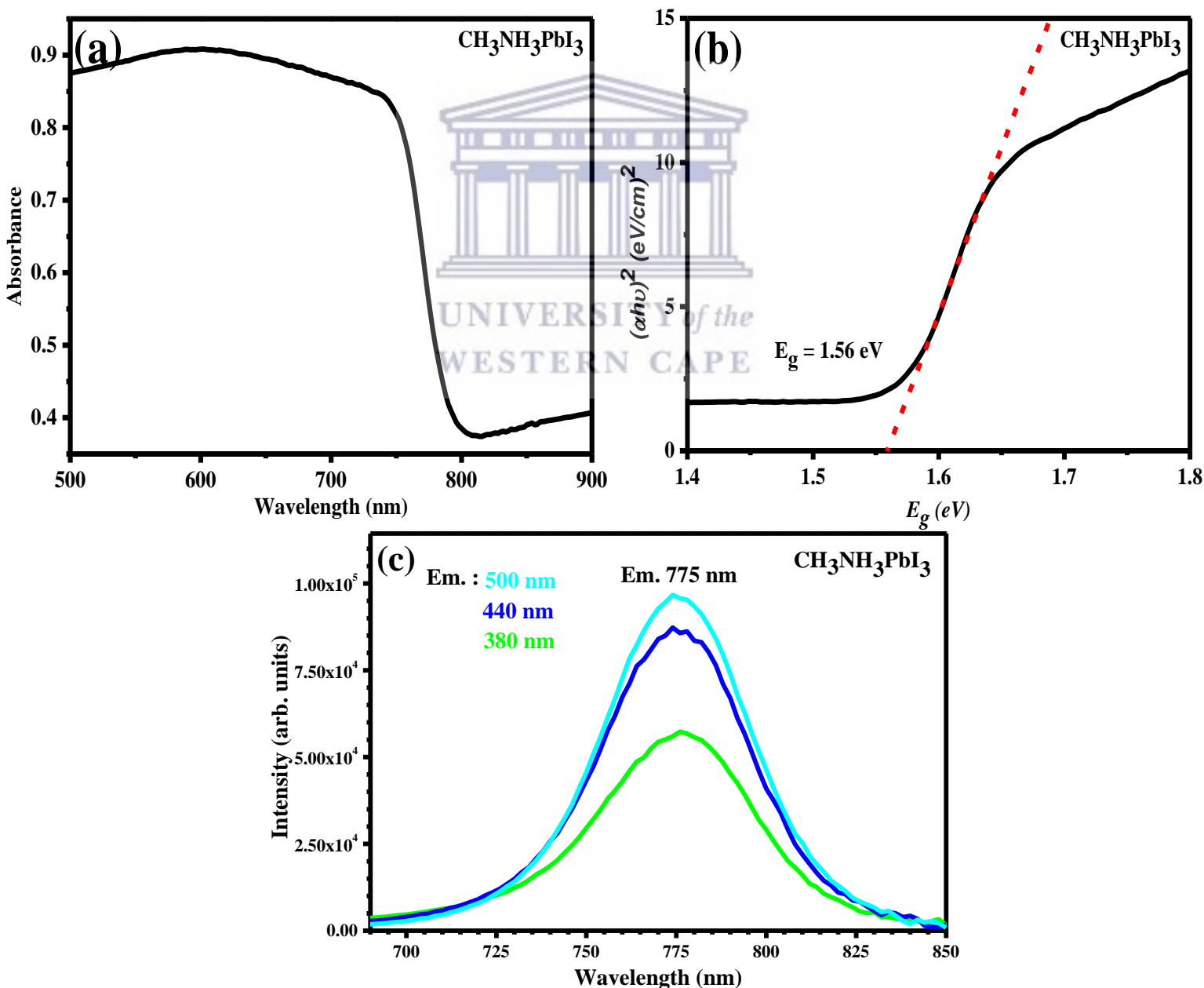


Figure 4.15: Absorption spectrum (a), $(\alpha h\nu)^2$ vs. $h\nu$ (b) and photoluminescence spectrum of $\text{CH}_3\text{NH}_3\text{PbI}_3$ (c).

The absorption spectrum of the pure tetragonal $\text{CH}_3\text{NH}_3\text{PbI}_3$ perovskite is given in **Figure 4.15 (a)**. The absorption spectrum shows that the pure (none-doped) material $\text{CH}_3\text{NH}_3\text{PbI}_3$ absorbs across most of the solar spectrum from ultra-violet visible region (500 nm) to the near infrared region (801 nm) [30,49]. The energy bandgap of the material was determined to be 1.56 eV by extrapolation to x-intercept of a linear plot of $(\alpha hv)^2$ vs. hv as shown in **Figure 4.15 (b)**. This energy bandgap value (i.e. 1.56 eV, good for sunlight absorption) compares very well with the one reported in literature for a perfect tetragonal hybrid perovskite thin film material [50,51].

Photoluminescence spectrum of pure tetragonal $\text{CH}_3\text{NH}_3\text{PbI}_3$ perovskite is given in **Figure 4.15 (c)**. The photoluminescence characterization technique is a useful tool for the study of optical properties and dynamic processes that take place in photovoltaic materials. During photoluminescence characterization, the incident light is bombarded on the material which subsequently excites an electron from the filled valence band and transitions it to conduction band, and this leaves a hole behind. The created electron hole pair then relaxes to the bottom of the conduction band and on top of the valence band, respectively. As the electron hole pairs recombine, a photon with energy equal to the energy bandgap of the material is emitted, and this process is called radiative recombination. For pure tetragonal $\text{CH}_3\text{NH}_3\text{PbI}_3$ excited at different wavelengths, i.e. 500, 440 and 380 nm, a sharp emission was invariably observed at a wavelength of 775 nm as shown in **Figure 4.15 (c)**. This demonstrates that the pure tetragonal $\text{CH}_3\text{NH}_3\text{PbI}_3$ perovskite thin film had a uniform particle size distribution. The invariable single photoluminescence emission at 775 nm further demonstrates that all the PbI_2 and $\text{CH}_3\text{NH}_3\text{I}$ starting materials were converted into $\text{CH}_3\text{NH}_3\text{PbI}_3$ during the annealing treatment of the thin film. The photoluminescence emission peak at 775 nm is close to the absorption onset at 801 nm indicating that the photoluminescence emission was mainly from the energy bandgap (~1.56 eV) rather than trap or sub-band states [52].

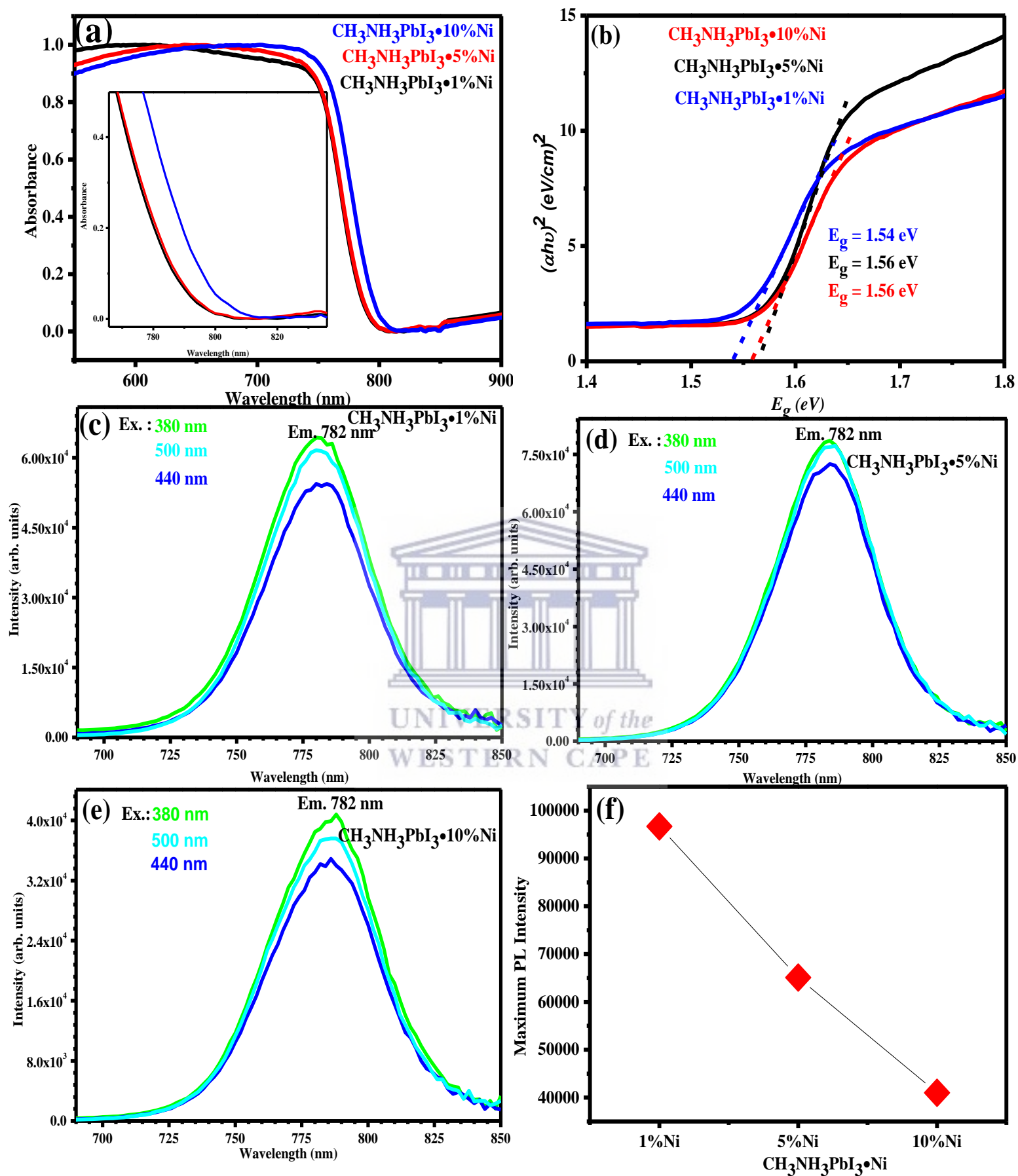
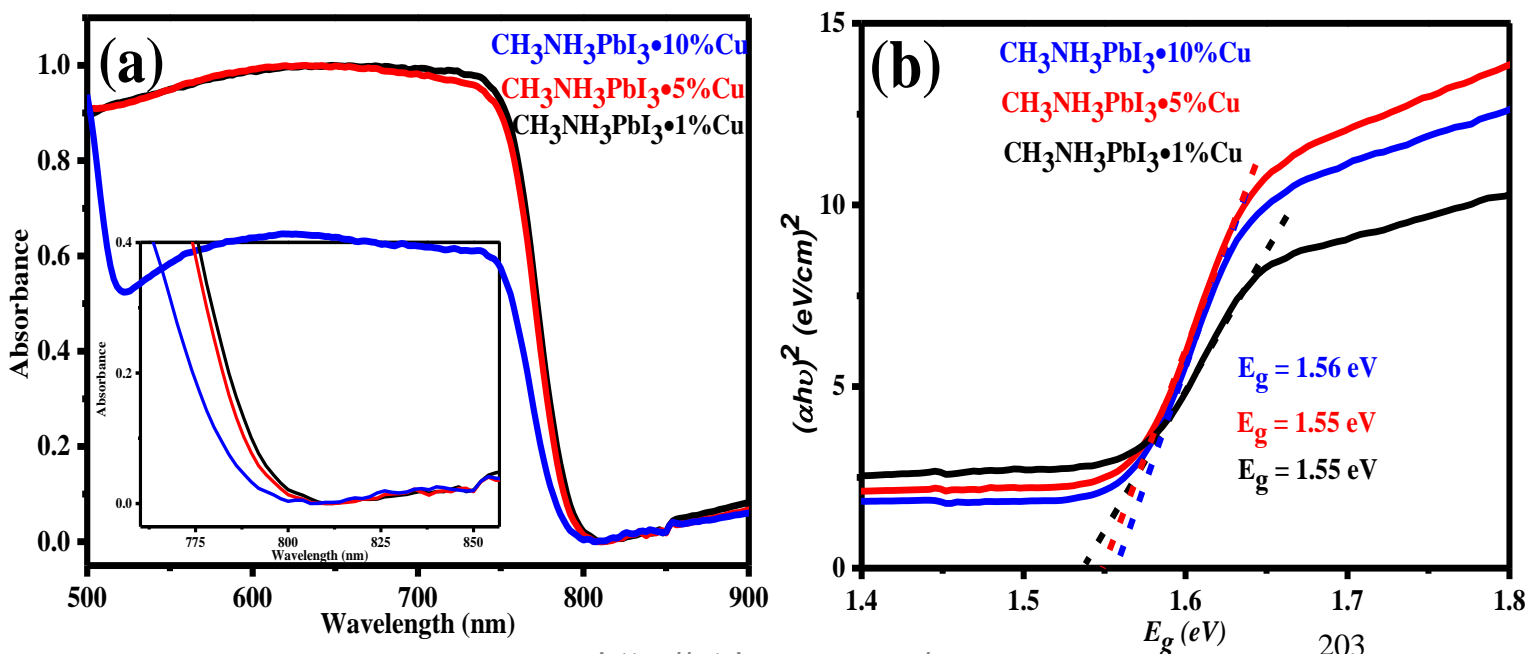


Figure 4.16: Absorption spectrum (a), $(\alpha h\nu)^2$ vs. $h\nu$ (b) and photoluminescence spectra (c, d, e) and photoluminescence quenching of $\text{CH}_3\text{NH}_3\text{PbI}_3 \cdot \text{Ni}$ thin films (f).

The absorption spectra of Ni doped $\text{CH}_3\text{NH}_3\text{PbI}_3\cdot\text{Ni}$ perovskite thin films are given in **Figure 4.16 (a)**. The absorption spectra show that the $\text{CH}_3\text{NH}_3\text{PbI}_3\cdot\text{Ni}$ perovskite thin films absorb in the same range as the pure tetragonal $\text{CH}_3\text{NH}_3\text{PbI}_3$ (undoped) from ultra-violet region (500 nm) to the near infrared region (800 to 811nm) across the solar spectrum. An insignificant redshift absorption by $\text{CH}_3\text{NH}_3\text{PbI}_3\cdot 10\%\text{Ni}$ perovskite thin film was observed which could suggest a slight (negligible) crystallite (grain) size increase by the dopant (i.e. 10%Ni). This observation shows that the 10%Ni dopant slightly improved the harvest of most of the solar spectrum. The energy bandgaps of Ni doped $\text{CH}_3\text{NH}_3\text{PbI}_3\cdot\text{Ni}$ perovskite thin films were determined to be 1.54, 1.56 and 1.56 eV for $\text{CH}_3\text{NH}_3\text{PbI}_3\cdot 1\%\text{Ni}$, $\text{CH}_3\text{NH}_3\text{PbI}_3\cdot 5\%\text{Ni}$ and $\text{CH}_3\text{NH}_3\text{PbI}_3\cdot 10\%\text{Ni}$, respectively, by extrapolation to zero of a linear plot of $(ah\nu)^2$ vs. $h\nu$ as shown in **Figure 4.16 (b)**. These energy bandgap values (i.e. 1.54 and 1.56 eV) are also in close proximity with the energy bandgap reported in literature for pure tetragonal $\text{CH}_3\text{NH}_3\text{PbI}_3$ [50,51]. The proximity of the energy bandgaps came as no surprise since it was observed from the XRD analyses that Ni dopant did not have a significant impact in the crystal lattice parameters of the pure tetragonal $\text{CH}_3\text{NH}_3\text{PbI}_3$ crystal structure.

The Ni doped $\text{CH}_3\text{NH}_3\text{PbI}_3\cdot\text{Ni}$ perovskite thin films were excited at different wavelengths, i.e. 500, 440 and 380 nm, and a sharp photoluminescence emission was invariably observed at a wavelength of 782 nm as shown in **Figure 4.16 (c), (d) and (e)**. This demonstrates that $\text{CH}_3\text{NH}_3\text{PbI}_3\cdot\text{Ni}$ perovskite thin films also had a uniform particle size distribution. The invariable single photoluminescence emission at 782 nm further demonstrates that all the PbI_2 , NiI_2 and $\text{CH}_3\text{NH}_3\text{I}$ starting materials were converted into $\text{CH}_3\text{NH}_3\text{PbI}_3\cdot\text{Ni}$ during the annealing treatment of the thin films. The invariable sharp emission at 782 nm demonstrated a redshift in comparison to the photoluminescence emission at 775 nm observed for pure tetragonal $\text{CH}_3\text{NH}_3\text{PbI}_3$.

It was observed from **Figure 4.16 (f)** that photoluminescence intensity decreased as the content of Ni dopant increased in the $\text{CH}_3\text{NH}_3\text{PbI}_3\cdot\text{Ni}$ perovskite thin films. This observation is called quenching effect which occurs as a result of energy transfer from the dopant (Ni) to the host ($\text{CH}_3\text{NH}_3\text{PbI}_3$). The quenching effect results in non-radiative recombination dynamics (reduction of the photoluminescence intensity) caused by structural defects (structural imperfections). Therefore, for Ni doped $\text{CH}_3\text{NH}_3\text{PbI}_3\cdot\text{Ni}$ perovskite thin films, quenching was anticipated due to dislocation densities (structural defects) imposed by Ni dopants as observed in **Figure 4.8 (a)** under structural analysis discussion above. The minor redshift photoluminescence emission; from $\text{CH}_3\text{NH}_3\text{PbI}_3$ (775 nm) to $\text{CH}_3\text{NH}_3\text{PbI}_3\cdot\text{Ni}$ (782 nm) was in agreement with the minor redshift absorption of the Ni doped $\text{CH}_3\text{NH}_3\text{PbI}_3\cdot\text{Ni}$ perovskite thin films; from $\text{CH}_3\text{NH}_3\text{PbI}_3$ (801 nm) to $\text{CH}_3\text{NH}_3\text{PbI}_3\cdot\text{Ni}$ (811 nm).



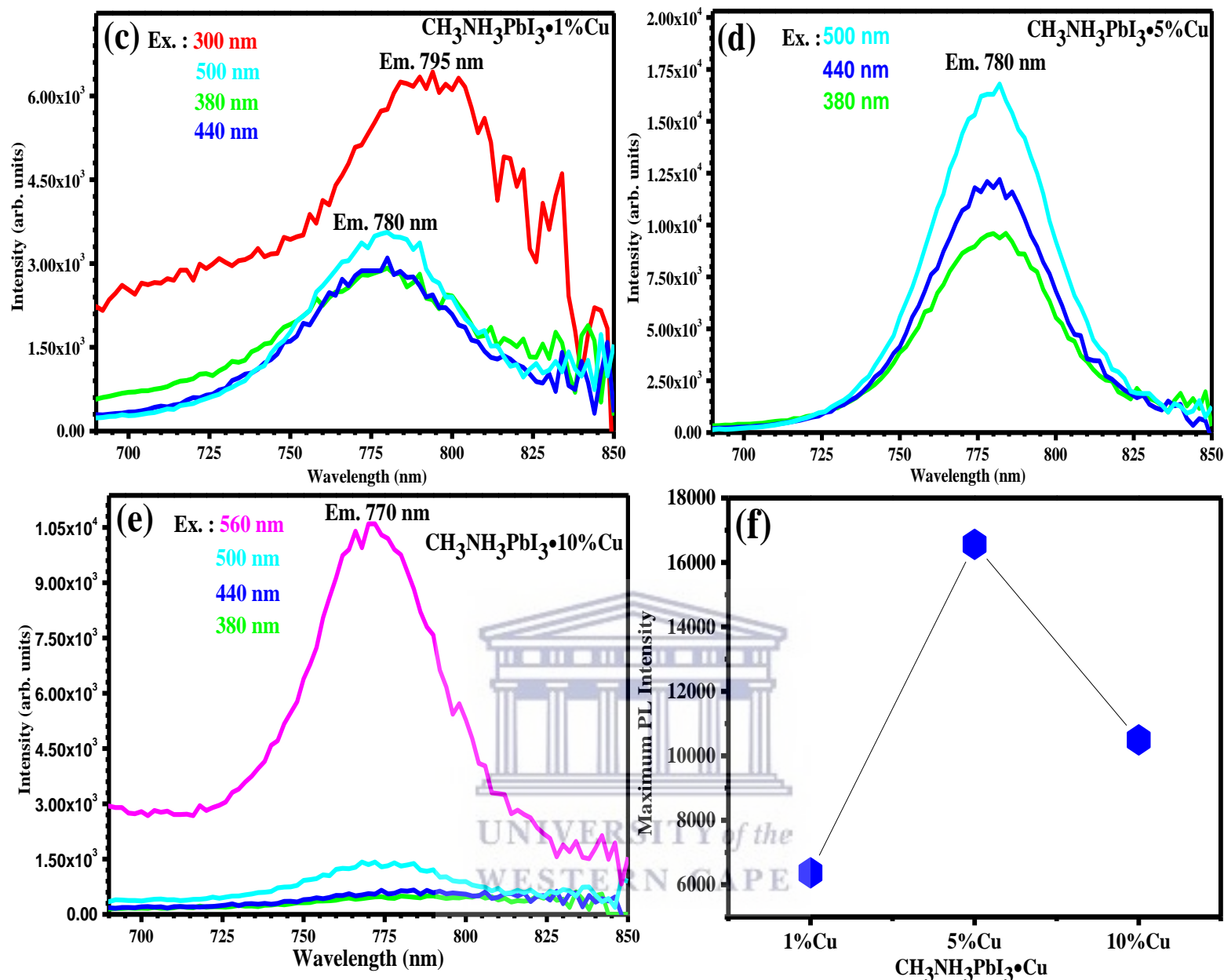


Figure 4.17: Absorption spectrum (a), $(ah\nu)^2$ vs. $h\nu$ (b) and photoluminescence spectra (c, d, e) and photoluminescence quenching (f) of CH₃NH₃PbI₃•Cu thin films.

The absorption spectra of Cu doped CH₃NH₃PbI₃•Cu perovskite thin films are given in **Figure 4.17 (a)**. The absorption spectra show that CH₃NH₃PbI₃•Cu perovskite thin films absorb from ultra-violet visible region (500 nm) to the near infrared region (800 nm) of the solar spectrum. However, a slight (almost negligible) blue-shift in absorption was observed for CH₃NH₃PbI₃•10%Cu (absorption band edge at 785nm) which could be ascribed to high degree of structural defects imposed by Cu dopant, see **Figure 4.8 (b)**. The energy bandgaps of Cu doped CH₃NH₃PbI₃•Cu perovskite thin films were determined to be 1.55, 1.55 and 1.56

eV for $\text{CH}_3\text{NH}_3\text{PbI}_3\cdot 1\%\text{Cu}$, $\text{CH}_3\text{NH}_3\text{PbI}_3\cdot 5\%\text{Cu}$ and $\text{CH}_3\text{NH}_3\text{PbI}_3\cdot 10\%\text{Cu}$, respectively, by extrapolation to zero of a linear plot of $(\alpha hv)^2$ vs. hv as shown in **Figure 4.17 (b)**. These energy bandgap values (i.e. 1.54 and 1.55 eV) are also in close proximity with the energy bandgap reported in literature for pure tetragonal $\text{CH}_3\text{NH}_3\text{PbI}_3$ [50,51].

The Cu doped $\text{CH}_3\text{NH}_3\text{PbI}_3\cdot\text{Cu}$ perovskite thin films were similarly excited at different wavelengths, i.e. 500, 440, 380 and 300 nm, and conversely a noisy (rough) photoluminescence emission was invariably observed at wavelengths 770 nm and 780 nm (implying a uniform particle size distribution) as shown in **Figure 4.17 (c), (d) and (e)**. The noisy (rough) photoluminescence emission demonstrates that $\text{CH}_3\text{NH}_3\text{PbI}_3\cdot\text{Cu}$ perovskite thin films had a high level of structural imperfections induced by Cu dopant as seen from **Figure 4.8 (b)**. The invariable sharp emission at 780 nm for $\text{CH}_3\text{NH}_3\text{PbI}_3\cdot 1\%$ and $\text{CH}_3\text{NH}_3\text{PbI}_3\cdot 5\%$ demonstrated a slight red-shift emission in comparison to the photoluminescence emission at 775 nm observed for pure tetragonal $\text{CH}_3\text{NH}_3\text{PbI}_3$, see **Figure 4.15 (c) and Figure 4.17 (c) and (d)**. A slight blue-shift emission was also observed for $\text{CH}_3\text{NH}_3\text{PbI}_3\cdot 10\%$ (emission at 770nm), see **Figure 4.17 (e)**. It was also observed from **Figure 4.17 (f)** that photoluminescence intensity ultimately decreased as the content of Cu dopant increased, i.e. $\text{CH}_3\text{NH}_3\text{PbI}_3\cdot 10\%\text{Cu}$. Thus, a quenching effect induced by Cu which occurs as a result of energy transfer from the dopant (Cu) to the host ($\text{CH}_3\text{NH}_3\text{PbI}_3$) was also observed. Therefore, for Cu doped $\text{CH}_3\text{NH}_3\text{PbI}_3\cdot\text{Cu}$ perovskite thin films, quenching was also anticipated due to high degree of dislocation densities (structural defects/imperfections) imposed by Cu dopants as observed in **Figure 4.8 (b)** under structural analysis discussion above (i.e. increase in structural defects as the Cu content increases).

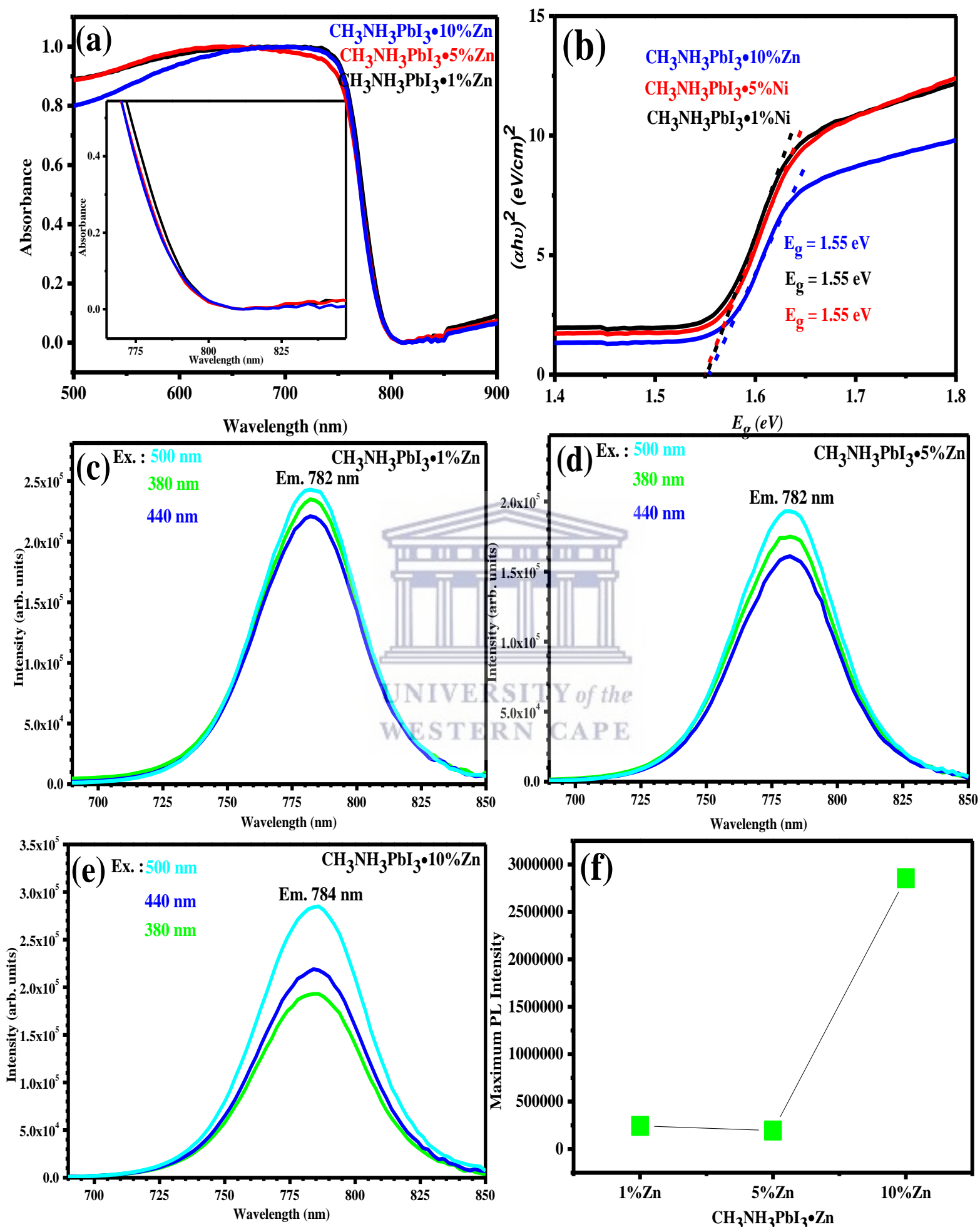


Figure 4.18: Absorption spectrum (a), $(\alpha h\nu)^2$ vs. $h\nu$ (b) and photoluminescence spectra (c, d, e) and photoluminescence quenching (f) of $\text{CH}_3\text{NH}_3\text{PbI}_3 \cdot \text{Zn}$ thin films.

The absorption spectra of Zn doped $\text{CH}_3\text{NH}_3\text{PbI}_3\cdot\text{Zn}$ perovskite thin films are given in **Figure 4.18 (a)**. The absorption spectra show that $\text{CH}_3\text{NH}_3\text{PbI}_3\cdot\text{Zn}$ perovskite thin films also absorb from ultra-violet visible region (500 nm) to the near infrared region (800 nm) across the solar spectrum similarly to $\text{CH}_3\text{NH}_3\text{PbI}_3\cdot\text{Ni}$ and $\text{CH}_3\text{NH}_3\text{PbI}_3\cdot\text{Cu}$, respectively. A near infrared absorption by $\text{CH}_3\text{NH}_3\text{PbI}_3\cdot\text{Zn}$ (800 nm) thin films equal to that of $\text{CH}_3\text{NH}_3\text{PbI}_3$ (800 nm) was observed which further suggests that the Zn dopant did not induce any changes to the crystal lattice parameters as seen from **Table 4.9** (i.e. this observation shows that the Zn dopant did not have a significant impact on the crystallite (grain size) of pure $\text{CH}_3\text{NH}_3\text{PbI}_3$ (host)). These energy bandgap values (i.e. 1.55 eV for all $\text{CH}_3\text{NH}_3\text{PbI}_3\cdot\text{Zn}$ thin film materials) are also in close proximity with the energy bandgap reported in literature for pure tetragonal $\text{CH}_3\text{NH}_3\text{PbI}_3$ [50,51]. Similarly to Ni and Cu doped perovskite thin films (i.e. ($\text{CH}_3\text{NH}_3\text{PbI}_3\cdot\text{Ni}$ and $\text{CH}_3\text{NH}_3\text{PbI}_3\cdot\text{Cu}$), Zn doped $\text{CH}_3\text{NH}_3\text{PbI}_3\cdot\text{Zn}$ perovskite thin films still demonstrated the potential for optoelectronic (photovoltaic) application since they have good absorption properties and the energy bandgap equal to that of the pure tetragonal $\text{CH}_3\text{NH}_3\text{PbI}_3$ perovskite thin film. The Zn doped $\text{CH}_3\text{NH}_3\text{PbI}_3\cdot\text{Zn}$ perovskite thin films were excited at different wavelengths, i.e. 500, 440 and 380 nm, and sharp photoluminescence emissions were invariably observed at a wavelength of 782 nm and 784 nm as shown in **Figure 4.18 (c), (d) and (e)**, respectively. This demonstrates that $\text{CH}_3\text{NH}_3\text{PbI}_3\cdot\text{Zn}$ perovskite thin films also had a uniform particle size distribution. The invariable single photoluminescence emissions at 782 nm and 784 nm further demonstrates that all the PbI_2 , ZnI_2 and $\text{CH}_3\text{NH}_3\text{I}$ starting materials were converted into $\text{CH}_3\text{NH}_3\text{PbI}_3\cdot\text{Zn}$ during the annealing treatment of the thin films. The invariable sharp emissions at 782 nm and 784 nm demonstrated a redshift in comparison to the photoluminescence emission at 775 nm observed for pure tetragonal $\text{CH}_3\text{NH}_3\text{PbI}_3$. In contrast to Ni and Cu doped perovskite thin films; ($\text{CH}_3\text{NH}_3\text{PbI}_3\cdot\text{Ni}$ and $\text{CH}_3\text{NH}_3\text{PbI}_3\cdot\text{Cu}$), it was also observed from **Figure 4.18 (f)** that

photoluminescence intensity increased as the content of Zn dopant increased. This observation suggests that Zn suppressed the non-radiative recombination emissions and as a result advanced radiative recombination emissions. Thus, a quenching effect was not observed for $\text{CH}_3\text{NH}_3\text{PbI}_3 \cdot \text{Zn}$ perovskite thin films (i.e. there was no energy transfer from Zn dopant to $\text{CH}_3\text{NH}_3\text{PbI}_3$). Therefore, for Zn doped $\text{CH}_3\text{NH}_3\text{PbI}_3 \cdot \text{Zn}$ perovskite thin films, the quenching effect was not observed due to lower degree of dislocation densities (structural defects/imperfections) demonstrated by Zn dopants as observed in **Figure 4.9 (b)** under structural analysis discussion above (i.e. decrease in structural defects as Zn content increases). It was also observed from **Figure 4.6 (c)** that as the Zn content increase in $\text{CH}_3\text{NH}_3\text{PbI}_3 \cdot \text{Zn}$ thin films, there was a decrease in the micro strain induced on the thin films during annealing treatment. Therefore Zn dopants relaxed the micro strain and reduced the concentration of structural defects (dislocation density) on $\text{CH}_3\text{NH}_3\text{PbI}_3 \cdot \text{Zn}$ thin films and promoted radiative recombination emissions [44], making the Zn dopant the best candidate amongst Ni and Cu for Pb substitution in $\text{CH}_3\text{NH}_3\text{PbI}_3$. This observation further suggests that Zn perovskites (doped $\text{CH}_3\text{NH}_3\text{Pb}_{1-x}\text{Zn}_x\text{I}_3$ or 100% Zn substituted perovskites will yield perovskite thin films $\text{CH}_3\text{NH}_3(\text{Pb}/\text{Zn})\text{I}_3$ materials with good intrinsic stability (owing to relaxed micro strain and lower structural imperfections), good optical properties (owing to advanced radiative recombination emissions) and ultimately advanced photovoltaic performance and durable solar cell devices [42].

In summary, the optical studies by UV-vis have demonstrated that the transition metal dopants; Ni, Cu and Zn, absorb in the same range as the pure tetragonal $\text{CH}_3\text{NH}_3\text{PbI}_3$ (i.e. from ultra violet (~550 nm) to near infrared region (~800 nm) of the solar spectrum [30,49] as seen from the results above and these absorptions resulted in energy bandgaps (i.e. 1.55 eV) virtually equal to the one reported in literature for pure tetragonal $\text{CH}_3\text{NH}_3\text{PbI}_3$ perovskite thin film [50,51]. Most of the solar energy is collected in the visible and near-

infrared (NIR) region of the solar spectrum, and therefore the absorption spectrum of the hybrid perovskite material must match with that of the solar spectrum in order to efficiently harvest the solar energy. Nonetheless, for a hybrid perovskite material with an energy bandgap that is too narrow, a collection of additional current is demonstrated by perovskite solar cell devices but with significantly low open-circuit voltage (V_{OC}). Conversely, for hybrid perovskite material with an energy bandgap that is too wide (2 eV), only a small portion of the solar energy can be harvested. Therefore, a hybrid perovskite material with an energy bandgap of around 1.4 – 1.6 eV is suitable for the development of single junction solar cell devices [53]. Thus, the NiCuZn hybrid perovskite thin film materials explored in this study have demonstrated a potential for application in single-junction solar cells owing to their narrow energy bandgap of ~ 1.55 eV and good material crystallinity observed in structural studies (i.e. 78.41%, 67.84% and 81.08% for $CH_3NH_3PbI_3 \cdot Ni$, $CH_3NH_3PbI_3 \cdot Cu$ and $CH_3NH_3PbI_3 \cdot Zn$, respectively). It has been reported in literature that the energy bandgap of hybrid perovskite materials can be narrowed through (i) increasing the in-plane M – I – M bond angle (via octahedral distortions), (ii) increasing the dimensionality of the $MI(X)_6$ network, and (iii) decreasing the electronegativity of the anions [54]. All hybrid perovskite thin film materials prepared in this study utilized methylammonium as the organic cation A. This organic cation A in the hybrid perovskite compound ABX_3 (where A = organic cation, B = metal and X = halide anions) plays a role of maintaining charge neutrality [55] of the whole hybrid perovskite crystal lattice. The size of an organic cation A has an impact on the optical, electronic and structural properties of hybrid perovskite material [5]. It has been reported in literature that the expansion and compression of the whole crystal lattice is dependent upon the size of organic cation A. The energy bandgap can be tuned by altering the B – X bond length and it can also be attained through a careful variation of the size of the organic cation that fits the between the corner sharing B – X octahedral [56,57]. New perovskite materials

synthesized by altering the organic cation A in ABX_3 halide compound have been explored. It was found that hybrid perovskite materials synthesized utilizing a larger ethylammonium cation demonstrated more widening of energy bandgap owing to 2H-type structural rearrangement as results of ethylammonium cation not being able to maintain a 3D tetragonal structure of perovskite crystal lattice [58]; however, the utilization of slightly larger formamidinium organic cation blended with methylammonium demonstrated better results for tuning the energy bandgap without perturbing the principal tetragonal hybrid perovskite crystal structure. Formamidinium lead iodide perovskite attained a narrower energy bandgap of 1.48 eV in comparison to 1.57 eV attained by methylammonium lead iodide [5]. Furthermore, the tuning of energy bandgap without perturbing the principal tetragonal crystal structure of the hybrid perovskite material was attained through the partial replacement of methylammonium with a smaller inorganic alkali metal cation, i.e. Cesium (Cs). The improvement in power conversion efficiency of hybrid perovskite was attained by narrowing the energy bandgap (improved light absorption across the solar spectrum) coupled with good material crystallinity [59]. In this study, all compounds utilized methylammonium as the organic cation A and this explains why there was no significant impact observed on the lattice parameters and the crystallite (grain) size. Hence, there was no significant impact on the energy bandgap observed (i.e. all compounds had an energy bandgap of ~ 1.55 eV). Moreover, all compounds utilized iodine as the halide anion indicating that the electronegativity of the halide anion was kept constant and hence there was no impact observed on the energy bandgap.

Photoluminescence studies exhibited slight redshift emissions (from 775 nm to ~ 780 nm for pure tetragonal $CH_3NH_3PbI_3$ and transition metal doped $CH_3NH_3PbI_3 \cdot Ni/Cu/Zn$ perovskite thin films, respectively) induced by Ni, Cu and Zn. This redshift effect was not pronounced in the absorption studies. Nonetheless, the minor redshift in emissions could be attributed to

fewer (reduced) defect states in the bulk [60]. The photoluminescence emission is typically interrelated to the recombination channel connected to the energy bandgap and trap state. The slight red shift emissions observed for NiCuZn doped hybrid perovskite thin films demonstrate that the transition metal dopants promote the removal of structural defects and reduce the trap density around the band edge, which could decrease the recombination loss and as a result improve the collection of photocurrent by the solar cell device. Photoluminescence studies further revealed the quenching effect induced by Ni and Cu which was attributed by the imposed micro strain and structural defects in the perovskite thin film materials, i.e. $\text{CH}_3\text{NH}_3\text{PbI}_3\cdot\text{Ni}$ and $\text{CH}_3\text{NH}_3\text{PbI}_3\cdot\text{Cu}$. However, for Zn doped thin film materials $\text{CH}_3\text{NH}_3\text{PbI}_3\cdot\text{Zn}$, a reverse effect was observed, Zn dopant advanced the radiative recombination emission which was exhibited in higher photoluminescence emission intensity as the Zn content was increased from 1 to 10%. These results were attributed to relaxed micro-strain; lower degree of structural imperfections and higher crystallinity (~81.08% on average) induced by Zn dopant. The improvement of crystallinity quality heightens the optical transition oscillation [61] and advances the photoluminescence emissions.

4.2.4 Microscopic analysis by High Resolution Scanning Electron Microscopy (HR-SEM)

The surface morphology and thin films quality of all the perovskite thin films deposited on ITO glass substrates were studied by HR-SEM technique. In this study, hybrid perovskite thin films were prepared via two step spin-coat deposition technique reported by Xiao *et al.* [62]. Firstly, the metal halides; PbI_2 , NiI_2 , CuI and ZnI_2 , dissolved in 8 mg/mL terephthalic acid (TPA)-dimethylformamide (DMF) were spin coated and annealed at 100°C on ITO glass substrates. Secondly, $\text{CH}_3\text{NH}_3\text{I}$ was deposited on top of the metal halides, spin coated and

annealed at 70°C to yield hybrid perovskite thin films; $\text{CH}_3\text{NH}_3\text{PbI}_3$, $\text{CH}_3\text{NH}_3\text{PbI}_3\cdot\text{Ni}$, $\text{CH}_3\text{NH}_3\text{PbI}_3\cdot\text{Cu}$ and $\text{CH}_3\text{NH}_3\text{PbI}_3\cdot\text{Zn}$. The terephthalic acid additive was utilized to stabilize the perovskite thin film materials from deterioration (degradation) upon exposure to air (oxygen) and humidity. The addition of terephthalic acid was inspired by the work reported by X. Hou *et al.* for the construction of efficient and stable perovskites via interconnecting perovskite grains [63]. The thin films preparation route was the same for all the compounds, the only varying factor was the addition of transition metal dopants; Ni, Cu and Zn at different concentrations (i.e. 1, 5 and 10%). So, the evolution of morphology will be discussed based on the impact of TPA additive as well as the variation and the concentration of transition metal dopants.

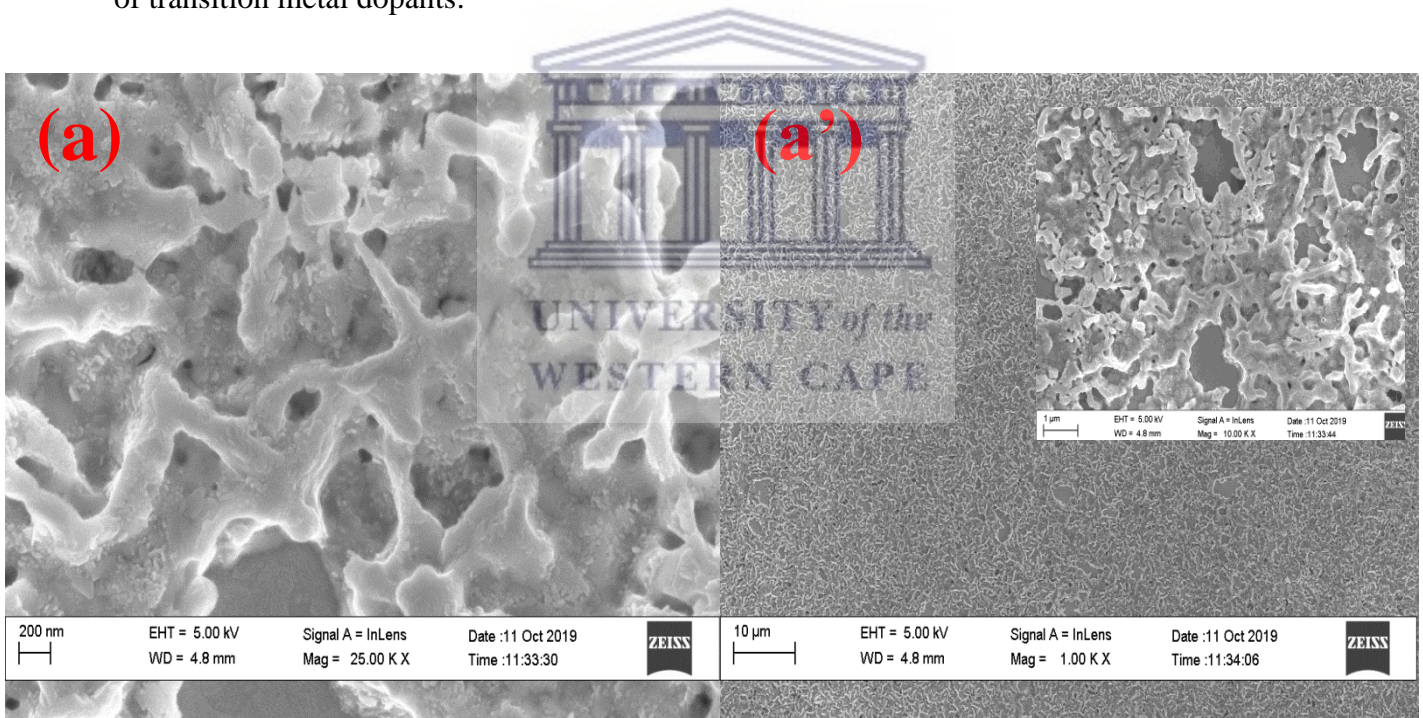
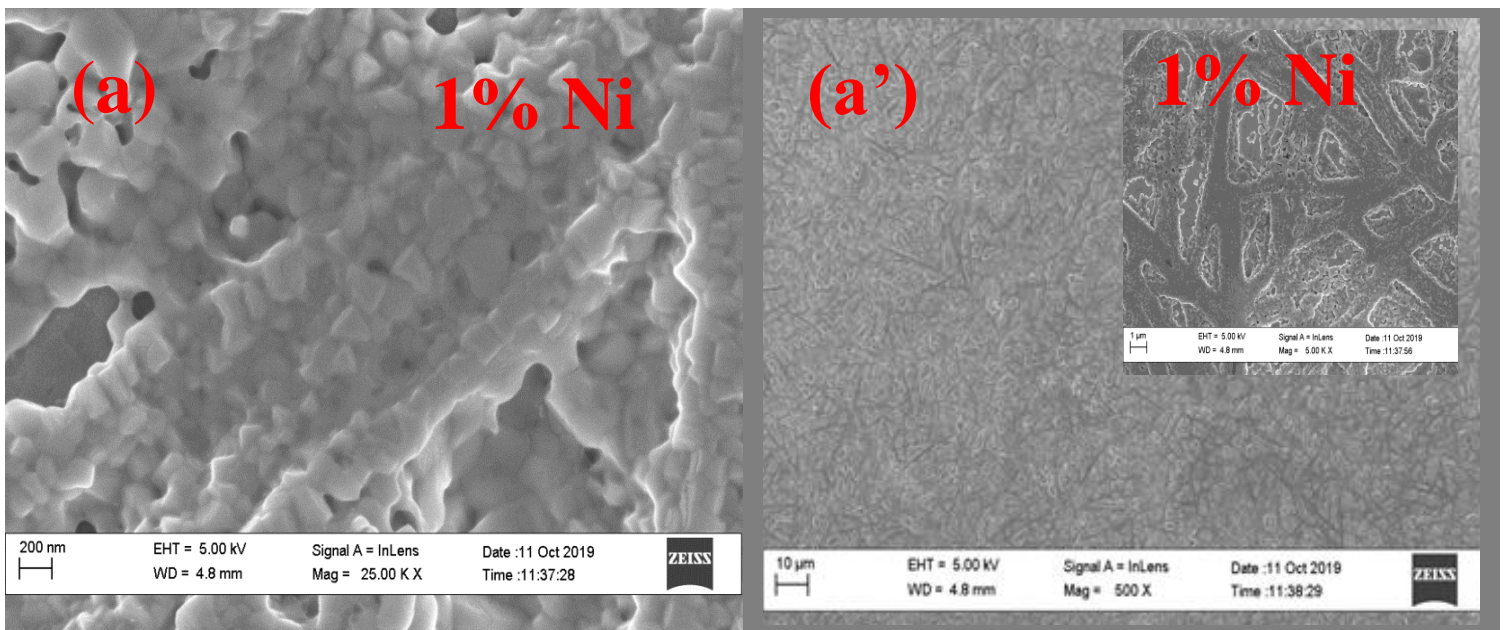
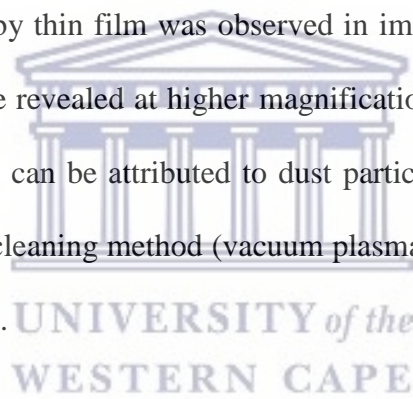


Figure 4.19: Top view HR-SEM images of pure tetragonal $\text{CH}_3\text{NH}_3\text{PbI}_3$ perovskite thin-films (a) morphology and (a') surface coverage.

The top view HR-SEM images of the pure tetragonal $\text{CH}_3\text{NH}_3\text{PbI}_3$ perovskite thin-films are illustrated in **Figure 4.19** above. An interesting morphology was observed for the pristine (un-doped) tetragonal $\text{CH}_3\text{NH}_3\text{PbI}_3$. The gathering of TPA molecule in the vicinity of hybrid

perovskite grain boundaries was observed and this was due to the rigidity property produced by the benzene ring in the TPA molecule. The TPA gathered at the vicinity of hybrid perovskite grain boundaries act a support template [62] and promote the perovskite nucleation with lateral growth in perovskite grain boundaries since the heterogeneous nucleation can reduce the nucleation free-energy hindrance in the grain boundaries [64]. The rich nucleation positions produced by the TPA molecule advance the growth of bar-shaped bridges which morphs into small sheet-shaped grains and some underneath hybrid perovskite grains are unified into interconnected hybrid perovskite communities (see **Figure 4.19 (a)**). This observation was in agreement with the findings of X. Hou *et al.* [63].

A poor ITO surface coverage by thin film was observed in image **(a')**. There were pinholes present in thin film which were revealed at higher magnifications of 10 μm (insert is 1 μm). The result of pinholes (cracks) can be attributed to dust particles on the surface of the ITO glass substrates. An advanced cleaning method (vacuum plasma cleaning method) is required for better ITO surface coverage.



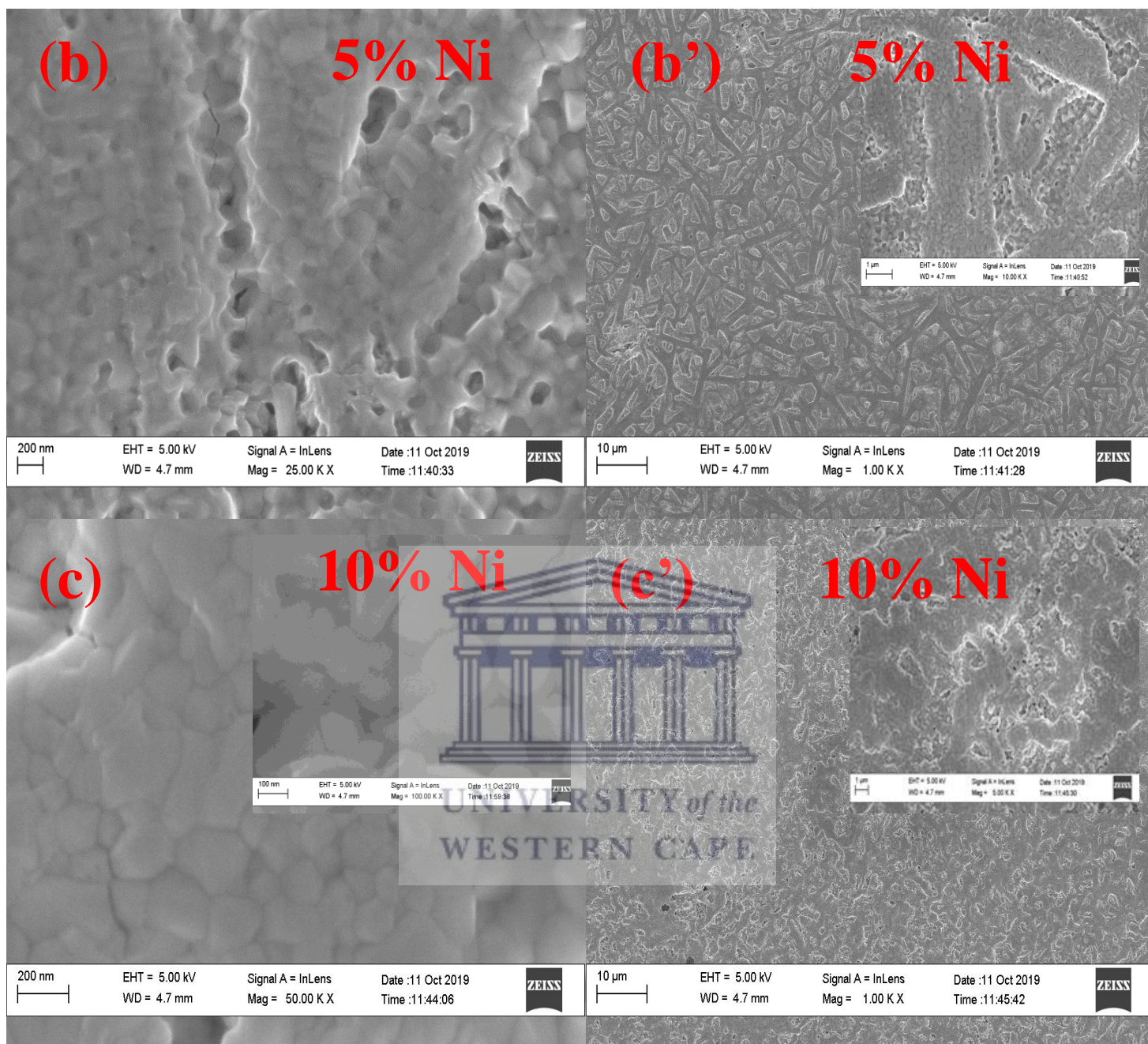
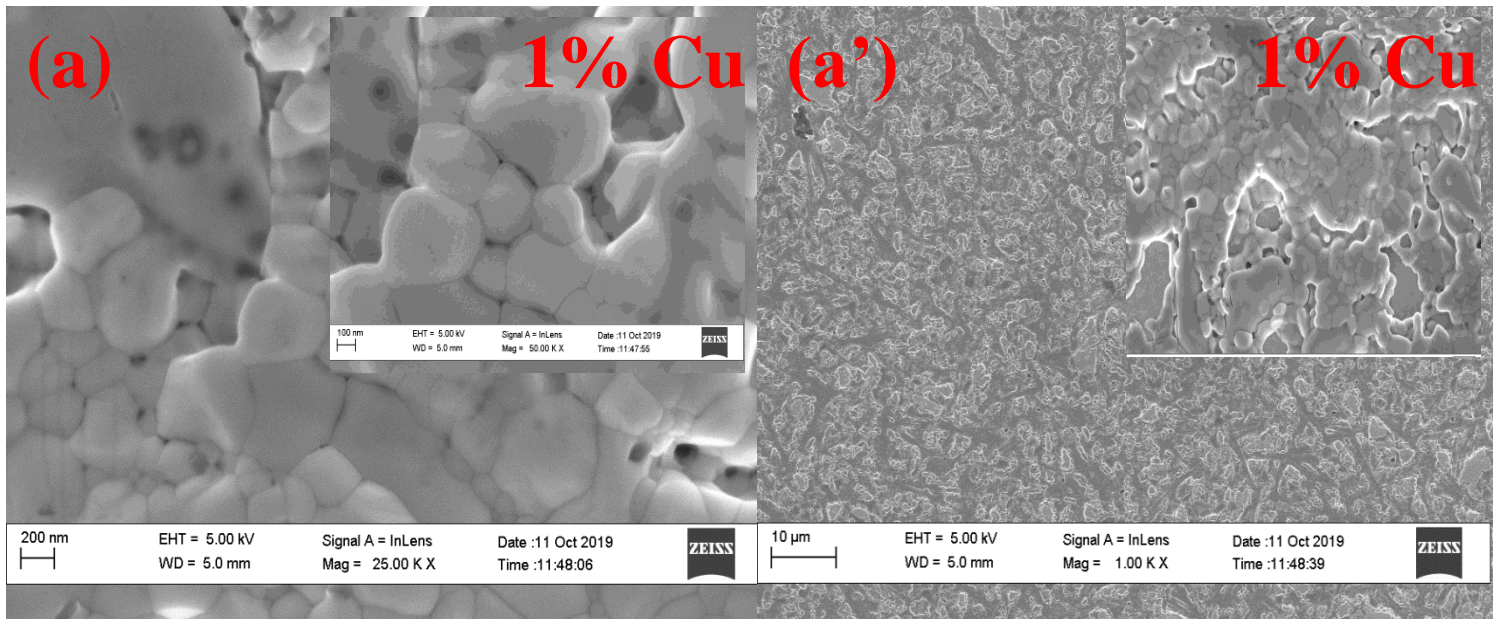
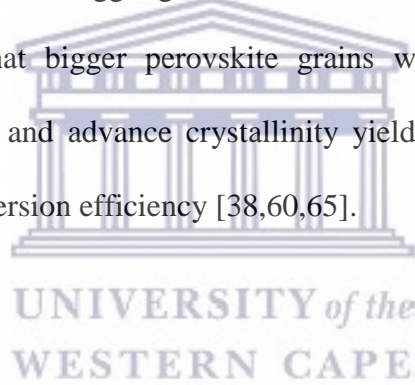


Figure 4.20: Top view HR-SEM images of Ni doped $\text{CH}_3\text{NH}_3\text{PbI}_3 \cdot \text{Ni}$ perovskite thin films; $\text{CH}_3\text{NH}_3\text{PbI}_3 \cdot 1\% \text{Ni}$ (a), $\text{CH}_3\text{NH}_3\text{PbI}_3 \cdot 5\% \text{Ni}$ (b) and $\text{CH}_3\text{NH}_3\text{PbI}_3 \cdot 10\% \text{Ni}$ (c).

The evolution of Ni doped $\text{CH}_3\text{NH}_3\text{PbI}_3 \cdot \text{Ni}$ perovskite thin films morphology is illustrated by top view HR-SEM images above. The small sheet-shaped perovskite grains were also observed at the vicinity of the hybrid perovskite grain boundaries at magnifications of 200 nm for $\text{CH}_3\text{NH}_3\text{PbI}_3 \cdot 1\% \text{Ni}$ and $\text{CH}_3\text{NH}_3\text{PbI}_3 \cdot 5\%$ the vicinity of the hybrid perovskite grain boundaries for $\text{CH}_3\text{NH}_3\text{PbI}_3 \cdot 10\% \text{Ni}$ as it was observed on pure tetragonal $\text{CH}_3\text{NH}_3\text{PbI}_3$, $\text{CH}_3\text{NH}_3\text{PbI}_3 \cdot 1\% \text{Ni}$ and $\text{CH}_3\text{NH}_3\text{PbI}_3 \cdot 5\% \text{Ni}$, see **Figure 4.20** (c). This observation

demonstrates that the Ni dopant at 10% concentration suppressed the assembly of TPA molecule in the vicinity of the perovskite grains during $\text{CH}_3\text{NH}_3\text{PbI}_3 \cdot 10\% \text{Ni}$ thin film materialization. Ni as seen from HR-SEM micrograph images; i.e. **Figure 4.20 (a) and (b)**. However, no small sheet-shaped grains were observed at Nonetheless, the materialized hybrid perovskite grains for $\text{CH}_3\text{NH}_3\text{PbI}_3 \cdot 10\% \text{Ni}$ thin film demonstrated high degree of interconnectedness between the crystal grains boundaries as there were no cracks (defects) observed. This observation further explains the slight red-shift in absorption (from 800 to 811 nm, see **Figure 4.16 (a)**) that was observed for $\text{CH}_3\text{NH}_3\text{PbI}_3 \cdot 10\% \text{Ni}$ thin film which was ascribed to the absence of smaller grains in the vicinity of the hybrid perovskite grain boundaries (i.e. only the underneath bigger grains absorbed across the solar spectrum). It has been reported in literature that bigger perovskite grains with fewer bulk defects, less scattering of grain boundaries and advance crystallinity yield the corresponding solar cell device with higher power conversion efficiency [38,60,65].



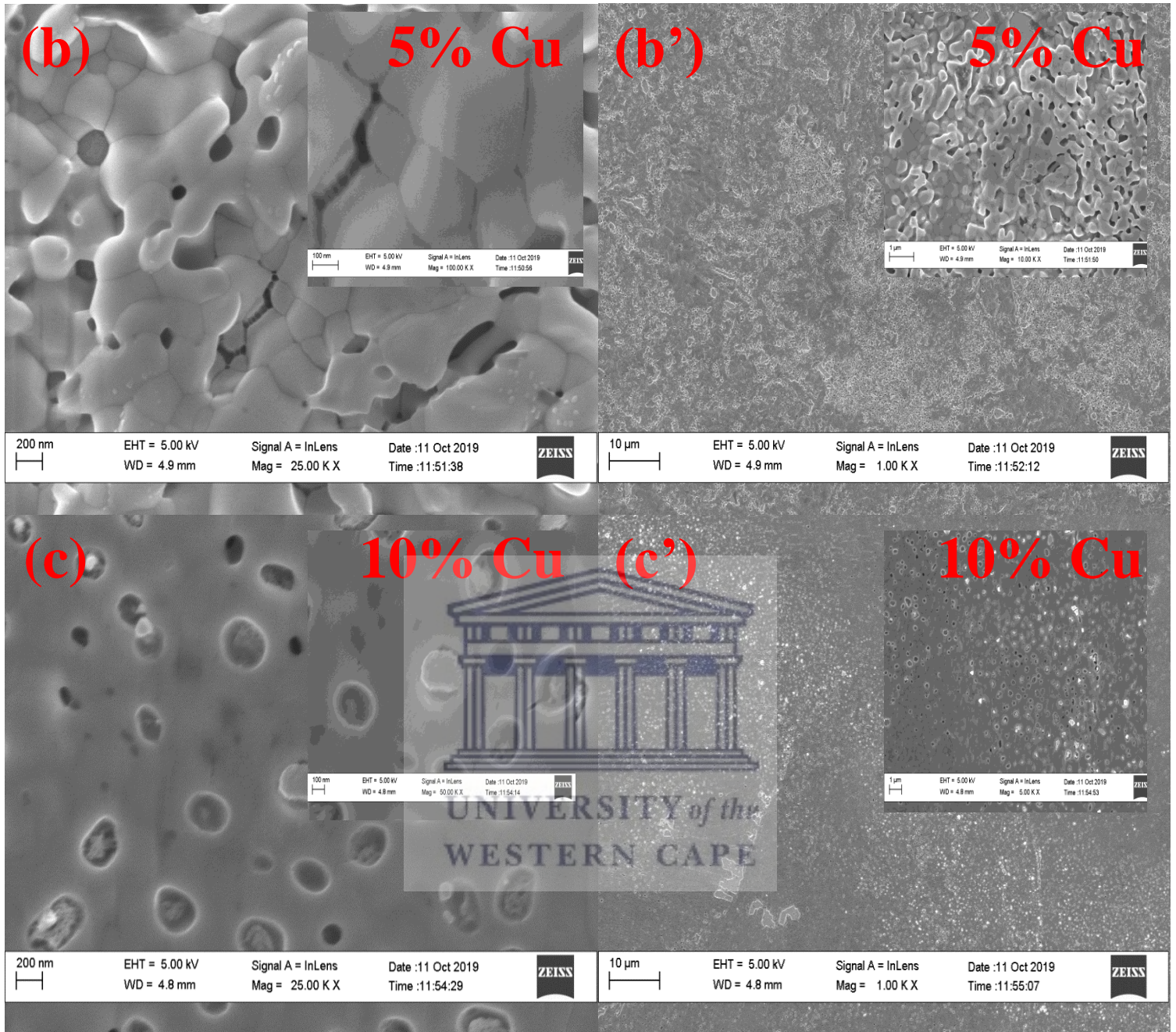
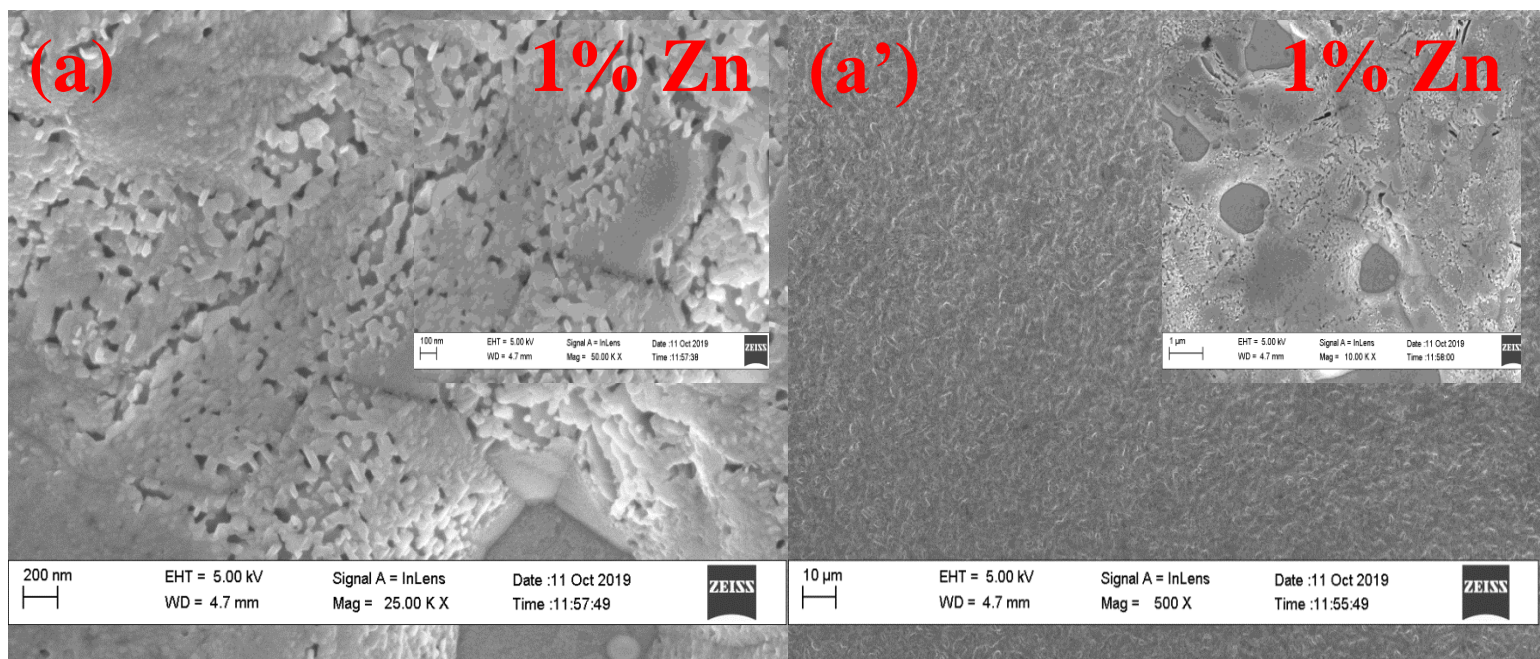


Figure 4.21: Top view HR-SEM images of Cu doped $\text{CH}_3\text{NH}_3\text{PbI}_3 \cdot \text{Cu}$ perovskite thin films; $\text{CH}_3\text{NH}_3\text{PbI}_3 \cdot 1\% \text{Cu}$ (a), $\text{CH}_3\text{NH}_3\text{PbI}_3 \cdot 5\% \text{Cu}$ (b) and $\text{CH}_3\text{NH}_3\text{PbI}_3 \cdot 10\% \text{Cu}$ (c).

The evolution of Cu doped $\text{CH}_3\text{NH}_3\text{PbI}_3 \cdot \text{Cu}$ perovskite thin films morphology is illustrated by top view HR-SEM images above. There were no small sheet-shaped grains observed at the vicinity of hybrid perovskite grain boundaries for all $\text{CH}_3\text{NH}_3\text{PbI}_3 \cdot \text{Cu}$ thin films as it was observed for pure tetragonal $\text{CH}_3\text{NH}_3\text{PbI}_3$, $\text{CH}_3\text{NH}_3\text{PbI}_3 \cdot 1\% \text{Ni}$ and $\text{CH}_3\text{NH}_3\text{PbI}_3 \cdot 5\% \text{Ni}$. This observation demonstrates that the Cu dopant suppressed the assembly of TPA molecule in the

vicinity of the perovskite grains during $\text{CH}_3\text{NH}_3\text{PbI}_3\cdot\text{Cu}$ thin films materialization. These grains exhibited excessive amount of defects as the Cu content was increased from 1 to 10% and they were also not tightly interconnected to each other signifying a high degree of dislocation density (structural defects) and micro-strain imposed by Cu content on the thin films. This observation was in agreement with the results observed in **Figure 4.6 (b)** and **Figure 4.8 (b)**; micro-strain started to increase as the Cu content increased to 10% and the dislocation density (structural defects) increased as the Cu content increased from 1 to 10%. A coarse $\text{CH}_3\text{NH}_3\text{PbI}_3\cdot 10\%\text{Cu}$ thin film with a lot of small unreacted and recrystallized CuI reagent surrounding the original/underneath hybrid perovskite grains was observed, see **Figure 4.21 (c)**. This observation explains a slight blue-shift in absorption and emission observed for $\text{CH}_3\text{NH}_3\text{PbI}_3\cdot 10\%\text{Cu}$ in **Figure 4.17 (a)** and **(e)** (i.e. a layer of CuI crystals surrounding the original hybrid perovskite grains affected the absorption and emission of $\text{CH}_3\text{NH}_3\text{PbI}_3\cdot 10\%\text{Cu}$). This observation also explains the suppression of radiative recombination dynamics (quenching effect) exhibited under photoluminescence studies for Cu doped $\text{CH}_3\text{NH}_3\text{PbI}_3\cdot\text{Cu}$ perovskite thin films, see **Figure 4.17 (f)**.



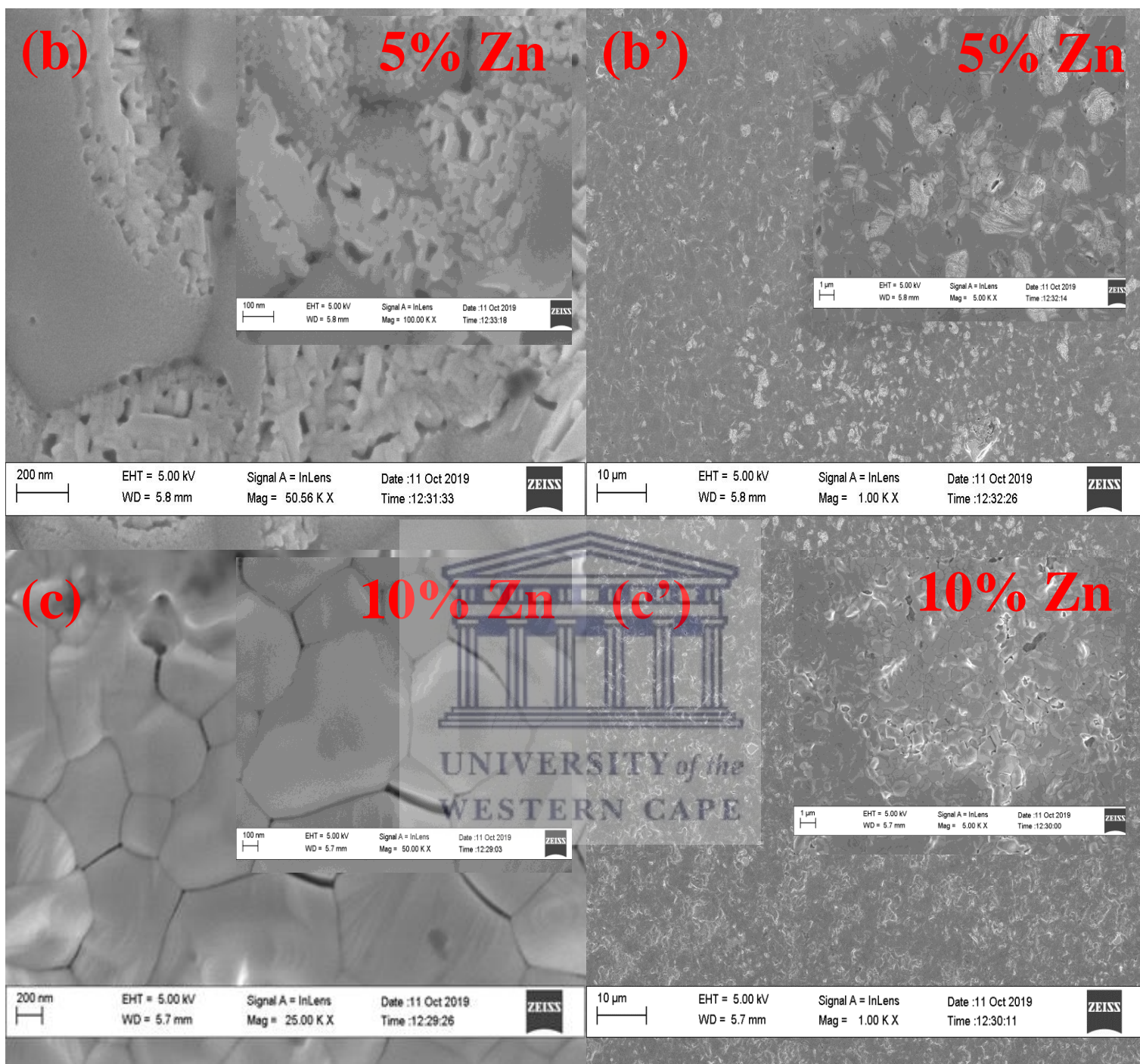


Figure 4.22: Top view HR-SEM images of Zn doped $\text{CH}_3\text{NH}_3\text{PbI}_3 \cdot \text{Zn}$ perovskite thin films; $\text{CH}_3\text{NH}_3\text{PbI}_3 \cdot 1\% \text{Zn}$ (a), $\text{CH}_3\text{NH}_3\text{PbI}_3 \cdot 5\% \text{Zn}$ (b) and $\text{CH}_3\text{NH}_3\text{PbI}_3 \cdot 10\% \text{Zn}$ (c).

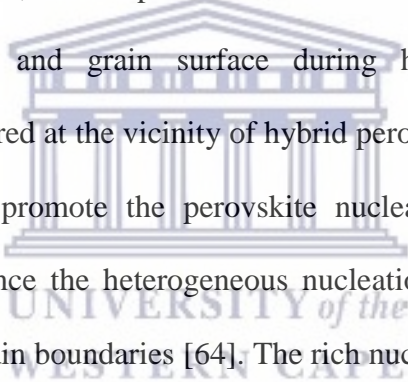
The evolution of Zn doped $\text{CH}_3\text{NH}_3\text{PbI}_3 \cdot \text{Zn}$ perovskite thin films morphology is illustrated by top view HR-SEM images above. A layer of smaller hybrid perovskite grains was observed at the vicinity of the perovskite grain boundaries at magnifications of 200 nm for $\text{CH}_3\text{NH}_3\text{PbI}_3 \cdot 1\% \text{Zn}$ and $\text{CH}_3\text{NH}_3\text{PbI}_3 \cdot 5\% \text{Zn}$ as seen from HR-SEM micrograph images; i.e. **Figure 4.22 (a) and (b)**. The formation of these small perovskite grains is attributed to the

excessive nucleation sites of TPA additive, further demonstrating the TPA molecules to easily segregate in the vicinity of hybrid perovskite grain boundaries. However, this layer was not observed at the vicinity of the hybrid perovskite grain boundaries for $\text{CH}_3\text{NH}_3\text{PbI}_3 \cdot 10\% \text{Ni}$, see **Figure 4.22 (c)**. This observation also demonstrates that the Zn dopant at 10% concentration suppressed the assembly of TPA molecules in the vicinity of the perovskite grains during $\text{CH}_3\text{NH}_3\text{PbI}_3 \cdot 10\% \text{Zn}$ thin film materialization. Nonetheless, the materialized hybrid perovskite grains for $\text{CH}_3\text{NH}_3\text{PbI}_3 \cdot 10\% \text{Zn}$ thin film demonstrated interconnectedness between the crystal grains boundaries with few cracks (defects). This observation further explains the slight red-shift in photoluminescence emission (from 782 to 784 nm, see **Figure 4.18 (e)**) that was observed for $\text{CH}_3\text{NH}_3\text{PbI}_3 \cdot 10\% \text{Zn}$ thin film which was ascribed to the absence of smaller grains in the vicinity of the hybrid perovskite grain boundaries.

One of the main challenges affecting the capability of researchers to develop high efficiency solar cell devices has been morphology control and crystallization of hybrid perovskite thin films in planar architecture [25,66,67]. It has been reported in literature that hybrid perovskite thin films with outstanding uniformity and big crystal sizes can be attained via meticulous control of the nucleation and growth processes [37]. Additionally, it has been demonstrated by many studies that bigger hybrid perovskite grains can decrease the interfacial area that impedes the collection of charge carriers. Bigger hybrid perovskite grains also exhibit fewer bulk defects and superior mobilities, thereby promoting higher collection of photo-generated charge carriers [60,68].

Despite the great attainments in advancing the crystallization process to obtain high-quality hybrid perovskite thin films with uniform morphology and big grain size through integrating additives into the perovskite structure, most reported studies are dedicated to the molecular cross-link or chelation with hybrid perovskite to enlarge the hybrid perovskite grain size and

smoothen the morphology of hybrid perovskite thin film [69–72]. The uncovered hybrid perovskite grains remain a main scientific problem to attain advance-performing and durable hybrid perovskite solar cells since the exposed grains are extremely vulnerable to moisture and oxygen [73,74]. Terephthalic acid (TPA) additive used in this study was integrated into metal halide precursors; PbI_2 , NiI_2 , CuI & ZnI_2 , during hybrid perovskite thin films preparation employing two-step deposition technique to remedy the uncovered grain boundaries. In the TPA molecule, the inflexible benzene ring is connected to two carboxyl groups at 1,4-symmetrical position. Owing to its inflexibility properties and the strong $\pi - \pi$ bonds, the benzene ring has a high cohesive energy [75] in comparison to other additives previously reported in literature, which promote the assembly of TPA molecules at the vicinity of grain boundaries and grain surface during hybrid perovskite thin film materialization. The TPA gathered at the vicinity of hybrid perovskite grain boundaries act as a support template [62] and promote the perovskite nucleation with lateral growth in perovskite grain boundaries since the heterogeneous nucleation can reduce the nucleation free-energy hindrance in the grain boundaries [64]. The rich nucleation positions produced by the TPA molecule advance the growth of bar-shaped bridges which morphs into small sheet-shaped grains and some underneath hybrid perovskite grains are unified into interconnected hybrid perovskite communities. At the same time, the ion migration of hybrid perovskite can be repressed by the strong matching between the Γ anion and the hydrogen bonds of hydroxyl groups in TPA, resulting in perovskite solar cell devices exhibiting advance photovoltaic performance with strong moisture resistance and thermal stability.



4.2.5 Microscopic analysis by Atomic Force Microscopy (AFM)

The surface topography (i.e. surface roughness) for all the perovskite thin films under investigation was evaluated utilising the Atomic Force Microscopy (AFM). Similar to HR-SEM studies, the evolution of surface topography will be discussed based on the content and variation of the transition metal dopants; Ni, Cu, and Zn.

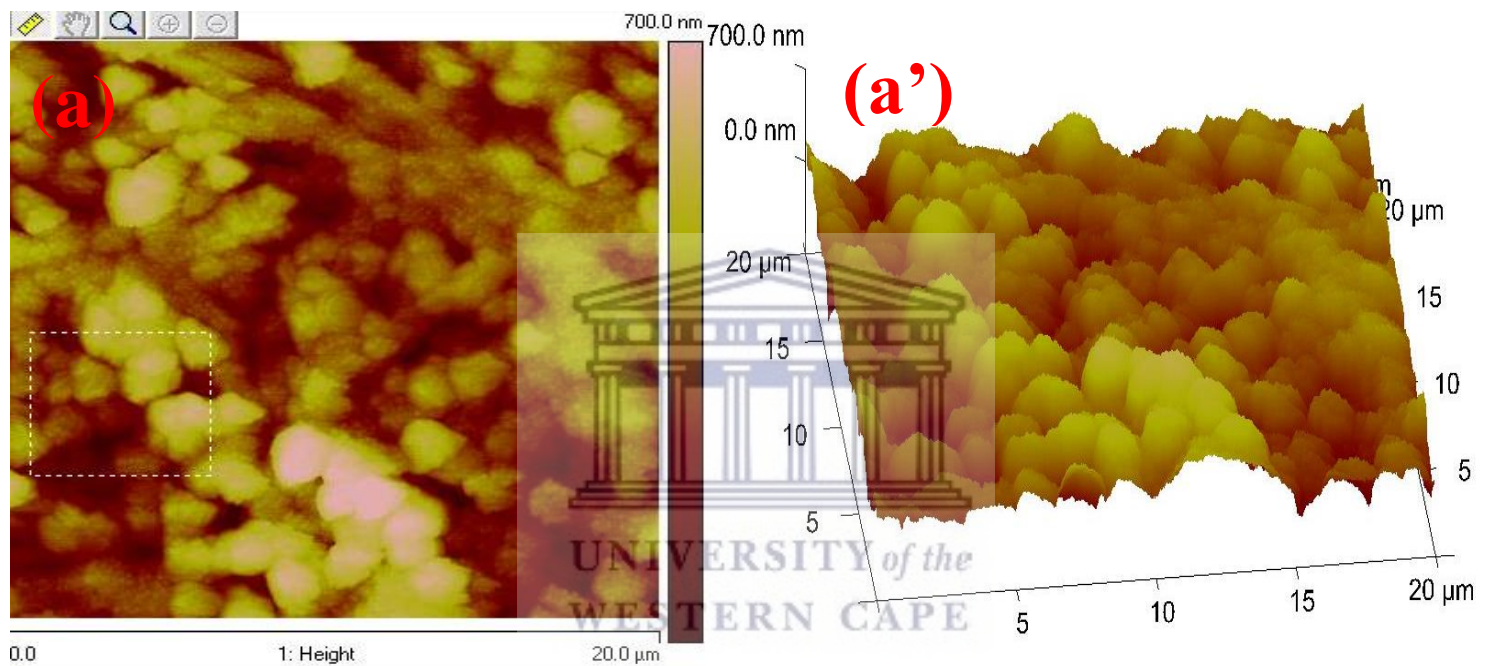


Figure: 4.23: Top view AFM images of pure tetragonal $\text{CH}_3\text{NH}_3\text{PbI}_3$ perovskite thin-film, 1D (a) and 3D (a') representation.

The AFM image of pure tetragonal $\text{CH}_3\text{NH}_3\text{PbI}_3$ is given above. The calculated root mean square roughness for the thin film was 113 nm, determined using nanoscope software. This roughness value will be utilised as a point of reference for the evaluation of the impact of transition metal dopants; Ni, Cu, and Zn, on the surface topography (roughness) of perovskite thin films.

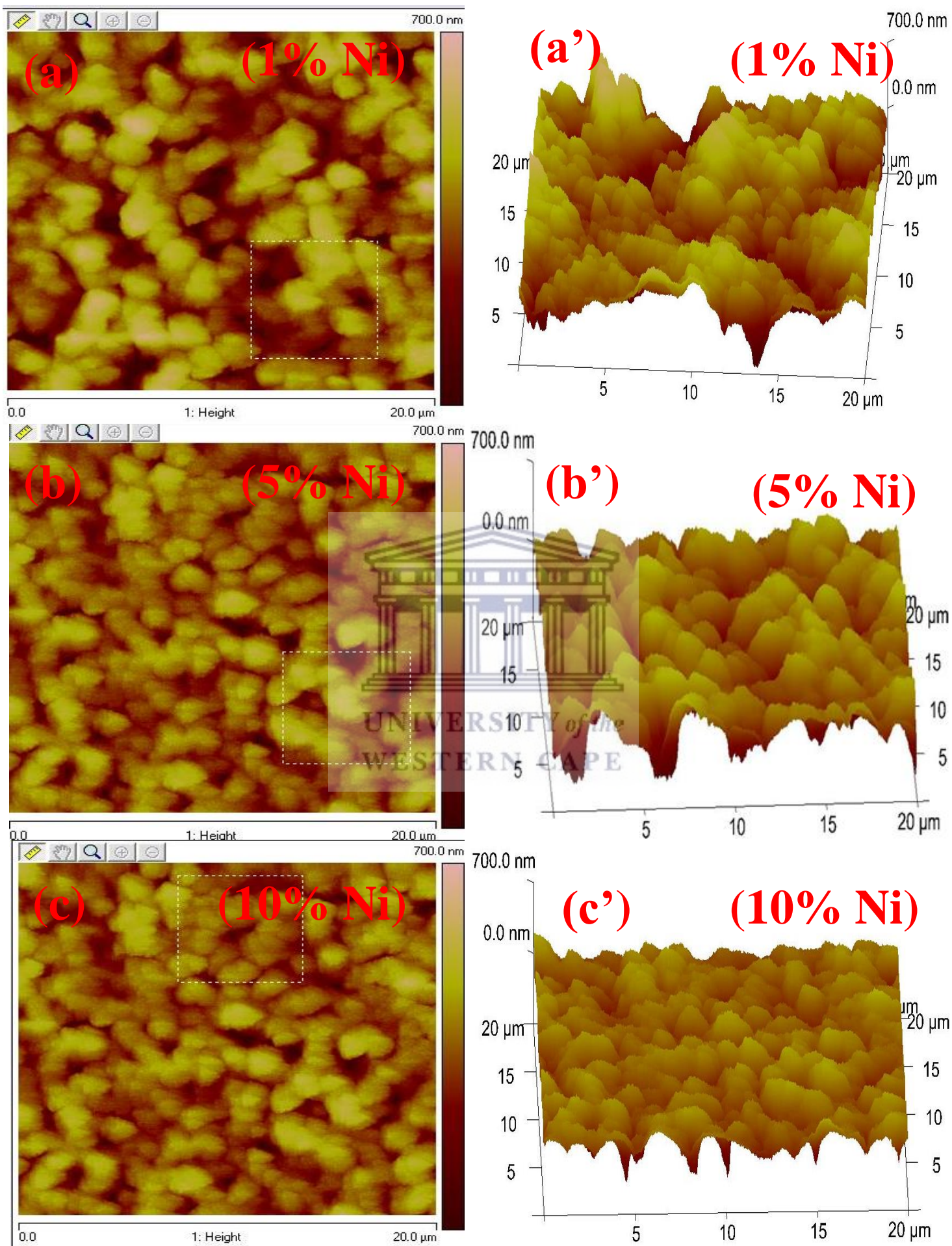
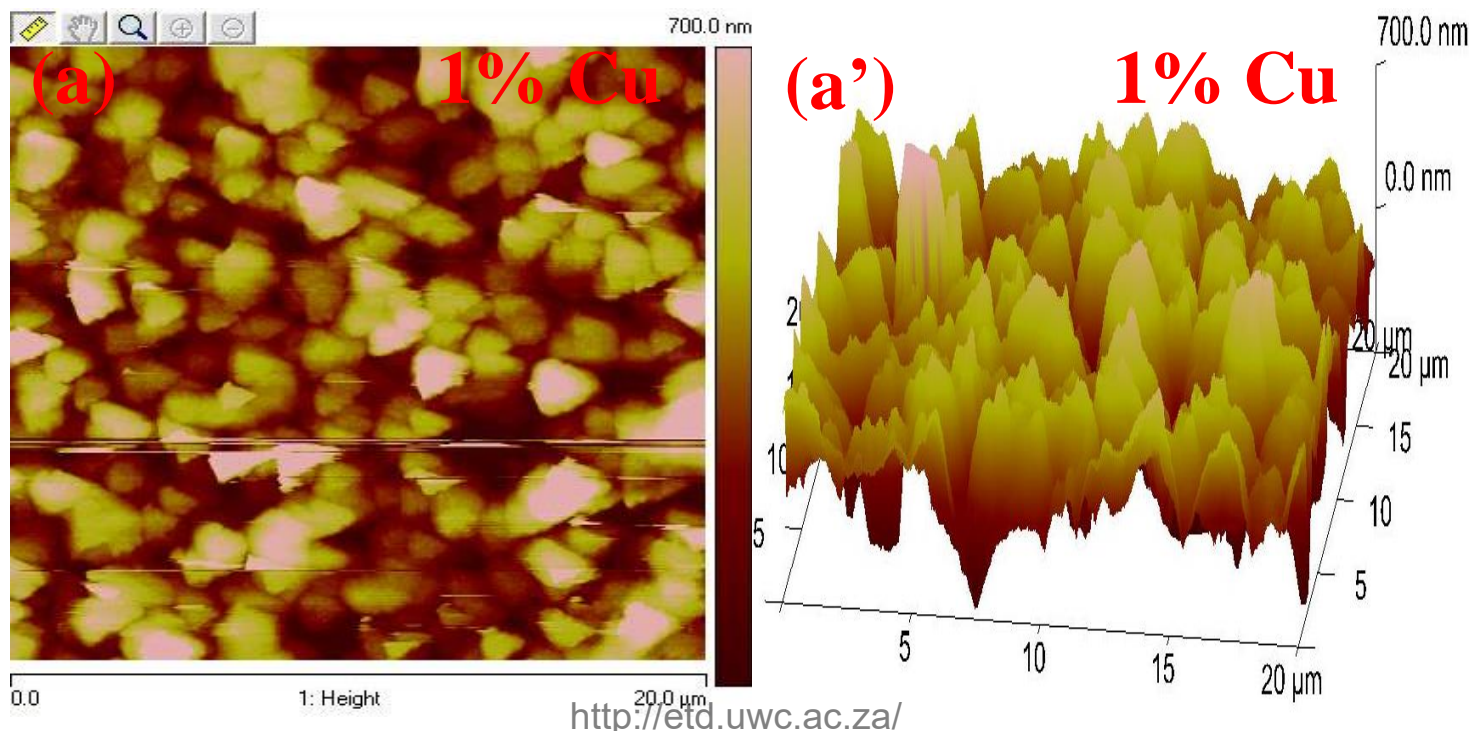


Figure: 4.24: Top view AFM images of Ni doped $\text{CH}_3\text{NH}_3\text{PbI}_3 \cdot \text{Ni}$ perovskite thin films; $\text{CH}_3\text{NH}_3\text{PbI}_3 \cdot 1\% \text{Ni}$ (a), $\text{CH}_3\text{NH}_3\text{PbI}_3 \cdot 5\% \text{Ni}$ (b) and $\text{CH}_3\text{NH}_3\text{PbI}_3 \cdot 10\% \text{Ni}$ (c).

The evolution of Ni doped $\text{CH}_3\text{NH}_3\text{PbI}_3 \cdot \text{Ni}$ perovskite thin films surface topography (roughness) is illustrated above by 1D and 3D views. The calculated root mean square roughness for $\text{CH}_3\text{NH}_3\text{PbI}_3 \cdot 1\% \text{Ni}$, $\text{CH}_3\text{NH}_3\text{PbI}_3 \cdot 5\% \text{Ni}$, $\text{CH}_3\text{NH}_3\text{PbI}_3 \cdot 10\% \text{Ni}$ were determined to be 111, 99.7 and 105 nm using nanoscope software, respectively. These values were lower than that of the pure tetragonal $\text{CH}_3\text{NH}_3\text{PbI}_3$ (113 nm) perovskite thin film demonstrating that Ni dopants generally decreased the surface roughness of the perovskite thin films. The $\text{CH}_3\text{NH}_3\text{PbI}_3 \cdot 10\% \text{Ni}$ exhibited the lowest surface roughness. This was in agreement with the top view HR-SEM results obtained in **Figure 4.20 (c)** which demonstrated that the Ni dopant at 10% concentration suppressed the assembly of TPA molecule in the vicinity of the perovskite grains during $\text{CH}_3\text{NH}_3\text{PbI}_3 \cdot 10\% \text{Ni}$ thin film materialization. This observation further explains the slight red-shift in absorption (from 800 to 811 nm, see **Figure 4.16 (a)**) that was observed for $\text{CH}_3\text{NH}_3\text{PbI}_3 \cdot 10\% \text{Ni}$ thin film which was ascribed to the absence of smaller grains in the vicinity (hence the lowest surface roughness) of the hybrid perovskite grain boundaries (i.e. only the underneath bigger grains absorbed across the solar spectrum).



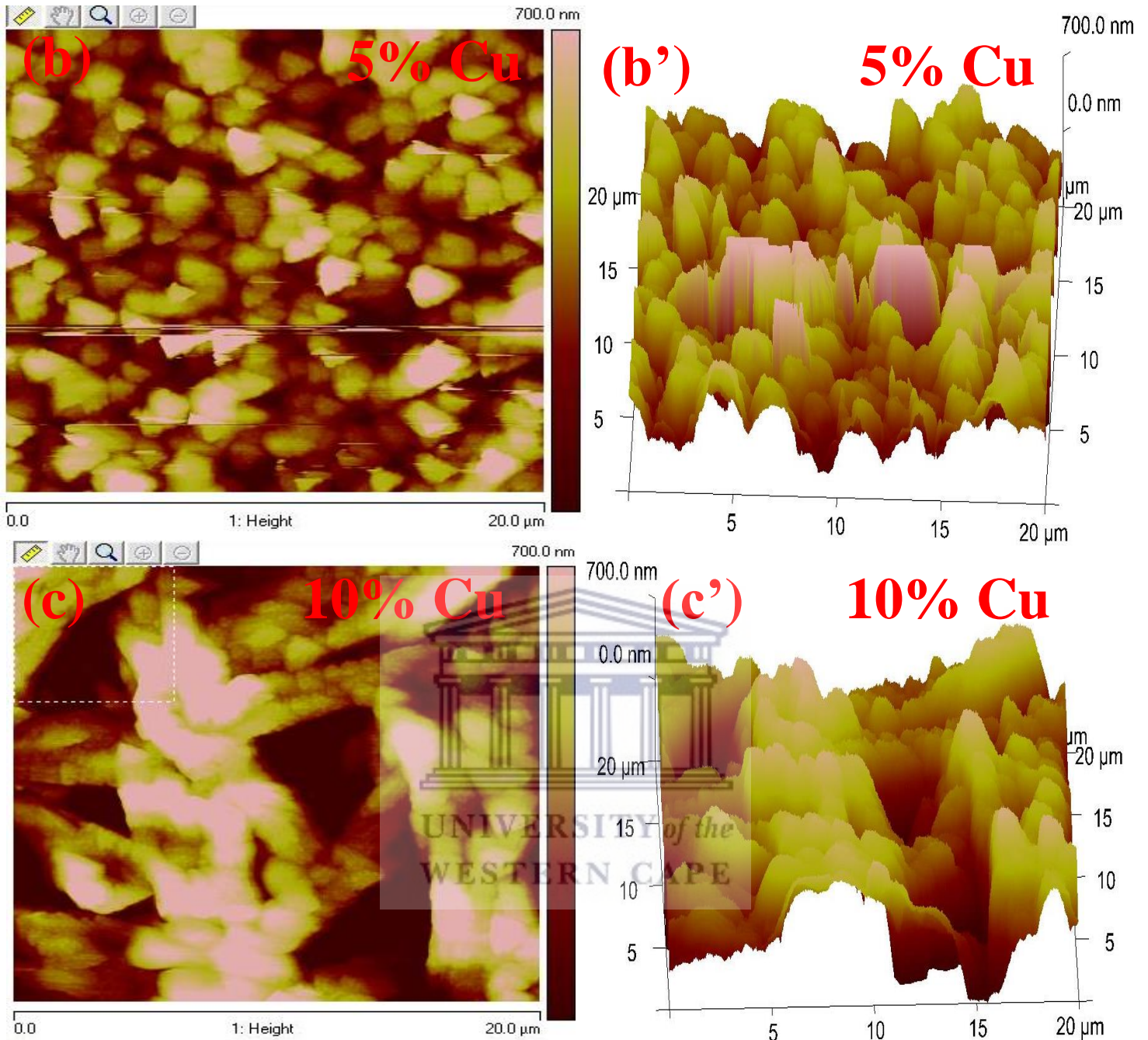
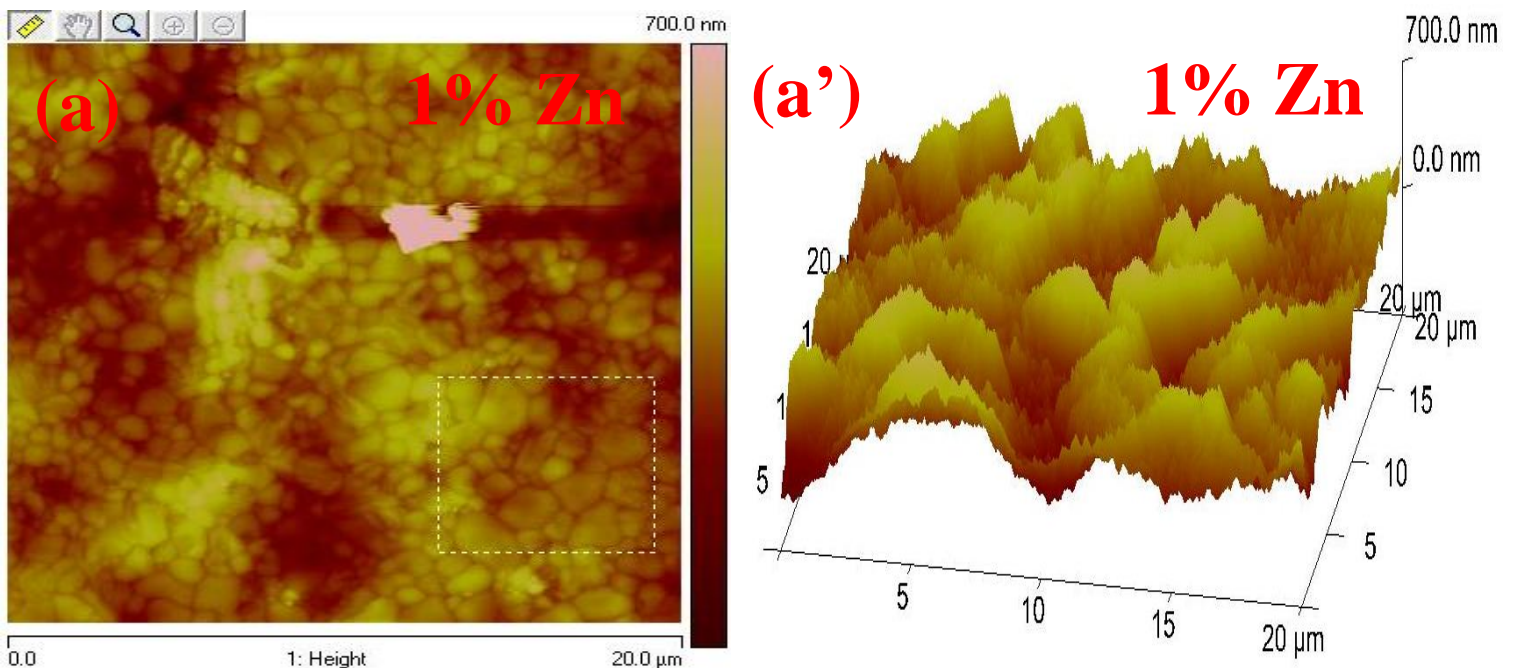
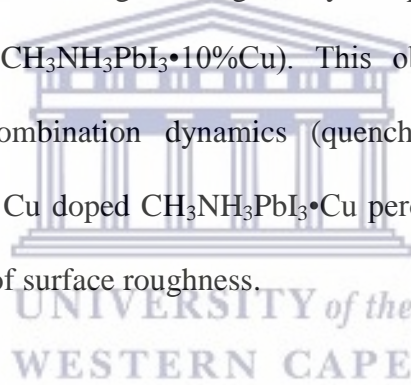


Figure: 4.25: Top view AFM images of Cu doped $\text{CH}_3\text{NH}_3\text{PbI}_3 \cdot \text{Cu}$ perovskite thin films; $\text{CH}_3\text{NH}_3\text{PbI}_3 \cdot 1\% \text{Cu}$ (a), $\text{CH}_3\text{NH}_3\text{PbI}_3 \cdot 5\% \text{Cu}$ (b) and $\text{CH}_3\text{NH}_3\text{PbI}_3 \cdot 10\% \text{Cu}$ (c).

The evolution of Cu doped $\text{CH}_3\text{NH}_3\text{PbI}_3 \cdot \text{Cu}$ perovskite thin films surface topography (roughness) is illustrated above by 1D and 3D views. The calculated root mean square roughness for $\text{CH}_3\text{NH}_3\text{PbI}_3 \cdot 1\% \text{Cu}$, $\text{CH}_3\text{NH}_3\text{PbI}_3 \cdot 5\% \text{Cu}$, $\text{CH}_3\text{NH}_3\text{PbI}_3 \cdot 10\% \text{Cu}$ were calculated to be 177, 289 and 331 nm using nanoscope software, respectively. These values were higher than that of the pure tetragonal $\text{CH}_3\text{NH}_3\text{PbI}_3$ (113 nm) and Ni doped

CH₃NH₃PbI₃•Ni (from 99 to 111 nm) perovskite thin films, respectively. These results demonstrated that Cu dopants increased the surface roughness of the perovskite thin films attributed to the surface defects (pink coloured grains) observed on the surface of the films, see **Figure 4.25**. This observation was in agreement with the HR-SEM results illustrated in **Figure 4.21**. Coarse CH₃NH₃PbI₃•Cu thin films with unreacted and recrystallized CuI reagent surrounding the original/underneath hybrid perovskite grains were observed, hence a tremendous increase in surface roughness. This observation; significant increase in surface roughness as the concentration of Cu dopant increased from 1 to 10%, explains a slight blue-shift in absorption and emission observed for CH₃NH₃PbI₃•10%Cu in **Figure 4.17 (a)** and **(e)** (i.e. a layer of CuI crystals surrounding the original hybrid perovskite grains affected the absorption and emission of CH₃NH₃PbI₃•10%Cu). This observation also explains the suppression of radiative recombination dynamics (quenching effect) exhibited under photoluminescence studies for Cu doped CH₃NH₃PbI₃•Cu perovskite thin films, see **Figure 4.17 (f)**, owing to high degree of surface roughness.



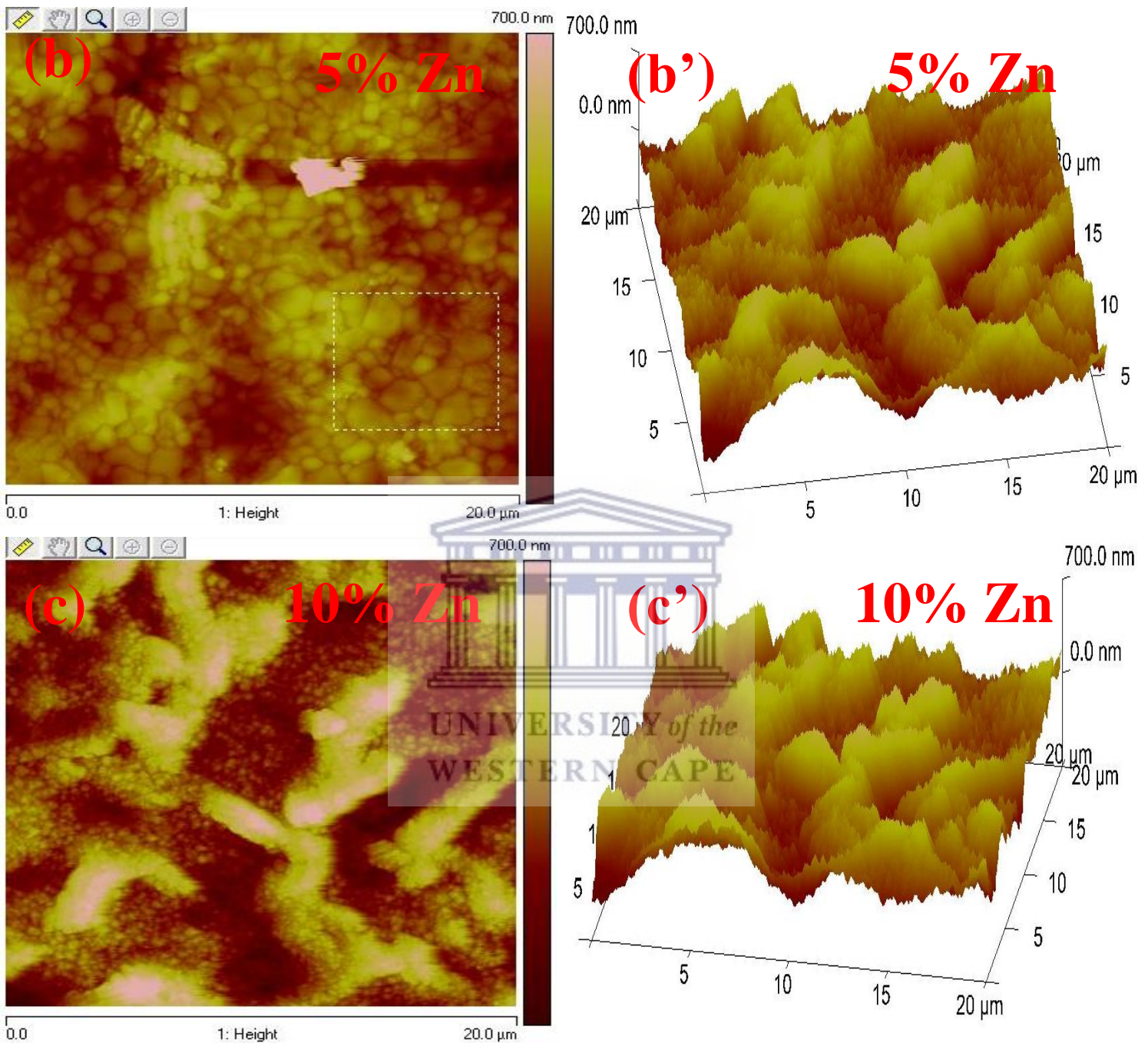


Figure 4.26: Top view AFM images of Zn doped $\text{CH}_3\text{NH}_3\text{PbI}_3 \cdot \text{Zn}$ perovskite thin films; $\text{CH}_3\text{NH}_3\text{PbI}_3 \cdot 1\% \text{Zn}$ (a), $\text{CH}_3\text{NH}_3\text{PbI}_3 \cdot 5\% \text{Zn}$ (b) and $\text{CH}_3\text{NH}_3\text{PbI}_3 \cdot 10\% \text{Zn}$ (c).

The evolution of Zn doped $\text{CH}_3\text{NH}_3\text{PbI}_3 \cdot \text{Zn}$ perovskite thin films surface topography (roughness) is illustrated above by 1D and 3D views. The calculated root mean square roughness for $\text{CH}_3\text{NH}_3\text{PbI}_3 \cdot 1\% \text{Zn}$, $\text{CH}_3\text{NH}_3\text{PbI}_3 \cdot 5\% \text{Zn}$, $\text{CH}_3\text{NH}_3\text{PbI}_3 \cdot 10\% \text{Zn}$ were determined to be 90.40, 79.10 and 83.60 nm using nanoscope software, respectively. These

values were the lowest compared to that of the pure tetragonal $\text{CH}_3\text{NH}_3\text{PbI}_3$ (113 nm), Ni doped $\text{CH}_3\text{NH}_3\text{PbI}_3\cdot\text{Ni}$ (from 99 to 111 nm), and Cu doped $\text{CH}_3\text{NH}_3\text{PbI}_3\cdot\text{Cu}$ (from 177 to 331 nm) hybrid perovskite thin films, respectively. These results demonstrated that Zn dopants reduced the surface roughness of the perovskite thin films which resulted in more compact (dense) thin films. This was also in agreement with the HR-SEM results illustrated in **Figure 4.22**. A layer of small perovskite grains at the vicinity of the hybrid perovskite grains was not observed for $\text{CH}_3\text{NH}_3\text{PbI}_3\cdot 10\%\text{Ni}$, see **Figure 4.22 (c)**, hence the thin film exhibited the lowest surface roughness of 83.60 nm. This observation further explains the slight red-shift in photoluminescence emission (from 782 to 784 nm, see **Figure 4.18 (e)**) that was observed for $\text{CH}_3\text{NH}_3\text{PbI}_3\cdot 10\%\text{Zn}$ thin film which was ascribed to the absence of smaller grains (confirmed by the lowest surface roughness of 83.60 nm) in the vicinity of the hybrid perovskite grain boundaries. Moreover, the low surface roughness observed for $\text{CH}_3\text{NH}_3\text{PbI}_3\cdot\text{Zn}$ thin films (relatively compact thin films) correlated very well with the observed relaxation of micro-strain and dislocation density as the Zn content was increased from 1 to 10%, see **Figure 4.6 (c)** and **Figure 4.8 (c)**, and with the observed highest degree of crystallinity (81.08%) as seen from **Table 4.11**. Hence, higher radiative recombination emissions were observed for $\text{CH}_3\text{NH}_3\text{PbI}_3\cdot\text{Zn}$ hybrid perovskite thin films [44], making the Zn dopant the best candidate amongst Ni, Cu, & Zn for Pb substitution in $\text{CH}_3\text{NH}_3\text{PbI}_3$.

4.3 DEVELOPMENT OF CZGSe-KESTERITE SOLAR CELLS

4.3.1 Stack Order and Reactive Annealing Pressure Variations

4.3.1.1 Raman spectroscopy analysis

Raman spectroscopy is a powerful characterization technique to study the molecular symmetry and chemical bonding properties of materials. Raman shifts are caused by the vibration of chemical bonding, and different chemical bonding have different force constants, which produces characteristic signals. The Raman spectra at an excitation wavelength of 532 nm for CZGSe absorbers with stack order; Mo/Cu(4nm, for 20s)/Zn/Cu/Ge (A) and Mo/Zn/Cu/Ge (B), synthesized at different reactive annealing pressures of; 700 mbar and 1bar, for comparisons are illustrated in **Figure 4.27**.

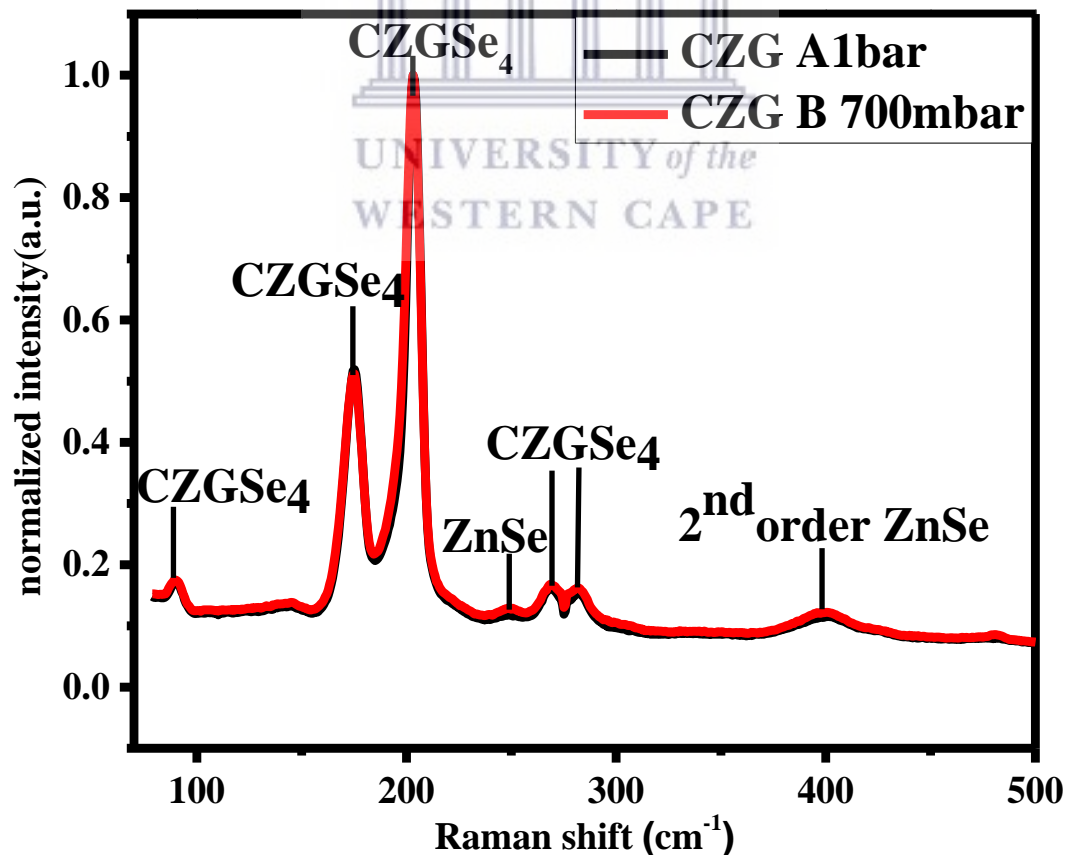


Figure 4.27: Raman spectra at an excitation wavelength of 532 nm for CZGSe thin films prepared at different annealing pressures; 700 mbar and 1bar.

The Raman spectra for the stack order Mo/Cu/Zn/Ge (C) were not included because the absorbers were damaged during wet-chemical bath etching/passivation stage in NH_4S (22% v/v, Alfar-Aesar, for 2 min). This observation demonstrated that the stack order Mo/Cu/Zn/Ge (C) was not ideal for the synthesis of CZGSe absorber material and consequently it was not further explored going forward with optimization experiments. The stack orders; Mo/Cu(4 nm, for 20s)/Zn/Cu/Ge (A) and Mo/Zn/Cu/Ge (B), are essentially similar, the only difference is a thin layer of Cu (4 nm, for 20s) deposited before Zn. The intense raman shifts at around 180 cm^{-1} and 206 cm^{-1} confirmed the pure germanium kesterite phase CZGSe phase formation, which are very close to the characteristic raman peak positions of pure tin kesterite CZTSe phase located at $172, 195, 234\text{ cm}^{-1}$ [18]. The ZnSe secondary phases on the surface of the CZGSe were confirmed at 250 and 400 cm^{-1} [76] and they were not pronounced with a green excitation wavelength of 532 nm . The best wavelength for the detection of ZnSe secondary phases is at 442 nm (blue wavelength) [77–80]. Both absorbers at different pressure conditions demonstrated good crystalline quality observed by sharp peaks for CZGSe pure phase.

4.3.1.2 High Resolution Scanning Electron Microscopy (HR-SEM) analysis

The HR-SEM cross-sectional area images were taken to evaluate the CZGSe grains quality and the contact between the absorber and the Mo-back contact interface. HR-SEM cross sectional area micrographs revealed that all the absorbers from different precursor stack orders under investigation at different pressure conditions exhibit a bilayer structure. Adequate quality of grains was observed towards the near surface of the absorber. The best precursor that gave the best quality of well-defined grains near the absorber surface was observed to be the one; Mo/Cu(4 nm, for 20s)/Zn/Cu/Ge (A). In this particular precursor-

stack order; a thin layer of Cu was first deposited for 20 s before depositing the Zn layer. The stack order: Mo/Cu(4 nm, for 20s)/Zn/Cu/Ge (A) prepared at 1bar exhibited better grain quality near the absorber surface when compared to the precursor Mo/Zn/Cu/Ge (B) (prepared at 1 bar).

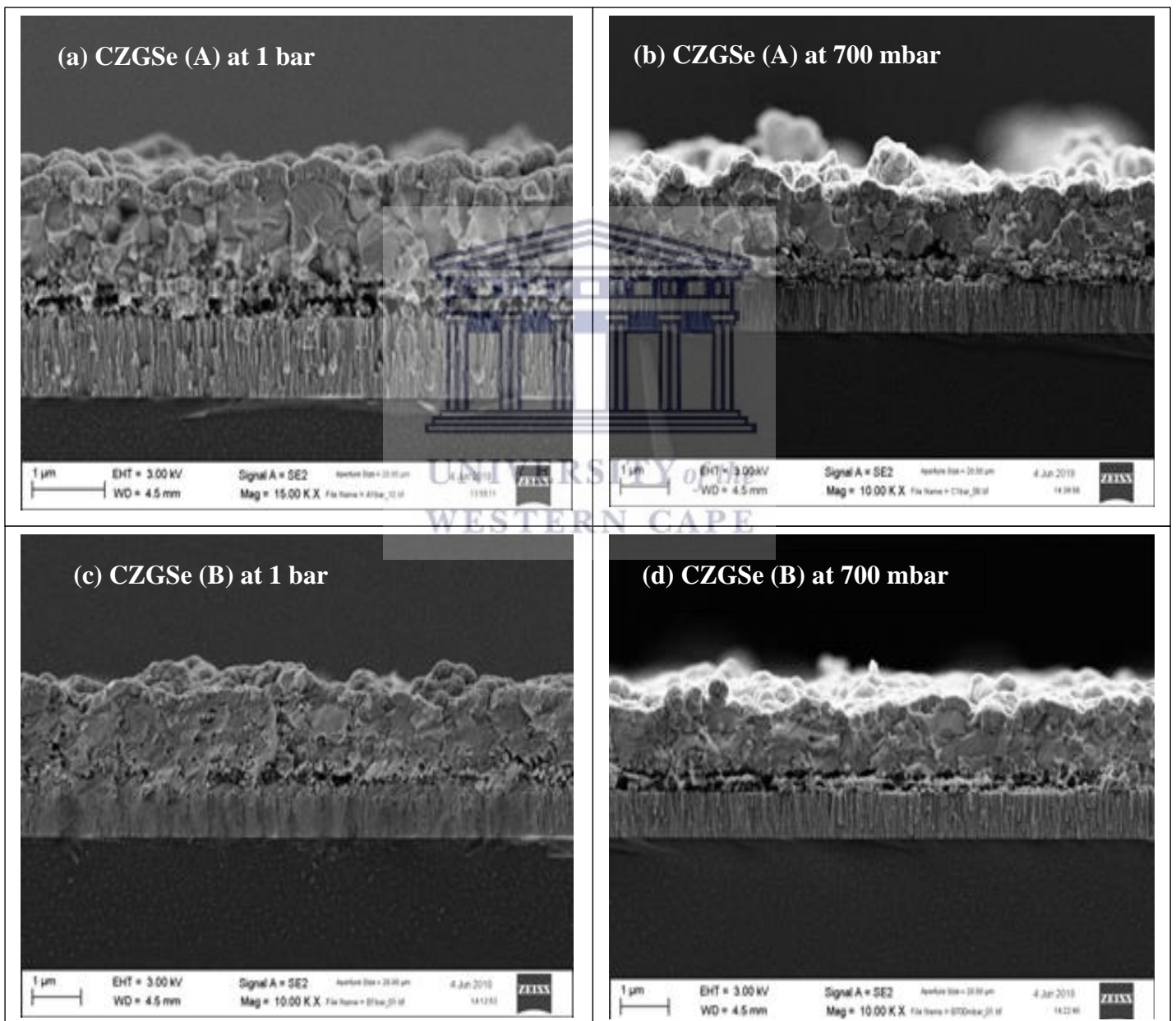


Figure 4.28: HR-SEM images (cross sectional area) for CZGSe devices prepared at 700 mbar and 1 bar.

From the cross sectional area micrographs images above it was concluded that the precursor stack-order does play a role in the quality of the absorber and Mo/Cu(4nm, for 20s)/Zn/Cu/Ge was considered to be the optimal precursor stack-order. From the results, it was also observed that the pressure at which the reactive annealing process is performed does play a role in the quality of the absorber and based on the cross sectional area micrograph images above, the optimum pressure for reactive selenization process was considered to be at 1 bar. The subsequent optimization experiments were thus performed employing the Mo/Cu(4 nm, for 20s)/Zn/Cu/Ge precursor stack-order at a pressure of 1 bar. A layer of voids was observed between the Mo back-contact and the absorber itself which leads to lack of adhesion on the Mo-back contact as seen in **Figure 4.28**. These voids could be due to the formation of volatile species during reactive selenization process at high temperatures. A thin layer of Sn was introduced between CZTS and the Mo back-contact region as a strategy to improve the adhesion by Kim *et al.* [81]. This achievement was ascribed to the lessening of ZnSe secondary phases. Yin *et al.* [82] revealed using nano-indentation that kesterites containing S exhibit improved adhesion to the Mo back-contact region than the pure Se kesterites, which is likely associated to the distinct mechanical properties of S and Se.

4.3.1.3 Photovoltaic performances of solar cell devices

After doing the Raman and HR-SEM cross sectional area analyses to investigate the optimal precursor stack-order and reactive annealing pressure, the ultimate task that followed was to investigate the impact on photovoltaic performance from these two factors (i.e., precursor stack order and reactive annealing pressure, i.e., at 700 mbar and 1bar). The results for the photovoltaic performance of different precursor stack-orders at different pressure conditions, i.e., 700 mbar and 1 bar are summarized in **Table 4.17** and **Table 4.18**.

Table 4.17. Record efficiencies for best performing devices annealed at 1bar.

Device	Eff.%	V _{OC} (mV)	J _{SC} (mA/cm ²)	FF. %
CZGSe (A)	5.0	564.53	17.60	50.53
CZGSe (B)	2.76	440.00	13.74	45.00

From **Table 4.17** it is observed that the device fabricated from the absorber prepared from the precursor stack-order Mo/Cu(4 nm, for 20s)/Zn/Cu/Ge annealed at pressure 1 bar exhibited good photovoltaic performance by attaining 5.0% power conversion efficiency, 564.53 mV open circuit voltage, 17.60 mA/cm² short-circuit current density and a fill factor of 50.53%. A remarkable advancement in the open circuit voltage of 564.53 mV was significant when compared to the previously reported value of 558 mV in literature by Leo Choubrac *et al.* [83] attained by extensive CdS buffer layer optimization studies. M Buffier *et al.* [84] reported a low power conversion efficiency of 0.3% with the corresponding J_{SC} = 3.4 mA/cm², V_{OC} = 253 mV and FF = 32%, employing Mo/Cu/Zn/Ge precursor stack order annealed at 460°C at a pressure of 1 bar in H₂Se environment. In M Buffier *et al.* [84] study, the Ge layer was deposited using e-beam evaporation technique in contrast to this study whereby the Ge layer was deposited by sputtering technique and the reactive selenization was carried out in Se+GeSe₂ environment. This achievement was attributed to better quality of grains towards the surface of the absorber which is demonstrated by the HR-SEM cross sectional area micrographs illustrated in **Figure 4.28 (a)**. This further suggests that the formation of the kesterite phase initially occurs at the Cu rich region as seen for the CZGSe (A) with precursor stack order: Mo/Cu(4 nm, for 20s)/Zn/Cu/Ge where Cu is deposited second to the top Ge layer.

Table 4.18. Record efficiencies for best performing devices annealed at 700 mbar.

Device	Eff.%	V_{OC} (mV)	J_{SC} (mA/cm ²)	FF.%
CZGSe (A)	1.17	270.00	11.25	38.17
CZGSe (B)	4.19	537.00	13.89	54.17

A significant drop in photovoltaic performance of the device fabricated from Mo/Cu(4 nm, for 20s)/Zn/Cu/Ge annealed at a pressure of 700 mbar was observed. This observation demonstrated that indeed the pressure during reactive selenization process plays a vital role in the absorber quality which will have an ultimate effect on the optoelectronic properties of the solar cell devices. In conclusion, the precursor stack-order Mo/Cu(4 nm, for 20s)/Zn/Cu/Ge annealed at a pressure of 1 bar yielded the optimal absorber and these conditions were employed in optimization experiments that followed.

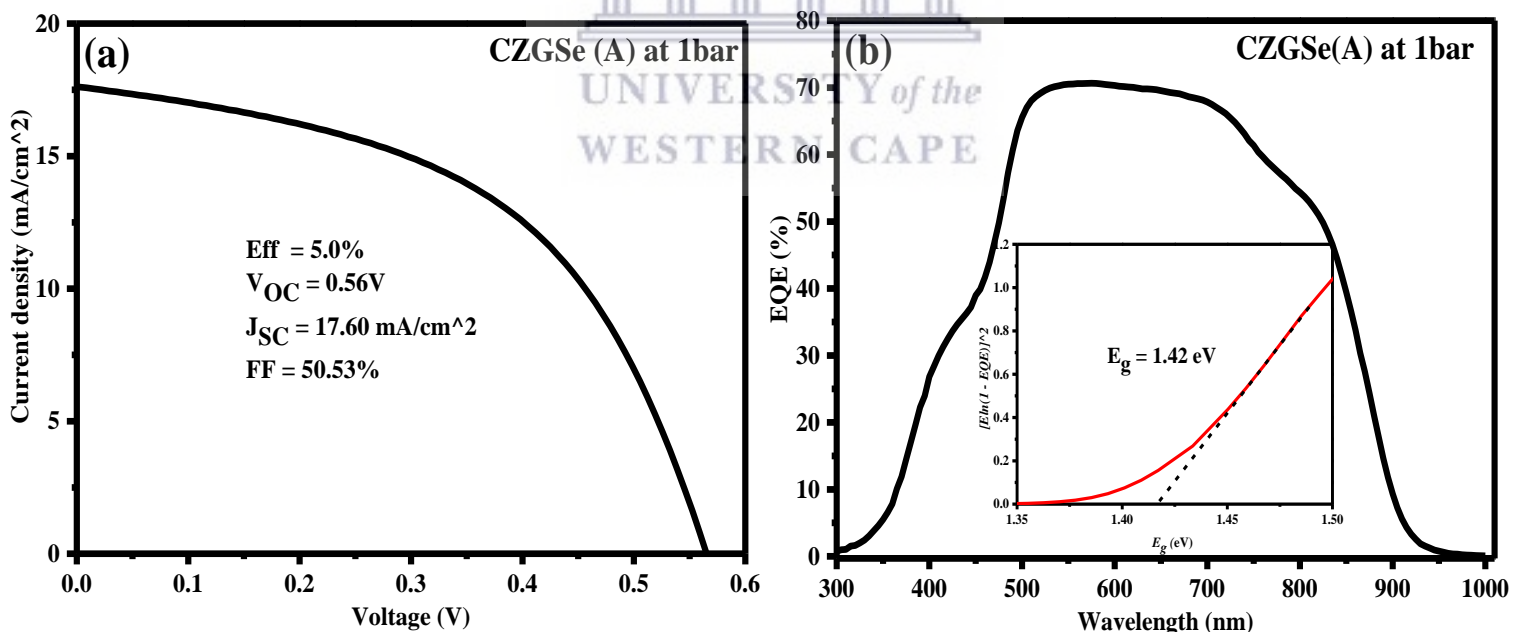


Figure 4.29: Record photovoltaic parameters of the best performing device (a) and external quantum efficiency (EQE) (b) for CZGSe (A).

The external quantum efficiency on the right elucidates that the origin of the improved open circuit voltage V_{OC} is found in the shorter wavelength range (~900 nm in comparison to

~1300 nm for CZTSe) related to the collection of charge carriers from regions deep within the absorber. The optical energy bandgap of CZGSe was determined from the external quantum efficiency (EQE) utilizing a fitting plot of $[E \ln \ln(1 - EQE)]^2$ vs. E ($E = hc/\lambda$, where h is the Plank's constant, c is the speed of light, and λ is the wavelength of the light) which also agree to the method used in the literature [85–87]. The optical energy bandgap was determined to be 1.42 eV ascribed to the improvement in open circuit voltage $V_{OC} = 564.3$ mV for the best performing device; CZGSe (A). This value of optical energy bandgap obtained in this study for pure germanium kesterite absorber CZGSe (1.42 eV) is consistent with theoretical and experimental results previously reported in literature [86,88,89]. . Studies have demonstrated that the energy bandgap of solar cell devices based on chalcogenides provide advance absorption properties in contrast to silicon based solar cells [90]. Moreover, the energy bandgap of the kesterite absorber can be optimized as per solar spectrum by either metal or chalcogenide substitutions [91]. Literature has also reported that the production of kesterite solar cells on module scale could be attained with direct energy bandgap chalcogenide thin film photovoltaics (PVs) with advance absorption properties in contrast to silicon based thin film PVs [92,93]. The earth-abundant, environmentally benign and economical CZTS based solar cells provide advance absorption coefficient $\sim 10^4 \text{ cm}^{-1}$ and the capability to modulate the optical energy bandgap from 1.0 to 1.5 eV achieved by incorporating elemental Se to better complement the solar energy spectrum [91,94,95].

The V_{OC} deficit was determined from the equation below;

$$V_{OC} \text{ deficit (mV)} = \frac{E_g}{q} - V_{OC} \text{ (mV)} \quad (10)$$

where E_g the energy bandgap, q is the electron charge and V_{OC} is the open circuit voltage.

The V_{OC} deficit for CZGSe (A) based solar cell was determined to be 563.64 mV. This value

demonstrates significant improvement in comparison to the value reported for advance efficiency (11.1%) solar cell based on CZTSSe [93]. The V_{OC} deficit is essentially the voltage loss defined as the difference between the energy bandgap the open circuit voltage of the solar cell device. For high efficiency CIGS and CdTe solar cells, voltage losses of $< 400\text{mV}$ are attainable. The best performing kesterite devices exhibit voltage losses (V_{OC} deficit) of around $550 - 600\text{ mV}$ [96]. Hence the value obtained in this study for the best performing device CZGSe (A) at 1bar is acceptable. The origin of V_{OC} deficit has been largely connected to potential fluctuation in kesterite absorber structure resulting in the reduction of the fundamental gap of the material and/or energy bandgap fluctuations (band tailing) [97–99]. Some of the plausible causes for the V_{OC} deficit often mentioned in literature include high defects concentration in the bulk and interfaces of the kesterite absorber (see **Figure 4.28**, the defects between Mo back contact and the CZGSe interface), elemental/compositional non-uniformities within the kesterite absorber and the unavoidable co-existence of several secondary phases (.i.e. ZnSe in this study) along with the kesterite absorber (CZGSe in this study) [99–101].

4.3.2 Annealing Temperature Variation Studies

4.3.2.1 X-ray Fluorescence Analysis

The purpose of XRF measurements was to confirm the desired thickness of Cu, Zn and Ge layers to attain a Cu-poor and Zn-rich regime while keeping the Ge content constant as already outlined in experimental details (see chapter 3). The deposited layers Cu ($\sim 200\text{ nm}$), Zn ($\sim 160\text{ nm}$) and Ge ($\sim 200\text{ nm}$) resulted in the desired ration $\text{Cu/Zn} = 1.60$ for the Cu-poor and Zn-rich regime $\text{Cu}_{1.8}\text{Zn}_{1.2}\text{GeSe}_4$ under investigation as shown in **Table 4.19**.

Table 4.19. XRF measurements of the CZGSe precursor.

Compound	Cu(nm)	Zn(nm)	Cu/Zn	Ge(nm)
CZGSe	206	168	1.60	219

In these optimization experiments, the XRF measurements of the absorber samples after reactive selenization processes (at different annealing temperatures) were taken for quantitative determination of chemical composition and the results are shown in **Table 4.20**.

Table 4.20. XRF measurements of CZGSe absorber after reactive selenization.

Temp (°C)	Cu(%)	Zn(%)	Ge(%)	Se(%)
500	23.37	14.00	16.44	46.19
525	22.41	13.41	15.26	48.92
535	21.97	13.43	15.14	49.46
550	22.11	13.48	14.97	49.44

It was observed that as the reactive annealing temperature was increased from 500 to 550 °C, there was a loss of Ge content from 16.44% to 14.97% and there was more inclusion of Se content into the absorber material from 46.19% to 49.44%, as seen in **Figure 4.30 (a)** and **(b)**.

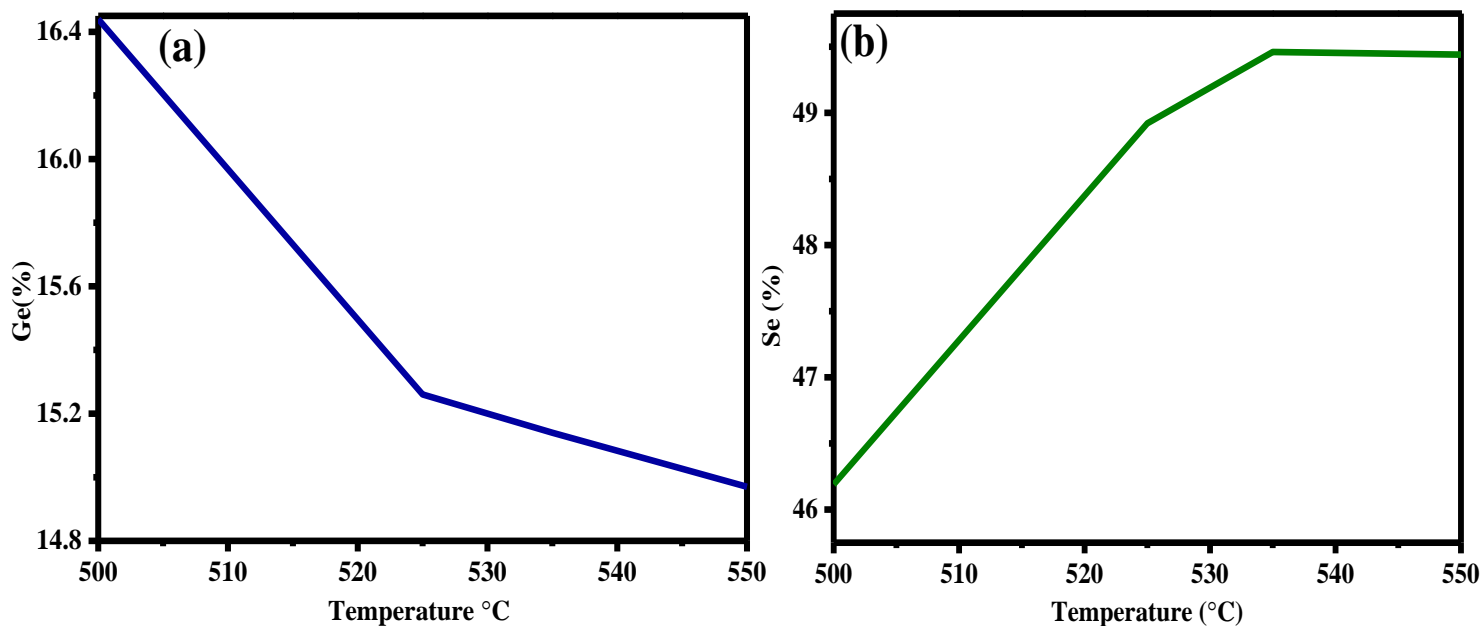
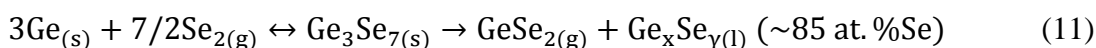


Figure 4.30: Ge content as a function of temperature (a). Se content as a function of temperature (b).

This observation can be explained by taking into consideration the Ge-Se phase diagram. Based on the reactive annealing profile followed in these experiments ($P = 1$ bar, $T = 500, 525, 535$ and 550°C), the Ge precursor layer is expected to form Ge_3Se_7 phase which melts incongruently at 385°C and decays into GeSe_2 (volatile phase) and Se-rich liquid phase ($\approx 85\%$ at% Se) [102]. These liquid phases promote crystal growth which elucidate the observed enlargement of grains towards the surface by HR-SEM cross-sectional area, see **Figure 4.33**. Since GeSe_2 is a volatile phase, its formation will consequently lead to a loss in Ge content (see **Figure 4.30 (a)**), analogous to the reported Sn loss in CZTSe kesterite absorber [103]. The crystallization growth promoted by liquid phase Ge and the observed loss in Ge content can be elucidated by the proposed reaction below;



The formation of the Ge-Se volatile phase (GeSe_2) and the rich Se liquid phase that promote the CZGSe absorber crystallization growth are outlined by the proposed reaction in equation (11) [19].

4.3.2.2 Raman spectroscopy analysis

The Raman spectra of CZGSe samples annealed at different temperatures confirmed the presence of the pure germanium kesterite CZGSe phase at 85.93, 148.73, 176.29, 205.1, 269.65, and 282.94 cm^{-1} which are very close to those of CZTSe phase [104] and ZnSe secondary phases at 250.84 cm^{-1} (1st order ZnSe) and 397.8, 449.34, 503.18 cm^{-1} (2nd order ZnSe) [76] as shown in **Figure 4.31** below.

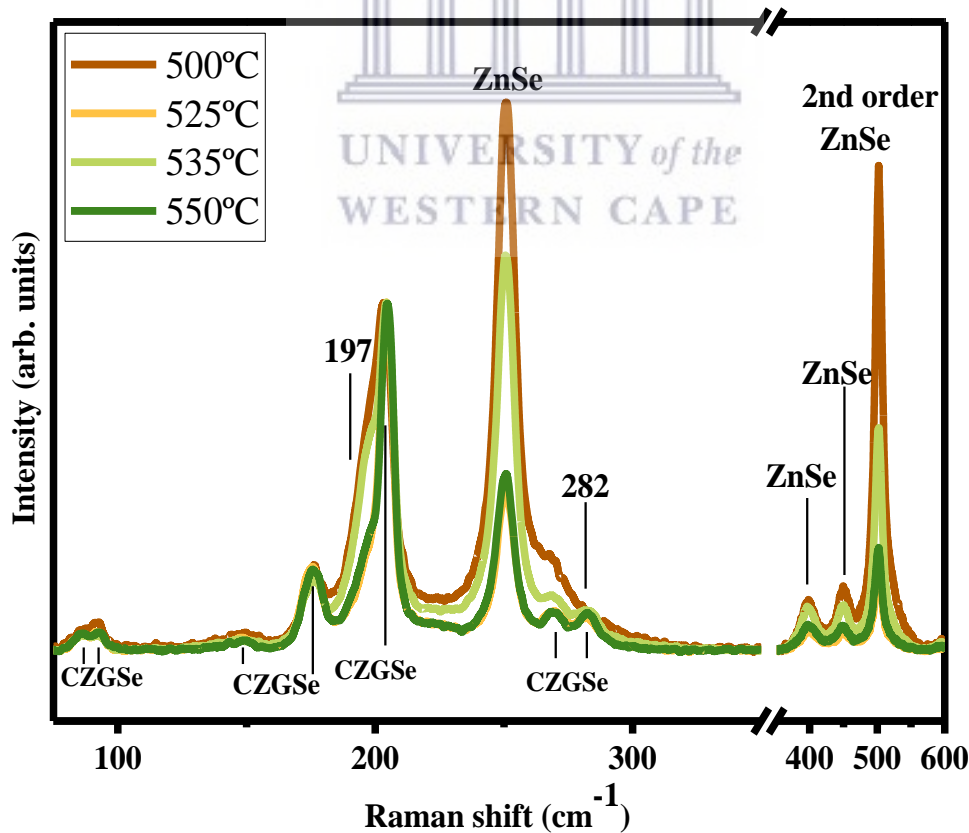
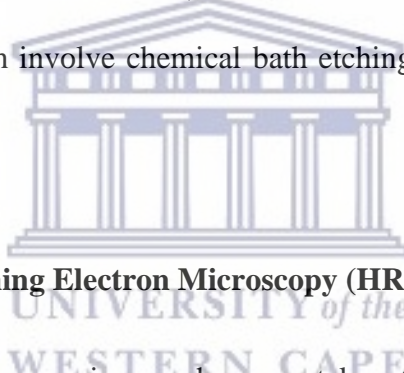


Figure 4.31: Raman spectra near the absorber CZGSe surface samples prepared at different temperatures (500, 525, 535 and 550 °C) at 442 nm excitation wavelength.

The sharp Raman peaks indicated good crystalline quality of the CZGSe absorbers. The high degree of crystallinity was attributed to Ge_xSe_y (~85% Se) liquid phase that acts as a crystallization flux agent during thermal annealing treatment [19]. The presence of ZnSe secondary phases has recently been reported to have a potential to degrade the overall photovoltaic performance of kesterite solar cells [105–107]. In all CZGSe samples, high content of ZnSe secondary phases was pronounced implying that NH_4S solution doesn't actually wash away or eliminate the ZnSe secondary phases. The effective removal of ZnSe secondary phases has been proposed by adapting an oxidation path utilizing $\text{KMnO}_4/\text{H}_2\text{SO}_4$ followed by rinsing of a kesterite absorber in a Na_2S solution [108]. These results (presence of ZnSe on the surface of CZGSe absorbers) called for the optimization experiments that followed in section 4.3.3 which involve chemical bath etching (CBE) studies with different solutions.



4.3.2.3 High Resolution Scanning Electron Microscopy (HR-SEM) analysis

The HR-SEM cross-sectional area micrographs were taken to evaluate the impact of the annealing temperature on the quality of the absorber and the interface between Mo and CZGSe absorber. As seen from **Figure 4.32** and **4.33**, the morphology of the absorber cross-sectional area still exhibit bilayer structural behaviour with an adequate quality of grains (enlarged grains with high degree of crystallinity) observed towards the near surface of the absorber. The enlarged grains observed towards the surface of the absorber is attributed to $\text{Ge}_x\text{Se}_{y(l)}$ (~85 at. %Se) liquid phase that promotes crystallization growth during thermal treatment as already mentioned in section 4.3.2.1. A layer of voids and blisters was also observed between the Mo-back contact and the CZGSe absorber interface.

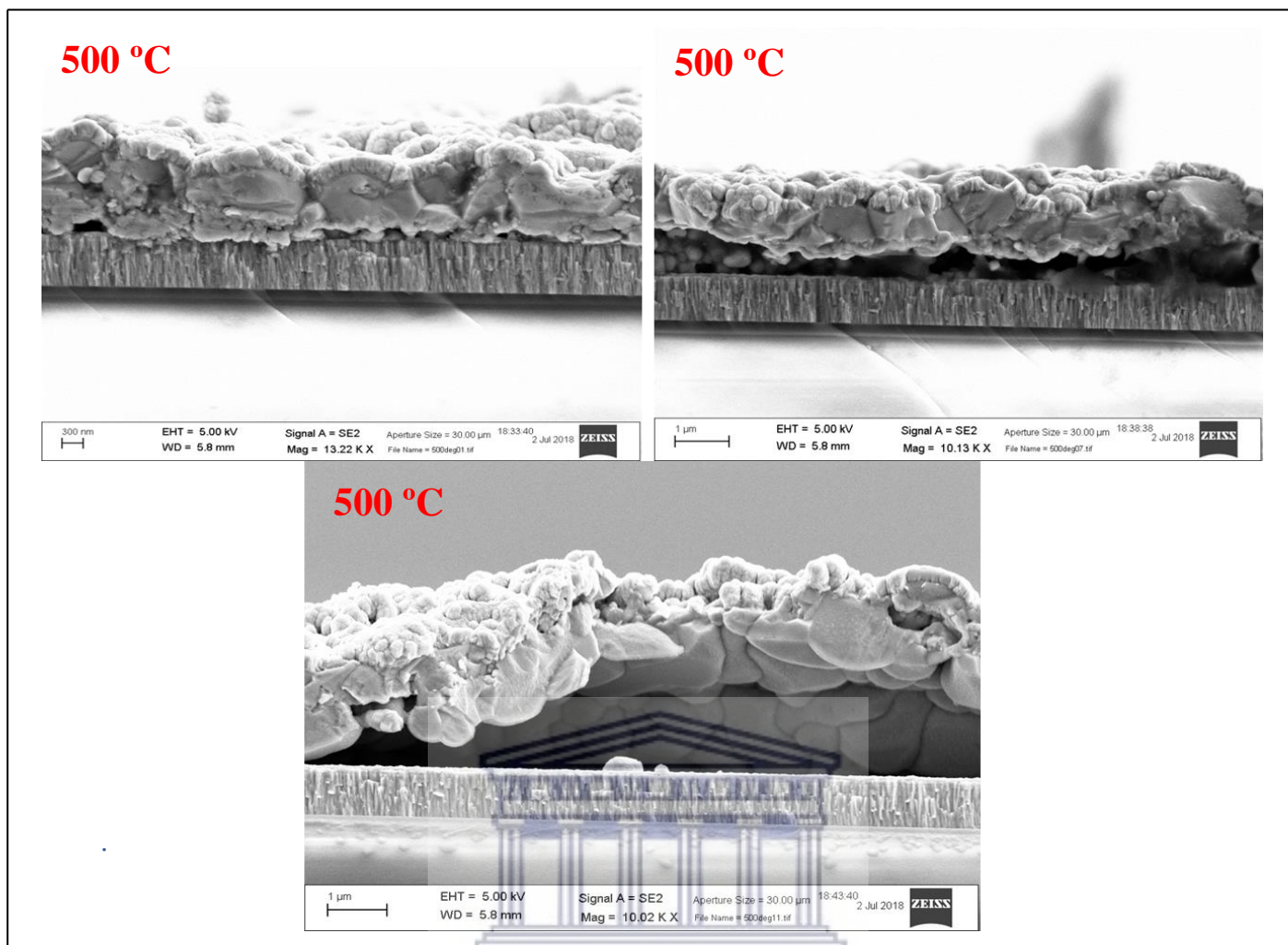


Figure 4.32: HR-SEM cross sectional area micrographs for CZGSe absorber annealed at 500 °C.

Solar cell devices fabricated from the absorber annealed at 500 °C did not work. This could be due to enlarged density of voids and blisters formed at the Mo back-contact and the CZGSe absorber interface as shown in **Figure 4.32** above. This observation further demonstrates that this layer has detrimental effects on the operation and photovoltaic performance of CZGSe solar cell devices as already mentioned in section 4.3.1.2. The formations of volatile species which result to issues on the Mo back-contact region (i.e. poor adhesion and the development of voids) remain an inherent challenge in the preparation of kesterite solar cell devices. A thin layer of Sn was introduced at the back region between the Mo back-contact and the CZTS absorber film to advance the adhesion at the interface [81]. The advanced adhesion was ascribed to the lessening of ZnSe secondary phases. Yin *et al.*

[82] used nano-indentation to advance the adhesion of kesterite absorbers to Mo back-contact and the results demonstrated that the S-containing kesterites show improved adhesion to Mo back-contact in comparison to the pure Se kesterites, attributed to the distinct mechanical properties of S & Se chalcogenides. Hence a poor adhesion was observed in this study for pure selenide kesterite absorber CZGSe to the Mo back-contact.

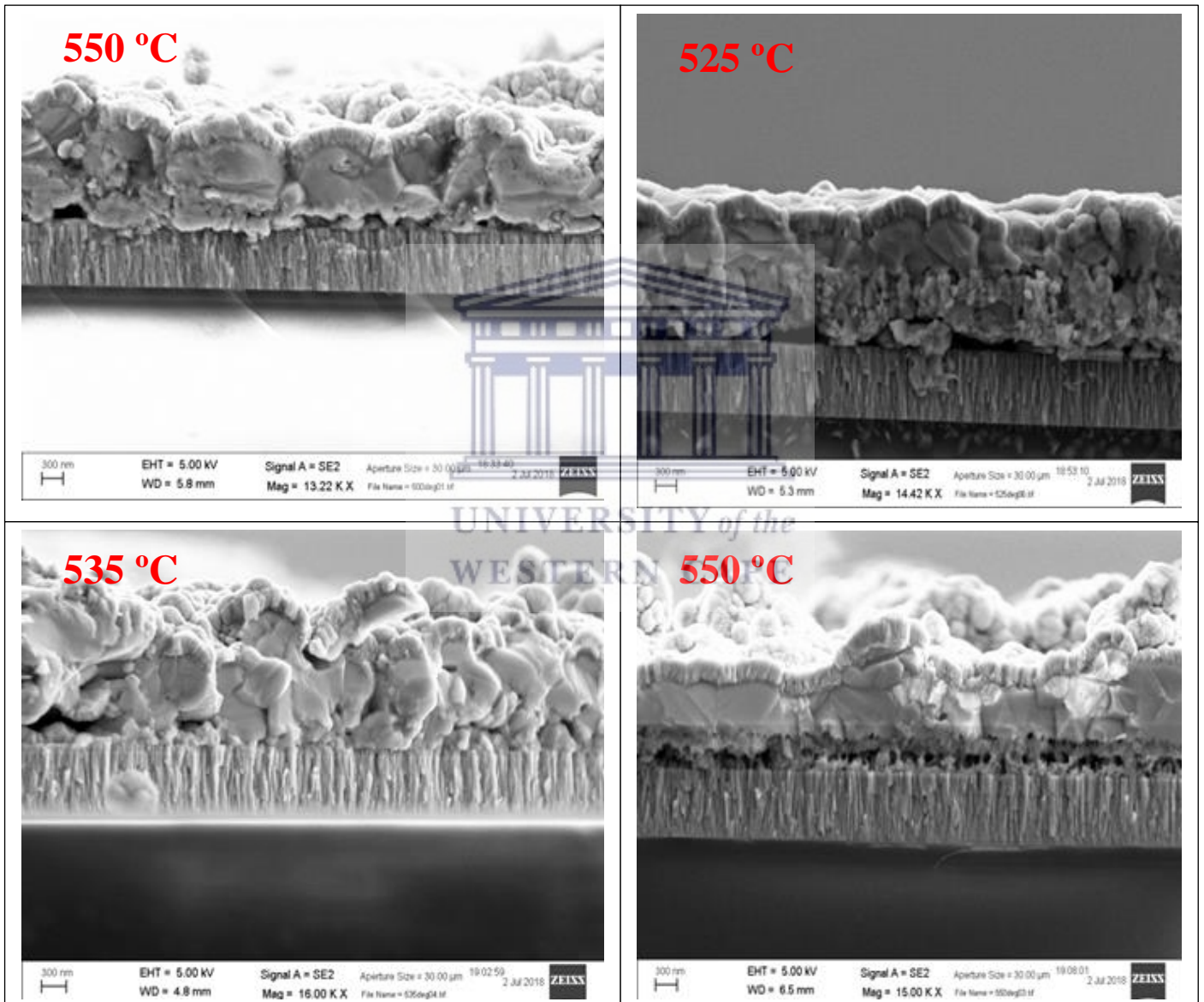


Figure 4.33: HR-SEM cross sectional area micrographs for CZGSe absorbers annealed at 500, 525, 535 and 5500 °C.

Malerba *et al.* published a study investigating the blistering result of the CZTS absorber films synthesised via co-sputtering deposition of precursors which was then followed by thermal

treatment [109]. The study revealed that the probability of the development of blisters is strongly connected to the pressure applied during co-sputtering; it can be significantly condensed at high pressures. The presence of voids at the Mo back region has been one of the challenges encountered in the preparation of kesterite solar cells. This challenge was encountered for both sulphide and selenide based kesterite absorber materials synthesized employing physical routes [107,110,111]. Research has clearly demonstrated that the density of voids mainly depends on parameters used during kesterite synthesis which include thermal annealing conditions [112,113] and the precursor stacking order followed regarding sequential co-sputtering technique [114]. The cause of the growth of these detrimental voids is still not clear but it is estimated to be connected to the stress at the Mo back region, the volatile species related to Sn (Ge in this study, .i.e. $\text{GeSe}_{2(g)}$ volatile phase that forms during thermal treatment) and the probable disintegration of kesterite absorbers in physical contact with Mo back-contact and/or low wetting properties of Cu on Mo during thermal treatment. In the past several years of research, some appealing technological resolutions have been recommended to repress the growth of voids at the Mo back-contact region and most of these resolutions depend on the utilization of an interlayer comprising of oxides [107], nitrides [115] and different metals [116] and they have demonstrated advances on both the morphology and the photovoltaic performance of the resultant solar cell devices. An interesting observation regarding the growth of voids at the Mo back-contact region has been reported; lamella samples prepared employing focused ion beam (FIB) [19,111,117] exhibit voids at the back-contact region. The authors ascribed the origin of voids development to the use of FIB technique, not the process of kesterite absorber film preparation itself, since the FIB technique can preferably sputter Zn and ZnX (X = S or Se).

4.3.2.4 Impact of the annealing temperature on the photovoltaic parameters

The results for the impact of the reactive annealing temperature on the photovoltaic parameters are summarized in **Table 4.21**. The parameters for the solar cell device of the precursor annealed at 500 °C are not included because the absorber did not survive the NH₄S etching (the absorber peeled off from Mo back-contact surface). In **Table 4.21**, only the record power conversion efficiencies are reported. It was observed that as the reactive annealing temperature was elevated from 525 to 550 °C, the photovoltaic parameters also advanced and this could be attributed to the improvements observed in crystallinity (enlarged grains towards the surface) demonstrated by HR-SEM results above, see **Figure 4.33**.

Table 4.21. Record efficiencies of the devices annealed at different temperatures.

Device	Eff.%	V _{OC} (mV)	J _{SC} (mA/cm ²)	FF.%
525 °C	3.18	452.50	14.97	47.08
535 °C	3.80	550.86	14.66	47.03
550 °C	5.00	567.94	17.18	51.17

The highest record power conversion efficiency, open circuit voltage, short circuit current density and the fill factor attained in these experiments was still in the range of 5.00%, 560 mV, 17 mA/cm² and 51%, respectively. This observation demonstrated that more factors on the optimization of the absorber and the overall solar cell device had to be taken into account. Nonetheless, these experiments demonstrated that the reactive annealing temperature thus have an effect on the photovoltaic performance of the CZGSe kesterite solar cell devices. An increase in all the parameters was observed; V_{OC} increased from 452.50 to 567.94 mV, J_{SC} increased from 14.97 to 17.18 mA/cm², FF increased from 47.08 to 51.17% and the power conversion efficiency increased from 3.18 to 5.00%. A noticeable advancement in open

circuit voltage of ~568.00 mV in comparison to the previous experiments (stack order and reactive annealing pressure variations, see section 4.3.1) where the highest attained open circuit voltage of ~565 mV was also observed.

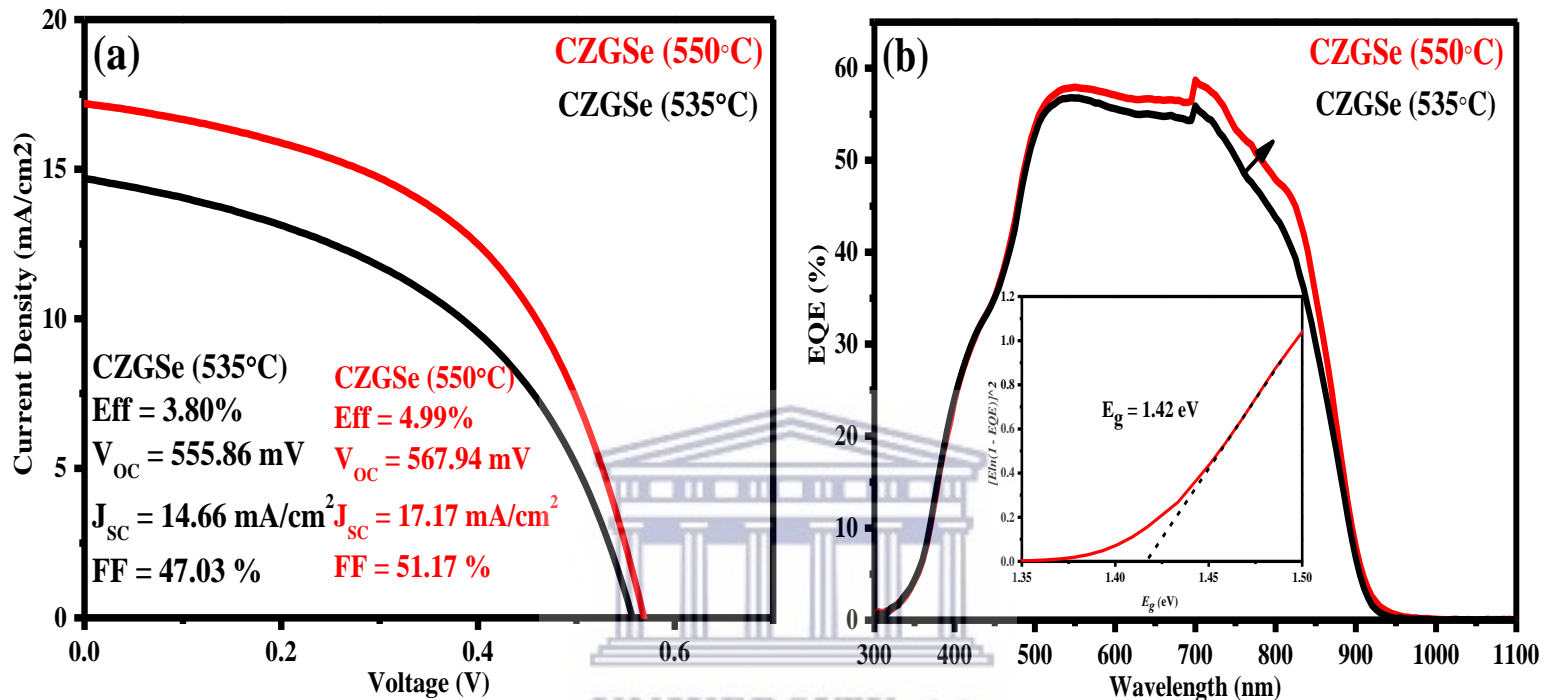


Figure 4.34: Record photovoltaic parameters of the best two performing devices (a) and external quantum efficiency (EQE) (b).

Kesterite solar cells based on pure selenide CZTSe absorber have recently demonstrated power conversion efficiency beyond 11% with an open circuit voltage of 423 mV [118]. The improvement in open circuit voltage of ~568.00 mV (attained without optimization of CdS buffer layer) in this study for pure selenide CZGSe absorber was significant when compared to 423 mV value and the previously reported value of 558 mV in literature by L. Choubrac *et al.* [83] attained through extensive CdS buffer layer optimization studies. The ZnSe secondary phases observed from Raman analysis and a bi-layer structure with voids between the Mo back-contact and the pure selenide CZGSe absorber interface remain a hurdle in improving the photovoltaic performance of the kesterite absorber prepared from the precursor with stack order; Mo/Cu(4nm, for20s)/Zn/Cu/Ge under investigation, indicating that more

optimization experiments had to be carried out. Generally, advance power conversion efficiencies are reported for kesterite absorber materials with Se-rich sulfo-selenide composition, which commonly result in advance open circuit voltage V_{OC} . This emphasizes the significance to ascertain and decrease voltage losses (lower the V_{OC} deficit) for these absorber materials [119,120]. Graphical representation of the highest performing devices is illustrated in **Figure 4.34**. The external quantum efficiency (EQE) of the devices also demonstrated that the reactive annealing temperature had an impact on the photo-physical properties of the absorber as the area under the curve slightly expanded, demonstrating that more photons were harvested for the precursor annealed at a very high temperature of 550 °C and this correlated with the record parameters of the highest performing solar cell device.

4.3.3 Chemical Bath Etching (CBE) studies with different solutions

Based on the phase diagram of $Cu_2Se-ZnSe-GeSe_2$ system [121], the growth of ZnSe binary phase (which are detrimental secondary phases) could be attributed to Zn over-stoichiometry (in Cu-poor and Zn-rich CZGSe regime followed in this study, see XRF results in section 4.3.3.1) and/or to the unfinished reaction between binary/ternary phases to materialize the quaternary compound. The photovoltaic performance gap between CZTS and CIGS solar cells [122–124] is ascribed to the growth of secondary phases, vacancies, antisites and self-compensating defect complexes in CZTS together with carrier recombination processes at different interfaces which have a negative impact on the power conversion efficiency of the CZTS solar cells. The aim of these experiments was to explore different solutions prepared under different conditions as an attempt to completely eliminate the ZnSe secondary from the surface of the CZGSe absorber.

4.3.3.1 X-ray Fluorescence Analysis

The XFR measurements of the CZGSe absorber after reactive selenization stage (thermal treatment in Se + GeSe₂ environment), .i.e. before CBE stage, are given in **Table 4.22** below.

Table 4.22. XRF measurements of the CZGSe absorber post reactive selenization.

Thickness (μm)	Cu (%)	Zn (%)	Ge (%)	Se (%)	Cu/(Zn+Ge)	Zn/Ge	Cu/Zn	Cu/Ge
1.341	17.19	14.16	11.39	57.26	0.67	1.24	1.21	1.51

The following etching solutions were used to wash away the ZnSe secondary phases and the results are given **Table 4.23**;

Cell A: NH₄S (22% v/v, Alfa-Aesar, for 2 min) + KCN (0.01 M for 40s)

Cell B: NH₄S (22% v/v, Alfa-Aesar, for 2 min)

Cell C: HCl (5% at 80°C for 40s)

Cell D: [KMnO₄ (0.01 M) + H₂SO₄ (1M)] for 40 s + NH₄S (22% v/v, Alfa-Aesar, for 2 min)

The optimum compositions [125–127] for the advance performing CZTSe kesterite solar cell devices have a Cu/(Zn+Sn) ratio around 0.7 – 0.9 and a Zn/Sn ratio around 1.1 – 1.25. This composition was adapted in this study for CZGSe absorber with Cu/(Zn+Ge) ratio around 0.67 and a Zn/Ge around 1.24, see **Table 4.22**. This Cu-poor and Zn-rich off-stoichiometry regime (Cu_{1.8}Zn_{1.2}GeSe₄ in this study) unsurprisingly lead to the growth (formation) of secondary phases, most probably ZnSe [128], which is an n-type semiconductor with a wide energy bandgap of 2.71 eV [129].

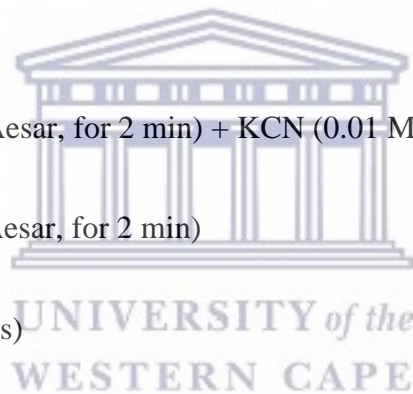


Table 4.23. XRF measurements of the CZGSe absorber post CBE stage.

Thickness (nm)	Cu (%)	Zn(%)	Ge(%)	Se(%)	Cu/(Zn+Ge)	Zn/Ge	Cu/Zn	Cu/Ge
Cell A: 1290	18.50	15.04	9.78	56.68	0.75	1.54	1.23	1.89
Cell B: 1295	18.18	14.83	9.83	57.17	0.74	1.51	1.23	1.85
Cell C: 1317	17.63	14.38	9.78	58.20	0.73	1.47	1.23	1.80
Cell D: 1283	18.03	13.46	9.85	58.60	0.77	1.37	1.34	1.83

A noticeable decrease in Ge content from ~11% (post reactive selenization .i.e. prior CBE stage) to 9% (post CBE stage) was observed as seen from **Table 4.22** and **4.23**. This observation indicated that GeSe₂ (Alfa-Aesar powder, 99.999%) that is used to compensate for the loss of Ge content after reactive selenization is not actually a suitable candidate for that purpose. It is then assumed that after reactive selenization there is still GeSe₂ (solid powder) distributed on the surface of the CZGSe absorber but not actually incorporated into the absorber itself. This observation is also substantiated by an increase observed in Zn/Ge ratio from ~1.2 (prior CBE stage) to ~1.5 (post CBE stage) and also by an increase in Cu/Ge ratio from ~1.5 (prior CBE stage) to ~1.8 (post CBE stage).

4.3.3.2 Raman spectroscopy analysis

Raman spectroscopy is an indispensable characterization technique employed in detecting the secondary phases in the CZTS or CZTS-Se (CZGSe in this study) absorber films since it not sensitive to long range order [130–134]. The lattice strain and the probable lattice distortions in the kesterite crystal structure can be estimated by careful examination of the peak shift. Raman spectroscopy is also a non-destructive technique employed to analyse the detrimental secondary phases in kesterite absorbers. Nevertheless, in most cases only information about the surface of the absorber film can be provided by Raman. Surface etching is needed in the

event when signals are acquired for the bulk into the sample. For each phase to be accurately identified, the optical penetration depth and resonant scattering needs to be determined first. The detrimental secondary phases in polycrystalline CZTS absorber films synthesized by sulfurization of stacked metallic layers deposited by dc magnetron sputtering technique was reported by Fernandes *et al.* [135]. In this study, the CZGSe absorber films were probed utilizing a blue excitation wavelength ($\lambda = 442$ nm) after CBE stage and the results are shown in **Figure 4.35**.

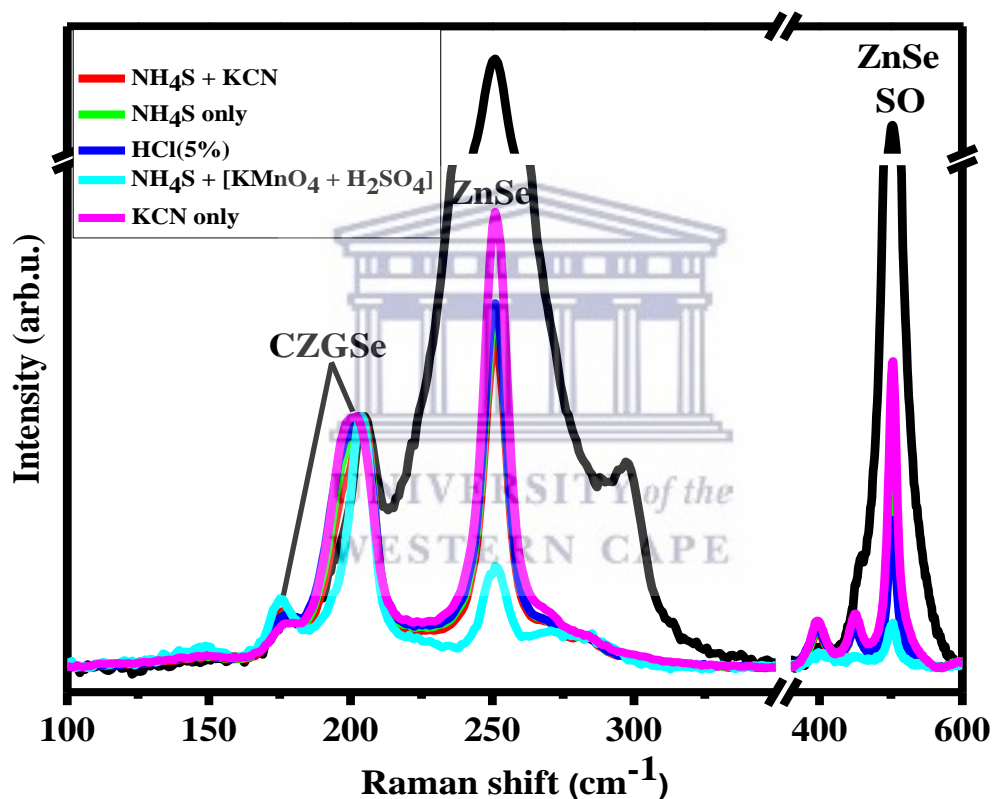
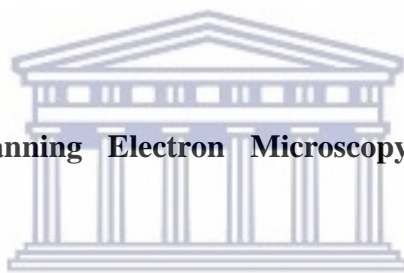


Figure 4.35: Raman spectra of CZGSe absorbers post CBE stage at an excitation wavelength of 442 nm.

The green excitation wavelength ($\lambda = 532$ nm) is utilized for identifying kesterite phases and Cu(S,Se) secondary phases, while the blue ($\lambda = 458$ nm) and the red ($\lambda = 785$ nm) are suitable for the identification of ZnSe and ZnS, respectively [77–80]. Hence in this study a blue excitation wavelength ($\lambda = 442$ nm) was employed for the identification of ZnSe secondary phases. As shown from **Figure 4.35**, the presence of first and second order ZnSe secondary

phases was still identified with sharp peaks at 249 and 500 cm^{-1} [76], respectively, for CZGSe absorbers corresponding to Cell A, B and C, demonstrating that these routes did not eliminate the ZnSe secondary phases from the surface of the absorber. A significant decrease in the concentration of ZnSe secondary phases was observed for the CZGSe absorber corresponding to Cell D which was etched using acidic permanganate solution followed by ammonium sulphate solution; Cell D: $[\text{KMnO}_4 (0.01 \text{ M}) + \text{H}_2\text{SO}_4 (1\text{M})]$ for 40s + NH_4S (22% v/v, Alfa-Aesar, for 2 min). This observation was in agreement that the effective removal of ZnSe secondary phases can be realized by adapting an oxidation path utilizing $\text{KMnO}_4/\text{H}_2\text{SO}_4$ followed by rinsing of a kesterite absorber in a Na_2S solution [108].

4.3.3.3 High-Resolution Scanning Electron Microscopy (HR-SEM) analysis and Photovoltaic Performance



The HR-SEM top view micrographs of CZGSe absorber etched following different routes are depicted in **Figure 4.35**. The HR-SEM top view micrograph images below firstly showed that different etching solutions have different effects on the surface of the CZGSe absorber material. The absorber etched using potassium cyanide solution followed by an ammonium sulphate solution $[\text{KCN} (0.1\text{M}) + (\text{NH}_4)_2\text{S}]$ did not show complete elimination of ZnSe secondary phases from the surface of the absorber. However, this combination of solutions demonstrated better effect compared to the absorber etched using $(\text{NH}_4)_2\text{S}$ solution only, as seen from **Figure 4.36** (top right). This observation demonstrated that use of $(\text{NH}_4)_2\text{S}$ does not wash away the ZnSe secondary phases at all. The other etching route followed was the use of hydrochloric acid HCl (5%) at 80°C which demonstrated undesired results as it is observed that the CZGSe absorber peeled off from the Mo back-contact (bottom left). This

route showed to be detrimental on the quality of the absorber and thus will ultimately have detrimental outcomes on the photovoltaic performance of the devices.

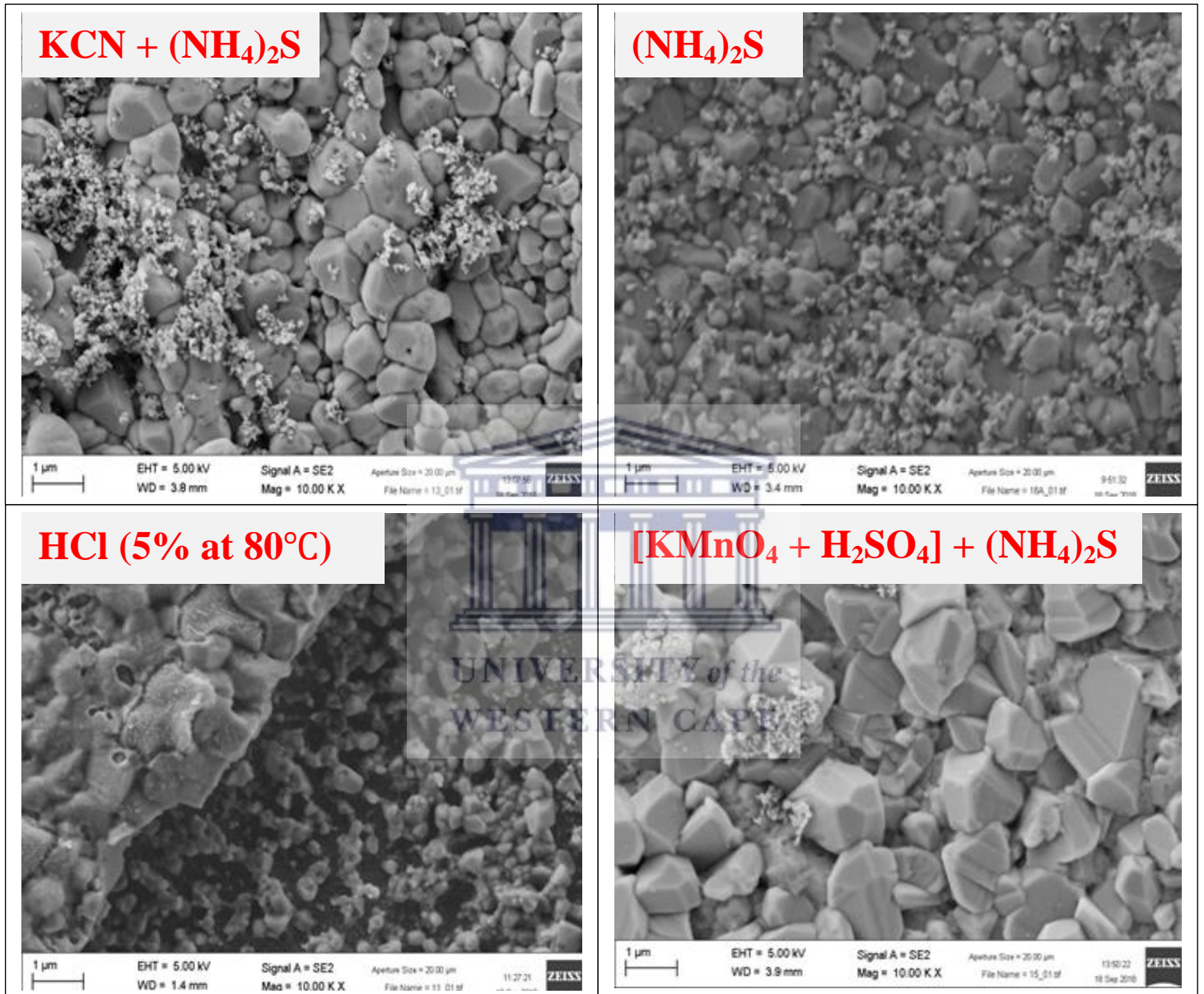


Figure 4.36: HR-SEM top view micrographs for the CZGSe absorbers etched with different solutions (post CBE).

The last etching route that was explored was using acidic permanganate solution followed by ammonium sulphate solution; Cell D: $[\text{KMnO}_4 (0.01 \text{ M}) + \text{H}_2\text{SO}_4 (1\text{M})]$ for 40s + NH_4S (22% v/v, Alfa-Aesar, for 2 min). This route demonstrated better results without compromising the quality of the CZGSe absorber as observed in **Figure 4.36** (bottom right)

and thus better photovoltaic performance was anticipated for the solar cell device fabricated from this absorber (Cell D). The photovoltaic performances of the devices are summarized in **Table 4.24** and **Figure 4.37** below.

Table 4.24. Photovoltaic parameters of CZGSe devices fabricated from absorbers etched with different solutions.

Device	Eff.%	$V_{OC}(mV)$	$J_{SC}(mA/cm^2)$	FF.%
Cell A	0.33±0.49	111.17±15.65	8.07±1.55	28.24±3.28
Cell B	0.62±0.61	202.22±17.00	8.58±1.36	29.33±5.14
Cell C	1.61±0.88	354.45±154.57	9.63±3.70	39.88±4.62
Cell D	1.99±1.27	253.17±172.84	10.90±1.83	34.60±6.80

The CZGSe solar cell device (Cell D) fabricated from the absorber etched with: $[KMnO_4$ (0.01 M) + H_2SO_4 (1M)] for 40s + NH_4S (22% v/v, Alfa-Aesar, for 2 min) showed high collection of current 10.90 ± 1.83 mA/cm² compared to other devices. The highest performing device was also from the this etching route which attained power conversion efficiency of 3.70%, open circuit voltage of 567.27 mV, short circuit current density of 13.34 mA/cm² and fill factor of 50.2%, see **Figure 4.37 (a)**. A significant advance in $V_{OC} = 567.27$ mV was still realized for CZGSe based solar devices developed in this study, and the photovoltaic parameters attained here are parallel to the highest values published in literature for CZTSe based solar cell devices [87,107,136,137]. The external quantum efficiency on the right also showed that the device fabricated from the absorber etched following $[KMnO_4$ (0.01 M) + H_2SO_4 (1M)] for 40s + NH_4S (22% v/v, Alfa-Aesar, for 2 min) route exhibited best carrier collections compared to other devices and this was confirmed by the bigger area under the blue EQE curve, see **Figure 4.37 (b)**. This observation demonstrated that the presence of ZnSe secondary phases on the surface of CZGSe absorber affects the absorption properties

owing to the fact that ZnSe (2.7 eV) [129] has a higher energy bandgap than the CZGSe absorber (≈ 1.42 eV). Although the highest attained power conversion efficiency for the best performing CZGSe device ($\approx 3.70\%$) was relatively small compared to the results reported for optimization experiments in section 4.3.1 and 4.3.2, these optimization studies demonstrated the effect of different etching routes utilized for the elimination of ZnSe secondary phases near the absorber surface and the impact on the photovoltaic performance of the solar devices.

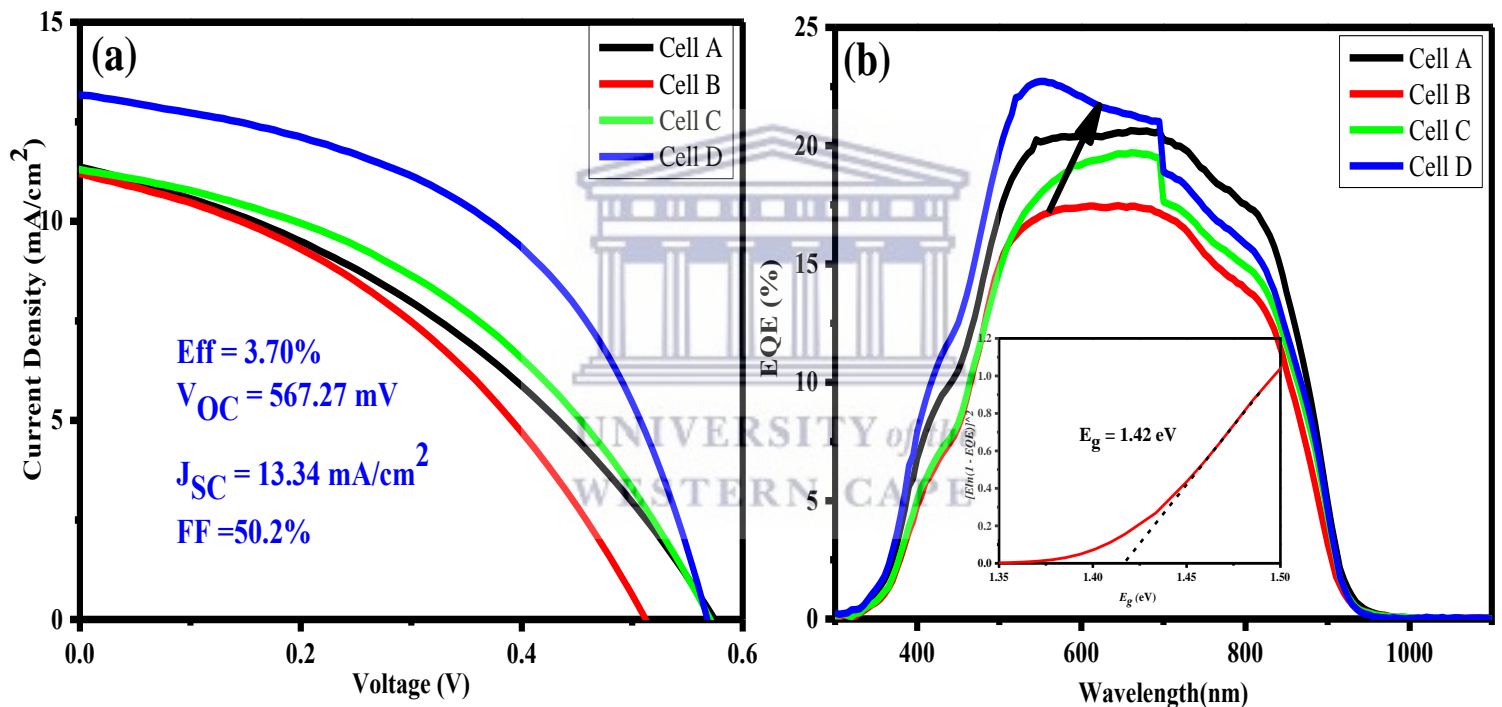


Figure 4.37: Record photovoltaic parameters of the best performing devices (a) and external quantum efficiency (EQE) (b).

The impact of ZnSe secondary phases in CZTSe kesterite solar cells has been reported in literature. The identification of ZnS at the back region of CZTS solar cells with power conversion efficiency of 8.4% [138] has been reported. However, the identification (location not specified) of ZnS in other solar cell devices corresponds with the 25% reduction in power conversion efficiency [139]. Moreover, the detrimental impact of ZnSe secondary phases on the surface of CZTS kesterite absorbers has also been reported [140]. A 50% upgrading in the

power conversion efficiency correlated to an increase in short-circuit current density J_{SC} , open circuit voltage (V_{OC}), and fill factor (FF) was realized after chemical etching in HCl (hence this route was explored in this study for CZGSe absorber). The direct correlations of ZnSe secondary phase (on the surface of the kesterite absorber) to the reduction of short-circuit current density J_{SC} has also been published in literature [141]. In these optimization experiments (CBE studies), the highest short circuit current $J_{SC} = 10.90 \pm 1.83 \text{ mA/cm}^2$ (see **Table 4.24**) was attained for Cell D fabricated from a CZGSe absorber with low concentration of ZnSe secondary phases on the surface, see **Figure 4.35** and **4.36**. Furthermore, a comprehensive examination of the impact of ZnSe secondary connected to its location (back regions and surface) on the kesterite absorber was also explored [142,143]. The presence of ZnSe located at the back region showed to be less detrimental for the solar cell device photovoltaic performance in contrast to when located at the surface region of the kesterite absorber. Hence these experiments; chemical bath etching (CBE) studies with different solutions, were crucial in this study for the optimization of CZGSe absorber and the resultant solar cell devices. A significant dilapidation of V_{OC} , J_{SC} , and FF was reported ZnSe secondary phases located on the surface of the kesterite absorber. It was also observed and stated that the presence of ZnSe secondary phases on the surface of kesterite absorber obstruct the foundation good ohmic contact with the CdS buffer layer.

It is clear from these studies that the successful elimination of secondary phases is essential to boost solar cell devices based on kesterite absorber; CZTS(e) (CZGSe in this study), in power conversion efficiency orientated commercialization contest. Only a few successful etching routes have been published for CZTS(e) kesterite absorbers. Etching only in deionized water (DIW) and in HCl [140] has demonstrated efficacy which was reflected in the power conversion efficiency for pure sulphur kesterite absorber; CZTS. The utilization of only bromine in methanol (Br_2/MeOH) mixed with HCl together with an extended etching in KCN

(5%) is also published in literature [126]. The utilization of Br_2/MeOH results in the reduction of Cu and Sn content at the surface of the kesterite absorber, showing selective elimination of a Cu-Sn-Se (CTSe) secondary phase; the utilization of HCl decreases the Zn content, connected to the elimination of ZnSe secondary phases. Nevertheless, an insignificant boost in power conversion efficiency is realized, rarely 0.5% is realized after etching with KCN (5%), the main boost is observed in the open circuit voltage V_{OC} . There is still no strong substantiation for the complete elimination of ZnSe secondary phases in pure-Se or rich-Se kesterite-based solar cell devices (CZGSe solar cell devices developed in this study) having a major effect on power conversion efficiency of the solar cell device. Hence even for the device Cell D: $[\text{KMnO}_4 (0.01 \text{ M}) + \text{H}_2\text{SO}_4 (1\text{M})]$ for 40s + NH_4S (22% v/v, Alfa-Aesar, for 2 min) in this study, the presence of ZnSe on CZGSe absorber surface could still be identified, see the top-view HR-SEM micrograph in **Figure 4.36** (bottom left). Remarkably, these solar cell devices (Se-pure or Se-rich kesterite-based devices) have the supreme power conversion efficiencies in the kesterites family [87,93]. The utilization of oxidizing agents to eliminate (etch) and lessen the ZnSe surface has been extensively reported in literature [144–146]. Detrimental residuals form on the surface of the kesterite absorber after treatment with oxidizing agents in acidic medium ($\text{KMnO}_4/\text{H}_2\text{SO}_4$); this is why a further chemical treatment (NH_4S (22% v/v, Alfa-Aesar, for 2 min)) is carried out as seen for the solar cell device: Cell D: $[\text{KMnO}_4 (0.01 \text{ M}) + \text{H}_2\text{SO}_4 (1\text{M})]$ for 40s + NH_4S (22% v/v, Alfa-Aesar, for 2 min). The elimination of these residual phases is carried out in aqueous solutions of CS_2 [146] or $(\text{NH}_4)_2\text{S}$ [144] (utilized in this study for Cell D). The improvement in photovoltaic performance for Cell D in comparison to other cells (A, B and C) is attributed to an improved p–n junction between the CZGSe absorber/CdS buffer layer interface (owing to low concentration of ZnSe secondary phases) in agreement with some results already reported in literature [143].

4.3.4 CdS buffer layer optimization

The utilization of elemental germanium as a surface dopant to improve the photovoltaic performance of solar cells based on tin-kesterite absorbers CZTSSe by improving the p-CZTSSe/n-CdS interface [117] has been demonstrated in many of the recent studies. This observation has also been made when few nanometers of germanium are deposited onto Mo back-contact preceding the CZTSSe absorber growth. A specific optimization of CdS buffer layer is therefore critical for the upgrading of photovoltaic performance since the absorber (CZGSe in this study)/CdS interface govern the working of the kesterite solar cell devices [147,148]. In the work reported by L. Choubrac *et al.* [83], the CdS chemical bath deposition (CBD) was optimized by investigating the impact of the bath temperature and the dipping time. The best photovoltaic performance for CZGSe based devices; Eff = 7.6%, $V_{OC} = 558$ mV, $J_{SC} = 22.8 \text{ mAcm}^{-2}$, and FF = 60%, was attained at a temperature $T = 52^\circ\text{C}$ and dipping time of $t = 5$ min. This performance was attributed to enriched CZGSe absorber coverage by CdS buffer layer and the optimal CdS thickness enough for advance p-CZGSe/n-CdS interface quality. So, these CBD parameters; $T = 52^\circ\text{C}$ and $t = 5$ min, were adapted in this optimization route as a strategy to improve the photovoltaic performance of CZGSe based solar cell devices developed in this study. The experimental details of this part of optimization studies are given in chapter 3. It was observed in the study reported by L. Choubrac *et al.* [83] that as the dipping time was extended to 7 min; there was a minimal deficit in current density attributed to the blue-shift in the absorption by the CdS buffer layer. This observation demonstrated that there was a significant degradation in p-CZGSe/n-CdS interface as the dipping time was extended to 7 min and beyond. This interface degradation was induced by the change in physico-chemical characteristics of the CdS buffer layer which is caused by the growth of ion-ion and cluster-cluster as the dipping duration is stretched beyond 7 min. The formation of these clusters on the CdS buffer layer has a detrimental

impact on the operation and the overall photovoltaic performance of the kesterite solar cell device hence these experiments were essential in developing optimal CZGSe based kesterite solar cell devices in this study.

4.3.4.1 XRF measurements

After thermal treatment (reactive selenization in Se + GeSe₂ environment), the Cu-poor and Zn-rich composition for Cu_{1.8}Zn_{1.2}GeSe₄ regime was confirmed with XRF measurements in **Table 4.25** with Cu/(Zn + Ge) = 0.67, Cu/Zn = 1.21 and Zn/Ge = 1.24.

Table 4.25. XRF measurements of the CZGSe absorber prior chemical bath etching (CBE).

Thickness (nm)	Cu (%)	Zn (%)	Ge (%)	Se (%)	Cu/(Zn + Ge)	Zn/Ge	Cu/Zn	Cu/Ge
1341	17.19	14.16	11.39	57.26	0.67	1.24	1.21	1.51

This Cu-poor and Zn-rich off-stoichiometry (Cu_{1.8}Zn_{1.2}GeSe₄ regime in this study) unsurprisingly leads to the growth (formation) of secondary phases during reactive selenization process at high temperature (535°C), most probably ZnSe [128]. The following etching solutions were used to wash away the ZnSe secondary phases and the results are given in **Table 4.26**;

Cell E: (NH₄)₂S (22% v/v, Alfa-Aesar, for 2 min) and

Cell F: [KMnO₄ (0.1M) + H₂SO₄ (1M)] for 40s + (NH₄)₂S (22% v/v, Alfa-Aesar, for 2 min).

Table 4.26. XRF measurements of the CZGSe absorbers post chemical bath etching (CBE).

Thickness (nm)	Cu (%)	Zn (%)	Ge (%)	Se (%)	Cu/(Zn + Ge)	Zn/Ge	Cu/Zn	Cu/Ge
Cell E:1298	17.71	14.41	9.72	58.16	0.73	1.48	1.23	1.82
Cell F: 1278	18.19	14.59	9.78	57.45	0.75	1.49	1.25	1.86

A noticeable decrease in Ge content from ~11% (after reactive selenization .i.e. prior CBE stage) to ~9% (post CBE stage) was again observed as seen from **Table 4.25** and **4.26**. This observation further demonstrated that GeSe₂ (Alfa-Aesar powder, 99.999%) that is used to compensate for the loss of Ge content after reactive selenization is not actually a suitable candidate for that purpose. It is then assumed that after reactive selenization there is still GeSe₂ (solid powder) distributed on the surface of the CZGSe absorber but not actually incorporated into the absorber itself. This observation is also substantiated by an increase observed in Zn/Ge ratio from ~1.2 (prior CBE stage) to ~1.5 (post CBE stage) and also by an increase in Cu/Ge ration from ~1.5 (prior CBE stage) to ~1.8 (post CBE stage). The two CBE routes were followed to further demonstrate the passivating capacity of the permanganate solution in acidic medium; KMnO₄/H₂SO₄, in contrast to the sulphate solution; (NH₄)₂S.

4.3.4.2 Photovoltaic performance measurements

The photovoltaic performances of the devices are summarized in **Table 4.27** and **Figure 4.38** below.

Table 4.27. Photovoltaic parameters of CZGSe devices fabricated with the optimized CdS buffer layer.

Devices	Eff.%	V_{oc} (mV)	J_{sc} (mA/cm ²)	FF.%
Cell E	1.72±0.88	353.52±17	10.88±3.04	40.38±3.57
Cell F	3.08±1.56	427.99±177	13.18±1.50	44.16±9.31

The results show noticeable improvements in the photovoltaic parameters when compared to the results obtained in the previous optimization experiments where the optimal CdS buffer layer parameters were not adapted.

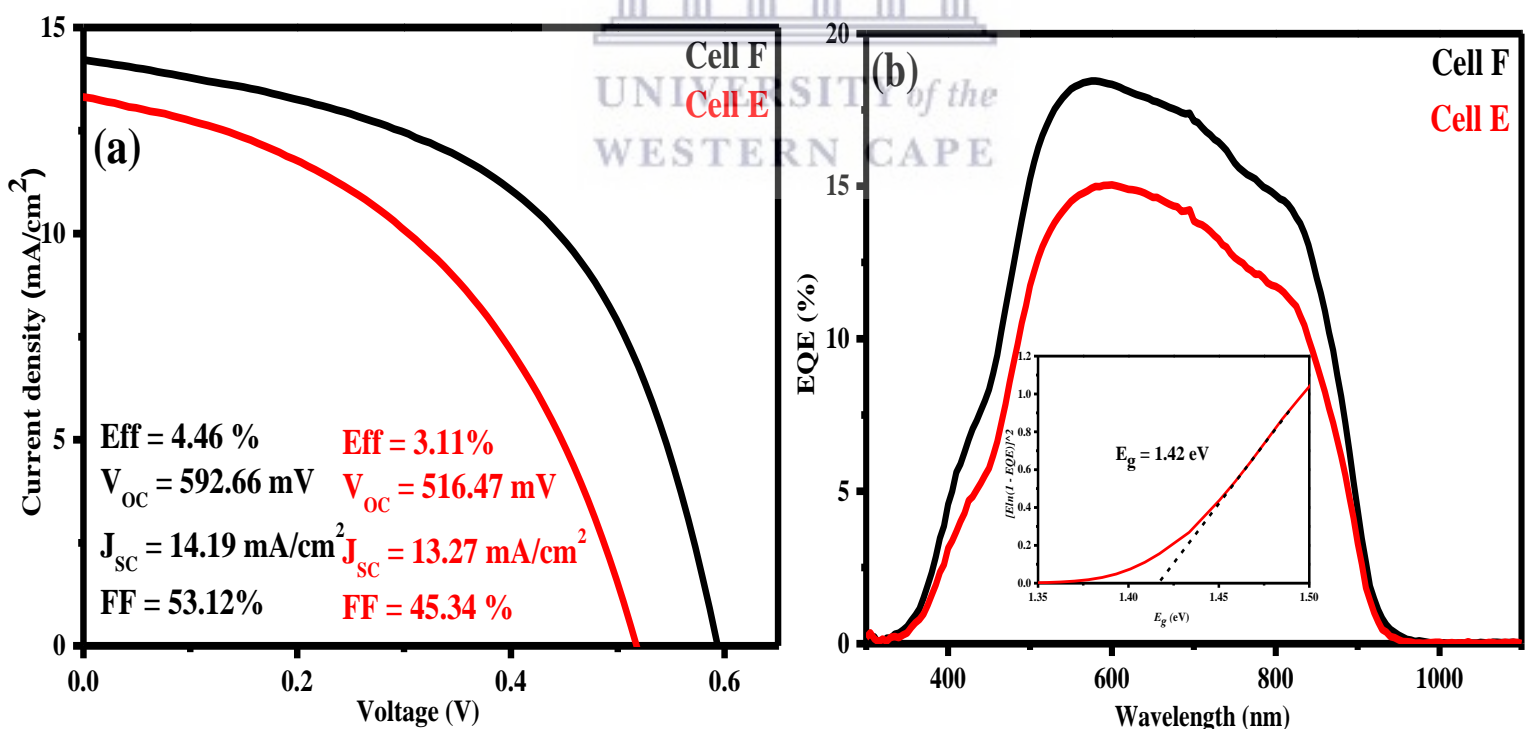


Figure 4.38: Record photovoltaic parameters for the best performing CZGSe devices (a) and external quantum efficiency (EQE) (b).

For CdS optimized solar cell devices fabricated from CZGSe absorbers etched with Cell F: [KMnO₄ (0.1M) + H₂SO₄ (1M)] for 40s + (NH₄)₂S (22% v/v, Alfa-Aesar, for 2 min); the devices attained an average power conversion efficiency of 3.08±1.56 %, open circuit voltage of 427.99±177 mV, short circuit current density of 13.18±1.50 mA/cm², and fill factor of 44.16±9.31% (Cell F, see **Table 4.27**) while devices with non-optimized CdS parameters (Cell D, see **Table 4.24**) attained average power conversion efficiency of 1.99±1.27%, open circuit voltage of 253.17±17 mV, short circuit current density of 10.90±1.83 mA/cm² and fill factor of 34.60±6.80%. The differences in these results are summarized in **Table 4.28** for clarity.

Table 4.28. Summary of photovoltaic parameters for CZGSe solar cell devices etched utilizing KMnO₄/H₂SO₄ followed by (NH₄)₂S passivation route.

Non-Optimized CdS buffer layer				
Device	Eff.%	V _{oc} (mV)	J _{sc} (mA/cm ²)	FF.%
Cell D	1.99±1.27	253.17±17	10.90±1.83	34.60±6.80
Optimized CdS buffer layer				
Cell F	3.08±1.56	427.99±177	13.18±1.50	44.16±9.31

A significant improvement in the photovoltaic parameters of CZGSe solar cell devices attributed to the optimized CdS buffer layer was confirmed by the results summarized in **Table 4.28**. These results show that indeed the optimization of the CdS buffer layer improves the p-CZGSe/n-CdS interface which governs the operation and the overall photovoltaic performance of the kesterite solar cell device [117,147,148]. The record photovoltaic parameters are given in **Table 4.29** and the graphical representation is given in **Figure 4.38**.

Table 4.29. Summary of record photovoltaic parameters for CZGSe solar cell devices etched utilizing $\text{KMnO}_4/\text{H}_2\text{SO}_4$ followed by $(\text{NH}_4)_2\text{S}$ passivation route.

Non-Optimized CdS buffer layer				
Device	Eff.%	V_{oc} (mV)	J_{sc} (mA/cm^2)	FF.%
Cell D	3.70	567.27	13.34	50.20
Optimized CdS buffer layer				
Cell F	4.46	592.66	14.19	53.12

A striking record open circuit voltage of 592.66 mV was observed for Cell F (optimized CdS buffer layer) transcending 558 mV attained by L. Choubrac *et al.* [83] (also with optimized CdS buffer layer). This was a remarkable achievement in this study. The external quantum efficiency on the right also showed that the solar cell device fabricated from the absorber etched following: $[\text{KMnO}_4 (0.1\text{M}) + \text{H}_2\text{SO}_4 (1\text{M})]$ for 40s + $(\text{NH}_4)_2\text{S}$ (22% v/v, Alfa-Aesar, for 2 min) route exhibited best carrier collections compared to the device fabricated from absorber etched following: $(\text{NH}_4)_2\text{S}$ (22% v/v, Alfa-Aesar, for 2 min) solution only and this was confirmed by the noticeable huge area under the black EQE curve (see **Figure 4.38 (b)**). The observed improvements were attributed to the passivation effect of the $\text{KMnO}_4/\text{H}_2\text{SO}_4$ oxidizing solution that results in low concentration of ZnSe secondary phases as well as the lower concentration of CdS clusters owing to the optimal CdS buffer layer parameters adapted in these studies [83].

Bibliography

- [1] F. Giustino, H.J. Snaith, Toward Lead-Free Perovskite Solar Cells, *ACS Energy Letters*. 1 (2016) 1233–1240. <https://doi.org/10.1021/acsenergylett.6b00499>.
- [2] S.A. Kulkarni, S.G. Mhaisalkar, N. Mathews, P.P. Boix, Perovskite Nanoparticles: Synthesis, Properties, and Novel Applications in Photovoltaics and LEDs, *Small Methods*. 3 (2019) 1800231. <https://doi.org/10.1002/smt.201800231>.
- [3] B. Conings, J. Drijkoningen, N. Gauquelin, A. Babayigit, J. D'Haen, L. D'Olieslaeger, A. Ethirajan, J. Verbeeck, J. Manca, E. Mosconi, F. De Angelis, H.G. Boyen, Intrinsic Thermal Instability of Methylammonium Lead Trihalide Perovskite, *Advanced Energy Materials*. 5 (2015) 1500477. <https://doi.org/10.1002/aenm.201500477>.
- [4] D. Bryant, N. Aristidou, S. Pont, I. Sanchez-Molina, T. Chotchunangatchaval, S. Wheeler, J.R. Durrant, S.A. Haque, Light and oxygen induced degradation limits the operational stability of methylammonium lead triiodide perovskite solar cells, *Energy and Environmental Science*. 9 (2016) 1655–1660. <https://doi.org/10.1039/c6ee00409a>.
- [5] G.E. Eperon, S.D. Stranks, C. Menelaou, M.B. Johnston, L.M. Herz, H.J. Snaith, Formamidinium lead trihalide: A broadly tunable perovskite for efficient planar heterojunction solar cells, *Energy and Environmental Science*. 7 (2014) 982–988. <https://doi.org/10.1039/c3ee43822h>.
- [6] C. McDonald, C. Ni, P. Maguire, P. Connor, J.T.S. Irvine, D. Mariotti, V. Svrcek, Nanostructured perovskite solar cells, *Nanomaterials*. 9 (2019) 1481. <https://doi.org/10.3390/nano9101481>.

- [7] Z. Shi, J. Guo, Y. Chen, Q. Li, Y. Pan, H. Zhang, Y. Xia, W. Huang, Lead-Free Organic–Inorganic Hybrid Perovskites for Photovoltaic Applications: Recent Advances and Perspectives, *Advanced Materials*. 29 (2017) 1605005. <https://doi.org/10.1002/adma.201605005>.
- [8] E. Koren, E. Lörtscher, C. Rawlings, A.W. Knoll, U. Duerig, Adhesion and friction in mesoscopic graphite contacts, *Science*. 348 (2015) 679–683. <https://doi.org/10.1126/science.aaa4157>.
- [9] Z.F. Shi, X.G. Sun, D. Wu, T.T. Xu, S.W. Zhuang, Y.T. Tian, X.J. Li, G.T. Du, High-performance planar green light-emitting diodes based on a PEDOT:PSS/CH₃NH₃PbBr₃/ZnO sandwich structure, *Nanoscale*. 8 (2016) 10035–10042. <https://doi.org/10.1039/c6nr00818f>.
- [10] L.N. Quan, F.P. García de Arquer, R.P. Sabatini, E.H. Sargent, Perovskites for Light Emission, *Advanced Materials*. 30 (2018) 1801996. <https://doi.org/10.1002/adma.201801996>.
- [11] H. Cho, S.H. Jeong, M.H. Park, Y.H. Kim, C. Wolf, C.L. Lee, J.H. Heo, A. Sadhanala, N.S. Myoung, S. Yoo, S.H. Im, R.H. Friend, T.W. Lee, Overcoming the electroluminescence efficiency limitations of perovskite light-emitting diodes, *Science*. 350 (2015) 1222–1225. <https://doi.org/10.1126/science.aad1818>.
- [12] J. Xing, Y. Zhao, M. Askerka, L.N. Quan, X. Gong, W. Zhao, J. Zhao, H. Tan, G. Long, L. Gao, Z. Yang, O. Voznyy, J. Tang, Z.H. Lu, Q. Xiong, E.H. Sargent, Color-stable highly luminescent sky-blue perovskite light-emitting diodes, *Nature Communications*. 9 (2018) 3541. <https://doi.org/10.1038/s41467-018-05909-8>.

- [13] C. Zhang, Y. Wang, X. Lin, T. Wu, Q. Han, Y. Zhang, L. Han, Effects of A site doping on the crystallization of perovskite films, *Journal of Materials Chemistry A*. 9 (2021) 1372–1394. <https://doi.org/10.1039/d0ta08656h>.
- [14] C. Shen, Y. Wu, S. Zhang, T. Wu, H. Tian, W.H. Zhu, L. Han, Stabilizing Formamidinium Lead Iodide Perovskite by Sulfonyl-Functionalized Phenethylammonium Salt via Crystallization Control and Surface Passivation, *Solar RRL*. 4 (2020) 2000069. <https://doi.org/10.1002/solr.202000069>.
- [15] W. Wang, M.T. Winkler, O. Gunawan, T. Gokmen, T.K. Todorov, Y. Zhu, D.B. Mitzi, Device characteristics of CZTSSe thin-film solar cells with 12.6% efficiency, *Advanced Energy Materials*. 4 (2014) 1301465. <https://doi.org/10.1002/aenm.201301465>.
- [16] J.J. Scragg, T. Ericson, T. Kubart, M. Edoff, C. Platzer-Björkman, Chemical insights into the instability of $\text{Cu}_2\text{ZnSnS}_4$ films during annealing, *Chemistry of Materials*. 23 (2011) 4625–4633. <https://doi.org/10.1021/cm202379s>.
- [17] R. Fonoll-Rubio, J. Andrade-Arvizu, J. Blanco-Portals, I. Becerril-Romero, M. Guc, E. Saucedo, F. Peiró, L. Calvo-Barrio, M. Ritzer, C.S. Schnohr, M. Placidi, S. Estradé, V. Izquierdo-Roca, A. Pérez-Rodríguez, Insights into interface and bulk defects in a high efficiency kesterite-based device, *Energy and Environmental Science*. 14 (2021) 507–523. <https://doi.org/10.1039/d0ee02004d>.
- [18] C.J. Hages, S. Levenco, C.K. Miskin, J.H. Alsmeier, D. Abou-Ras, R.G. Wilks, M. Bär, T. Unold, R. Agrawal, Improved performance of Ge-alloyed CZTGeSSe thin-film solar cells through control of elemental losses, *Progress in Photovoltaics: Research and Applications*. 23 (2015) 376–384. <https://doi.org/10.1002/pip.2442>.

- [19] S. Giraldo, M. Neuschitzer, T. Thersleff, S. L6pez-Marino, Y. S1nchez, H. Xie, M. Colina, M. Placidi, P. Pistor, V. Izquierdo-Roca, K. Leifer, A. P6rez-Rodr6guez, E. Saucedo, Large Efficiency Improvement in $\text{Cu}_2\text{ZnSnSe}_4$ Solar Cells by Introducing a Superficial Ge Nanolayer, *Advanced Energy Materials*. 5 (2015) 1501070. <https://doi.org/10.1002/aenm.201501070>.
- [20] W. Shockley, H.J. Queisser, Detailed balance limit of efficiency of p-n junction solar cells, *Journal of Applied Physics*. 32 (1961) 510–519. <https://doi.org/10.1063/1.1736034>.
- [21] B.H. Lee, K.S. Gour, V. Karade, J.S. Jang, J. Kim, E. Jo, M.G. Gang, D.M. Lee, I.J. Lee, J. Park, J.H. Kim, Effect of Ge nanolayer stacking order on performance of CZTSSe thin film solar cells, *Materials Letters*. 284 (2021) 128981. <https://doi.org/10.1016/j.matlet.2020.128981>.
- [22] S. Feng, P. Lv, D. Ding, R. A, T. Liu, P. Su, W. Yang, J. Yang, W. Fu, H. Yang, Enhanced photovoltaic property and stability of perovskite solar cells using the interfacial modified layer of anatase TiO_2 nanocuboids, *Vacuum*. 166 (2019) 255–263. <https://doi.org/10.1016/j.vacuum.2019.05.025>.
- [23] D. Shi, V. Adinolfi, R. Comin, M. Yuan, E. Alarousu, A. Buin, Y. Chen, S. Hoogland, A. Rothenberger, K. Katsiev, Y. Losovyj, X. Zhang, P.A. Dowben, O.F. Mohammed, E.H. Sargent, O.M. Bakr, Low trap-state density and long carrier diffusion in organolead trihalide perovskite single crystals, *Science*. 347 (2015) 519–522. <https://doi.org/10.1126/science.aaa2725>.

- [24] M.I. Saidaminov, A.L. Abdelhady, B. Murali, E. Alarousu, V.M. Burlakov, W. Peng, I. Dursun, L. Wang, Y. He, G. MacUlan, A. Goriely, T. Wu, O.F. Mohammed, O.M. Bakr, High-quality bulk hybrid perovskite single crystals within minutes by inverse temperature crystallization, *Nature Communications*. 6 (2015) 7586.
<https://doi.org/10.1038/ncomms8586>.
- [25] N.J. Jeon, J.H. Noh, Y.C. Kim, W.S. Yang, S. Ryu, S. Il Seok, Solvent engineering for high-performance inorganic-organic hybrid perovskite solar cells, *Nature Materials*. 13 (2014) 897–903. <https://doi.org/10.1038/nmat4014>.
- [26] K. Frohna, T. Deshpande, J. Harter, W. Peng, B.A. Barker, J.B. Neaton, S.G. Louie, O.M. Bakr, D. Hsieh, M. Bernardi, Inversion symmetry and bulk Rashba effect in methylammonium lead iodide perovskite single crystals, *Nature Communications*. 9 (2018) 1829. <https://doi.org/10.1038/s41467-018-04212-w>.
- [27] J. Burschka, N. Pellet, S.J. Moon, R. Humphry-Baker, P. Gao, M.K. Nazeeruddin, M. Grätzel, Sequential deposition as a route to high-performance perovskite-sensitized solar cells, *Nature*. 499 (2013) 316–319. <https://doi.org/10.1038/nature12340>.
- [28] Q. Chen, H. Zhou, Z. Hong, S. Luo, H.S. Duan, H.H. Wang, Y. Liu, G. Li, Y. Yang, Planar heterojunction perovskite solar cells via vapor-assisted solution process, *Journal of the American Chemical Society*. 136 (2014) 622–625.
<https://doi.org/10.1021/ja411509g>.
- [29] S. Sun, T. Salim, N. Mathews, M. Duchamp, C. Boothroyd, G. Xing, T.C. Sum, Y.M. Lam, The origin of high efficiency in low-temperature solution-processable bilayer organometal halide hybrid solar cells, *Energy and Environmental Science*. 7 (2014) 399–407. <https://doi.org/10.1039/c3ee43161d>.

- [30] A. Kojima, K. Teshima, Y. Shirai, T. Miyasaka, Organometal halide perovskites as visible-light sensitizers for photovoltaic cells, *Journal of the American Chemical Society*. 131 (2009) 6050–6051. <https://doi.org/10.1021/ja809598r>.
- [31] J.H. Im, C.R. Lee, J.W. Lee, S.W. Park, N.G. Park, 6.5% Efficient Perovskite Quantum-Dot-Sensitized Solar Cell, *Nanoscale*. 3 (2011) 4088–4093. <https://doi.org/10.1039/c1nr10867k>.
- [32] T. Baikie, Y. Fang, J.M. Kadro, M. Schreyer, F. Wei, S.G. Mhaisalkar, M. Graetzel, T.J. White, Synthesis and crystal chemistry of the hybrid perovskite (CH₃NH₃)PbI₃ for solid-state sensitised solar cell applications, *Journal of Materials Chemistry A*. 1 (2013) 5628–5641. <https://doi.org/10.1039/c3ta10518k>.
- [33] D.B. Mitzi, Synthesis, structure, and properties of organic-inorganic perovskites and related materials, in: *Progress in Inorganic Chemistry*, 2007: pp. 1–121. <https://doi.org/10.1002/9780470166499.ch1>.
- [34] V.M. Goldschmidt, Die Gesetze der Krystallochemie, *Die Naturwissenschaften*. 14 (1926) 477–485. <https://doi.org/10.1007/BF01507527>.
- [35] M.M. Lee, J. Teuscher, T. Miyasaka, T.N. Murakami, H.J. Snaith, Efficient hybrid solar cells based on meso-superstructured organometal halide perovskites, *Science*. 338 (2012) 643–647. <https://doi.org/10.1126/science.1228604>.
- [36] A. Dualeh, N. Tétreault, T. Moehl, P. Gao, M.K. Nazeeruddin, M. Grätzel, Effect of annealing temperature on film morphology of organic-inorganic hybrid perovskite solid-state solar cells, *Advanced Functional Materials*. 24 (2014) 3250–3258. <https://doi.org/10.1002/adfm.201304022>.

- [37] P.W. Liang, C.Y. Liao, C.C. Chueh, F. Zuo, S.T. Williams, X.K. Xin, J. Lin, A.K.Y. Jen, Additive enhanced crystallization of solution-processed perovskite for highly efficient planar-heterojunction solar cells, *Advanced Materials*. 26 (2014) 3748–3754. <https://doi.org/10.1002/adma.201400231>.
- [38] Z. Xiao, Q. Dong, C. Bi, Y. Shao, Y. Yuan, J. Huang, Solvent Annealing of Perovskite-Induced Crystal Growth for Photovoltaic-Device Efficiency Enhancement, *Advanced Materials*. 26 (2014) 6503–6509. <https://doi.org/10.1002/adma.201401685>.
- [39] S. Pang, H. Hu, J. Zhang, S. Lv, Y. Yu, F. Wei, T. Qin, H. Xu, Z. Liu, G. Cui, NH₂CH=NH₂PbI₃: An alternative organolead iodide perovskite sensitizer for mesoscopic solar cells, *Chemistry of Materials*. 26 (2014) 1485–1491. <https://doi.org/10.1021/cm404006p>.
- [40] J. Zhao, Y. Deng, H. Wei, X. Zheng, Z. Yu, Y. Shao, J.E. Shield, J. Huang, Strained hybrid perovskite thin films and their impact on the intrinsic stability of perovskite solar cells, *Science Advances*. 3 (2017) 5616. <https://doi.org/10.1126/sciadv.aao5616>.
- [41] F. Haque, M. Wright, M.A. Mahmud, H. Yi, D. Wang, L. Duan, C. Xu, M.B. Upama, A. Uddin, Effects of Hydroiodic Acid Concentration on the Properties of CsPbI₃ Perovskite Solar Cells, *ACS Omega*. 3 (2018) 11937–11944. <https://doi.org/10.1021/acsomega.8b01589>.
- [42] C. Ran, J. Xu, W. Gao, C. Huang, S. Dou, Defects in metal triiodide perovskite materials towards high-performance solar cells: Origin, impact, characterization, and engineering, *Chemical Society Reviews*. 47 (2018) 4581–4610. <https://doi.org/10.1039/c7cs00868f>.

- [43] G.K. Williamson, R.E. Smallman, III. Dislocation densities in some annealed and cold-worked metals from measurements on the X-ray Debye-Scherrer spectrum, *Philosophical Magazine*. 1 (1956) 34–46.
<https://doi.org/10.1080/14786435608238074>.
- [44] T.W. Jones, A. Osherov, M. Alsari, M. Sponseller, B.C. Duck, Y.K. Jung, C. Settens, F. Niroui, R. Brenes, C. V. Stan, Y. Li, M. Abdi-Jalebi, N. Tamura, J.E. MacDonald, M. Burghammer, R.H. Friend, V. Bulović, A. Walsh, G.J. Wilson, S. Lilliu, S.D. Stranks, Lattice strain causes non-radiative losses in halide perovskites, *Energy and Environmental Science*. 12 (2019) 596–606. <https://doi.org/10.1039/c8ee02751j>.
- [45] P.J.F. Moulder, W.F. Stickle, J.F. Sebol, *Handbook of XPS*, Phy Elect Inc., (1995).
- [46] L. Dimesso, M. Wussler, T. Mayer, E. Mankel, W. Jaegermann, Inorganic alkali lead iodide semiconducting $APbI_3$ (A = Li, Na, K, Cs) and NH_4PbI_3 films prepared from solution: Structure, morphology, and electronic structure, *AIMS Materials Science*. 3 (2016) 737–755. <https://doi.org/10.3934/matricsci.2016.3.737>.
- [47] S. Tsunekawa, T. Fukuda, A. Kasuya, Blue shift in ultraviolet absorption spectra of monodisperse CeO_{2-x} nanoparticles, *Journal of Applied Physics*. 87 (2000) 1318–1321.
<https://doi.org/10.1063/1.372016>.
- [48] J. Tauc, Optical properties and electronic structure of amorphous Ge and Si, *Materials Research Bulletin*. 3 (1968) 37–46. [https://doi.org/10.1016/0025-5408\(68\)90023-8](https://doi.org/10.1016/0025-5408(68)90023-8).
- [49] H.S. Kim, C.R. Lee, J.H. Im, K.B. Lee, T. Moehl, A. Marchioro, S.J. Moon, R. Humphry-Baker, J.H. Yum, J.E. Moser, M. Grätzel, N.G. Park, Lead iodide perovskite sensitized all-solid-state submicron thin film mesoscopic solar cell with efficiency exceeding 9%, *Scientific Reports*. 2 (2012) 591. <https://doi.org/10.1038/srep00591>.

- [50] X. Fan, X. Peng, S. Zhang, Y. Xiang, Fabrication of planar heterojunction perovskite solar cells, in: 2014 International Symposium on Next-Generation Electronics, ISNE 2014, IEEE, 2014. <https://doi.org/10.1109/ISNE.2014.6839359>.
- [51] N.G. Park, Perovskite solar cells: An emerging photovoltaic technology, *Materials Today*. 18 (2015) 65–72. <https://doi.org/10.1016/j.mattod.2014.07.007>.
- [52] S.D. Stranks, G.E. Eperon, G. Grancini, C. Menelaou, M.J.P. Alcocer, T. Leijtens, L.M. Herz, A. Petrozza, H.J. Snaith, Electron-hole diffusion lengths exceeding 1 micrometer in an organometal trihalide perovskite absorber, *Science*. 342 (2013) 341–344. <https://doi.org/10.1126/science.1243982>.
- [53] F. Meillaud, A. Shah, C. Droz, E. Vallat-Sauvain, C. Miazza, Efficiency limits for single-junction and tandem solar cells, *Solar Energy Materials and Solar Cells*. 90 (2006) 2952–2959. <https://doi.org/10.1016/j.solmat.2006.06.002>.
- [54] J.L. Knutson, J.D. Martin, D.B. Mitzi, Tuning the band gap in hybrid tin iodide perovskite semiconductors using structural templating, *Inorganic Chemistry*. 44 (2005) 4699–4705. <https://doi.org/10.1021/ic050244q>.
- [55] I. Borriello, G. Cantele, D. Ninno, Ab initio investigation of hybrid organic-inorganic perovskites based on tin halides, *Physical Review B - Condensed Matter and Materials Physics*. 77 (2008) 235214. <https://doi.org/10.1103/PhysRevB.77.235214>.
- [56] J.H. Noh, S.H. Im, J.H. Heo, T.N. Mandal, S. Il Seok, Chemical management for colorful, efficient, and stable inorganic-organic hybrid nanostructured solar cells, *Nano Letters*. 13 (2013) 1764–1769. <https://doi.org/10.1021/nl400349b>.

- [57] D. Mitzi, Wiley, New York :, 1999.
- [58] J.H. Im, J. Chung, S.J. Kim, N.G. Park, Synthesis, structure, and photovoltaic property of a nanocrystalline 2H perovskite-type novel sensitizer (CH₃CH₂NH₃)PbI₃, *Nanoscale Research Letters*. 7 (2012) 353. <https://doi.org/10.1186/1556-276X-7-353>.
- [59] H. Choi, J. Jeong, H.B. Kim, S. Kim, B. Walker, G.H. Kim, J.Y. Kim, Cesium-doped methylammonium lead iodide perovskite light absorber for hybrid solar cells, *Nano Energy*. 7 (2014) 80–85. <https://doi.org/10.1016/j.nanoen.2014.04.017>.
- [60] W. Nie, H. Tsai, R. Asadpour, J.C. Blancon, A.J. Neukirch, G. Gupta, J.J. Crochet, M. Chhowalla, S. Tretiak, M.A. Alam, H.L. Wang, A.D. Mohite, High-efficiency solution-processed perovskite solar cells with millimeter-scale grains, *Science*. 347 (2015) 522–525. <https://doi.org/10.1126/science.aaa0472>.
- [61] K.S. Shim, H.K. Yang, B.K. Moon, J.H. Jeong, S.S. Yi, K.H. Kim, Improved photoluminescence of pulsed-laser-ablated Y_{1-x}Gd_xVO₄:Eu³⁺ thin film phosphors by Gd substitution, *Applied Physics A: Materials Science and Processing*. 88 (2007) 623–626. <https://doi.org/10.1007/s00339-007-4053-2>.
- [62] L. Steemers, M.J. Wanner, A.W. Ehlers, H. Hiemstra, J.H. Van Maarseveen, A Short Covalent Synthesis of an All-Carbon-Ring [2]Rotaxane, *Organic Letters*. 19 (2017) 2342–2345. <https://doi.org/10.1021/acs.orglett.7b00877>.
- [63] X. Hou, S. Huang, W. Ou-Yang, L. Pan, Z. Sun, X. Chen, Constructing Efficient and Stable Perovskite Solar Cells via Interconnecting Perovskite Grains, *ACS Applied Materials and Interfaces*. 9 (2017) 35200–35208. <https://doi.org/10.1021/acsami.7b08488>.

- [64] A. Cacciuto, S. Auer, D. Frenkei, Onset of heterogeneous crystal nucleation in colloidal suspensions, *Nature*. 428 (2004) 404–406.
<https://doi.org/10.1038/nature02397>.
- [65] D. Liu, L. Wu, C. Li, S. Ren, J. Zhang, W. Li, L. Feng, Controlling $\text{CH}_3\text{NH}_3\text{PbI}_{3-x}\text{Cl}_x$ Film Morphology with Two-Step Annealing Method for Efficient Hybrid Perovskite Solar Cells, *ACS Applied Materials and Interfaces*. 7 (2015) 16330–16337.
<https://doi.org/10.1021/acsami.5b03324>.
- [66] D. Liu, T.L. Kelly, Perovskite solar cells with a planar heterojunction structure prepared using room-temperature solution processing techniques, *Nature Photonics*. 8 (2014) 133–138. <https://doi.org/10.1038/nphoton.2013.342>.
- [67] L. Zhu, J. Shi, S. Lv, Y. Yang, X. Xu, Y. Xu, J. Xiao, H. Wu, Y. Luo, D. Li, Q. Meng, Temperature-assisted controlling morphology and charge transport property for highly efficient perovskite solar cells, *Nano Energy*. 15 (2015) 540–548.
<https://doi.org/10.1016/j.nanoen.2015.04.039>.
- [68] J.H. Im, I.H. Jang, N. Pellet, M. Grätzel, N.G. Park, Growth of $\text{CH}_3\text{NH}_3\text{PbI}_3$ cuboids with controlled size for high-efficiency perovskite solar cells, *Nature Nanotechnology*. 9 (2014) 927–932. <https://doi.org/10.1038/nnano.2014.181>.
- [69] X. Li, M. Ibrahim Dar, C. Yi, J. Luo, M. Tschumi, S.M. Zakeeruddin, M.K. Nazeeruddin, H. Han, M. Grätzel, Improved performance and stability of perovskite solar cells by crystal crosslinking with alkylphosphonic acid ω -ammonium chlorides, *Nature Chemistry*. 7 (2015) 703–711. <https://doi.org/10.1038/nchem.2324>.

- [70] B. Li, C. Fei, K. Zheng, X. Qu, T. Pullerits, G. Cao, J. Tian, Constructing water-resistant $\text{CH}_3\text{NH}_3\text{PbI}_3$ perovskite films: Via coordination interaction, *Journal of Materials Chemistry A*. 4 (2016) 17018–17024. <https://doi.org/10.1039/c6ta06892h>.
- [71] D. Bi, C. Yi, J. Luo, J.D. Décoppet, F. Zhang, S.M. Zakeeruddin, X. Li, A. Hagfeldt, M. Grätzel, Polymer-templated nucleation and crystal growth of perovskite films for solar cells with efficiency greater than 21%, *Nature Energy*. 1 (2016) 16142. <https://doi.org/10.1038/nenergy.2016.142>.
- [72] Y. Zhao, J. Wei, H. Li, Y. Yan, W. Zhou, D. Yu, Q. Zhao, A polymer scaffold for self-healing perovskite solar cells, *Nature Communications*. 7 (2016) 10228. <https://doi.org/10.1038/ncomms10228>.
- [73] A. Dualeh, P. Gao, S. Il Seok, M.K. Nazeeruddin, M. Grätzel, Thermal behavior of methylammonium lead-trihalide perovskite photovoltaic light harvesters, *Chemistry of Materials*. 26 (2014) 6160–6164. <https://doi.org/10.1021/cm502468k>.
- [74] Z. Lin, J. Chang, H. Zhu, Q.H. Xu, C. Zhang, J. Ouyang, Y. Hao, Enhanced planar heterojunction perovskite solar cell performance and stability using PDDA polyelectrolyte capping agent, *Solar Energy Materials and Solar Cells*. 172 (2017) 133–139. <https://doi.org/10.1016/j.solmat.2017.07.022>.
- [75] M. Reche-Tamayo, M. Moral, A.J. Pérez-Jiménez, J.C. Sancho-García, Theoretical determination of interaction and cohesive energies of weakly bound cycloparaphenylene molecules, *Journal of Physical Chemistry C*. 120 (2016) 22627–22634. <https://doi.org/10.1021/acs.jpcc.6b05781>.

- [76] X. Fontane, V. Izquierdo-Roca, A. Fairbrother, M. Espindola-Rodriguez, S. Lopez-Marino, M. Placidi, T. Jawhari, E. Saucedo, A. Perez-Rodriguez, Selective detection of secondary phases in $\text{Cu}_2\text{ZnSn}(\text{S},\text{Se})_4$ based absorbers by pre-resonant Raman spectroscopy, Conference Record of the IEEE Photovoltaic Specialists Conference. (2013) 2581–2584. <https://doi.org/10.1109/PVSC.2013.6745001>.
- [77] E. Saucedo, V. Izquierdo-Roca, C.M. Ruiz, L. Parissi, C. Broussillou, P.P. Grand, J.S. Jaime-Ferrer, A. Pérez-Rodríguez, J.R. Morante, V. Bermúdez, Key role of Cu-Se binary phases in electrodeposited CuInSe_2 precursors on final distribution of Cu-S phases in $\text{CuIn}(\text{S},\text{Se})_2$ absorbers, *Thin Solid Films*. 517 (2009) 2268–2271. <https://doi.org/10.1016/j.tsf.2008.10.144>.
- [78] X. Fontañ, L. Calvo-Barrio, V. Izquierdo-Roca, E. Saucedo, A. Pérez-Rodriguez, J.R. Morante, D.M. Berg, P.J. Dale, S. Siebentritt, In-depth resolved Raman scattering analysis for the identification of secondary phases: Characterization of $\text{Cu}_2\text{ZnSnS}_4$ layers for solar cell applications, *Applied Physics Letters*. 98 (2011) 181905. <https://doi.org/10.1063/1.3587614>.
- [79] A. Redinger, K. Hönes, X. Fontañ, V. Izquierdo-Roca, E. Saucedo, N. Valle, A. Pérez-Rodríguez, S. Siebentritt, Detection of a ZnSe secondary phase in coevaporated $\text{Cu}_2\text{ZnSnSe}_4$ thin films, *Applied Physics Letters*. 98 (2011) 101907. <https://doi.org/10.1063/1.3558706>.
- [80] A. Fairbrother, V. Izquierdo-Roca, X. Fontané, M. Ibáñez, A. Cabot, E. Saucedo, A. Pérez-Rodríguez, ZnS grain size effects on near-resonant Raman scattering: Optical non-destructive grain size estimation, *CrystEngComm*. 16 (2014) 4120–4125. <https://doi.org/10.1039/c3ce42578a>.

- [81] S. Kim, M. Oh, W.K. Kim, Effect of Sn-layer addition to precursors on characteristics of $\text{Cu}_2\text{ZnSn}(\text{S},\text{Se})_4$ thin-film solar cell absorber, *Thin Solid Films*. 549 (2013) 59–64. <https://doi.org/10.1016/j.tsf.2013.07.054>.
- [82] X. Yin, T.J. Huang, C. Tang, M. Du, L. Sun, Z. Shen, H. Gong, Significantly different mechanical properties and interfacial structures of $\text{Cu}_2\text{ZnSn}(\text{S},\text{Se})_4$ films prepared from metallic and sulfur-contained precursors, *Solar Energy Materials and Solar Cells*. 134 (2015) 389–394. <https://doi.org/10.1016/j.solmat.2014.12.033>.
- [83] L. Choubac, G. Brammertz, N. Barreau, L. Arzel, S. Harel, M. Meuris, B. Vermang, 7.6% CZGSe Solar Cells Thanks to Optimized CdS Chemical Bath Deposition, *Physica Status Solidi (A) Applications and Materials Science*. 215 (2018) 1800043. <https://doi.org/10.1002/pssa.201800043>.
- [84] M. Buffière, H. Elanzeery, S. Oueslati, K. Ben Messaoud, G. Brammertz, M. Meuris, J. Poortmans, Physical characterization of $\text{Cu}_2\text{ZnGeSe}_4$ thin films from annealing of Cu-Zn-Ge precursor layers, *Thin Solid Films*. 582 (2015) 171–175. <https://doi.org/10.1016/j.tsf.2014.09.024>.
- [85] D.B. Mitzi, O. Gunawan, T.K. Todorov, K. Wang, S. Guha, The path towards a high-performance solution-processed kesterite solar cell, *Solar Energy Materials and Solar Cells*. 95 (2011) 1421–1436. <https://doi.org/10.1016/j.solmat.2010.11.028>.
- [86] Q. Shu, J.H. Yang, S. Chen, B. Huang, H. Xiang, X.G. Gong, S.H. Wei, $\text{Cu}_2\text{Zn}(\text{Sn},\text{Ge})\text{Se}_4$ and $\text{Cu}_2\text{Zn}(\text{Sn},\text{Si})\text{Se}_4$ alloys as photovoltaic materials: Structural and electronic properties, *Physical Review B - Condensed Matter and Materials Physics*. 87 (2013) 115208. <https://doi.org/10.1103/PhysRevB.87.115208>.

- [87] I. Repins, C. Beall, N. Vora, C. Dehart, D. Kuciauskas, P. Dippo, B. To, J. Mann, W.C. Hsu, A. Goodrich, R. Noufi, Co-evaporated $\text{Cu}_2\text{ZnSnSe}_4$ films and devices, *Solar Energy Materials and Solar Cells*. 101 (2012) 154–159.
<https://doi.org/10.1016/j.solmat.2012.01.008>.
- [88] D.B. Khadka, J.H. Kim, Band gap engineering of alloyed $\text{Cu}_2\text{ZnGe}_x\text{Sn}_{1-x}\text{Q}_4$ (Q = S,Se) films for solar cell, *Journal of Physical Chemistry C*. 119 (2015) 1706–1713.
<https://doi.org/10.1021/jp510877g>.
- [89] G.M. Ford, Q. Guo, R. Agrawal, H.W. Hillhouse, Earth abundant element $\text{Cu}_2\text{Zn}(\text{Sn}_{1-x}\text{Ge}_x)\text{S}_4$ nanocrystals for tunable band gap solar cells: 6.8% Efficient device fabrication, *Chemistry of Materials*. 23 (2011) 2626–2629.
<https://doi.org/10.1021/cm2002836>.
- [90] M.A. Halim, Characterization of Defects in $\text{Cu}_2\text{ZnSn}(\text{S},\text{Se})_4$ Solar Cell Material, University of Tsukuba, 2016.
https://tsukuba.repo.nii.ac.jp/record/39112/file_preview/DA07664.pdf.
- [91] S.C. Riha, B.A. Parkinson, A.L. Prieto, Compositionally tunable $\text{Cu}_2\text{ZnSn}(\text{S}_{1-x}\text{Se}_x)_4$ nanocrystals: Probing the effect of Se-inclusion in mixed chalcogenide thin films, *Journal of the American Chemical Society*. 133 (2011) 15272–15275.
<https://doi.org/10.1021/ja2058692>.
- [92] T.K. Todorov, K.B. Reuter, D.B. Mitzi, High-efficiency solar cell with earth-abundant liquid-processed absorber, *Advanced Materials*. 22 (2010) 0904155.
<https://doi.org/10.1002/adma.200904155>.

- [93] T.K. Todorov, J. Tang, S. Bag, O. Gunawan, T. Gokmen, Y. Zhu, D.B. Mitzi, Beyond 11% efficiency: Characteristics of state-of-the-art $\text{Cu}_2\text{ZnSn}(\text{S},\text{Se})_4$ Solar Cells, *Advanced Energy Materials*. 3 (2013) 34–38.
<https://doi.org/10.1002/aenm.201200348>.
- [94] S. Siebentritt, S. Schorr, Kesterites-a challenging material for solar cells, *Progress in Photovoltaics: Research and Applications*. 20 (2012) 512–519.
<https://doi.org/10.1002/pip.2156>.
- [95] K. Ramasamy, M.A. Malik, P. O'Brien, The chemical vapor deposition of $\text{Cu}_2\text{ZnSnS}_4$ thin films, *Chemical Science*. 2 (2011) 1170–1172.
<https://doi.org/10.1039/c0sc00538j>.
- [96] J. Kim, B. Shin, Strategies to reduce the open-circuit voltage deficit in $\text{Cu}_2\text{ZnSn}(\text{S},\text{Se})_4$ thin film solar cells, *Electronic Materials Letters*. 13 (2017) 373–392.
<https://doi.org/10.1007/s13391-017-7118-1>.
- [97] T. Gokmen, O. Gunawan, T.K. Todorov, D.B. Mitzi, Band tailing and efficiency limitation in kesterite solar cells, *Applied Physics Letters*. 103 (2013) 103506.
<https://doi.org/10.1063/1.4820250>.
- [98] J. Krustok, R. Josepson, T. Raadik, M. Danilson, Potential fluctuations in $\text{Cu}_2\text{ZnSnSe}_4$ solar cells studied by temperature dependence of quantum efficiency curves, *Physica B: Condensed Matter*. 405 (2010) 3186–3189.
<https://doi.org/10.1016/j.physb.2010.04.041>.
- [99] S. Oueslati, G. Brammertz, M. Buffière, C. Köble, T. Oualid, M. Meuris, J. Poortmans, Photoluminescence study and observation of unusual optical transitions in $\text{Cu}_2\text{ZnSnSe}_4/\text{CdS}/\text{ZnO}$ solar cells, *Solar Energy Materials and Solar Cells*. 134 (2015)

- 340–345. <https://doi.org/10.1016/j.solmat.2014.10.041>.
- [100] I.L. Repins, M.J. Romero, J. V. Li, S.H. Wei, D. Kuciauskas, C.S. Jiang, C. Beall, C. Dehart, J. Mann, W.C. Hsu, G. Teeter, A. Goodrich, R. Noufi, Kesterite successes, ongoing work, and challenges: A perspective from vacuum deposition, *IEEE Journal of Photovoltaics*. 3 (2013) 439–445. <https://doi.org/10.1109/JPHOTOV.2012.2215842>.
- [101] S. Siebentritt, Why are kesterite solar cells not 20% efficient?, *Thin Solid Films*. 535 (2013) 1–4. <https://doi.org/10.1016/j.tsf.2012.12.089>.
- [102] S. Stølen, H.B. Johnsen, C.S. Bøe, T. Grande, O.B. Karlsten, Stable and metastable phase equilibria in the GeSe₂-Se system, *Journal of Phase Equilibria*. 20 (1999) 17–28. <https://doi.org/10.1361/105497199770335901>.
- [103] A. Redinger, D.M. Berg, P.J. Dale, S. Siebentritt, The consequences of kesterite equilibria for efficient solar cells, *Journal of the American Chemical Society*. 133 (2011) 3320–3323. <https://doi.org/10.1021/ja111713g>.
- [104] M. Klenk, O. Schenker, V. Alberts, E. Bucher, Control of two-step growth processes of chalcopyrite thin films by X-ray fluorescence spectroscopy, *Applied Surface Science*. 173 (2001) 62–68. [https://doi.org/10.1016/S0169-4332\(00\)00876-X](https://doi.org/10.1016/S0169-4332(00)00876-X).
- [105] T. Tanaka, T. Sueishi, K. Saito, Q. Guo, M. Nishio, K.M. Yu, W. Walukiewicz, Existence and removal of Cu₂Se second phase in coevaporated Cu₂ZnSnSe₄ thin films, *Journal of Applied Physics*. 111 (2012) 053522. <https://doi.org/10.1063/1.3691964>.
- [106] A. Fairbrother, X. Fontané, V. Izquierdo-Roca, M. Espíndola-Rodríguez, S. López-Marino, M. Placidi, L. Calvo-Barrio, A. Pérez-Rodríguez, E. Saucedo, On the formation mechanisms of Zn-rich Cu₂ZnSnS₄ films prepared by sulfurization of

- metallic stacks, *Solar Energy Materials and Solar Cells*. 112 (2013) 97–105.
<https://doi.org/10.1016/j.solmat.2013.01.015>.
- [107] S. López-Marino, M. Placidi, A. Pérez-Tomás, J. Llobet, V. Izquierdo-Roca, X. Fontané, A. Fairbrother, M. Espíndola-Rodríguez, D. Sylla, A. Pérez-Rodríguez, E. Saucedo, Inhibiting the absorber/Mo-back contact decomposition reaction in $\text{Cu}_2\text{ZnSnSe}_4$ solar cells: The role of a ZnO intermediate nanolayer, *Journal of Materials Chemistry A*. 1 (2013) 8338–8343. <https://doi.org/10.1039/c3ta11419h>.
- [108] S. López-Marino, Y. Sánchez, M. Placidi, A. Fairbrother, M. Espíndola-Rodríguez, X. Fontané, V. Izquierdo-Roca, J. López-García, L. Calvo-Barrio, A. Pérez-Rodríguez, E. Saucedo, ZnSe etching of Zn-Rich $\text{Cu}_2\text{ZnSnSe}_4$: An oxidation route for improved solar-cell efficiency, *Chemistry - A European Journal*. 19 (2013) 14814–14822.
<https://doi.org/10.1002/chem.201302589>.
- [109] C. Malerba, M. Valentini, C.L. Azanza Ricardo, A. Rinaldi, E. Cappelletto, P. Scardi, A. Mittiga, Blistering in $\text{Cu}_2\text{ZnSnS}_4$ thin films: correlation with residual stresses, *Materials and Design*. 108 (2016) 725–735.
<https://doi.org/10.1016/j.matdes.2016.07.019>.
- [110] C. Yan, K. Sun, F. Liu, J. Huang, F. Zhou, X. Hao, Boost Voc of pure sulfide kesterite solar cell via a double CZTS layer stacks, *Solar Energy Materials and Solar Cells*. 160 (2017) 7–11. <https://doi.org/10.1016/j.solmat.2016.09.027>.
- [111] T. Thersleff, S. Giraldo, M. Neuschitzer, P. Pistor, E. Saucedo, K. Leifer, Chemically and morphologically distinct grain boundaries in Ge-doped $\text{Cu}_2\text{ZnSnSe}_4$ solar cells revealed with STEM-EELS, *Materials and Design*. 122 (2017) 102–109.
<https://doi.org/10.1016/j.matdes.2017.02.077>.

- [112] S. Hwang, D.H. Kim, D.H. Son, K.J. Yang, D. Nam, H. Cheong, J.K. Kang, S.I. In, Effects of a pre-annealing treatment (PAT) on $\text{Cu}_2\text{ZnSn}(\text{S},\text{Se})_4$ thin films prepared by rapid thermal processing (RTP) selenization, *Solar Energy Materials and Solar Cells*. 143 (2015) 218–225. <https://doi.org/10.1016/j.solmat.2015.06.059>.
- [113] Y. Wei, D. Zhuang, M. Zhao, Q. Gong, R. Sun, L. Zhang, X. Lyu, X. Peng, G. Ren, Y. Wu, J. Wei, Effects of selenium atmosphere on grain growth for CZTSe absorbers fabricated by selenization of as-sputtered precursors, *Journal of Alloys and Compounds*. 755 (2018) 224–230. <https://doi.org/10.1016/j.jallcom.2018.04.311>.
- [114] M. Abusnina, M. Matin, H.R. Moutinho, J.L. Blackburn, J. Alleman, C. DeHart, B. To, M. Al-Jassim, Suppression of the Cu_{2-x}S Secondary Phases in CZTS Films Through Controlling the Film Elemental Composition, *IEEE Journal of Photovoltaics*. 5 (2015) 1470–1475. <https://doi.org/10.1109/JPHOTOV.2015.2447834>.
- [115] S. Zhuk, T.K.S. Wong, E. Tyukalova, A. Guchhait, D.H.L. Seng, S. Tripathy, T.I. Wong, M. Sharma, H. Medina, M. Duchamp, L.H. Wong, G.K. Dalapati, Effect of TaN intermediate layer on the back contact reaction of sputter-deposited Cu poor $\text{Cu}_2\text{ZnSnS}_4$ and Mo, *Applied Surface Science*. 471 (2019) 277–288. <https://doi.org/10.1016/j.apsusc.2018.11.227>.
- [116] H. Guo, C. Ma, K. Zhang, X. Jia, X. Wang, N. Yuan, J. Ding, Dual function of ultrathin Ti intermediate layers in CZTS solar cells: Sulfur blocking and charge enhancement, *Solar Energy Materials and Solar Cells*. 175 (2018) 20–28. <https://doi.org/10.1016/j.solmat.2017.09.052>.
- [117] S. Giraldo, T. Thersleff, G. Larramona, M. Neuschitzer, P. Pistor, K. Leifer, A. Pérez-Rodríguez, C. Moisan, G. Dennler, E. Saucedo, $\text{Cu}_2\text{ZnSnSe}_4$ solar cells with 10.6%

- efficiency through innovative absorber engineering with Ge superficial nanolayer, *Progress in Photovoltaics: Research and Applications*. 24 (2016) 1359–1367.
<https://doi.org/10.1002/pip.2797>.
- [118] Y.S. Lee, T. Gershon, O. Gunawan, T.K. Todorov, T. Gokmen, Y. Virgus, S. Guha, $\text{Cu}_2\text{ZnSnSe}_4$ thin-film solar cells by thermal co-evaporation with 11.6% efficiency and improved minority carrier diffusion length, *Advanced Energy Materials*. 5 (2015) 1401372. <https://doi.org/10.1002/aenm.201401372>.
- [119] D.B. Mitzi, O. Gunawan, T.K. Todorov, A.R.D. Barkhouse, Prospects and performance limitations for Cu-Zn-Sn-S-Se photovoltaic Technology, *Philosophical Transactions of the Royal Society A: Mathematical, Physical and Engineering Sciences*. 371 (2013) 110432. <https://doi.org/10.1098/rsta.2011.0432>.
- [120] T.K. Todorov, K.B. Reuter, D.B. Mitzi, Photovoltaic Devices: High-Efficiency Solar Cell with Earth-Abundant Liquid-Processed Absorber (*Adv. Mater.* 20/2010), *Advanced Materials*. 22 (2010) 1090073 n/a-n/a.
<https://doi.org/10.1002/adma.201090073>.
- [121] Y.E. Romanyuk, O. V. Parasyuk, Phase equilibria in the quasi-ternary $\text{Cu}_2\text{Se-ZnSe-GeSe}_2$ system, *Journal of Alloys and Compounds*. 348 (2003) 195–202.
[https://doi.org/10.1016/S0925-8388\(02\)00852-6](https://doi.org/10.1016/S0925-8388(02)00852-6).
- [122] K. Wang, O. Gunawan, T. Todorov, B. Shin, S.J. Chey, N.A. Bojarczuk, D. Mitzi, S. Guha, Thermally evaporated $\text{Cu}_2\text{ZnSnS}_4$ solar cells, *Applied Physics Letters*. 97 (2010) 143508. <https://doi.org/10.1063/1.3499284>.

- [123] S. Chen, A. Walsh, X.G. Gong, S.H. Wei, Classification of lattice defects in the kesterite $\text{Cu}_2\text{ZnSnS}_4$ and $\text{Cu}_2\text{ZnSnSe}_4$ earth-abundant solar cell absorbers, *Advanced Materials*. 25 (2013) 1522–1539. <https://doi.org/10.1002/adma.201203146>.
- [124] S. Ahmed, K.B. Reuter, O. Gunawan, L. Guo, L.T. Romankiw, H. Deligianni, A high efficiency electrodeposited $\text{Cu}_2\text{ZnSnS}_4$ solar cell, *Advanced Energy Materials*. 2 (2012) 253–259. <https://doi.org/10.1002/aenm.201100526>.
- [125] H. Katagiri, K. Jimbo, Development of rare metal-free CZTS-based thin film solar cells, in: *Conference Record of the IEEE Photovoltaic Specialists Conference*, IEEE, 2011: pp. 003516–003521. <https://doi.org/10.1109/PVSC.2011.6186707>.
- [126] M. Mousel, A. Redinger, R. Djemour, M. Arasimowicz, N. Valle, P. Dale, S. Siebentritt, HCl and Br_2 -MeOH etching of $\text{Cu}_2\text{ZnSnSe}_4$ polycrystalline absorbers, *Thin Solid Films*. 535 (2013) 83–87. <https://doi.org/10.1016/j.tsf.2012.12.095>.
- [127] D.A.R. Barkhouse, R. Haight, N. Sakai, H. Hiroi, H. Sugimoto, D.B. Mitzi, Cd-free buffer layer materials on $\text{Cu}_2\text{ZnSn}(\text{S}_x\text{Se}_{1-x})_4$: Band alignments with ZnO, ZnS, and In_2S_3 , *Applied Physics Letters*. 100 (2012) 193904. <https://doi.org/10.1063/1.4714737>.
- [128] J.J. Scragg, P.J. Dale, D. Colombara, L.M. Peter, Thermodynamic aspects of the synthesis of thin-film materials for solar cells, *ChemPhysChem*. 13 (2012) 3035–3046. <https://doi.org/10.1002/cphc.201200067>.
- [129] S. and C.P. Kasap, *Wide-Bandgap II-VI Semiconductors: Growth and Properties*: In, *Springer Handbook of Electronic and Photonic Materials*, Springer US, Berlin, 2007.
- [130] M. Ganchev, J. Iljina, L. Kaupmees, T. Raadik, O. Volobujeva, A. Mere, M. Altosaar, J. Raudoja, E. Mellikov, Phase composition of selenized $\text{Cu}_2\text{ZnSnSe}_4$ thin films determined by X-ray diffraction and Raman spectroscopy, *Thin Solid Films*. 519

- (2011) 7394–7398. <https://doi.org/10.1016/j.tsf.2011.01.388>.
- [131] P.A. Fernandes, P.M.P. Salomé, A.F. da Cunha, Growth and Raman scattering characterization of $\text{Cu}_2\text{ZnSnS}_4$ thin films, *Thin Solid Films*. 517 (2009) 2519–2523. <https://doi.org/10.1016/j.tsf.2008.11.031>.
- [132] J. He, L. Sun, S. Chen, Y. Chen, P. Yang, J. Chu, Composition dependence of structure and optical properties of $\text{Cu}_2\text{ZnSn}(\text{S},\text{Se})_4$ solid solutions: An experimental study, *Journal of Alloys and Compounds*. 511 (2012) 129–132. <https://doi.org/10.1016/j.jallcom.2011.08.099>.
- [133] D. Park, D. Nam, S. Jung, S. An, J. Gwak, K. Yoon, J.H. Yun, H. Cheong, Optical characterization of $\text{Cu}_2\text{ZnSnSe}_4$ grown by thermal co-evaporation, *Thin Solid Films*. 519 (2011) 7386–7389. <https://doi.org/10.1016/j.tsf.2011.01.142>.
- [134] A. Khare, B. Himmetoglu, M. Johnson, D.J. Norris, M. Cococcioni, E.S. Aydil, Calculation of the lattice dynamics and Raman spectra of copper zinc tin chalcogenides and comparison to experiments, *Journal of Applied Physics*. 111 (2012) 083707. <https://doi.org/10.1063/1.4704191>.
- [135] P.A. Fernandes, P.M.P. Salomé, A.F. Da Cunha, Study of polycrystalline $\text{Cu}_2\text{ZnSnS}_4$ films by Raman scattering, *Journal of Alloys and Compounds*. 509 (2011) 7600–7606. <https://doi.org/10.1016/j.jallcom.2011.04.097>.
- [136] G. Brammertz, M. Buffière, Y. Mevel, Y. Ren, A.E. Zaghi, N. Lenaers, Y. Mols, C. Koeble, J. Vleugels, M. Meuris, J. Poortmans, Correlation between physical, electrical, and optical properties of $\text{Cu}_2\text{ZnSnSe}_4$ based solar cells, *Applied Physics Letters*. 102 (2013) 013902. <https://doi.org/10.1063/1.4775366>.

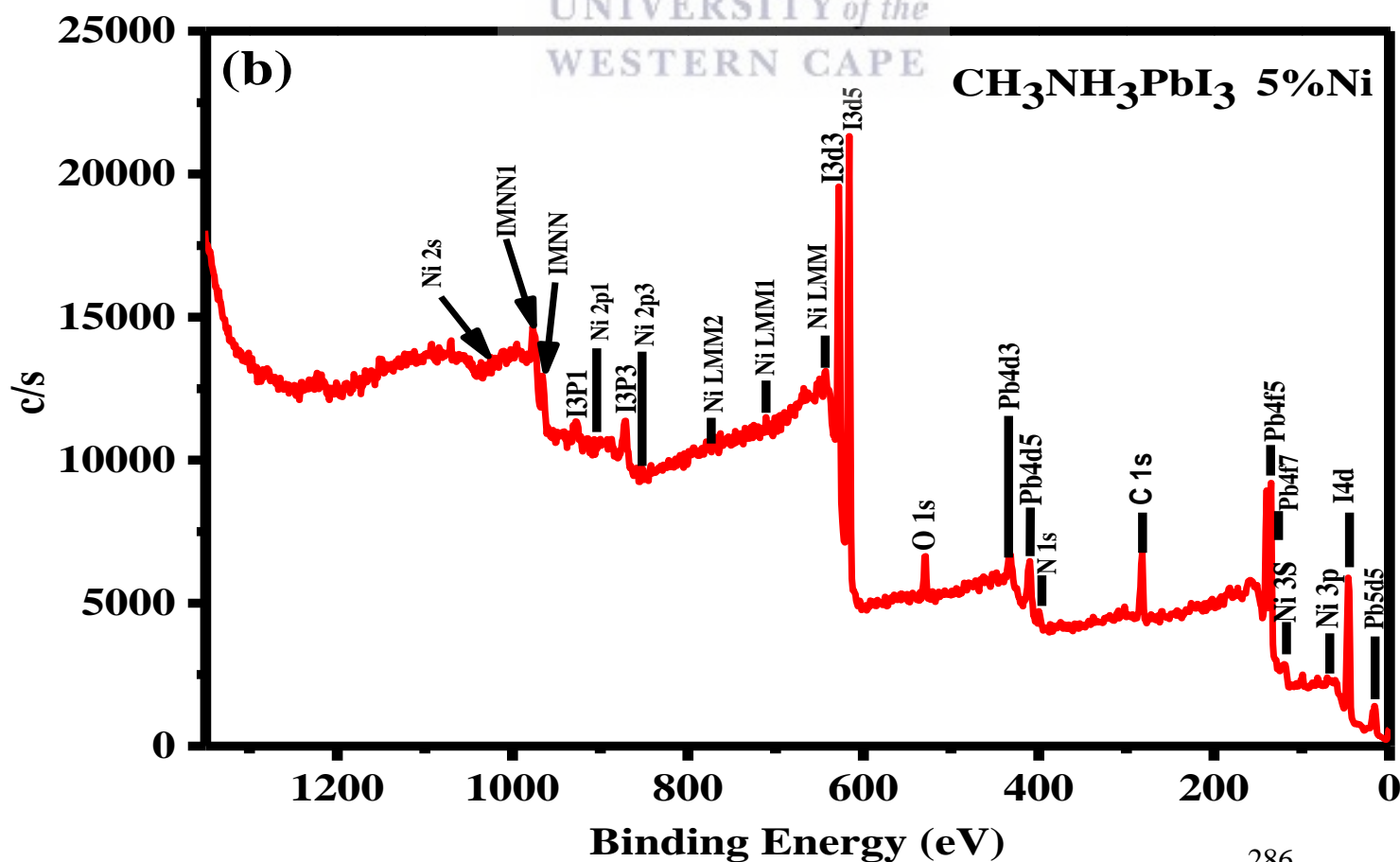
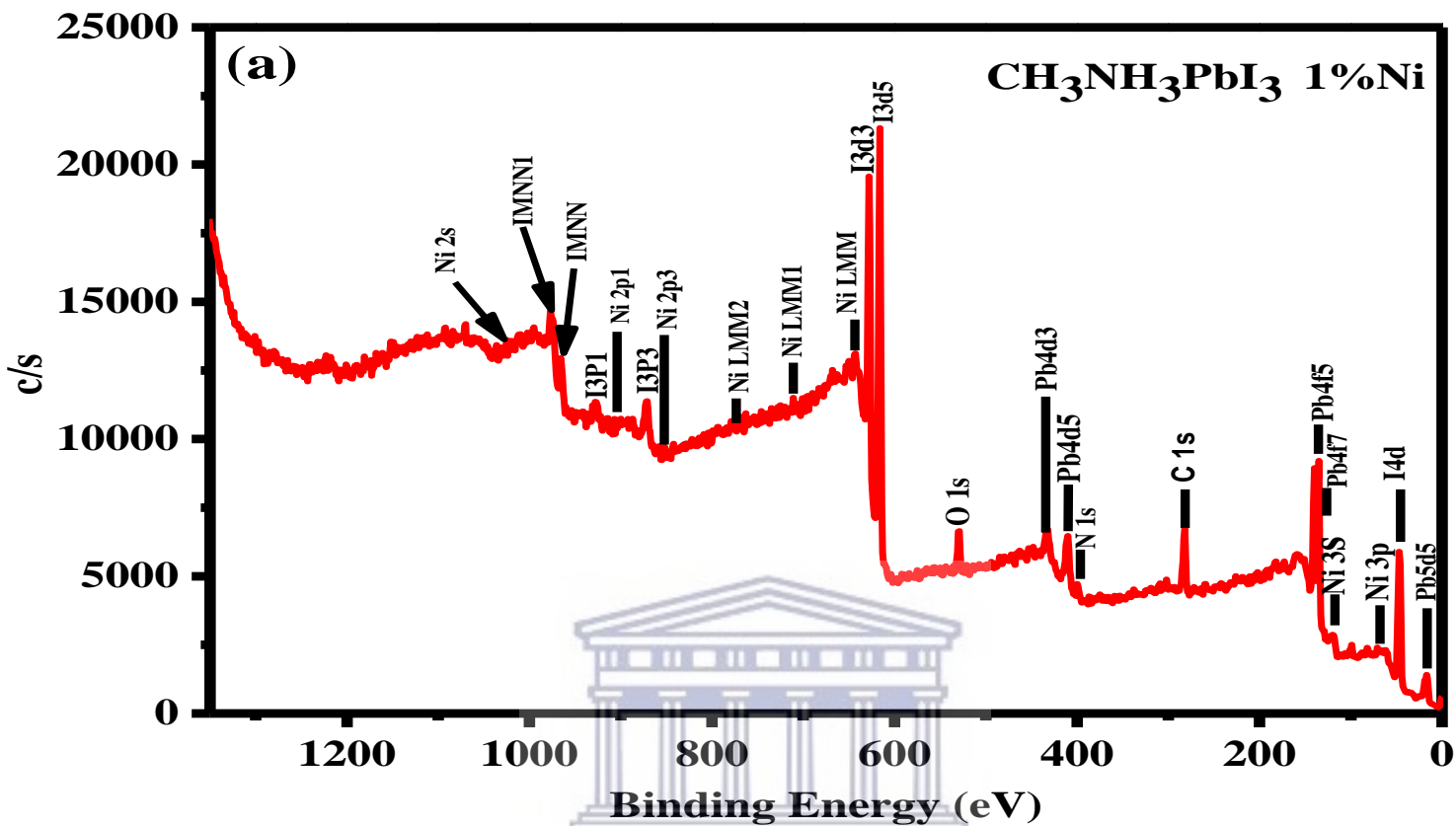
- [137] L. Guo, Y. Zhu, O. Gunawan, T. Gokmen, V.R. Deline, S. Ahmed, L.T. Romankiw, H. Deligianni, Electrodeposited $\text{Cu}_2\text{ZnSnSe}_4$ thin film solar cell with 7% power conversion efficiency, *Progress in Photovoltaics: Research and Applications*. 22 (2014) 58–68. <https://doi.org/10.1002/pip.2332>.
- [138] B. Shin, O. Gunawan, Y. Zhu, N.A. Bojarczuk, S.J. Chey, S. Guha, Thin film solar cell with 8.4% power conversion efficiency using an earth-abundant $\text{Cu}_2\text{ZnSnS}_4$ absorber, *Progress in Photovoltaics: Research and Applications*. 21 (2013) 72–76. <https://doi.org/10.1002/pip.1174>.
- [139] J. Just, D. Ltzenkirchen-Hecht, R. Frahm, S. Schorr, T. Unold, Determination of secondary phases in kesterite $\text{Cu}_2\text{ZnSnS}_4$ thin films by x-ray absorption near edge structure analysis, *Applied Physics Letters*. 99 (2011) 262105. <https://doi.org/10.1063/1.3671994>.
- [140] A. Fairbrother, E. García-Hemme, V. Izquierdo-Roca, X. Fontané, F.A. Pulgarín-Agudelo, O. Vigil-Galán, A. Pérez-Rodríguez, E. Saucedo, Development of a selective chemical Etch to improve the conversion efficiency of Zn-rich $\text{Cu}_2\text{ZnSnS}_4$ solar cells, *Journal of the American Chemical Society*. 134 (2012) 8018–8021. <https://doi.org/10.1021/ja301373e>.
- [141] J. Timo Wätjen, J. Engman, M. Edoff, C. Platzer-Björkman, Direct evidence of current blocking by ZnSe in $\text{Cu}_2\text{ZnSnSe}_4$ solar cells, *Applied Physics Letters*. 100 (2012) 173510. <https://doi.org/10.1063/1.4706256>.

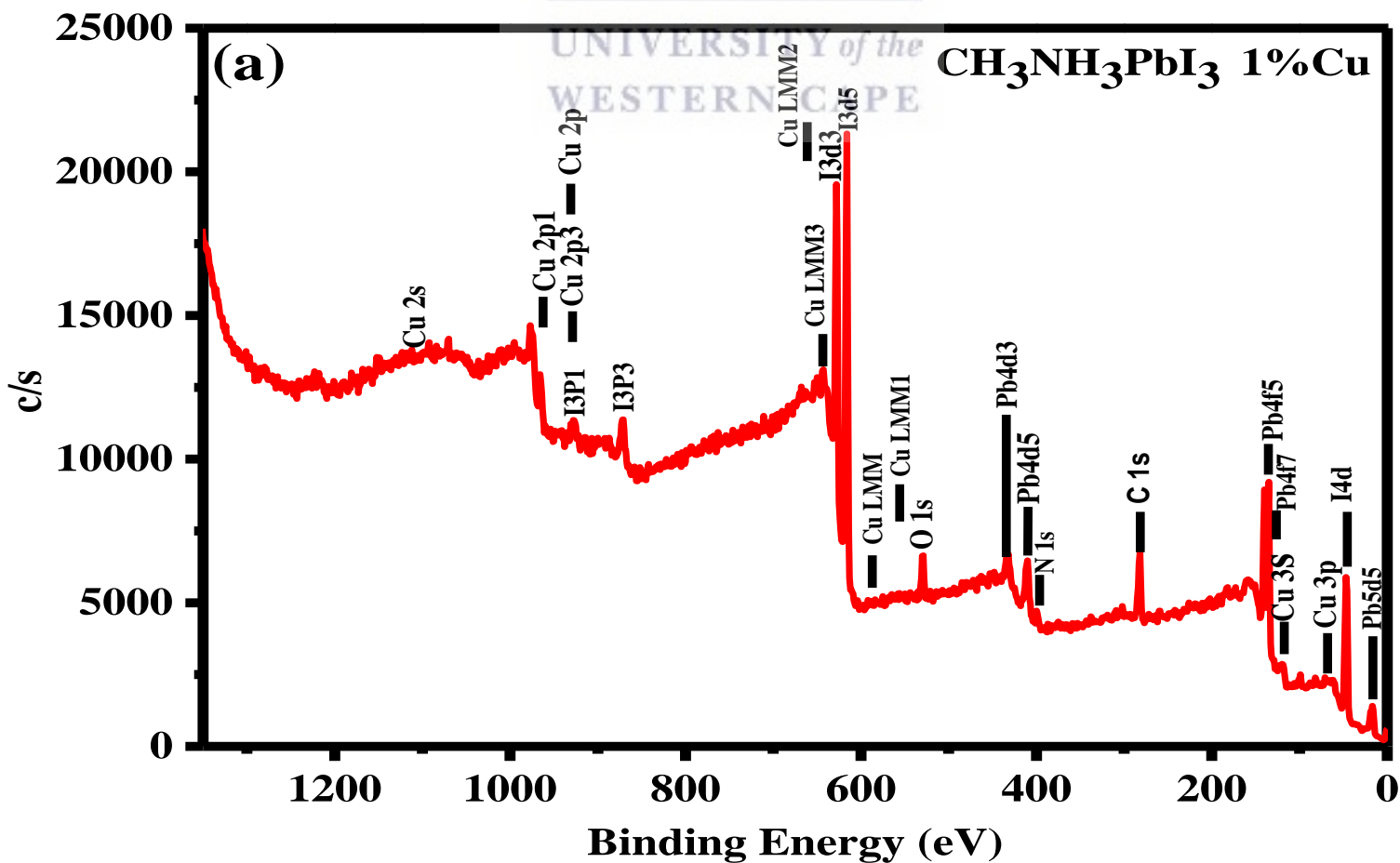
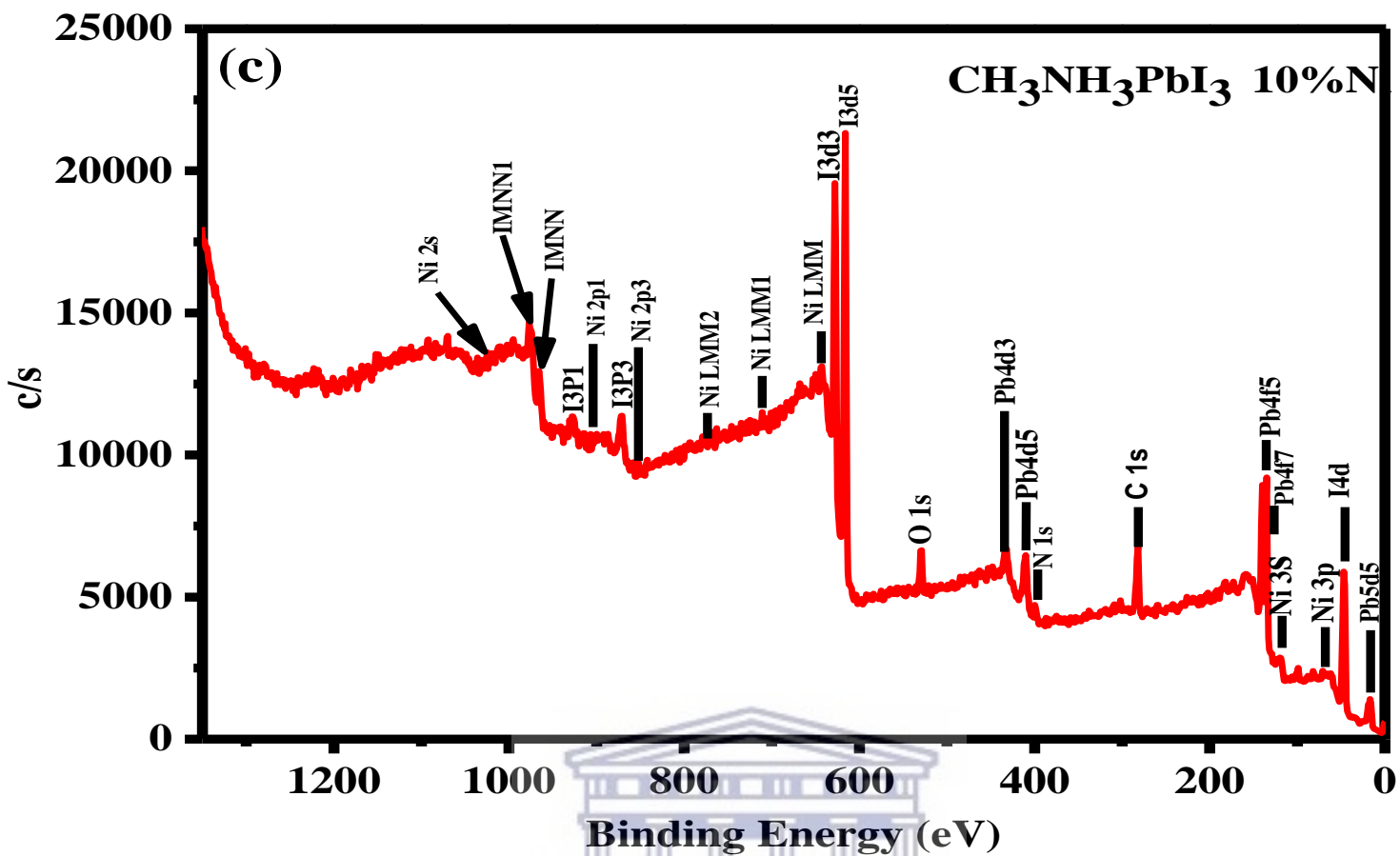
- [142] N. Vora, J. Blackburn, I. Repins, C. Beall, B. To, J. Pankow, G. Teeter, M. Young, R. Noufi, Phase identification and control of thin films deposited by co-evaporation of elemental Cu, Zn, Sn, and Se, *Journal of Vacuum Science & Technology A: Vacuum, Surfaces, and Films*. 30 (2012) 051201. <https://doi.org/10.1116/1.4732529>.
- [143] W.C. Hsu, I. Repins, C. Beall, C. Dehart, G. Teeter, B. To, Y. Yang, R. Noufi, The effect of Zn excess on kesterite solar cells, *Solar Energy Materials and Solar Cells*. 113 (2013) 160–164. <https://doi.org/10.1016/j.solmat.2013.02.015>.
- [144] A. Osinsky, Y. Qiu, J. Mahan, H. Temkin, S.A. Gurevich, S.I. Nesterov, E.M. Tanklevskaia, V. Tretyakov, O.A. Lavrova, V.I. Skopina, Novel wet chemical etch for nanostructures based on II-VI compounds, *Applied Physics Letters*. 71 (1997) 509–511. <https://doi.org/10.1063/1.119593>.
- [145] E.M. Gavrishchuk, E.Y. Vilkova, O. V. Timofeev, U.P. Borovskikh, E.L. Tikhonova, Etching behavior of CVD zinc selenide in inorganic acid solutions, *Inorganic Materials*. 43 (2007) 579–583. <https://doi.org/10.1134/S0020168507060039>.
- [146] M.W. Cho, K.W. Koh, K. Morikawa, K. Arai, H.D. Jung, Z. Zhu, T. Yao, Y. Okada, Surface treatment of ZnSe substrate and homoepitaxy of ZnSe, *Journal of Electronic Materials*. 26 (1997) 423–428. <https://doi.org/10.1007/s11664-997-0113-9>.
- [147] M.A. Contreras, M.J. Romero, B. To, F. Hasoon, R. Noufi, S. Ward, K. Ramanathan, Optimization of CBD CdS process in high-efficiency Cu(In,Ga)Se₂-based solar cells, *Thin Solid Films*. 403–404 (2002) 204–211. [https://doi.org/10.1016/S0040-6090\(01\)01538-3](https://doi.org/10.1016/S0040-6090(01)01538-3).

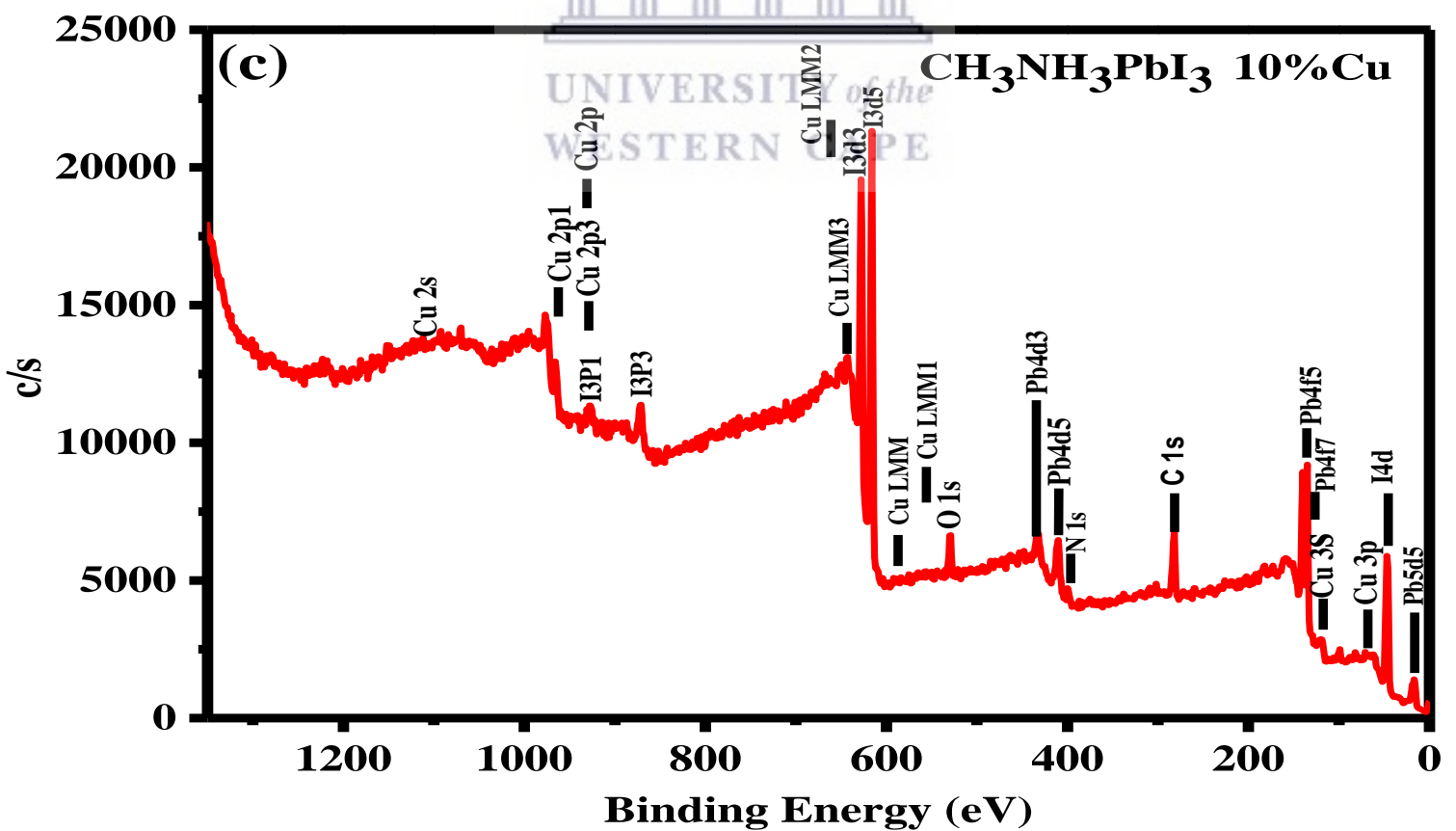
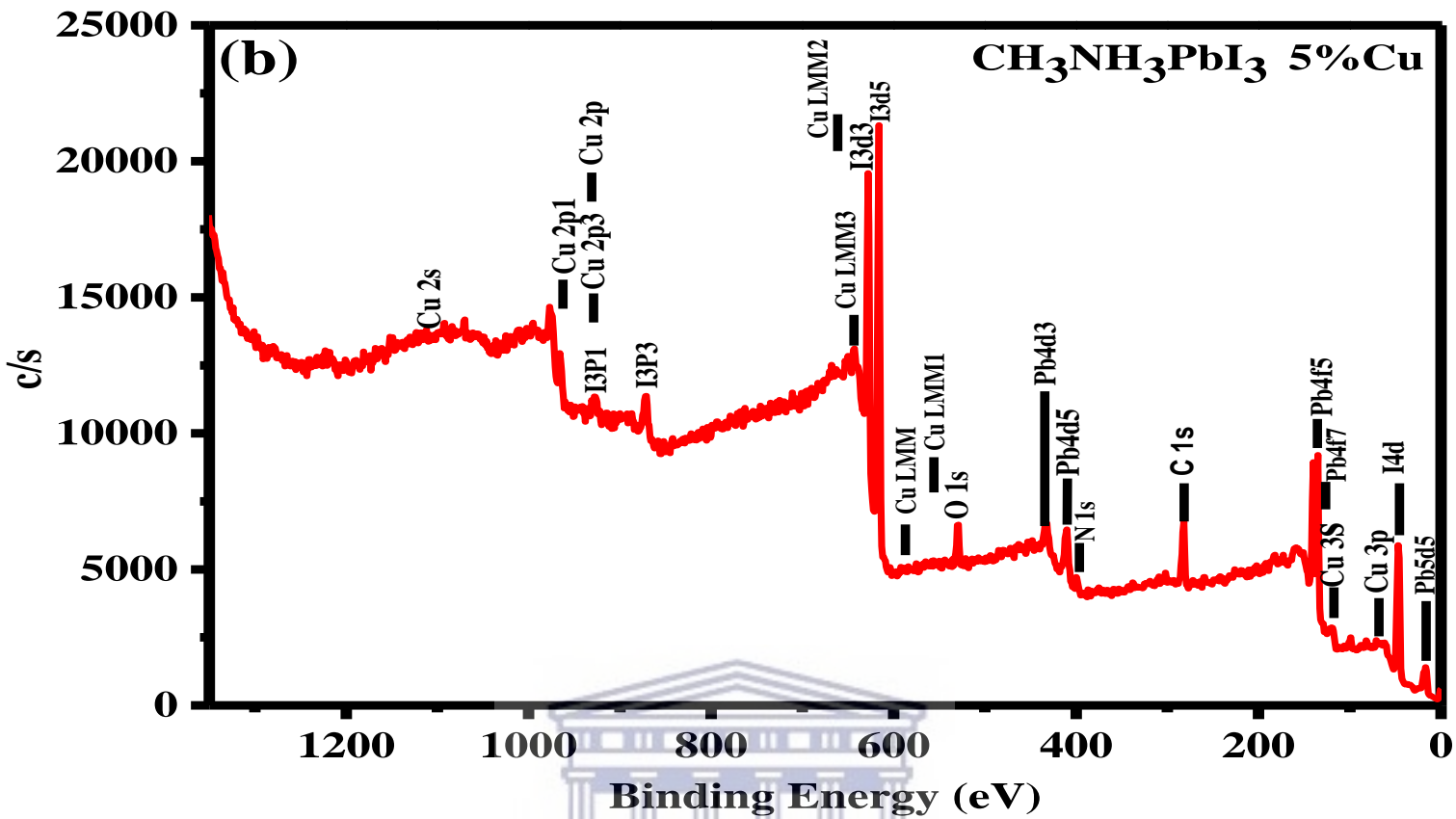
- [148] M. Neuschitzer, Y. Sanchez, S. L6pez-Marino, H. Xie, A. Fairbrother, M. Placidi, S. Haass, V. Izquierdo-Roca, A. Perez-Rodriguez, E. Saucedo, Optimization of CdS buffer layer for high-performance $\text{Cu}_2\text{ZnSnSe}_4$ solar cells and the effects of light soaking: Elimination of crossover and red kink, *Progress in Photovoltaics: Research and Applications*. 23 (2015) 1660–1667. <https://doi.org/10.1002/pip.2589>.

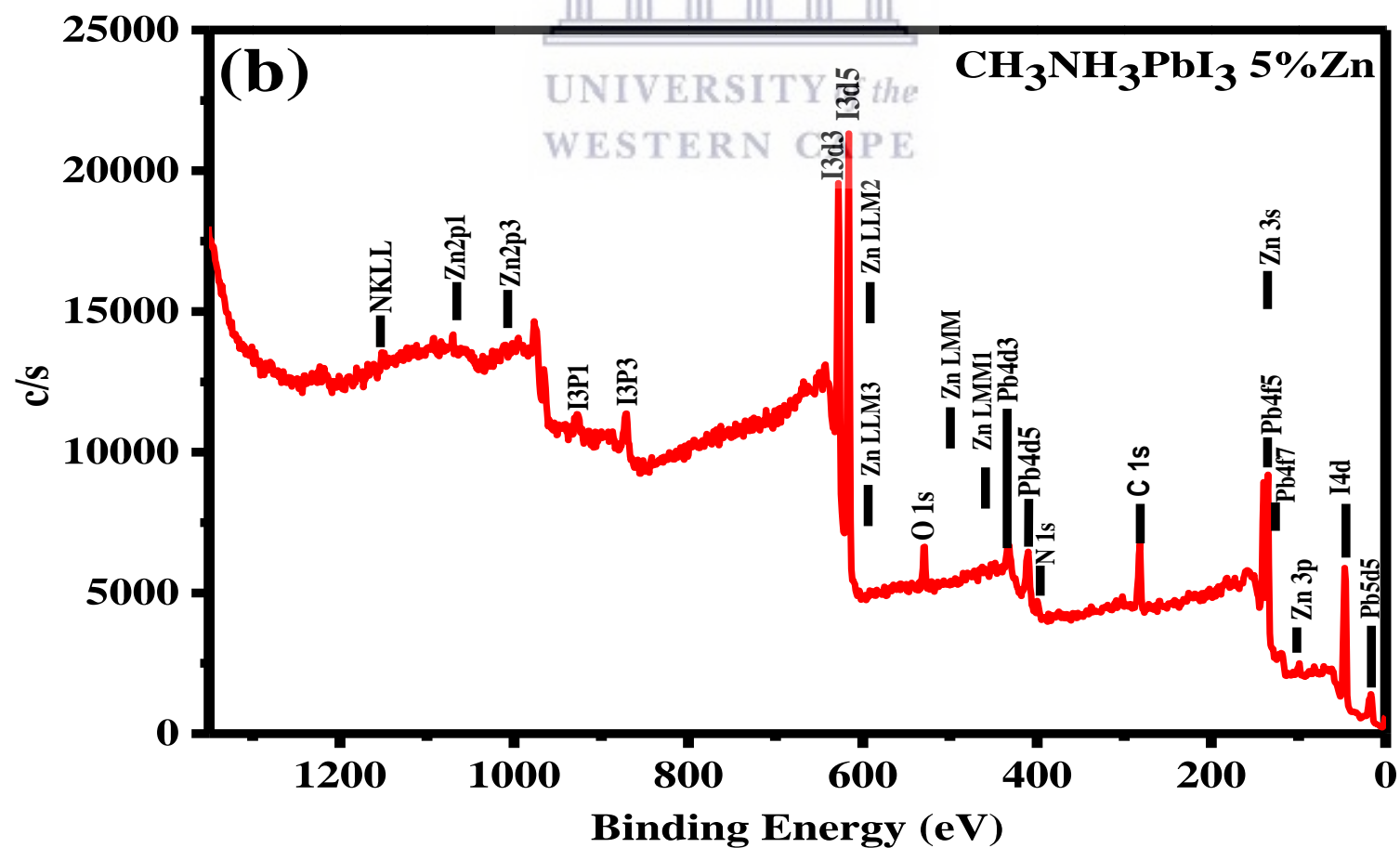
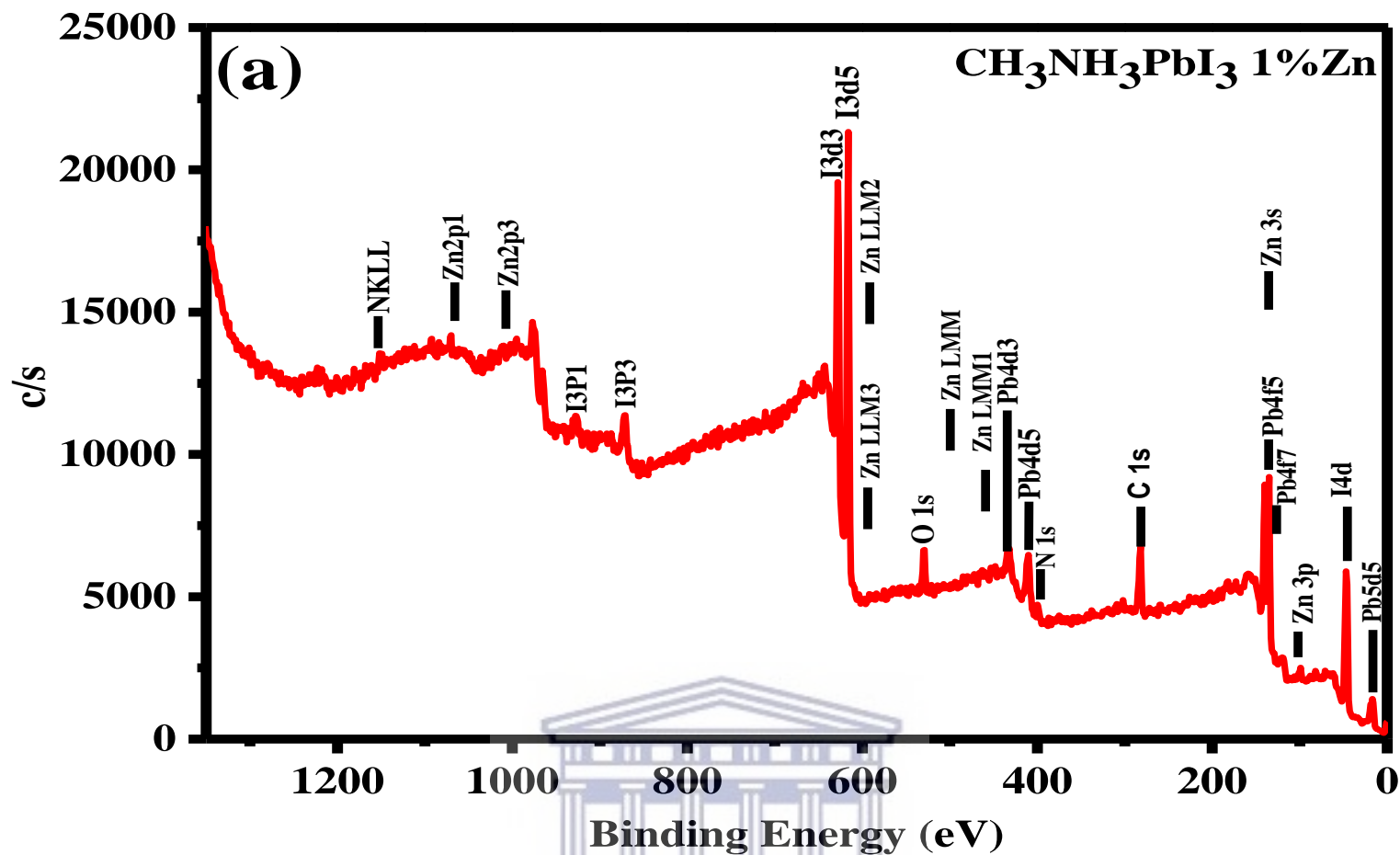


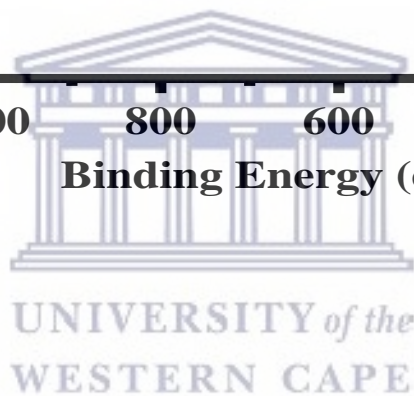
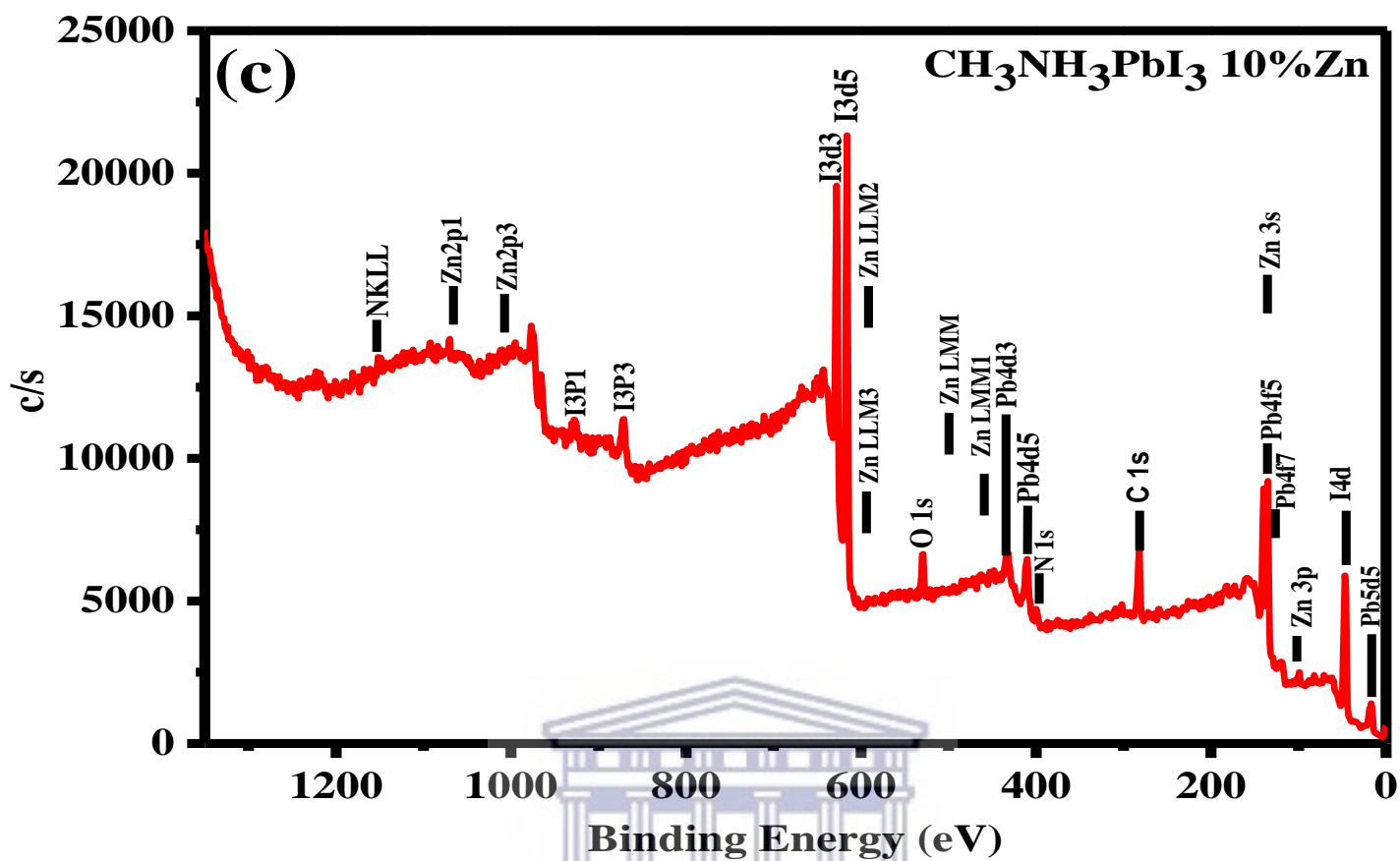
Supporting Information











CHAPTER 5

Conclusive summary and recommendations

5.1 GENERAL CONCLUSIONS

5.1.1 NiCuZn hybrid perovskite thin films

In this study, air-stable hybrid perovskite thin films incorporating earth abundant and non-toxic transition metals which include Ni, Cu & Zn; $\text{CH}_3\text{NH}_3\text{PbI}_3\cdot\text{Ni}$, $\text{CH}_3\text{NH}_3\text{PbI}_3\cdot\text{Cu}$ & $\text{CH}_3\text{NH}_3\text{PbI}_3\cdot\text{Zn}$, were prepared following a two-step solution deposition technique to address the issue of eco-toxicity posed by metal Pb and the poor stability against air (oxygen) and humidity (moisture). The terephthalic acid (TPA) additive was utilized to stabilize the perovskite thin film materials from deterioration (degradation) upon exposure to air (oxygen) and humidity. XPS measurements; wide scan survey and high resolution core level spectra, confirmed the elemental composition of all the materials under investigation. The Pb4f and I3d doublets displaying spin-orbit splitting into Pb4f_{5/2} & Pb4f_{7/2} and I3d_{5/2} & I3d_{3/2} were confirmed by high resolution core level spectra in all thin film materials. The C1s and N1s signals were also confirmed to exist on the surface of all the thin films. High resolution core level XPS measurements also demonstrated the presence of transition metal dopants; Ni, Cu, & Zn, the Ni2P doublet displaying spin-orbit splitting into Ni2P_{1/2} & Ni2P_{3/2} was observed, the Cu2P doublet displaying spin-orbit splitting into Cu2P_{1/2} & Cu2P_{3/2} was observed and Zn2P_{1/2} was also observed. From the XPS measurements, the successful incorporation of the transition metal dopants; Ni, Cu & Zn, into the perovskite crystal structure was confirmed.

All hybrid perovskite thin films materials in this study confirmed a pure perovskite phase in the tetragonal crystal system without a significant impact on the lattice parameters and space group. The preferential orientation of prominent peaks was illustrated towards (110), (112), (211), (202), (220), (310), (312), (224), and (314) which perfectly fits the pure phase tetragonal crystal system (space group $I4/mcm$) with lattice parameters; $a = b = 8.8390 \text{ \AA}$, $c = 12.6950 \text{ \AA}$, $\alpha = \beta = \gamma = 90^\circ$, (Volume of cell (10^6 pm^3): 991.83). The strong diffraction peaks observed at crystal planes of (110) and (220) confirmed the formation of pure tetragonal perovskite crystal structure. The lattice parameters were determined to be $a = b = 8.865 \text{ \AA}$ and $c = 12.6950 \text{ \AA}$ which compared very well with the ones reported in literature for pure tetragonal perovskite $\text{CH}_3\text{NH}_3\text{PbI}_3$ with $I4/mcm$ space group. The crystallite sizes for all thin films materials under investigation were determined to be $\text{CH}_3\text{NH}_3\text{PbI}_3$ (33.71 nm), $\text{CH}_3\text{NH}_3\text{PbI}_3 \cdot \text{Ni}$ (32 to 36 nm), $\text{CH}_3\text{NH}_3\text{PbI}_3 \cdot \text{Cu}$ (32 to 37 nm) and $\text{CH}_3\text{NH}_3\text{PbI}_3 \cdot \text{Zn}$ (35 to 42 nm). This shows that the transition metals Ni, Cu and Zn did not significantly shrink or expand the crystal structure of the traditional pure phase $\text{CH}_3\text{NH}_3\text{PbI}_3$ perovskite. This was ascribed to the unvarying size of organic cation A in the hybrid perovskite compound ABX_3 (where A = organic cation, B = metal and X = halide anions). It has been reported in literature that the expansion and compression of the whole crystal lattice is dependent upon the size of organic cation A. In this study, all thin film compounds utilized methylammonium as the organic cation A and this explains why there was no significant impact observed on the lattice parameters and the crystallite (grain) size. On average; the degree of crystallinity for $\text{CH}_3\text{NH}_3\text{PbI}_3$, $\text{CH}_3\text{NH}_3\text{PbI}_3 \cdot \text{Ni}$, $\text{CH}_3\text{NH}_3\text{PbI}_3 \cdot \text{Cu}$ and $\text{CH}_3\text{NH}_3\text{PbI}_3 \cdot \text{Zn}$ were determined to be 75.30%, 78.41%, 67.84% and 81.08%, respectively. Ni^{2+} and Zn^{2+} doped perovskites demonstrated an improved crystallinity property which is beneficial for optimum photovoltaic cell performance. XRD analysis also revealed that the two-step solution deposition technique employed in this study resulted in strained (micro-strain) hybrid

perovskite thin films with structural imperfections also known as dislocation density which are detrimental for the stability, optical properties and ultimately the photovoltaic performance of hybrid perovskite solar cells. The relaxation of micro-strain which resulted in reduced defect concentration (dislocation density) was largely observed for Zn doped hybrid perovskite thin films $\text{CH}_3\text{NH}_3\text{PbI}_3 \cdot \text{Zn}$. Therefore, $\text{CH}_3\text{NH}_3\text{PbI}_3 \cdot \text{Zn}$ thin films showed better potential/capacity for improved intrinsic stability, superior hole extraction capacity at the perovskite/hole transport layer boundary, increased carrier mobility and ultimately advanced photovoltaic performance.

Optical studies by UV-vis spectroscopy have demonstrated that the transition metal doped perovskite thin films largely absorb in the same range as the pure tetragonal $\text{CH}_3\text{NH}_3\text{PbI}_3$ (i.e. from ultra violet visible region (~550 nm) to near infrared region (~800 nm) of the solar spectrum) as seen from the results and these absorptions resulted in energy bandgaps (i.e. 1.55 eV) virtually equal to the one reported in literature for pure tetragonal $\text{CH}_3\text{NH}_3\text{PbI}_3$ perovskite thin film. In this study, all thin film compounds utilized methylammonium as the organic cation A and this explains why there was no significant impact observed on the lattice parameters (the B – X bond length was not altered) and the crystallite (grain) size (i.e. crystallite sizes were in close proximity to one another). Hence, there was no significant impact on the energy bandgap observed (i.e. all compounds had an energy bandgap of ~1.55 eV). Moreover, all compounds utilized iodine as the halide anion indicating that the electronegativity of the halide anion was kept constant and hence there was no impact observed on the energy bandgap. Thus, the NiCuZn hybrid perovskite thin film materials explored in this study have demonstrated a potential for application in single-junction solar cells owing to their narrow energy bandgap of ~1.55 eV.

Photoluminescence (PL) studies demonstrated slight redshift emissions (from 775 nm to ~780 nm for pure tetragonal $\text{CH}_3\text{NH}_3\text{PbI}_3$ and transition metal doped $\text{CH}_3\text{NH}_3\text{PbI}_3 \cdot \text{Ni/Cu/Zn}$

perovskite thin films, respectively). Photoluminescence studies further revealed the quenching effect induced by Ni and Cu which was attributed to imposed micro strain and dislocation density (structural defects) in the perovskite thin film materials, i.e. $\text{CH}_3\text{NH}_3\text{PbI}_3\cdot\text{Ni}$ and $\text{CH}_3\text{NH}_3\text{PbI}_3\cdot\text{Cu}$. However, for Zn doped thin film materials $\text{CH}_3\text{NH}_3\text{PbI}_3\cdot\text{Zn}$, a reverse effect was observed, Zn dopant advanced the radiative recombination emissions which was exhibited in higher photoluminescence emission intensity as the Zn content was increased from 1 to 10%. These results were attributed to relaxed micro-strain and lower degree of structural imperfections induced by Zn.

The evolution of surface morphology for all perovskite thin films was studied using HR-SEM technique. An interesting morphology was observed for the pristine (un-doped) tetragonal $\text{CH}_3\text{NH}_3\text{PbI}_3$. A layer of small sheet-shaped perovskite grains was observed at the vicinity of the hybrid perovskite grain boundaries at 200 nm magnifications. This morphology was attributed to the rich nucleation positions produced by the TPA molecule gathered at the vicinity of the hybrid perovskite grains which enhances the growth of bar-shaped bridges that morphs into small sheet-shaped perovskite grains. The underneath hybrid perovskite grains unified into interconnected hybrid perovskite communities. This morphology was in agreement with the morphology observed in the study reported in literature for the construction of efficient and stable perovskites via interconnecting perovskite grains. Nevertheless, it was observed that Ni and Zn dopants at 10% concentration suppressed the growth of sheet-shaped perovskite grains at the vicinity of $\text{CH}_3\text{NH}_3\text{PbI}_3\cdot 10\%\text{Ni}$ and $\text{CH}_3\text{NH}_3\text{PbI}_3\cdot 10\%\text{Zn}$ thin films, respectively. The materialized hybrid perovskite grains for $\text{CH}_3\text{NH}_3\text{PbI}_3\cdot 10\%\text{Ni}$ thin film demonstrated high degree of interconnectedness between the crystal grains boundaries as there were no cracks (defects) observed and only few defects were observed for $\text{CH}_3\text{NH}_3\text{PbI}_3\cdot 10\%\text{Zn}$ thin film. The layer of small sheet-shaped perovskite grains (relatively wider energy bandgap) at the vicinity of hybrid perovskite grains affected

the absorptions and photoluminescence emissions; slight redshift absorptions and photoluminescence emissions were observed for $\text{CH}_3\text{NH}_3\text{PbI}_3 \cdot 10\% \text{Ni}$ and $\text{CH}_3\text{NH}_3\text{PbI}_3 \cdot 10\% \text{Zn}$ thin films due to the absence of these small sheet-shaped perovskite grains, respectively. On the other hand, Cu doped thin films $\text{CH}_3\text{NH}_3\text{PbI}_3 \cdot \text{Cu}$ exhibited undesirable morphology of excessive amount of surface defects as the Cu content was increased from 1 to 10% suggesting a high degree of dislocation density (structural defects) and micro-strain imposed by Cu content on the thin films. A coarse $\text{CH}_3\text{NH}_3\text{PbI}_3 \cdot 10\% \text{Cu}$ thin film with a lot of small unreacted and recrystallized CuI reagent surrounding the original/underneath hybrid perovskite grains was observed. The $\text{CH}_3\text{NH}_3\text{PbI}_3 \cdot \text{Cu}$ thin films morphology explained the observed slight blue-shift in absorptions and photoluminescence emissions attributed to the excessive amount of surface defects imposed by Cu dopant. The AFM results obtained in this study correlated with the HR-SEM results. Reduced surface roughness was observed for thin films devoid of a layer of small sheet-shaped perovskite grains at the vicinity of hybrid perovskite grain boundaries; i.e. $\text{CH}_3\text{NH}_3\text{PbI}_3 \cdot 10\% \text{Ni}$ and $\text{CH}_3\text{NH}_3\text{PbI}_3 \cdot 10\% \text{Zn}$, respectively. AFM results revealed that the Cu dopant resulted in $\text{CH}_3\text{NH}_3\text{PbI}_3 \cdot \text{Cu}$ hybrid perovskite thin films with drastically heightened surface roughness attributed to the surface defects (also observed in top-view HR-SEM images), see **Figure 4.21** and **Figure 4.24**. AFM also revealed that the Zn dopant produced relatively more compact (dense) $\text{CH}_3\text{NH}_3\text{PbI}_3 \cdot \text{Zn}$ hybrid perovskite thin films. The experimental results obtained in this study demonstrated that Zn doped $\text{CH}_3\text{NH}_3\text{PbI}_3 \cdot \text{Zn}$ hybrid perovskite thin films exhibited high crystallinity quality, reduced micro-strain and dislocation density (structural defects) as well as improved surface morphology corroborated by relatively compact (dense) surface topography. As a result, intense radiative recombination emissions (good for photovoltaic applications) were observed for $\text{CH}_3\text{NH}_3\text{PbI}_3 \cdot \text{Zn}$ thin films, positioning Zn dopant as the best candidate amongst Ni and Cu for Pb-substitution in the

traditional $\text{CH}_3\text{NH}_3\text{PbI}_3$. This study contributes substantially to the ongoing research in quest for non-toxic (environmentally benign) and air stable hybrid perovskite thin film materials for photovoltaic applications.

5.1.2 Development of CZGSe kesterite solar cells

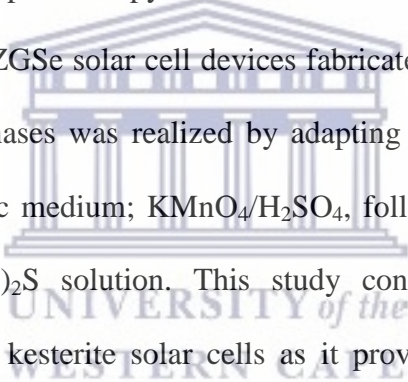
$\text{Cu}_2\text{ZnSn}(\text{S},\text{Se})_4$ (CZTSSe) kesterite absorber materials have emerged as potential candidates for earth abundant and non-toxic photovoltaics with great prospects for long-term sustainability in the arena of solar cell technology. However, the low open circuit voltage has been the main limitation for advance photovoltaic performance of the current CZTSSe kesterite solar cells in comparison to other solar cell technologies. The energy bandgap of a given semiconductor material is the main limitation for its open circuit voltage. The voltage loss is an adequate measure for comparing different technologies with different energy bandgap values. The voltage loss is defined as the difference between the energy bandgap potential and the open circuit voltage. Voltage losses of <400 mV can be attained for high efficiency CIGS and CdTe devices while the best kesterite devices can exhibit voltage losses around 550 – 600 mV. The remarkable beneficial impact demonstrated by nanometric Ge layers on the photovoltaic performance, especially on the open circuit voltage of sequentially processed $\text{Cu}_2\text{ZnSnSe}_4$ (CZTSe) solar cells has been reported recently. Moreover, the partial replacement of Sn atoms by Ge atoms has demonstrated advance absorber material quality for the kesterite crystal lattice.

In this study, the development of pure germanium kesterite $\text{Cu}_{1.2}\text{Zn}_{1.8}\text{GeSe}_4$ (CZGSe) solar cells was explored and it was inspired by the beneficial impacts demonstrated by nanometric layers of Ge (as well partial substitution of Sn atoms by Ge atoms) on photovoltaic performance (especially the open circuit voltage; V_{OC}) and advance material quality of

CZTSe-based solar cells reported in literature. A sequential sputtering/co-sputtering two-step technique was employed to produce solar cells with Mo/p-CZGSe/n-CdS/i-ZnO:ITO architecture. HR-SEM cross-sectional area analyses demonstrated that the sequential deposition of the precursor stack order: Mo/Cu(4nm, for 20s)/Zn/Cu/Ge yielded the CZGSe kesterite grains with good quality. The overall cross-sectional areal morphology of the CZGSe absorber exhibited a bilayer structural behaviour with an adequate quality of grains (enlarged grains with high degree of crystallinity) observed towards the near surface of the absorber. The enlarged grains observed towards the surface of the absorber are attributed to $\text{Ge}_x\text{Se}_{y(l)}$ (~85 at.%Se) liquid phase (crystallization flux) that promotes crystallization growth during thermal treatment. The optimal annealing parameters; annealing temperature $T = 535\text{ }^\circ\text{C}$, dwelling time $t = 15\text{ min}$, pressure $P = 1\text{ bar}$ and $20\text{ }^\circ\text{C/min}$ heating rate yielded absorbers with good crystalline quality as demonstrated by the Raman measurements. The optimal CZGSe absorber (1.42 eV) produced in this study yielded a corresponding solar cell device which attained 5.0% power conversion efficiency, 564.53 mV open circuit voltage, and 17.60 mA/cm^2 short-circuit current density and a fill factor of 50.53%. A remarkable advancement in the open circuit voltage of 592.66 mV attained through CdS buffer layer optimization studies was significant in comparison to the previously reported value of 558 mV in literature. This remarkable achievement was due to improved p-CZGSe/n-CdS junction that rules the operation of the kesterite solar cell devices. The V_{OC} deficit for CZGSe based solar cell in this study was determined to be 563.64 mV. This value demonstrates significant improvement in comparison to the value reported for advance power conversion efficiency (11.1%) for solar cells based on CZTSSe and it is also in the 500 – 600 mV range for the best performing kesterite devices.

The formations of volatile species (i.e. $\text{GeSe}_{2(g)}$ volatile phase that forms during thermal treatment) which result to issues on the Mo back-contact region (i.e. poor adhesion and the

development of voids revealed by HR-SEM cross-sectional area micrographs) remain an inherent challenge in the preparation of kesterite solar cell devices. The cause of the growth of these detrimental voids is still not clear but it is estimated to be connected to the stress at the Mo back region, the volatile species related to Ge (.i.e. $\text{GeSe}_{2(g)}$ volatile phase that forms during thermal treatment) and the probable disintegration of the CZGSe kesterite absorber in physical contact with Mo back-contact and/or low wetting properties of Cu on Mo during thermal treatment. This layer showed detrimental effects on the operation and photovoltaic performance of CZGSe solar cell devices developed in this study and it has limited the power conversion efficiency to values $\leq 5.0\%$. The presence of detrimental ZnSe (2.7 eV) secondary phases revealed by Raman spectroscopy has been another limitation to the overall photovoltaic performance of CZGSe solar cell devices fabricated in this study. The effective removal of ZnSe secondary phases was realized by adapting an oxidation path utilizing a permanganate solution in acidic medium; $\text{KMnO}_4/\text{H}_2\text{SO}_4$, followed by rinsing of a CZGSe kesterite absorber in a $(\text{NH}_4)_2\text{S}$ solution. This study contributes substantially to the development of CZGSe based kesterite solar cells as it provides a baseline standard and inspires future studies with the goal of improving the CZGSe absorber quality and power conversion efficiency beyond 5%.



5.2 RECOMMENDATIONS AND SUGGESTED FUTURE WORK

5.2.1 NiCuZn hybrid perovskite thin films

The first recommendation is that the hybrid perovskite thin films doped with higher concentrations (i.e. from 10 to 50%) of transition metals; Ni, Cu & Zn, must be explored using two step solution deposition technique to better study and understand the impact of these transition metals on the crystal structure, optical and microscopic properties of the traditional pure $\text{CH}_3\text{NH}_3\text{PbI}_3$. Photovoltaic devices with n-i-p planar heterojunction (PHJ) archetype employing the transition metal doped hybrid perovskites; $\text{CH}_3\text{NH}_3\text{PbI}_3\cdot\text{Ni}$, $\text{CH}_3\text{NH}_3\text{PbI}_3\cdot\text{Cu}$ and $\text{CH}_3\text{NH}_3\text{PbI}_3\cdot\text{Zn}$, as the active layer, Spiro-MeOTAD polymer as the hole transporting material, Au as the metal anode and Fluorine Tin Oxide (FTO) as the transparent cathode must be fabricated and tested under simulated solar irradiation (i.e. 1 SUN) to study the photovoltaic performance of these novel hybrid perovskite thin film materials. Secondly, a complete 100% substitution of Pb (Pb-free hybrid perovskites) by Ni, Cu & Zn must be carried out and the fundamental studies must also be conducted to understand the newly formed crystal structure, the optical, microscopic and photovoltaic properties of these novel materials.

Solution-based techniques are still believed to be a good attempt to attain inexpensive and large-area perovskite thin films although thin films prepared by chemical vapour deposition (CVD) techniques generally demonstrates high quality perovskite grains and compact perovskite thin films with advanced surface coverage. Leyden *et al.* [1] have reported that the CVD technique has potential for the fabrication of large area hybrid perovskite thin films which is important for industrialization and commercialization. This technique can be conducted under ambient conditions which makes it a competitive technique for the deposition of perovskite thin films. So, for future work, large area and Pb-free hybrid

perovskite photovoltaic cell modules based on transition metals; Ni, Cu and Zn, must be explored via CVD technique.

5.2.2 Development of CZGSe kesterite solar cells

As already mentioned in the discussion in chapter 4, the formations of volatile species (i.e. $\text{GeSe}_{2(g)}$ volatile phase that forms during thermal treatment) which result to issues on the Mo back-contact region (i.e. poor adhesion and the development of voids revealed by HR-SEM cross-sectional area micrographs) remain an inherent challenge in the preparation of CZGSe kesterite solar cell devices. It has also been reported in literature that the presence of secondary phases (ZnSe in case of CZGSe in this study), defects and defect-complexes at the Mo/CZGSe junction (voids and blisters revealed by HR-SEM cross-sectional area in this study) result in high carrier recombination and the ZnSe (2.7 eV) secondary phases with energy bandgap higher than that of CZGSe (1.42 eV) kesterite absorber, results in high series resistance and diminish the fill factor and the corresponding short circuit current which ultimately lead to an overall poor photovoltaic performance of the CZGSe based solar cells.

There are many strategies that have been reported in literature to improve the Mo/CZTS interface to mitigate/reduce the secondary phases, defects (i.e. voids and blisters) and defect complexes and improve the overall photovoltaic performance. These strategies will be applied in this study for CZGSe based solar cells to improve the overall photovoltaic performance;

- (i) An intermediate layer of Ag will be deposited onto the Mo back contact to repress the growth of defects (i.e. voids and blisters) as well as ZnSe secondary phases and MoSe_2 that forms in the CZGSe absorber layer and at

the Mo/CZGSe junction, respectively. This interface layer has been reported in literature to reduce the series resistance and carrier recombination and boost the power conversion efficiency from 2.3% to 4.4% for CZTS based solar cells [2].

- (ii) A thin layer of TiN (10 – 20 nm) has also been reported in literature by Scragg *et al.* [3] to mitigate the growth of ZnSe secondary phases and the defects that grow at the Mo/CZTS junction. So, in this study, this strategy will be explored by depositing a nanometric layer of TiN (10 – 20 nm) onto Mo before growing the CZGSe absorber to improve the Mo/CZGSe interface.
- (iii) A layer of ZnO thin film has also been reported to modify the Mo/CZTS junction and improve the overall photovoltaic performance [4]. For CZGSe based solar cells in this study, this metal oxide will also be deposited onto Mo back contact before growing the CZGSe absorber layer to improve the Mo/CZGSe interface.
- (iv) The improvement of open circuit voltage of CZTS based solar cells ($V_{OC} = 780$ mV and the corresponding power conversion efficiency of 8.8%) attained utilizing a Cu double layer, Cu-rich layer proximate to the Mo junction and Cu-poor layer proximate to the top of the surface, has been reported in literature by Tajima *et al.* [5]. This Cu double layer strategy will be explored in this study for CZGSe based solar cells.
- (v) It was observed that germanium di-selenide $GeSe_2$ (Alfa-Aesar powder, 99.999%) that is used to compensate for the loss of Ge content after reactive selenization is not actually a suitable candidate for that purpose. It was then assumed that after reactive selenization there is still $GeSe_2$ (solid powder) distributed on the surface of the CZGSe absorber but not actually incorporated

into the absorber itself as seen from XRF results. So, a new candidate; germanium mono-selenide GeSe (Alfa-Aesar powder, 99.999%), will be utilized in tandem with Se, i.e. Se + GeSe, during reactive selenization process at high temperature to compensate for germanium loss.

The power conversion efficiency of solar cell devices is intrinsically limited by a factor called Shockley-Queiser limit, regardless of how good a solar cell material is. The Shockley-Queiser limit calculates the theoretical maximal values of different solar cell parameters. Solar cell devices with multiple junctions like tandem solar cells have been reported in literature as an effective approach for attaining high power conversion efficiency and surmount Shockley-Queiser limit in single junction solar cells. Tandem solar cells consist of a top-cell (wider energy bandgap) and a regular bottom-cell (narrower energy bandgap). So, for future work, a low-cost and non-toxic kesterite absorber material $\text{Cu}_2\text{ZnGe}(\text{S}_x\text{Se}_{1-x})$ (CZGSSe) with energy bandgap that can be tuned from 1.4 to 2.0 eV will be explored and utilized as a wider energy bandgap material for the top cell to interface with the low cost and less toxic perovskite material $\text{Cs}_{0.25}\text{FA}_{0.75}\text{Pb}_{0.5}\text{Sn}_{0.5}\text{I}_3$ with narrower energy bandgap of 1.2 eV utilized as a regular bottom cell to produce high efficiency kesterite-perovskite $\text{Cu}_2\text{ZnGe}(\text{S}_x\text{Se}_{1-x})\text{-Cs}_{0.25}\text{FA}_{0.75}\text{Pb}_{0.5}\text{Sn}_{0.5}\text{I}_3$ tandem solar cells.

Bibliography

- [1] M.R. Leyden, Y. Jiang, Y. Qi, Chemical vapor deposition grown formamidinium perovskite solar modules with high steady state power and thermal stability, *Journal of Materials Chemistry A*. 4 (2016) 13125–13132. <https://doi.org/10.1039/c6ta04267h>.
- [2] H. Cui, X. Liu, F. Liu, X. Hao, N. Song, C. Yan, Boosting $\text{Cu}_2\text{ZnSnS}_4$ solar cells efficiency by a thin Ag intermediate layer between absorber and back contact, *Applied Physics Letters*. 104 (2014) 041115. <https://doi.org/10.1063/1.4863951>.
- [3] J.J. Scragg, T. Kubart, J.T. Wätjen, T. Ericson, M.K. Linnarsson, C. Platzer-Björkman, Effects of back contact instability on $\text{Cu}_2\text{ZnSnS}_4$ devices and processes, *Chemistry of Materials*. 25 (2013) 3162–3171. <https://doi.org/10.1021/cm4015223>.
- [4] X. Liu, H. Cui, W. Li, N. Song, F. Liu, G. Conibeer, X. Hao, Improving $\text{Cu}_2\text{ZnSnS}_4$ (CZTS) solar cell performance by an ultrathin ZnO intermediate layer between CZTS absorber and Mo back contact, *Physica Status Solidi - Rapid Research Letters*. 8 (2014) 966–970. <https://doi.org/10.1002/pssr.201409052>.
- [5] S. Tajima, T. Itoh, H. Hazama, K. Ohishi, R. Asahi, Improvement of the open-circuit voltage of $\text{Cu}_2\text{ZnSnS}_4$ solar cells using a two-layer structure, *Applied Physics Express*. 8 (2015) 082302. <https://doi.org/10.7567/APEX.8.082302>.